Evaluation and modelling of particle collection efficiency of electrostatic precipitation

P Jacobs

orcid.org/0000-0002-5205-0160

Dissertation accepted in fulfilment of the requirements for the degree *Master of Engineering Chemical Engineering* at the North-West University

Supervisor:	FH Conradie
Co-supervisor:	HWJP Neomagus

Graduation:	June 2023
Student number:	28570618

PREFACE

Declaration of authorship

I, Petronella (Ronel) Jacobs, hereby declare that the dissertation entitled: ***Evaluation and modelling of particle collection efficiency of electrostatic precipitation,*** which I herewith submit to the North-West University is in compliance with the requirements set for the degree: Master's in Chemical Engineering, is my own work, has been text-edited in accordance with the requirements and has not already been submitted to any other university.

P Jacobs (Student)

Signed on the 18th day of November 2022

Conference papers and presentations

P. Jacobs, F.H. Conradie, H.W.J.P. Neomagus, "Particle Collection Efficiency of Various Electrode Configurations during Electrostatic Precipitation," in *Conference of the National Association for Clean Air (NACA)*, Kempton Park, South Africa, 2022.

P. Jacobs, F.H. Conradie, H.W.J.P. Neomagus, "Computational modelling of the particle collection efficiency of an electrostatic precipitator with various electrode configurations and ash feed conditions," in *Conference of the Eskom Power Plant Engineering Institute (EPPEI)*, Midrand, South Africa, 2022.

Acknowledgements

I firstly want to thank my Heavenly Father for blessing me with the opportunity to pursue this degree and for giving me the strength and guidance to complete the work successfully.

Secondly, I would like to thank my supervisors, Dr. Frederik Conradie and Prof. Hein Neomagus for providing guidance and support throughout the completion of the project.

I further want to thank all of the university staff at the Engineering and Natural and Agricultural Sciences departments, who I consulted for assistance in upgrading the experimental setup and advice on the modelling work completed for this study. I would also like to acknowledge the EPPEI Emissions Specialisation Centre for partly funding the research of this project and NACA for providing me with the opportunity to present my work at their annual conference in Johannesburg on 5 – 7 October 2022.

Lastly, I want to thank my family for their never-ending love and support and for always believing in me.

ABSTRACT

Many South-African power plants use wire-plate electrostatic precipitators (ESPs); however, these ESPs, in practice, have yet to meet the expected high particle collection efficiencies and present relatively low collection rates under the current operating conditions. The characteristically high resistivity of South-African coal fly ashes contributes to the low collection efficiencies of the ESPs. Therefore, the operational configuration of these ESPs needs to be refined to improve the unit performance.

Experimental research was conducted on a laboratory-scale version of the industrial ESPs. An in-depth examination of the structural components and most significant contributing factors of ESP performance was carried out. The investigation was undertaken on a fundamental level to gain a detailed understanding of the basic working principles of the ESP unit and its response to different operating variables. This information was translated into several models (statistical, computational fluid dynamic, and empirical) that could be used to improve ESP collection efficiencies.

The ESP experimental data were first fitted to a quadratic response surface model (RSM). The RSM model was used to predict how – and to what extent – different variables affect the ESP collection efficiency. An analysis of variance (ANOVA) on the RSM model revealed that electrode geometry, collection plate spacing, and ash resistivity were the most significant factors affecting ESP efficiency. The number of discharge electrodes showed less remarkable yet notable effects on the collection efficiency, while the electrode spacing effects were almost negligible for non-shielding conditions.

Furthermore, a computational fluid dynamic (CFD) model was developed to describe the particle collection efficiency of an ESP with various electrode configurations and ash properties. The coupled air flow profiles, electrostatic field, and particle trajectories were modelled using the relevant physics relations in STAR-CCM+. Three-dimensional geometries of the ESP section were created in NX-12, and served as the simulation domains for the CFD model in STAR-CCM+. The CFD model exhibited a good correlation with the experimental data.

Two South-African coal fly ashes with -75 μm and -150+75 μm particle size fractions were used as feeds to the ESP for the experiments. Particle size distribution, particle density, X-ray fluorescence, and resistivity analyses were performed to study the effects of the related ash properties on ESP efficiency. Both ashes delivered low resistivity readings (10^{10} – 10^{11} Ω.cm) at atmospheric conditions. The higher resistivity ash showed shorter voltage ranges but better particle collection rates than the lower resistivity ash. The ESP performance was also evaluated for various ash feed loadings and deteriorated with decreased particle concentrations in the air. This was correlated to larger interdependencies between the fluid dynamic, particle dynamic, and electrostatic fields, making it more difficult to collect ash particles from low particle concentrations in the ESP, as opposed to bulk particle loads.

The CFD model was used to interpret the results from the ESP experiments. G-spike, sawtooth, and threaded rod geometries were considered for discharge electrodes in the ESP. The G-spike and sawtooth electrode designs produced high current densities, yielding up to 99% collection efficiencies. The threaded rod electrodes presented smaller current densities, with lower efficiencies (< 93%) than the other electrode geometries. The current and field distributions were unique for each electrode geometry and showed strong correlations with the particle flow patterns in the ESP. Shielding effects were observed for several ESP configurations, especially those involving G-spike electrodes. The shielding degree increased for smaller electrode spacings and larger plate spacings, notably reducing current densities and particle collection rates.

The particle collection efficiencies were also computed using the empirical Deutsch-Anderson and Matts-Öhnfeldt equations. The Deutsch-Anderson model assumes ideal ESP conditions, yielding modelled efficiencies 10 – 20% higher than the measured values. The Matts-Öhnfeldt model, on the other hand, produced accurate efficiency predictions with k-values ranging from 0.2 to 0.9 for various ESP operating conditions.

Keywords: *Fly ash, electrostatic precipitation, particle collection efficiency, CFD modelling, response surface modelling, Deutsch-Anderson, Matts-Öhnfeldt*

TABLE OF CONTENTS

LIST OF FIGURES

LIST OF TABLES

NOMENCLATURE

Experimental calculations		
Symbol	**Description**	**Units**
A_e	Electrode face area	cm^2
A_{Duct}	Duct cross-sectional area	m^2
A_{Nozzle}	Sampling nozzle area	m^2
D_{Nozzle}	Sampling nozzle diameter	m
I	Current	A
$(m_f)_i$	Gravimetric filter mass initial	g
$(m_f)_f$	Gravimetric filter mass final	g
m_G	Total gravimetric particle mass	g
m_s	Particle sample mass on thimble filter	g
$(n_{DT})_{in}$	DustTrak particle concentration at ESP inlet	$mg.m^{-3}$
$(n_{DT})_{out}$	DustTrak particle concentration at ESP outlet	$mg.m^{-3}$
$(n_G)_{in}$	Gravimetric particle concentration at ESP inlet	$mg.m^{-3}$
$(n_G)_{out}$	Gravimetric particle concentration at ESP outlet	$mg.m^{-3}$
Q_{Air}	Air sampling flow rate	$m^3.s^{-1}$
Q_s	Sampling volume flow rate	$m^3.s^{-1}$
Q_T	Total volume flow rate across duct	$m^3.s^{-1}$
t_a	Ash layer thickness	cm
t_{Run}	Total time of experimental run	s
V	Applied voltage	V
v_{Air}	Air sampling velocity	$m.s^{-1}$
V_s	Sampling volume of particle-laden air	m^3
V_T	Total volume of particle-laden air	m^3
Greek symbol	**Description**	**Units**
η_{DT}	Collection efficiency measured by DustTrak	%
η_G	Collection efficiency measured by thimble	%
ρ_r	Electrical resistivity of ash	$\Omega.cm$

Response surface modelling		
Symbol	**Description**	**Units**

x_i	Normalised level for factor i	-
y	Response variable	-

Greek symbol	**Description**	**Units**
β	Model coefficient	-
ϵ	Error term	-
η_{RSM}	Collection efficiency computed by RSM model	%

Computational fluid dynamic model – Air flow

Symbol	**Description**	**Units**
A_{Duct}	Duct cross-sectional area	m^2
D_H	Hydraulic diameter	m
I_t	Turbulence intensity	%
l_e	Eddy length-scale	m
l_t	Turbulence length-scale	m
L_x	Collection plate length	m
P	Absolute pressure	Pa
P_S	Standard pressure	Pa
P_w	Wetted perimeter	m
R	Universal gas constant	$\mathrm{J.(mol.K)^{-1}}$
Re_{D_H}	Hydraulic Reynolds number	-
R_S	Specific gas constant	$\mathrm{J.kg^{-1}.K^{-1}}$
S_y	Plate spacing	m
t	Time	s
T	Absolute temperature	K
T_S	Standard temperature	K
u	Air velocity	$\mathrm{m.s^{-1}}$
u_0	Air velocity at ESP inlet	$\mathrm{m.s^{-1}}$

Greek symbol	**Description**	**Units**
μ_f	Air dynamic viscosity	$\mathrm{kg.(m.s)^{-1}}$
μ_t	Turbulent viscosity	$\mathrm{kg.(m.s)^{-1}}$
ρ_f	Air density	$\mathrm{kg.m^{-3}}$
τ_t	Turbulence time-scale	s

τ_v	Momentum relaxation constant	s

Computational fluid dynamic model – Electrostatic field

Symbol	Description	Units
A_s	Electrode spike surface area	m^2
c	Molar ion concentration	$\mathrm{mol.\,m^{-3}}$
D_i	Ion diffusivity	$\mathrm{m^2.\,s^{-1}}$
D_ϕ	Electric flux density	$\mathrm{C.\,m^{-2}}$
E	Electric field strength	$\mathrm{V.\,m^{-1}}$
E_0	Onset electric field strength	$\mathrm{V.\,m^{-1}}$
F	Faraday's constant	$\mathrm{C.\,mol^{-1}}$
g_0	Air dielectric strength	$\mathrm{V.\,m^{-1}}$
J	Current density	$\mathrm{A.\,m^{-2}}$
J_s	Electrode spike current density	$\mathrm{A.\,m^{-2}}$
K_i	Ion mobility	$\mathrm{m^2.\,(V.\,s)^{-1}}$
m	Roughness factor in Peek's law	-
r_e	Equivalent thread electrode radius	m
z_i	Charge number	-

Greek symbol	Description	Units
δ	Standardisation factor	-
ε_0	Permittivity of free space	$\mathrm{F.\,m^{-1}}$
ε_c	Permittivity of air	$\mathrm{F.\,m^{-1}}$
ρ_c	Space charge density	$\mathrm{C.\,m^{-3}}$
ρ_d	Particle space charge density	$\mathrm{C.\,m^{-3}}$
ρ_i	Ion space charge density	$\mathrm{C.\,m^{-3}}$
σ	Air conductivity	$\mathrm{S.\,m^{-1}}$
τ_c	Turbulent charge time constant	s
τ_q	Charge time constant	s
ϕ	Electric potential	V

Computational fluid dynamic model – Particle dynamics

Symbol	Description	Units
A_p	Particle projected area	m^2
C_D	Drag coefficient	-

d_p	Particle diameter	m
F_c	Coulomb force	N
F_d	Drag force	N
F_g	Gravitational force	N
F_p	Pressure gradient force	N
g	Gravitational acceleration	$\mathrm{m.s^{-2}}$
m_p	Particle mass	kg
P_s	Static pressure	Pa
q_p	Particle charge	C
q_s	Particle saturation charge	C
Re_p	Particle Reynolds number	-
u_p	Particle velocity	$\mathrm{m.s^{-1}}$
V_p	Particle volume	$\mathrm{m^3}$
v_s	Particle slip velocity	$\mathrm{m.s^{-1}}$

Greek symbol	**Description**	**Units**
ε_r	Particle relative permittivity	-
η_C	Collection efficiency computed by CFD model	%
ρ_p	Particle density	$\mathrm{kg.m^{-3}}$
φ_p	Particle volume fraction	-

Empirical modelling

Symbol	**Description**	**Units**
A_P	Collection plate face area	$\mathrm{m^2}$
k	Matts-Öhnfeldt model constant	-
L	Half collection plate spacing	m
Q_f	Air volume flow rate	$\mathrm{m^3.s^{-1}}$
w	Particle migration velocity	$\mathrm{m.s^{-1}}$

Greek symbol	**Description**	**Units**
η_D	Collection efficiency computed by Deutsch-Anderson model	%
η_M	Collection efficiency computed by Matts-Öhnfeldt model	%

Subscripts

a	ash
c	Coulomb /charge
d	drag
e	electrode / equivalent / Eddy
f	fluid (air) / final
g	gravitational
i	ion / initial
p	particle
q	charge
r	relative / resistivity
s	spike / slip / static / saturation
t	turbulent
v	momentum
w	wetted
x	x-direction (horizontal)
y	y-direction (ESP cross-section)
C	CFD model
D	Deutsch-Anderson
G	gravimetric
H	hydraulic
M	Matts-Öhnfeldt
P	plate
S	standard / specific
T	total
0	inlet / initial / reference

Abbreviations

ANOVA	Analysis of variance
AQA	Air Quality Act
ASTM	American Society for Testing and Materials
CCD	Central composite design
CFD	Computational fluid dynamic
DC	Direct current
DT	DustTrak
EHD	Electrohydrodynamic
ESP	Electrostatic precipitator
FE	Finite-element
FV	Finite-volume
HEPA	High-efficiency particulate air
IEA	International Energy Agency
IEEE	Institute of Electrical and Electronic Engineers
ISO	International Organisation for Standardization
MES	Minimum emission standards
PM	Particulate matter
PSD	Particle size distribution
RMSE	Root mean-squared error
RSM	Response surface methodology
SCA	Specific collecting area
STP	Standard temperature and pressure
XRF	X-ray fluorescence
3-D	Three-dimensional

1. INTRODUCTION

In this chapter, the background and rationale for the current research are explained. Furthermore, the aim and objectives of this study are discussed.

1.1 BACKGROUND AND MOTIVATION

The leading abatement technology for harmful particulate matter (PM) emissions from South Africa's use of coal for power generation is electrostatic precipitators, and it is essential to achieve the maximum dust collection efficiencies of these process units. Coal is currently the largest source of electricity worldwide, having a 37% contribution to the global power supply [1]. Statistical analyses from the International Energy Agency (IEA) suggest that 22% of the world's power will still originate from coal by the year 2040 [2]. Therefore, coal is expected to remain the predominant form of electrical energy for the following two decades at the least. South Africa extensively utilizes its coal resources for power generation – especially compared to alternative power sources. According to the Department of Energy, South Africa derives 77% of its electricity from coal. Coal mines and power plants are also significant employment providers, and global coal exports support more than 40% of the country's annual export income. This further justifies the high economic value of coal for South Africa [3].

South Africa largely resorts to coal-related energy because coal resources are more abundant and less expensive than other forms of energy in the country. In addition, South Africa established coal-fired power stations in the late eighteen hundreds already and is, therefore, properly familiarised with and equipped for this type of technology [4]. Furthermore, South Africa's remaining coal reserve amounts to more than 50 billion tonnes, which is enough to sustain the country's current power consumption rate for another 200 years. For these reasons, coal is considered the most reliable and affordable energy source for South Africa [5]. Therefore, the aspiration toward the phasing out of coal-fired power plants and the exploitation of alternative energies is not driven by a limited coal supply, but rather an attempt to minimise greenhouse gas (GHG) emission rates and slow down climate change.

Coal is not the cleanest type of energy and significantly increases global air pollution levels. Coal-fired power plants have been reported to produce considerable amounts of harmful emissions, like sulphur oxides (SO_x), nitrogen oxides (NO_x), carbon oxides (CO_x), particulate matter, and several other greenhouse gases [5]. PM emissions comprise small airborne solid or liquid particles that pose various environmental and public health risks. Suspended particulates are generally distinguished into particles with diameters smaller than 10 μm (PM_{10}) and particles smaller than 2.5 μm ($PM_{2.5}$). $PM_{2.5}$ is considered more harmful to humans as the finer particles can penetrate deeper into the lungs and cause more extensive damage than coarse particles [2].

Due to South Africa's extensive use of coal-generated power over the years, it has become one of the top-listed countries for the highest levels of air pollution worldwide. Closer investigations have revealed that PM emissions are one of the primary forms of air pollution in South Africa and significantly contributes to

the country's mortality rate [6]. Fine suspended particles take weeks to settle out and are carried over many kilometres by air currents, resulting in large areas with high levels of air pollution. Particles in the air typically form smog, which drastically reduces the normal visibility range. Other environmental impacts of PM emissions include enhanced rates of climate change and inhibiting effects on the growth of natural plant life [2].

According to statistics, PM pollution also causes severe health problems for chronically exposed individuals, which encompasses around 50 million South-African citizens. Coal typically contains several harmful and even carcinogenic substances, many of which are incombustible minerals that constitute the particulate emissions of coal-fired boiler units [7]. When inhaled, these substances can cause heart failure and severe respiratory illnesses that often lead to early death [2]. Some coal-related species, like mercury (Hg), are highly toxic bio-accumulative chemicals that cause kidney failure, reproductive problems, and damage to the central nervous system [8].

The Department of Environmental Affairs of South Africa addressed the risks of air pollution by implementing strict regulations for industrial-scale units to limit their particulate, sulphur dioxide (SO_2), and NO_x emissions. These regulations are called minimum emission standards (MES) and are defined in Section 21 of the *National Environmental Management: Air Quality Act, 2004* [9]. The MES specified for solid fuel combustion processes are summarised in Table 1-1.

Table 1-1. Emission limits for solid fuel combustion, given by the NEM: AQA (2004) [9]

Criteria pollutant	**Plant status**	**Emission limit ($mg.Nm^{-3}$)***
Particulate matter ($PM_{2.5}$ and PM_{10})	New	50
	Existing	100
Sulphur dioxide (SO_2)	New	500
	Existing	3 500
Nitrogen oxides (NO_x)	New	750
	Existing	1 100

*Limits defined for concentrations normalised to 273 K, 101.3 kPa, and 10% O_2

The MES compelled existing power plants ("commissioned before the day of publication of the regulations" – 31 March 2010) to meet the 100 $mg.Nm^{-3}$ PM emission limit by the year 2015. On the other hand, newly commissioned plants were required to meet the more stringent PM emission limit of 50 $mg.Nm^{-3}$ immediately. However, all South-African power plants (new and existing) have been subjected to the 50 $mg.Nm^{-3}$ MES since 2020, and plants that exceed this PM limit stand the risk of forced legal closure [9].

Various types of particulate abatement technology have been developed and applied over the years to reduce the PM emissions of industrial-scale processes. The most common methods of PM control include cyclone separators, fabric filters, wet scrubbers, and electrostatic precipitators (ESPs). Fabric filters and ESPs are the most widely used for PM emission reduction in practice as this equipment exhibit the best performances, with particulate collection efficiencies as high as 99.9% [10].

ESPs have been preferred over fabric filters for PM control at coal-fired power plants in South Africa since ESPs are more robust and demonstrate larger effective operating ranges than fabric filters [11]. However, the ESPs in use have delivered unsatisfactory PM collection rates, which caused most South-African power plants to fail to comply with the specified emission standards [12].

The low efficiencies of ESPs at power stations in South Africa could be attributed to the ongoing energy crisis in the country. To compensate for the significant energy shortage, South-African power plants have operated the equipment at maximum capacity for long periods without performing routine maintenance . As a result, the plant units, including ESPs, have shown drastic decreases in performance over time [12].

Another reason for the low particle collection efficiencies of ESPs in this country could be the characteristically high mineral (ash) content of South-African coals compared to that of other countries, which might have been undercalculated at the ESP design stage. The larger fraction of incombustible matter in South Africa's coal produces larger volumes of fly ash (PM) emissions that need to be captured by the ESPs [13]. South-African coals are also low in sodium (Na) and lithium (Li) contents and produce high-resistivity fly ashes. High ash resistivity makes particle collection in ESPs more complicated and reduces ESP efficiencies [12].

South Africa has 18 active coal-fired power stations, and 15 of these stations are owned and operated by Eskom. In 2015, 60% of Eskom's power plants produced PM emissions far higher than the 50 $mg.Nm^{-3}$ limit that needed to be met within the next five years from that time. Some of the plants also exceeded the 100 $mg.Nm^{-3}$ emission limit that should already have been enforced by 2015 [12].

For that reason, Eskom replaced the existing ESPs at five of their power stations with more effective fabric filters to remove higher concentrations of PM from the emissions of these stations [11]. New Eskom power plants are also equipped with fabric filters rather than ESPs [14]. However, fabric filters do not tolerate high temperatures and gas volumes as well as ESPs and, therefore, require more frequent maintenance. In addition, even though fabric filters might show higher efficiencies initially, these efficiencies can decrease significantly after weathering, which could eventually result in lower PM removal rates compared to ESPs [11].

On top of the high maintenance and upkeep costs of fabric filters, retrofitting of existing ESPs with fabric filters is very expensive. Furthermore, the increased pressure on South-African power stations to satisfy the growing electricity demand allows no time for shut-down to perform the retrofitting, so approximately 50% of these stations still use ESPs [12]. Therefore, the focus has recently shifted from substituting ESPs with fabric filters to optimising the ESPs already in use to deliver collection efficiencies equivalent to that of fabric filters [15].

1.2 PROBLEM STATEMENT, AIM & OBJECTIVES

1.2.1 PROBLEM STATEMENT

Computational modelling presents a valuable basis on which the ESP process can be investigated and its particle collection efficiencies maximised by determining the best ESP configurations and operating conditions. However, the reliability of such a computational model first needs to be confirmed before it can be applied to ESPs in practice. This can only be achieved by verifying the model against an adequate amount of experimental data, which can be expensive and difficult to obtain when a high degree of accuracy is required. For this reason, many computational models from past studies have not been experimentally validated, and universally applicable experimental data on the ESP process is limited.

A large number of ESP experiments can provide information to develop the much-needed database that will be invaluable for future ESP modelling research. Experimentation on a small-scale demonstration unit of an ESP makes it possible to perform a detailed investigation of the ESP process and its fundamental principles. This is important to understand how ESPs work and to secure a reliable foundation upon which the model can be created. The small size of such an ESP laboratory setup also allows for more accurate measurements since the experiments can be carried out in a controlled environment.

Little attention has been given to the experimentation and modelling of the effects of variable and, especially, higher ash loadings on the particle collection efficiencies in ESPs. In addition, almost no information regarding the collection rates of different types of ash in a specific ESP could be found in previous studies, which shows the lack of research in this regard. Furthermore, most of the available ESP data and models are based on the wire discharge electrode geometry. Therefore, special consideration should be given to ESP experiments and models involving different irregular-shaped discharge electrodes.

New experimental data can be useful for the verification of previous experimental results, the progression of the current knowledge on the functioning of ESPs, and the refinement of existing ESP models. Additional ESP data can also be used to define generalised correlations, such as statistical models, that can be applied for the validation of previous and future models. A new computational model can also be developed, which can be evaluated against the empirical Deutsch-Anderson and Matts-Öhnfeldt models that have been commonly used for ESP designs in the past. This will provide valuable insight into whether an improved accuracy was achieved for the modelled collection efficiencies in ESPs.

1.2.2 AIM

The aim of this study is to develop a computational model that describes the particle collection efficiency for different discharge electrode and collection plate configurations and fly ash feed conditions in a laboratory-scale ESP.

1.2.3 OBJECTIVES

To achieve the aim of this study, the following objectives have been formulated:

1. Perform experiments to determine the effects of fly ash loading, type of ash, electrode geometry, and electrode settings on collection efficiency
2. Develop an improved computational model to simulate the interactive air flow profiles, particle trajectories, and electrostatic field in the ESP
3. Develop a model that accounts for the effect of fly ash resistivity on particle collection efficiency
4. Validate the computational model against experimental measurements
5. Use the model to investigate the fundamental principles involved in the ESP process
6. Apply the model to predict the particle collection efficiency for different fly ash feeds and electrode settings
7. Compare the collection efficiencies calculated with the computational model to the corresponding efficiencies predicted by the empirical Deutsch-Anderson and Matts-Öhnfeldt equations

1.3 SCOPE

The ESP experiments will be performed with coal fly ash samples from two South-African power stations. A small (-75 μm) and a large (-150+75 μm) particle size fraction will be used for each of the two ashes. The electrode type and arrangement, plate-to-electrode spacing, and fly ash feed concentration will be varied. The types of electrodes that will be investigated include the novel G-spike™ electrodes, sawtooth electrodes, and threaded rod electrodes with similar properties to the conventional wire electrodes. The electrode and plate material type will remain the same for all the experiments. The electrical system related measurements will be the voltage and current (the investigation of the rectification unit is outside the scope of this study). The solid particle concentration will be measured both gravimetrically, giving a cumulative value, and online, providing an instantaneous reading. This will be translated to a particle collection efficiency, which will be used as the indicator of performance to compare different configurations of the ESP. A two-level factorial design will be used because of the unique nature of each experiment, the number of variables, and the complex interactions of all the elements of the system. This approach will provide a large general knowledge base for the validation and comparison of different models. A statistical (RSM), computational fluid dynamic (CFD), and two empirical (Deutsch-Anderson and Matts-Öhnfeldt) models will be generated. The plate spacing, electrode spacing, number of electrodes, ash loading, electrode geometry, and type of ash (particle size and resistivity) are the only variables considered for the RSM model. The CFD model will include the conservation of mass and momentum, continuous and dispersed phase flow in the Lagrangian framework, electromagnetism and electrostatic potential, field charging, and turbulent dispersion models with two-way coupling. All the models will be used to evaluate the collection efficiencies for different ESP conditions with the changing of air flow, particle flow, and electric fields.

1.3.1 LIMITATIONS OF THIS STUDY

- The ESP experiments in this study are limited to a small-scale demonstration unit of an ESP and do not represent industrial-scale ESPs in practice
- The conclusions reached on the effect of inlet particle concentration on the collection efficiency are valid for experimental conditions, but may not be applicable to full-scale ESPs
- The relative magnitudes of the mechanisms operating in a full-scale ESP could differ from those investigated in the current study – for instance, the effects of gravity and turbulence relative to the electrostatic field
- The resistivity experiments are performed at ambient temperature and relative humidity conditions, similar to that in the laboratory-scale ESP setup, which are different from actual ESP conditions
- The temperature and relative humidity in the ESP channel are not regulated and fluctuate between experimental runs, which could have an effect on the ash resistivity
- Estimated values are used for the fly ash permittivity in the CFD model, since this parameter could not be measured experimentally
- The air velocity in the ESP channel is measured periodically in-between runs, instead of continuously during the experiments

1.4 REPORT OUTLINE

The report comprises six chapters: introduction, literature study, experimental procedure, model development, results and discussion, and conclusions and recommendations. The introductory chapter provides background on the reason for the research and the focus of the study. The literature review provides a more comprehensive discussion of the different aspects of electrostatic precipitation, especially those relevant to the results observed in this study. The experimental procedure includes a description of the experimental design followed for the ESP experiments and an explanation of the working of the ESP experimental setup. This chapter further provides information on the different strategies used to collect, store, and process data for further analysis. The model development chapter comprises a detailed outline of the modelling process and relevant mathematical equations used for the computational and empirical models. The different boundary conditions and input parameters for the models are also discussed. The results and discussion chapter first provides information on the findings of the fly ash characterisation analyses. This is followed by the observations made with the RSM model. Next, the different results obtained from the CFD model are discussed and compared to the results from the empirical models. In the last chapter, the main conclusions made from the results of this study are summarised. A list of recommendations is subsequently given to consider for future research on ESPs.

2. LITERATURE REVIEW

The following section elaborates on the different techniques of electrostatic precipitation. Furthermore, additional information regarding the working of ESPs is given. Several design considerations and problems typically encountered in ESPs are also discussed. Finally, the existing modelling strategies for describing ESP processes are investigated.

2.1 ESP TECHNOLOGIES

The different types of electrostatic precipitator technologies found in the industry are summarised in Table 2-1, according to information obtained from [15], [16], and [17].

Table 2-1. Types of ESP technologies [15]–[17]

ESP Type	Features	Advantages	Disadvantages
Wire-plate	• Flat plate collection electrodes • Wire discharge electrodes • Wires placed in rows between plates • Gas flow parallel to plates • Rappers remove dust	• Dry conditions • Simple operation • Suitable for large-scale particulate removal • Conventional ESP – most well-known • Versatile and robust	• Large unit • High installation cost • Rapping mechanism limited to dry particles • Insufficient removal of sub-micron and high-resistivity particles
Wet	• Water droplets capture dust particles for collection • Water conditioning for improved conduction • Water spray washes deposited dust from collection electrodes	• Suitable for wet, sticky, volatile, or high resistivity dust • Effective collection of fine particles • Potential for gas scrubbing applications	• Expensive • Require corrosion-resistant materials of construction • Produces slurry that is difficult to work with
Tubular	• Tube-shaped collection electrodes • Discharge wires situated on tube axes • Vertical gas flow • Wet removal technique	• Closed system (no gas escape) • Minimal re-entrainment • Suitable for adhesive, precious or hazardous materials	• Uneven current distribution • All disadvantages associated with wet ESPs
Two-stage	• Consists of two chambers • Particles charged in 1st chamber • Particles collected in 2nd chamber	• Longer residence times for particle charging and collection • Prevent back-corona • Smaller unit size • Economical	• Not suitable for large-scale applications • Not customisable

As seen in Table 2-1, various ESP technologies exist for different types of particulate abatement applications. Wet ESPs and two-stage ESPs are more advanced and exhibit higher collection efficiencies for tenacious dust particles than conventional wire-plate ESPs. Still, these technologies are generally complex, expensive, and limited to small-scale applications [16].

Wire-plate ESPs, on the other hand, present the most satisfactory performances at the widest range of operating conditions. Furthermore, the wire-plate ESP technology is the most suitable for removing high

concentrations of particulate matter from the large-volume flue gas of coal-fired power plants in an affordable manner [15]. Correspondingly, most ESPs implemented in South African power stations are wire-plate type ESPs, which is the main topic of discussion in the current study.

2.2 ESP OPERATION

An illustration of a typical wire-plate ESP and its different components is given in Figure 2-1. The ESP unit comprises a large rectangular chamber with diverging and converging sections at the front and rear ends, respectively. When flue gas enters the ESP, the increase in duct cross-sectional area from the inlet nozzle to the ESP chamber causes a reduction in the gas velocity. This allows the contaminated gas to maintain a longer residence time in the ESP for maximum particulate removal from the gas stream [18]. Perforated distribution grids are fitted over the front of the ESP to produce a uniform gas velocity across the chamber and evenly disperse particulates throughout the gaseous medium. This improves particle charging and collection in the ESP [19].

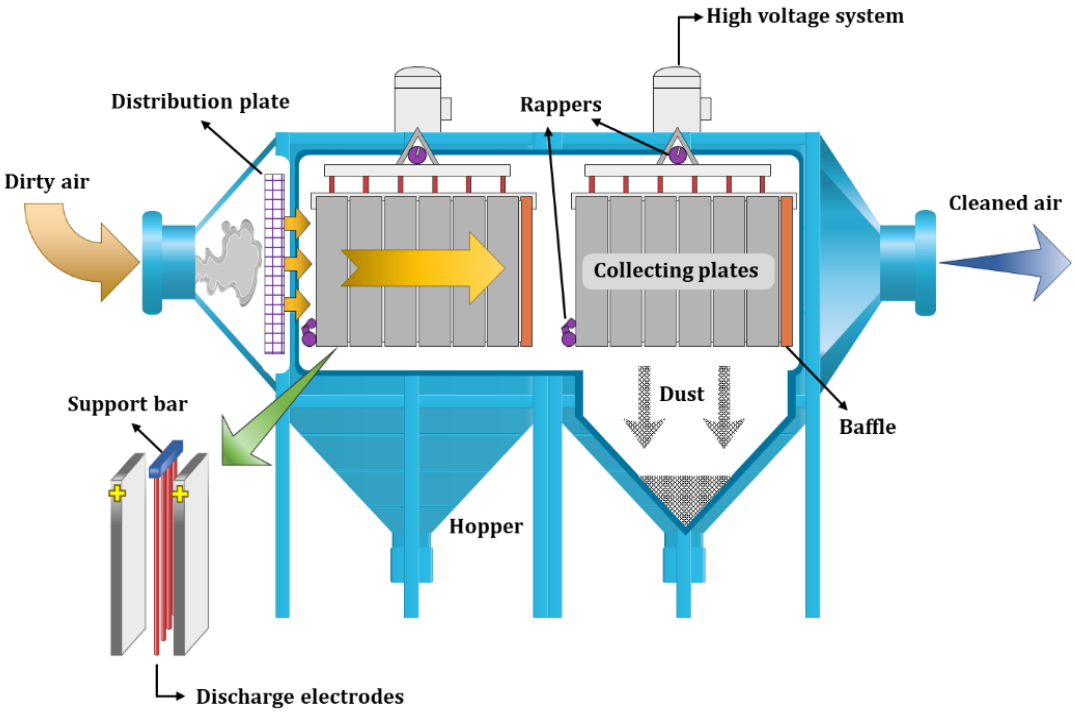

Figure 2-1. Typical industrial-scale wire-plate ESP, adapted from [19]

The electrostatic precipitation process includes two main steps for the removal of particles from the emissions at coal-fired power plants and other industries. The first step involves the electrostatic charging of particulates in the effluent gas from industrial units. In the following step, charged particles are captured on collection electrodes to be extracted from the gas flow [16]. This is achieved with electrostatic fields generated by multiple discharge electrodes that are located inside the ESP chamber [15].

In the case of wire-plate ESPs, the collection electrodes are flat plates installed in parallel. The discharge electrodes are series of long conductive wires mounted vertically to overhead support bars between the plate pairs. High-voltage direct current (DC) electricity is applied over each group of discharge electrodes

to impart a negative polarity to the electrodes [18]. On the other hand, the collection plates are electrically grounded and take on the role of the opposite polarity. Consequently, an electric potential gradient develops between the electrodes and collection plates, which generates the electrostatic field [16].

Corona current discharge forms around the electrodes if sufficient power is supplied for the resultant field intensity to exceed a certain threshold. The corona fields ionise the gas molecules in close vicinity to create local regions of negative space charge [18]. Suspended fly ash particles that pass through these regions attain a negative charge upon contact with the gas ions in the corona fields [20]. Charged particles are subjected to electrostatic attraction forces exerted by the grounded collection plates. This causes the particles to travel toward the collection plates along electric field lines and deposit on the plate surfaces. In effect, the particles exit the gas stream, resulting in a reduced particle concentration in the gas released into the atmosphere at the ESP outlet [15].

With time, the collected dust accumulates in layers on the collection plates, and the ESP collection efficiency decreases due to an accompanied weakened field intensity. In some cases, excessive dust build-up can cause back-corona with severe re-entrainment losses, which can significantly compromise the ESP performance [21]. To prevent this from happening, dust deposits are regularly removed from the collection plates with specialised rapping equipment. The rappers are small hammer-shaped tools used to apply high-frequency vibrations to the tops and sides of the collection plates and effectively detach dust layers from the plate surfaces. Separate hopper bins are situated under every plate-electrode assembly to capture dust discards that are subsequently transported away from the ESP unit on conveyor belts, or via hydraulic conveying systems in the case of South African ESPs [19].

Several design considerations are important for ESPs to function properly and cost-effectively. These include structural features and gas flow conditions, which are discussed more comprehensively in the following sections [22].

2.3 PRECIPITATOR SIZING AND DESIGN

The specific collecting area (SCA) is the most common sizing parameter used in the design of ESPs to date. The SCA of an ESP defines the total plate surface area available for particle collection relative to the volumetric flow rate of gas through the ESP [23]. Accordingly, a higher SCA ratio corresponds to a bigger ESP unit with a larger effective collection area. The selection of the best SCA for an ESP is a trade-off between low installation and operational costs for a smaller unit size and high collection efficiencies for a larger collection plate area and chamber volume [24].

Turner *et al.* (1988) provided sizing criteria and a step-by-step procedure to choose SCA values for different ESP applications with various types of particulate feeds based on the desired collection efficiency outcome. The steps include the subsequent determination of the ESP efficiency, particle escape fraction, operating temperature, the presence or absence of back-corona, and the minimum particle size to be collected in the ESP. The SCA value is obtained from tabulated empirical data for the corresponding ESP scenario. This strategy is, however, limited to rough estimations of the precipitator size and should only be applied to the

initial draft of the ESP design. Furthermore, the SCA values are associated with ESP conditions of negligible re-entrainment losses, which is not true for ESPs in practice [22].

Another popular ESP design methodology is that formulated by the Deutsch-Anderson equation, with which the plate area is sized for a particular efficiency as a function of gas volume flow and particle migration velocity toward the plates. The Deutsch-Anderson model assumes perfect flow distributions and constant particle properties, similar to optimum-case ESPs [25].

A common observation repeatedly reported in previous research is that the collection efficiency increases with increased electric field intensities. Correspondingly, an ideal scenario of an ESP entails maximum electric field intensities, such that a smaller unit size can be implemented to obtain the required collection efficiencies [22]. Furthermore, the highest field intensities are attained at the maximum voltage limit for a particular ESP setup. An ESP's operating voltage range depends on several factors, including the collection plate and discharge electrode configurations, the gas phase conditions, and the particle phase characteristics. Therefore, a good ESP design incorporates all of these aspects in the selection of a configuration with the widest voltage range and the strongest electric field for a specific ESP unit size [26].

2.4 FLOW CONDITIONS IN ESPs

Electrostatic precipitation involves a complex system of interrelated processes where the electric field, gas flow, and particle flow conditions are all affected by one another [15]. The gaseous and particulate flows in ESPs are considered in more detail in the following sections.

2.4.1 GAS PHASE CONDITIONS

The gas flow through the ESP significantly affects its particle collection efficiency and should be appropriately regulated. The best ESP performances have been reported for uniform gas flows, with velocities ranging from 0.6 $m.s^{-1}$ to 2.4 $m.s^{-1}$ [16]. Gas flow rates in the outlet ducts of industrial process units are too high for adequate electrostatic precipitation. Therefore, gas velocities are typically reduced at the ESP inlet by means of expanding joint sections between the duct and ESP chamber. This was previously explained in Section 2.2. In some practical systems, potential efficiency losses are compensated for by oversized ESP units that can accommodate gas volumes slightly larger than theoretical quantities [22].

Irregular gas flow profiles are undesirable as it can produce localised gas velocities that deviate far from what the ESP was originally designed for, which can ultimately lead to unanticipated collection efficiency reduction. Therefore, flow distribution structures, such as baffles or distribution plates, are often installed inside the duct in front of the ESP entrance to maintain an evenly distributed gas velocity throughout the ESP [16].

The gas flow through the ESP is strongly dependent on physical conditions, like temperature, pressure, and relative humidity. Changes in temperature and pressure can alter the gas density and viscosity, which are contributing factors in the turbulence degree, particle settling velocities, and fluid drag forces that influence the flow of suspended particles [22]. In addition, the gas density and volume are inversely proportional

parameters. Since the ESP capacity is customised for a specific gas flow rate, changes in the gas volume have secondary effects on the gas velocity through the ESP. While the ESP is flexible for variable flows within a specified operating range, excessive fluctuations in gas velocity can significantly impede ESP performance [16]. The gas density further affects the ion mobility, which governs the movement of ions in the electric field and, therefore, determines the current distribution through the ESP [23].

Gas temperature and humidity levels are also important aspects that influence particle resistivity, which affects the particles' behaviour and, therefore, the collection of particles in the ESP. However, since regulating such parameters in large-scale applications is a complex and expensive procedure, ESPs are designed to comply with the existing gas conditions [22]. On the other hand, particle resistivity is also dependent on the gas composition [23] and can be manipulated by the injection of conditioning agents into the gas phase. Conditioning agents often used in practice include sulphur trioxide (SO_3), ammonium (NH_3), sodium chloride (NaCl), and water. These substances are supplied in specific amounts according to the particles' inherent resistivity and the gas's physical properties in the ESP [16].

2.4.2 PARTICLE PHASE CONDITIONS

The particle flow is a critical parameter in determining the ESP collection efficiency. The movement of charged particles is controlled by electrostatic, aerodynamic, gravitational, and other forces that act on the particles as a function of their electrical, structural, and chemical attributes [27].

One of the key parameters regarding particle flow in an ESP that will receive focus in the current section is the particle loading – or the concentration of particles in the gaseous phase. Firstly, the particle phase can modify the gas flow by increasing or decreasing the turbulence degree in the gas medium. The matter of whether the particles' overall effect on the turbulent energy in the ESP is induction or inhibition-oriented depends on the average size of the particles [28].

The experiments of Kulick *et al*. (1994) demonstrated the influence of particles with 50 – 90 μm average diameters on the turbulent airflow regime through a channel. These particle sizes were confirmed to fall below the Kolmogorov length scale for the corresponding channel flow conditions. This criterion served as confirmation that the particles were small enough that micro-scale interactions between turbulent currents and particle flows were significant [29]. According to Kulick *et al*., higher velocities and mass fractions of finer particles decreased the turbulence in the channel, especially in the lateral-flow direction. The results from [29] were reproduced by Yamamoto *et al.* (2001), who further concluded that the particle-particle and particle-wall interactions were the governing factors for the reduced turbulence with small particles [30].

In a study by Tsuji *et al.* (1984), it was noted that larger particles enhanced turbulence in vertical-channel flows, while smaller particles resulted in reduced turbulence intensities for the same flow system. Furthermore, for intermediate-sized particles, turbulence effects were discovered to increase in the central region and decrease at the sides of the vertical channel [31]. These findings were supported by Gore and Crowe (1989), who determined a reference ratio of 0.1 for the particle diameter (d_p) relative to the turbulent length scale (l_t) [see Eq. 4.37, Section 4.2.6]. For particle-gas flows with a d_p/l_t ratio above 0.1, increased

particle loadings would lead to a higher degree of turbulence. Conversely, flows with a d_p/l_t value below 0.1 would reduce turbulence effects at higher particle concentrations [32].

Hetsroni (1989) later concluded that coarse particles with large Reynolds numbers contributed to turbulence and fine particles with small Reynolds numbers alleviated it [33]. Kussin and Sommerfield (2002) confirmed this also to be the case in horizontal particle-gas flow systems [34]. Finally, Gai *et al*. (2020) reinstated these observations in a more recent study and developed a numerical model that incorporates all of the abovementioned findings to compute the turbulence change due to particle flows [28].

In turn, gas turbulence can affect the particle flows and promote collection by improving particle dispersion in the ESP. Alternatively, excessive turbulence can produce high gas velocities near the plates, which can cause particles on the plates to re-entrain in the gas stream, thereby reducing the ESP efficiency [22].

Gai *et al*. defined separate flow regimes for one-way, two-way, and four-way gas-particle interactions based on the relative turbulence effects and particle fractions, using information reported in the work of Yamamoto *et al.* (2001) [30]. In general, for particle mass fractions below 10^{-6}, particle effects on the gas flow are insignificant, and only one-way interactions from the gas phase on the particle phase are present. Two-way interactions between the particle and gas phases exist for mass fractions between 10^{-6} and 10^{-3}. Finally, particle mass fractions above 10^{-3} correspond to the four-way coupling regime, which involves both particle-particle and particle-gas interactions [28].

For more significant ash loadings (≥ 1 $g.m^{-3}$), the particles can also have an influence on the electric field. High concentrations of particles in the corona charging regions can enhance the local space charge. If the space charge around the electrodes becomes too large, it can deform the surrounding field lines, which can suppress the current density in the areas between two electrodes. This will lead to lower collection efficiencies due to slower particle charging rates and weaker electrostatic attraction forces between the particles and collection plates [35].

Furthermore, high particle volume fractions in the gas increase dust layer accumulation rates on the collection plates. For a dust layer thickness beyond approximately 5 mm, the ESP demonstrates considerably weakened current-voltage relationships and, therefore, drastically lower electric field intensities, which can decrease collection efficiencies by more than 50%. Large amounts of high resistivity particles on the collection plates will further lead to earlier sparkovers, which can significantly restrict the ESP's field generation and particle collection capacity (see Section 2.6.2) [36].

Therefore, the fly ash loading must be carefully monitored to ensure the best ESP performance with the highest particle collection efficiencies. This requires a more in-depth analysis of particle characteristics, the most important of which include the particle size distribution of poly-dispersed dusts and the particle resistivity [22]. These concepts are elaborated in Sections 2.5 – 2.6.

2.5 FLY ASH PSD IN ESPs

The particle size distribution (PSD) of the fly ash to be collected from the emissions of coal-fired power plants is an important factor for ESP performance, especially regarding the particle charging and collection processes in the ESP [15].

According to Coulomb's law for electrostatics, the strength of the electrostatic attraction force between the particle and collection plate surface increases as the charge on the particle increases. The charge acquired by a particle in an electrostatic field is directly proportional to the particle's volume. Correspondingly, particles of larger size and, effectively, larger volume typically experience stronger electrostatic attraction toward the collection plates and travel at higher velocities to the plate surfaces [27].

The same principle applies to the gravitational, fluid drag, and other body forces that act on the entire particle volume. As a result, larger particles also attain higher terminal velocities than smaller particles and consequently demonstrate higher settling rates in ESPs. Therefore, fly ash comprising coarser particles should theoretically exhibit higher collection efficiencies through electrostatic collection and gravitational settling in ESPs [37]. This concept was already tested in previous research studies.

Kim *et al.*(2001) performed experimental research on a pilot-scale single-stage ESP to determine the effect of various ash properties on particle collection efficiency. Regarding the ash PSD in particular, it was found that fly ash with an average particle diameter of 16 μm showed higher collection efficiencies than finer fly ash with an average particle diameter of 11 μm [37].

In another study by Chengfeng *et al.* (2004), PSD analyses were conducted on the fly ash discards from the series of hoppers of ESPs at four power plants in China. These results showed a characteristic maximum coarseness for the ash from the first hopper at the front of the ESP and a sequential decrease in the average particle size along the range of hoppers to the end of the ESP. It was also observed that the first hopper contained the largest volume of collected ash and that each subsequent hopper contained a smaller quantity than the previous one [38].

This confirmed that large particles were easily and effectively collected, shortly after entering the ESP, whereas finer particles were collected later in the downstream hopper bins. Chengfeng *et al.* attributed this to the ESP's high initial collection efficiencies for large particles, which gradually decreased as the average size of remaining particles in the gas decreased. Sarkar *et al.* (2012) completed similar experiments for fly ash samples from the hoppers of industrial-scale ESPs at an Indian coal-fired power plant [39] and obtained findings analogous to that of Chengfeng *et al.* (2004) [38].

2.6 FLY ASH RESISTIVITY IN ESPs

The electrical resistivity of fly ash is one of the main factors determining the efficiency of ESPs. It is, therefore, an important ash property that has been extensively investigated in electrostatic precipitation [40].

2.6.1 ELECTRICAL RESISTIVITY OF FLY ASH

The resistivity of a material is a measure of its resistance to the flow of electric current. Though it is a characteristic material property, mainly dependent on chemical composition, resistivity also varies with changes in surroundings, such as temperature and humidity. An important note regarding resistivity in the following discussion is that this property is inversely proportional to conductivity. When the conductive ability of a species increases, its resistivity decreases, and vice versa [41].

Several studies have been conducted on the resistivity of different substances to investigate this quality as a function of various factors. The most important factors that affect fly ash resistivity in electrostatic precipitators and that will be focused on in this study include flue gas temperature and relative humidity, electric field strength, and ash composition [42].

Fly ash resistivity exists in two forms – surface resistivity and volume resistivity – depending on whether conduction primarily occurs on the particle surface or throughout the entire particle volume. Volume conduction dominates at temperatures in the range of 250 – 450 °C and takes place through internal charge transfer by sodium (Na) ions [43], as well as electrical conduction [42] in the fly ash. On the other hand, surface conduction is predominant at temperatures below 125 – 150 °C. This type of conduction occurs due to the adsorption of moisture and ionic species from the flue gas onto the ash to form a conductive layer on the ash surface. The surface conduction mechanism depends on the flue gas composition and temperature, the electric field magnitude, and the chemical properties of the ash. The ash's alkali metal ion content is particularly important for surface conduction since these ions are the primary means of charge transport on the ash surface [43].

Besides the alkali metals, such as sodium (Na), potassium (K), and lithium (Li) already mentioned, other components in fly ash are also known to affect electrical resistivity significantly. These elements include silicon (Si), aluminium (Al), calcium (Ca), magnesium (Mg), and iron (Fe) [36], and the specific contribution of each are summarised in Table 2-2.

Table 2-2. Effect of fly ash composition on resistivity, obtained from [44] and [45]

Chemical species	Description	Effect on resistivity
Sodium oxide (Na_2O)	Ionic charge carrier	Increase
Potassium oxide (K_2O)	Ionic charge carrier	Increase
Lithium oxide (Li_2O_3)	Ionic charge carrier	Increase
Iron oxide (Fe_2O_3)	Increases chemical solubility	Increase
Silica (SiO_2)	Electrical insulator	Decrease
Alumina (Al_2O_3)	Electrical insulator	Decrease
Calcium oxide (CaO)	Compacts lattice structure	Decrease
Magnesium oxide (MgO)	Compacts lattice structure	Decrease

As previously stated, alkali metal ions, especially sodium ions, can considerably reduce the resistivity of fly ash since these are charge-carrying species that support ionic conduction. According to Bickelhaupt

(1975), the resistivity of fly ash is not directly affected by its iron content. Instead, the presence of Fe promotes the dissolution of chemicals in the ash, which increases the concentration of potassium ions that, in turn, reduces the resistivity due to its conductive properties [43].

On the contrary, covalent compounds like Silica (SiO_2) and Alumina (Al_2O_3) are electrical insulators that prevent the flow of current, thereby increasing the electrical resistivity of ash [44]. Furthermore, oxides of calcium (CaO) and magnesium (MgO) have been reported to obstruct the ion flow for charge transport, which further increases fly ash resistivity [45]. Although all of the stated chemicals contribute to fly ash resistivity to some extent, some effects are more significant than others. The Na, K, and Li contents, for instance, are said to have a more notable impact on the resistivity than Fe, Ca, and Mg, which, in turn, have a more significant effect on resistivity than Si and Al compounds [45].

Elemental sulphur (S) commonly observed in coal forms sulphur oxides (SO_2 and SO_3) during combustion. The SO_3 gas reacts with moisture on the surface of ash particles to form an electrolytic solution of sulphuric acid (H_2SO_4), which increases surface conduction [41]. In industry, this process is artificially enhanced by injecting additional SO_3 and moisture into the flue gas to reduce the fly ash resistivity for better particle collection in ESPs. This technique is known as flue gas conditioning and is commonly implemented for high-resistivity ash applications [16].

It was previously stated that flue gas temperature also plays an important role in fly ash resistivity. In a study by Zheng *et al*. (2018), fly ash resistivity increased as temperature increased to 100 – 200 °C. Beyond this temperature range, resistivity values gradually decreased with a further rise in temperature. They attributed this to the fact that the temperature regime determines whether conduction is mainly volume-based or surface-based.

At temperatures below 100 °C, conduction is strictly driven by the surface mechanism, which is strongly dependent on surface moisture for the production of a conductive medium on particle surfaces. As temperature increases, the amount of moisture that physically adsorbs onto the ash particles decreases, leading to an increase in surface resistivity. The resistivity increases until it reaches a specific temperature between 100 °C and 200 °C, where conduction transitions to the volume mechanism. In this case, elevated temperatures improve conduction by promoting the release of ions and increasing ion mobility for better charge transfer, which decreases volume resistivity [45].

The relative humidity of the flue gas is another noteworthy parameter pertaining to resistivity, mainly because water dissolves the chemical components of fly ash to produce ionic species that transport charge across the ash surface. Furthermore, the fly ash resistivity decreases with an increase in electric field strength, corresponding to a higher charge concentration available in the flue gas for transmission to the suspended particles. In addition, the electrostatic forces control the movement of ions in the ash particles. This causes all the ions to migrate to the side of the ash particle closest to the collection plate, facilitating stronger attraction toward the plate surface [43].

Fly ash resistivity is susceptible to change under the influence of an electric field beyond a certain threshold value. This occurs due to an increase in electron transfer between neighbouring fly ash particles through the Schottky effect [46]. The Schottky effect occurs when the electric field applied over a conducting material – in this case, ash – is strong enough to intensify the characteristic thermionic emission of the ash particles at a specific temperature.

Thermionic emission is a term that describes the release of electrons from a conductor surface using thermal energy sourced from the conductor itself [47]. The electric field lines provide guided paths along which electrons can travel. The additional energy supplied by the electric field accelerates the dissipation of electrons from the particle surfaces to increase the thermionic emission of individual ash particles. This improves electron transfer through the ash volume, which decreases fly ash resistivity [48].

2.6.2 EFFECT OF ASH RESISTIVITY ON ESP PERFORMANCE

The fly ash resistivity significantly affects particle collection efficiency in terms of particle charging and migration rates, particle adhesion to plate surfaces, and back-corona. In an ideal case, a particle's resistivity should be such that it can charge and migrate fast enough to be removed from the gas stream before it exits the ESP. Secondly, collected particles should gradually release the acquired charge to prevent charge build-up in the ash layer, yet slow enough to maintain attraction to the plate [42].

Fly ash particles with low electrical resistivity are easily charged due to the particles' good conduction to current flow. These charges are, however, small, which causes the particles to move at slow migration velocities toward the collection plates under the influence of weak electrostatic forces [43]. Furthermore, once a low resistivity particle deposits on the plate surfaces, it loses most of its charge just as quickly as it gained charge in the first place. Since the particle now has a smaller polarity gradient with the plate, its adhesion forces are weakened. This causes it to dislodge and become re-entrained in the gas stream, leading to a decrease in collection efficiency [44].

Conversely, excessively high fly ash resistivities can present different problems in ESPs. Firstly, due to the high electrical resistance of high resistivity ash, its particles exhibit slow initial charging rates. In addition, high resistivity particles struggle to release charge after being collected on the plates. This causes an accumulation of charge in the ash on the plate surfaces, eventually triggering the dielectric breakdown of gas in the ash layer – an occurrence known as back-corona. Back-corona interferes with the particle charging process (see Section 2.7.3) and decreases particle collection efficiency [40].

Bucher (1970) and Chandra (2009) distinguished fly ash resistivity into several categories according to its effect on ESP performance (summarised in Table 2-3).

Table 2-3. Classes of fly ash resistivity in electrostatic precipitators obtained from [49] and [44]

Resistivity range (Ω.cm)	Level	Effect on efficiency	Reason(s)
$10^3 – 10^8$	Low	Decrease	Loses charge upon contact with collection plate → re-entrains in gas
$10^8 – 10^{11}$	Intermediate	Increase	Charged easily Maintains sufficient charge to stay on plates
$10^{11} – 10^{13}$	High	Decrease	Difficult to charge → slow migration to plates Accumulates charge on plates → sparkover

Due to South African coal's low sulphur content, the fly ash emissions of South Africa's power stations typically have high resistivities in the order of 10^{11} Ω.cm or more. This poses considerable limitations in the operating conditions of ESPs, due to the early initiation of a sparkover caused by electrical breakdown [50].

According to Mizuno (2000) and Roberts *et al*. (2000), the ESP performance can be subdivided into regions of high re-entrainment for dust resistivities below 10^4 Ω.cm, normal operation for ~10^5 – 5×10^{10} Ω.cm, and high back-corona above 10^{12} Ω.cm [51], [52]. This is shown in Figure 2-2.

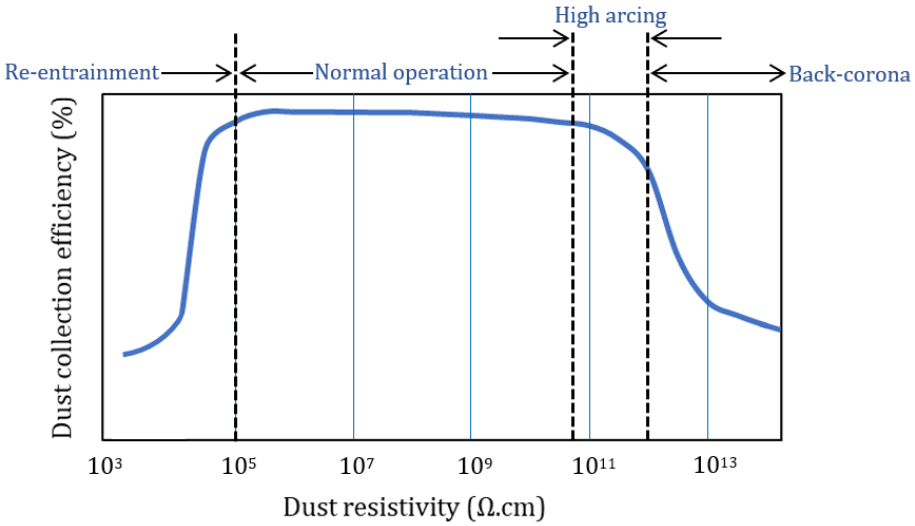

Figure 2-2. ESP collection efficiency as a function of dust resistivity, adapted from [51] and [52]

2.7 PROBLEMS IN ESPs

Numerous problems frequently encountered in ESPs have been preventing this equipment from achieving the desired operating efficiencies. Some of the most common and significant issues associated with ESPs include unsatisfactory electric field intensities, efficiency losses by means of re-entrainment, excessive sparkovers, electrostatic shielding, and uneven particle-laden flow distributions [16].

2.7.1 WEAK ELECTROSTATIC FIELD

High electric field intensity is crucial for ESPs to deliver high particle collection efficiencies. ESPs can produce electric fields of insufficient strength due to a variety of reasons [22].

The first and most logical reason is an inadequate voltage supply [16]. High voltage input requirements result from the ineffective design of discharge electrodes or improper selections of discharge electrode and collection plate configurations. Such ESP assemblies consume more power and return smaller current outputs, which often lead to lower-than-expected field intensities [15].

The shape and size of a discharge electrode significantly influence the electrode's ability to generate current discharge in the ESP. Accordingly, the characteristic current-voltage relationship of a specific discharge electrode design determines the resulting electric field intensity in the ESP [53]. Furthermore, the field and current density directly relate to the particle charging efficiency, which is the first fundamental step of the electrostatic precipitation process [15].

The positioning of discharge electrodes relative to one another and the collection plates also plays an important role in the electrostatic field properties. Certain ESP setups can significantly restrict the maximum voltage supply, drastically lowering the peak electric field strength and decreasing particle collection efficiency [54]. Therefore, electrode and plate settings must be selected to create complimentary combinations that form the strongest electrostatic fields [22].

Another cause of weak electric fields in ESPs is the under-sizing of discharge and collecting electrodes due to the over-simplification of design equations. This is a well-known problem for the Deutsch-Anderson relation, which excludes numerous variables from the computation of the particle migration velocities, resulting in SCA ratios that are too low for realistic ESP systems. Consequently, the collection efficiencies attained during operation are considerably lower than theoretical values [16].

An excess of dust deposits on the collection plates can also have dampening effects on the electrostatic attraction forces and, therefore, reduce the electric field intensity [36]. This stresses the importance of a high-efficiency rapping system to properly remove particulates from the collection plates [16].

Other factors, like high resistivity dust and shielding effects, contribute to weakened fields and decreased current densities [15]. These aspects are further discussed in Sections 2.7.3 and 2.7.4 that follow.

2.7.2 PARTICLE RE-ENTRAINMENT

Particles with larger diameters form stronger electrostatic attraction forces with the oppositely charged collection plates and travel at higher speeds to the plate interfaces. This can improve the collection efficiencies of such particles to some extent. However, as Zhang *et al*. (2005) stated, larger particles demonstrate higher tendencies to rebound from the plate surfaces and re-entrain in the gas current due to their high kinetic energies. Conversely, smaller particles show higher probabilities of adhesion to the plates and present better initial collection efficiencies than coarse particles [55].

Nevertheless, smaller, lightweight particles settle much slower after rapping than large, heavy particles of the same density. This drastically increases the re-entrainment efficiency losses associated with fine particulates [16]. Considering the substantially different behaviours of fine and coarse particles, the assumption of mono-dispersity for particle flows when sizing ESPs can result in significantly higher or lower re-entrainment losses than expected [22].

Particle re-entrainment can also occur due to ineffective rapping procedures, back-corona, high particle resistivities, and extreme turbulence [56]. These matters are discussed in Sections 2.6.2, 2.7.3, and 2.7.5.

2.7.3 BACK-CORONA

As previously stated in Section 2.6.2, particles of high resistivity exhibit a strong retention of the electrostatic charges conferred upon them by the current-emitting discharge electrodes. Since negligible amounts of charge escape the layers of high-resistivity dust on the collection plates, the charge intensity grows as the particulate mass accumulates on the plate faces [57]. As is the case with any dielectric medium, the air in the voids of the dust layer has a dielectric breakdown voltage limit, which, if exceeded, triggers microscopic discharges in the air [16].

The charge build-up in the deposited dust accelerates the climb to the dielectric point, leading to a premature electric breakdown in the air (back-corona). Back-corona is responsible for producing positively-charged ions at the collection plates [58]. The positive ions neutralise the negative charges on the ash particles, causing the particles to submit to the gas stream and escape the ESP or migrate to the discharge electrodes. This finally leads to severe efficiency losses and should be prevented at all costs [59].

Figure 2-3 shows the extreme impact of particle re-entrainment that occurs as a result of back-corona on the collection plates in an ESP.

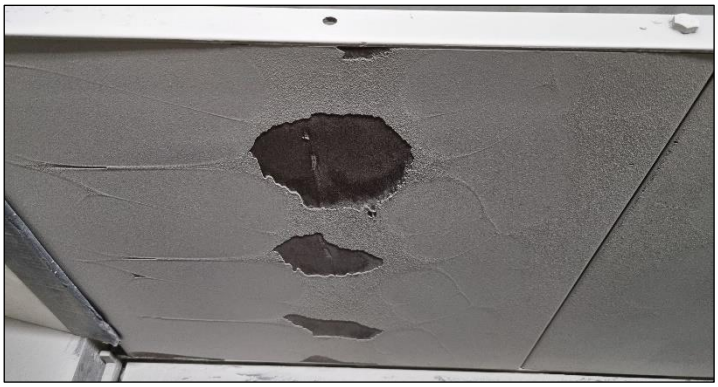

Figure 2-3. Dielectric breakdown in deposited dust on ESP collection plate

Several strategies have been proposed and employed to prevent back-corona in ESPs. Firstly, collection plates need to be cleaned regularly. Different cleaning mechanisms exist for practical ESP systems, but high-frequency rapping is most commonly used in flat-plate ESPs [16] (see Figure 2-1, Section 2.2).

The second prevention technique entails the alteration of particle resistivities by the modification of the flue gas composition with the use of conditioning agents [44]. This procedure has been briefly explained

before in Section 2.4.2. Temperature regulation is another popular strategy for back-corona inhibition and can be executed throughout the entire gas volume in the ESP or directly on the discharge electrodes [16].

In some cases, it is possible to replace fuel materials with higher-quality substitutes. However, this strategy is seldomly followed since fuel sources are generally limited and location-specific [16]. Alternatively, pulsed voltage power can be applied over the electrodes to alleviate unstable charges within the ESP [60]. Furthermore, conventional stainless steel discharge electrodes can be exchanged for semiconductive electrode materials [16].

2.7.4 SHIELDING

Electrostatic shielding is a physical phenomenon characterised by weakened field intensities for two or more overlapping electric fields. The conflicting fields work in opposite directions, which causes distortions in the field lines at the intersection of the field profiles. This decreases the field strength and current density in these regions. Shielding is often encountered in ESP systems that contain multiple discharge electrodes, and its effects can be overpowering if improper electrode and collection plate settings are used [61].

ESP configurations with shielding effects present more significant power input requirements to obtain the desired field intensities, which can compromise the ESP's particle-capturing ability. Chen *et al.* (2022) used mathematical models to calculate the shielding degree for different electrode-electrode distances, electrode-plate distances, electrode sizes, and the number of electrodes at various voltages for a wire-plate ESP. The study concluded that changes in the shielding degree were increasingly prominent for adjustments to electrode spacing, voltage supply, electrode diameter, and plate spacing in the corresponding order. Further investigation showed that shielding effects directly correlate to efficiency losses [62].

The research of Chen *et al.* (2022) was supported by a previous study from Arif *et al*. (2018) [15], who used experimental data from Lawless (1980) [58] and Kasdi (2016) [63] to develop a computational model of the ESP process. Both studies agreed that shielding increased for smaller electrode spacings, larger numbers of discharge electrodes, and wider plate spacings and that plate spacing showed the largest influence on the shielding degree. Arif *et al*. (2018) found the electrode count and the distance between discharge electrodes to pose much more significant effects on the shielding degree than the voltage supply. Though Chen *et al.* (2022) suggested a different order of significance, the studies were consistent in the conclusion that little-to-no change in the shielding degree occurred across a range of voltages.

Shielding originates between adjacent electrodes and intensifies toward the central electrodes. Therefore, adding more outer electrodes to the configuration increases the degree of shielding, which subsequently leads to a reduction in current density across the inner electrodes. A decrease in discharge electrode spacing causes an increase in shielding effects due to an increase in the overlapping of electric fields between electrode pairs. Furthermore, since the electric field intensity is linearly dependent on the applied voltage, the degree of shielding remains relatively constant for a change in voltage [61].

Also, smaller plate spacings enhance the electric field intensity on individual electrodes, which aids in forming more even field distributions across the electrode assembly, resulting in lessened shielding effects.

Arif *et al*. (2018) considered this an indication of an ESP's increased susceptibility to shielding effects at the lower field and current densities [15].

2.7.5 INSUFFICIENT FLOW DISTRIBUTION

Uniform gas and particle flow profiles are crucial for the best ESP performances – a condition that typically corresponds to the optimum reference-case. In addition, stable flow conditions present uniform distributions of temperature, kinetic energy, and other ESP parameters. This type of flow delivers the highest particle collection efficiencies and is, therefore, the most desired in ESPs [64].

On the other hand, irregular flows lead to localised high-velocity and low-velocity regions that can notably affect the collection of particles on the plates. High gas velocities at the collection plate interfaces can result in significant particle re-entrainment losses and increased particle volume fractions in the effluent gas stream [17]. Furthermore, increased flow speeds decrease particle residence times in the ESP, reducing the time available for particles to exit the gas stream via the plates or through gravitational settling [35]. On the contrary, sufficient velocities are required to produce enough turbulence for particles to be properly distributed in the gas, which is necessary for effective particle collection [17].

Therefore, the best solution regarding flow conditions in ESPs involves a compromise between these two aspects. Such conditions are beneficial for electrostatic precipitation and can be successfully achieved if the gas velocity is uniform throughout the entire ESP [16].

2.8 MODELLING OF ESPs

Electrostatic precipitation conditions are challenging to replicate in experimental setups due to the high degree of interaction between the electrostatic and flow fields in the ESP. Furthermore, ESP experiments are tedious, and particulate sampling procedures are complex. Therefore, different modelling strategies have been investigated to generate data representative of actual ESP conditions quickly and easily [15].

The earliest modelling methods mainly focused on empirical techniques, such as the model presented by Deutsch and Anderson. However, this model applies to a small range of ESP operating conditions and describes an oversimplified version of the precipitation process [65]. Cooperman (1984) addressed this with an alternative model that complies with wider collection plate distances, high resistivity dusts, larger plate-to-gas velocity relations, and other ESP variations. Nevertheless, both of these methods predominantly use the SCA ratio as the main design parameter and do not actively account for parameters other than the collection area and gas flow rate. Also, empirical models are limited to manual calculations and cannot properly incorporate re-entrainment effects and irregularities in ESPs [66].

Modern modelling procedures follow more advanced approaches and use specialised software to describe the correlations between the electrostatics and flow conditions in ESPs on a computational basis [15]. The relationships between the electrostatics, fluid, and particle phases in an ESP are demonstrated in Figure 2-4.

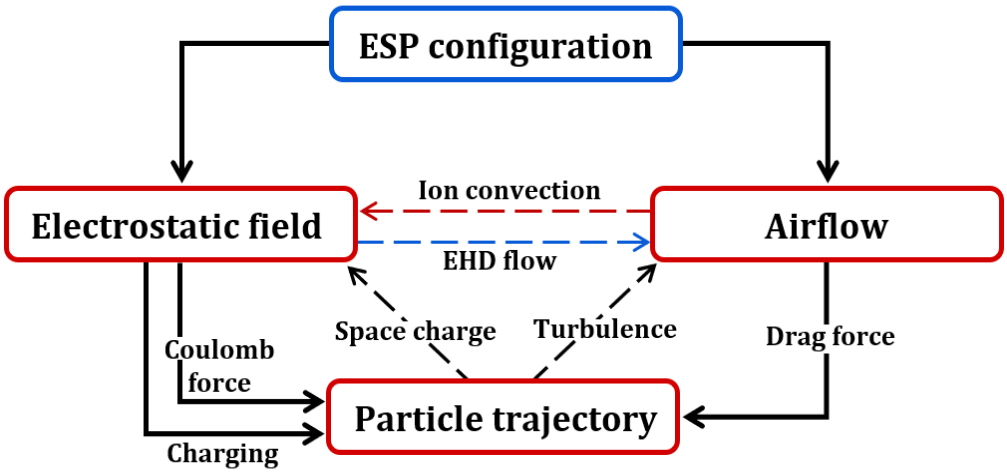

Figure 2-4. Interactions between electrostatic, fluid dynamic, and particle dynamic fields in ESPs, adapted from [15] and [36]

The main interactions in ESPs are those that involve the effects of the discharge electrode and collection plate settings on the electrostatic field and the gas flow patterns. Firstly, the design used for the discharge electrodes in the ESP determines the electrostatic field strength [67]. Furthermore, since each type of electrode presents a unique charge distribution, the shape of the electric field around the electrode is specific to the electrode geometry. Also, as previously mentioned, the total face area is important for the sizing of collection plates in an ESP [22].

The electrode and plate positioning further plays a significant role in the development of an electric potential gradient, which provides the basis for the generation of an electrostatic field. In addition, factors like shielding intensity and voltage operating ranges that differ for various electrode configurations can significantly alter the characteristics of the electric field [15]. The ESP setup also determines the gas flow regime (laminar, transition, or turbulent), which affects the unit's gas and particulate flow profiles [68].

The effects of electrode settings on ESP performance have been extensively investigated with increased attention to detail in subsequent research studies. Chang and Bai (2000) numerically compared the particle collection efficiencies for wire discharge electrodes with various diameters, electrode spacings and collection plate spacings. A general increase in collection efficiency was noted for a decrease in wire diameter at a constant electric field strength. However, the collection efficiency only increased to a certain point for decreased wire-to-wire and plate-to-plate distances. Correspondingly, the best combinations of wire and plate spacings varied for different field and current density conditions [54].

Brocilo *et al.* (2003) extended the research to sub-micron particles and evaluated the collection efficiencies for wire-type and spike-type discharge electrodes. A modified Deutsch model was applied to predict the collection efficiencies, with which it was deduced that spike electrodes show significantly higher collection rates for fine particles than the original wire electrodes [69]. Feldkamp *et al.* (2010) successfully developed generalised CFD models for the gas and particle flows in wire-plate ESPs and fabric filters, with the aim of using these models for design and retrofitting purposes [70].

Jedrusik and Świerczok (2013) examined the current density distributions and collection efficiencies of discharge electrodes with tinplate fins and pointed spikes. It was found that uniform current distributions are crucial for obtaining high collection efficiencies with fine dusts [71]. Adamiak (2013) reviewed previous modelling strategies followed to predict the collection efficiencies of wire-plate ESPs, with a specific focus on the two-way coupling between the electrostatic and flow fields. Adamiak subsequently provided a summary of numerous existing model approaches at the time and observed a general improvement in the modelling accuracy for more recent studies [72].

Guo *et al*. (2014) presented a numerical model to describe the electric field characteristics of wire-plate and point-plate ESP setups, with additional attention to the shapes and directions of the electrode tips. Guo *et al*. formulated a new injection law for the space charge density in the ESP and tested the model with empirical and experimental data to confirm its accuracy [73]. Kasdi (2016) modelled the current density distributions and current-voltage relationships of discharge wires for various wire spacings, wire diameters, and numbers of wires and found a good agreement with experimental values [63].

Zheng *et al.* (2018) defined a current distribution model for a wet-type ESP with other discharge electrode geometries, including smooth wires, single-spike, double-spike, triple-spike, and sawtooth electrodes. The spike length, spacing, and rotation were also varied to identify the configuration with the best efficiency. The triple-spike electrodes were noted to demonstrate the highest current densities and collection efficiencies [26].

Arif *et al*. (2018) developed a computational model to be implemented in an investigation of the shielding effects for different electrode quantities, electrode spacings, and plate spacings in a wire-plate ESP [61]. The conclusions drawn from the study of Arif *et al*. were previously discussed in Section 2.7.4. A later study by Chen *et al.* (2022) confirmed that shielding effects are predominantly attributed to incorrect wire-to-plate distances, while factors like wire diameter, voltage, and wire spacing showed less notable shielding effects [62].

When electric field intensities are high enough, the field lines induce secondary flow patterns within the gas phase, known as electrohydrodynamic (EHD) flow. Multiple studies have been conducted with the main focus of interpreting the EHD flow and its effects on particle collection [74]. Secondary EHD flow occurs when fast-moving gas ions in the corona fields strike stationary neutral gas molecules and cause them to transition to a dynamic state by supplying them with kinetic energy. The motions of neutral gas molecules produced by EHD effects contribute to the particle flow behaviour in the ESP [70].

According to Feldkamp *et al.* (2010), the size of the EHD effect varies based on the polarity of the current discharge and the gas flow speed in the ESP [70]. This statement was supported by Podliński *et al.* (2009), who examined the EHD flow for spike-type discharge electrodes. Podliński *et al.* found that the EHD intensity was higher for negative-polarity supply voltages than for positive polarities and that the EHD effects increased with an increase in applied voltage [75]. This study further confirmed that the EHD flow varies for different positions across the ESP, and exhibits the largest influence on the gas flow near the first

spike of the first discharge electrode. Finally, Podliński *et al.* concluded that the EHD effects improved the collection of sub-micron particles with diameters in the range of 0.25 – 0.50 μm [75].

Farnoosh *et al*. (2010) investigated the EHD effects for laminar and turbulent gas flow conditions with velocities between 0.1 $m.s^{-1}$ and 1.0 $m.s^{-1}$. The corresponding impacts on collection efficiency were studied for 1 μm, 5 μm, 10 μm, and 50 μm particles. The research of Farnoosh *et al*. included both experimental and numerical modelling analysis techniques and determined EHD flow to be negligible when the gas velocity exceeded 1.0 $m.s^{-1}$. Furthermore, the EHD flow was discovered to notably improve the collection of small particulates (≤ 1 μm diameter) but to show almost no effect on the flows of larger particles [67].

Dong *et al*. (2019) developed a numerical model to describe the EHD flow at the spike tips on opposite sides of the discharge electrodes and at the front and back of the ESP channel. Their results showed that the vortices at the first electrode's spikes directed the particles toward the plates and that these vortices predominantly resulted from gas turbulence and drag forces rather than EHD flow. This is applicable to negative DC voltages of 19 – 28 kV and gas velocities between 0.4 $m.s^{-1}$ and 1.3 $m.s^{-1}$ [76].

Guo *et al*. (2019) also simulated the EHD flow in a wire-plate ESP and reported increased gas velocities at the plate interfaces and subsequent decreased efficiencies for parallel arrangements of spike-type electrodes. Conversely, EHD flow was observed to facilitate uniform gas and particle flow distributions, which increased the ESP's particle collection efficiency. It was further noted that EHD effects showed large contributions to the dust layer patterns on the collection plates, which was particularly visible at low gas velocities [74]. All of the abovementioned studies ultimately concluded that complex flow patterns within ESPs are due to the combined turbulence and EHD effects [77].

On the other hand, for weak electric fields and high gas velocities, gas currents direct the flow of ions between the collection plates – a phenomenon known as ion convection. In this way, the electrostatic and fluid dynamic fields can directly affect one another. However, this is rarely the case, as electrically-driven ions generally travel at much higher speeds than gas molecules do through diffusion. Therefore, the gas flow effect on the electric field is typically negligible compared to the electric field effect on gas flow and is often disregarded for modelling purposes – a condition known as one-way coupling [55].

Secondary interactions in ESPs include the effects of the electrostatic field and gas flow on the particle motions and vice versa. The electric field and current discharge intensities are directly related since both result from the current supplied to the discharge electrodes and the electrostatic properties of the electrode-plate setup [26]. The corona fields provide the particles with negative charges at rates proportional to the local current densities, which, once again, depend on the electrode features and field intensity. Coulomb attraction forces form between the charged particles and collection plates, and the magnitudes of these forces are also determined by the strength of the electrostatic field [15].

Furthermore, a particle's charging rate determines the time until it starts to migrate to the nearest plate for collection after entering the ESP. The speed at which the particle flows to the collection surface is then dependent on the strength of the electrostatic attraction force that draws the particle to the plate. Therefore,

the electric field strength in the ESP is one of the main factors controlling particle flow patterns and collection efficiencies [78]. The particulate phase also affects the electric field conditions. Dust properties, like particle size and shape and especially resistivity, determine the charging rates, saturation charges, and plate adhesion strength of the particles in the ESP. In addition, the particle loading can notably change the space charge in the ESP, which, in turn, determines the particle deposition on the collection plates [79]. These considerations have been formerly discussed in the preceding sections.

Particle trajectories in ESPs also depend on the gas flow currents and drag forces, and gas conditions, like temperature, humidity, and chemical composition, significantly impact the particle resistivity (see Section 2.6.1). Furthermore, gas diffusion charging mechanisms can sometimes control particle charging rates, which defines the second link between the gas and particulate phases [34]. A particle's size, density, and mass contribute to its susceptibility to the gas flow and small, lightweight particles are generally more prone to turbulent effects than coarse particulates [29]. The particle loading is another aspect of the gas-particle two-way coupling since the particles can lessen or enhance the degree of turbulence in the ESP to an extent [33].

Kussin and Sommerfield (2002) measured the particle and air flows in a horizontal tube. The results showed that interactions between the two phases are, in fact, of noteworthy size, specifically regarding their corresponding relations to the wall surface roughness [34].

Skodras *et al.* (2006) simulated the physics inside an ESP by incorporating two-way couplings between the particle flow, gas flow, and electric field. The results showed that fine particles exhibit low collection efficiencies, and increased applied voltages and gas-particle residence times in the ESP delivered the best improvements in collection rates [78].

In another study by Gai *et al.* (2020), the effects of the particle phase on the gas-phase turbulence were confirmed through experimental and numerical modelling techniques [28].

3. EXPERIMENTAL PROCEDURE

The procedures followed for preparing the fly ash samples to be used in the ESP experiments are explained in the current chapter. The prepared ash samples were successively characterised by means of several analytical techniques, which are also discussed. Furthermore, a description of the experimental setup and strategy used for the ESP runs is given.

3.1 FLY ASH PREPARATION

The unprocessed samples included fly ashes from the hopper bins of ESPs at two separate coal-fired power stations in South Africa (A and B). Recent studies conducted by Arif *et al.* (2018) [15] and Ribberink *et al.* (2018) [41] used samples that were derived through analogous processes from the same fly ash batches used in the current study. The similarity of the fly ash samples made the results from the three studies more comparable, which is beneficial for the corresponding research. The steps followed for the preparation of the samples in this study are illustrated in Figure 3-1.

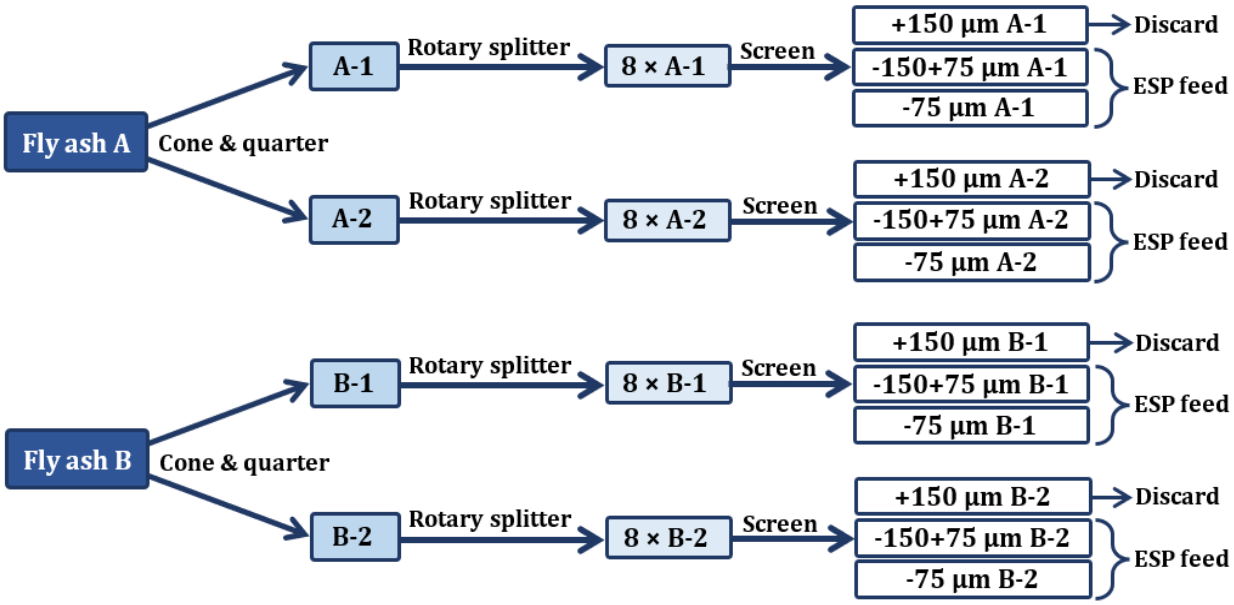

Figure 3-1. Fly ash sample preparation

After thorough mixing, the original fly ash samples from stations A and B were equally cone-and-quartered into four sub-samples – two half-sized samples of ash A and two half-sized samples of ash B. Every sub-sample was further divided into eight equal homogeneous parts with the use of a rotary sample splitter. Each of the resulting samples was split into a +150 µm oversize fraction, a -150+75 µm intermediate-size fraction, and a -75 µm undersize fraction, using vibrating screens with 150 µm and 75 µm size apertures. The +150 µm oversize fractions were discarded, while the -150+75 µm and -75 µm size fractions were characterised and used in the feeds of the ESP runs.

3.2 FLY ASH CHARACTERISATION

The fly ash samples were characterised according to their physical, chemical, and electrical properties. The analytical characterisation methods are further discussed in the following sections.

3.2.1 PHYSICAL AND CHEMICAL PROPERTIES

The different analysis methods used to determine the properties of the fly ash in this study are summarised in Table 3-1.

The physical properties that were tested for the fly ash samples in this study include the particle size distribution (PSD) and the particle density.

The PSDs of the -150+75 μm and -75 μm size fractions of fly ash A and B were analysed with the use of a Malvern Mastersizer 2000 instrument. The PSD measurements were taken according to the procedure described by the International Organization for Standardization (ISO) in standard 13320 of 2009.

The skeletal density provides information on the true volume of the ash. These measurements were conducted through Pycnometry analyses in a Stereopycnometer Model SPY-4 from Quantachrome Instruments. Inert helium (He) gas was used as a displacement fluid to fill the voids between the particles in the ash.

The mineralogical compositions of fly ash A and B were determined through X-ray fluorescence (XRF) analyses according to standard D4326 defined by the American Society for Testing and Materials (ASTM).

Table 3-1. Analytical measurement techniques for fly ash samples

Fly ash property	Characterisation method	Instrumentation
Particle size distribution (PSD)	• Laser diffraction • ISO Standard 13320 of 2009	Malvern Mastersizer 2000
Chemical composition	• X-ray fluorescence (XRF) • ASTM Standard D4326	Bureau Veritas Testing and Inspections South Africa
Particle density	• Pycnometer method • Helium (He) inert gas	Stereopycnometer Model SPY-4 (Quantachrome Instruments)

3.2.2 FLY ASH RESISTIVITY

The resistivity of each fly ash sample was measured at ambient temperature and humidity conditions for applied voltages ranging from 1.25 – 4.0 kV, according to Standard 548-1984 from the Institute of Electrical and Electronics Engineers (IEEE) [80]. The experimental setup used for the resistivity measurements consists of an oven and a supply voltage control panel, as shown in Figure 3-2.

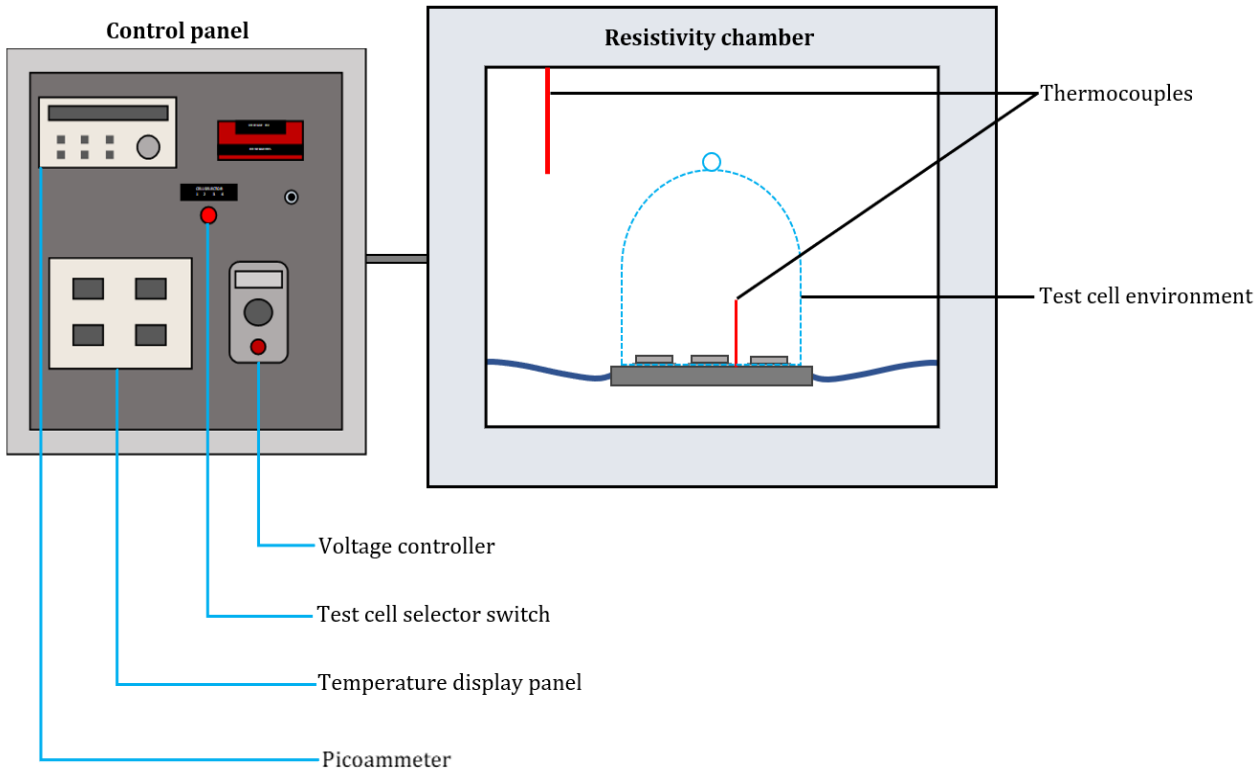

Figure 3-2. Experimental setup for fly ash resistivity measurements

The resistivity oven contains three test cells and a dummy load cell that are covered with a glass dome to create a temperature-controlled chamber. This is illustrated in Figure 3-3. In this case, the temperature and humidity were maintained at atmospheric conditions (20 – 26 ºC and 35 – 58% relative humidity) for the resistivity measurements.

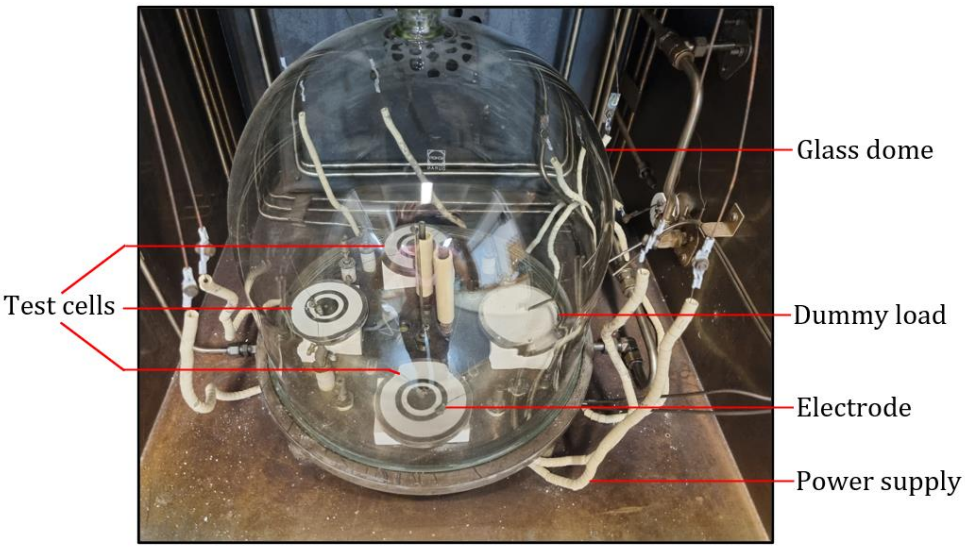

Figure 3-3. Resistivity test cells

The dummy load cell contained a fly ash sample of known resistivity. The resistivity results from the dummy load were compared to the reference resistivity value to monitor the consistency of the readings. The test cells were filled with fly ash samples, which were compacted and levelled with the test cell

surfaces. Each cell was contacted with two electrodes – one for current measurement and the other for electrical grounding. Negative high-voltage power was supplied to the test cells, and the current through every cell's fly ash content was measured.

At each voltage increment, ten current readings were recorded and averaged for a specific ash sample. The current data for the ash samples generally exhibited linear trends with the applied voltage. The voltage-current (V-I) relationships for the different ash samples are portrayed on the plots in Figure A. 2, Appendix A-1.2. The resistivity of a fly ash sample was calculated with Eq. 3.1 [41].

$$\rho_r = \left(\frac{V}{I}\right)\left(\frac{A_e}{t_a}\right) \qquad \text{E 3.1}$$

where ρ_r is the ash resistivity $[\Omega.\,\mathrm{cm}]$, A_e is the electrode face area $[\mathrm{cm}^2]$, t_a is the ash layer thickness $[\mathrm{cm}]$, and V/I is the voltage-to-current ratio $[\Omega]$, obtained from the inverse slope of the current versus voltage plots in Figure A. 2.

To evaluate the repeatability of the experimentally determined resistivities, the same fly ash sample was loaded into the three test cells and the dummy load (Cell 2). The ash resistivities measured by the different test cells were then compared with the use of resistivity ratios. The resistivity ratio between a pair of test cells was calculated from the higher resistivity reading relative to the lower resistivity reading, and a ratio smaller than 2.0 indicated a satisfactory degree of correspondence [80]. Ratios of 1.2, 1.2, and 1.0 were obtained for Cells 3:1, 3:4, and 1:4, respectively, which shows a high degree of cross-bowl repeatability for the resistivity results. Once repeatability was confirmed, the actual resistivity measurements were performed, where different fly ash samples were loaded into the various test cells and their resistivities determined. The resistivity measurements were repeated three times and on different days, using different test samples of every ash, and subsequently averaged. This was to minimise the bias associated with the preparation of the ash samples and the daily and hourly variation in temperature and humidity conditions.

3.3 ELECTROSTATIC PRECIPITATION

The ESP experiments were conducted according to a specific strategy to minimise the number of runs, which is explained in the subsequent section. The experimental setup, data collection, and data processing techniques for the ESP runs are also discussed.

3.3.1 EXPERIMENTAL DESIGN

Due to the many interacting factors involved in the ESP process, the experimentation on this topic can be very extensive and time-consuming. Furthermore, since the ESP variables are interrelated, it is not feasible to investigate them independently. Therefore, the ESP experimental plan was carefully designed to maximise the value of the results obtained with the smallest possible number of runs.

First, the factors with the largest influences on the ESP collection efficiency were identified through a set of screening experiments. The ESP factors under consideration for this study include the discharge electrode geometry, number of discharge electrodes, electrode spacing, collection plate spacing, ash loading, ash

PSD, and ash resistivity. The screening experiments were conducted according to a two-level fractional factorial (2^{k-p}) design. In this type of design, k is the number of factors, and 2 denotes that each factor has two different settings (levels). Furthermore, the value of p indicates the number of generators, which represents the degree to which the number of experiments was reduced [81].

Figure 3-4 illustrates the trade-off table from Dunn (2021) [82] that was used to select the appropriate fractional factorial design for the ESP screening experiments.

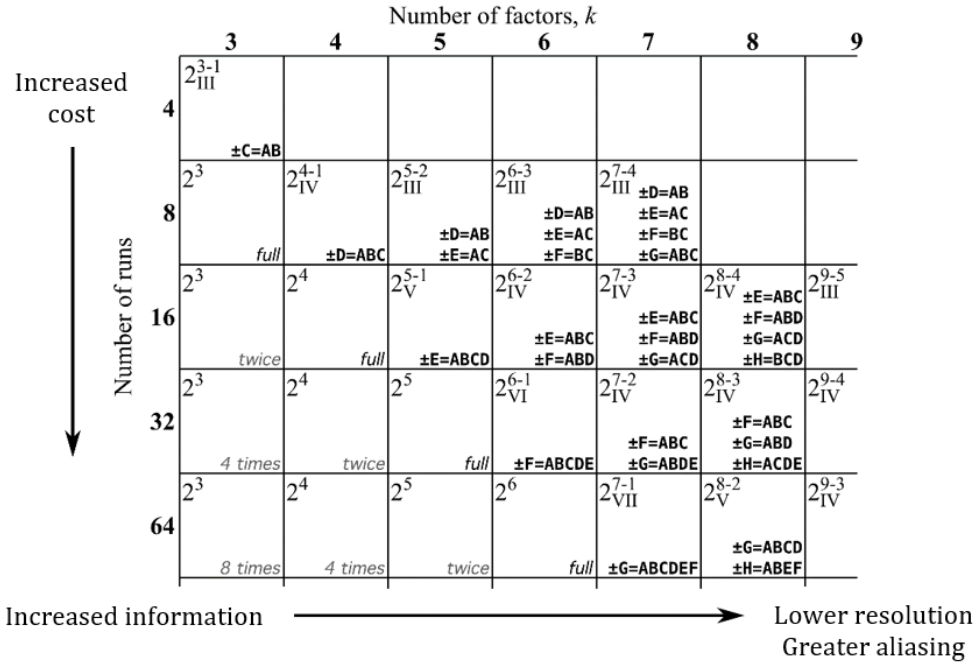

Figure 3-4. Fractional factorial design trade-off table, obtained from [82]

A resolution IV, quarter fraction factorial design was decided upon to provide the best compromise between fewer experimental runs and more useful information. This is expressed as 2^{6-2}, and corresponds to 16 screening runs in total. Due to the limited availability of the -150+75 μm size fraction of fly ash A and B, the screening runs used only feeds that comprised samples in the -75 μm size fraction. This excluded the fly ash PSD as a variable in the screening runs. The remaining factors evaluated in the screening process and the corresponding high (+) and low (-) level settings of each are listed in Table 3-2.

Table 3-2. ESP factors (A – F) and levels (+ or -) for screening experiments

Level	Plate spacing (A)	Electrode spacing (B)	Number of electrodes (C)	Ash loading (D)	Electrode geometry (E = ABC)	Type of ash (F = ABD)
+	160 mm	80	2	3 mg.m^{-3}	G-Spike	A
−	400 mm	175	3	18 mg.m^{-3}	Thread	B

The selection of factors E and F in the screening experiments were determined by the generators ABC and ABD, respectively, which relates to the products of the levels of the four main factors (A – D). This is demonstrated in Table 3-3. The settings for the full set of screening experiments are provided in Appendix A-2.1.

Table 3-3. Settings for the factorial design of the screening experiments

Run	A	B	C	D	E = ABC	F = ABD
n = 1	+	+	+	+	+	+
2	-	+	+	+	-	-
3	+	-	+	+	-	-
4	-	-	+	+	+	+
5	+	+	-	+	-	+
6	-	+	-	+	+	-
7	+	-	-	+	+	-
⋮						
N = 16	-	-	-	-	-	-

The 2^{6-2} factorial design strategy accounted for first-order and second-order effects of different variables in the ESP, which significantly reduced the number of experimental runs required to obtain the needed information. The data from the screening experiments were subsequently translated into a linear response surface methodology (RSM) model. The preliminary RSM model was used to determine the most important ESP factors to focus on in the actual ESP experiments (see Section 4.1).

Using the Minitab data analysis software, a full central composite design (CCD) methodology was developed for the actual ESP experiments. The experimental design included three block variables (one for each type of discharge electrode geometry), four continuous factors (plate spacing, electrode spacing, ash loading, and the number of electrodes), and one categorical factor (type of ash). The CCD plan entailed 32 cube points, 16 axial points, 8 cube centre points, and 4 axial centre points, with an α-value of 1 and a total of 60 experimental runs. The different types of points are illustrated in Figure 3-5, which shows an example of central composite designs for two factors (left) and three factors (right). The setup of the CCD procedure in the Minitab software is explained in more detail in Appendix A-2.6.

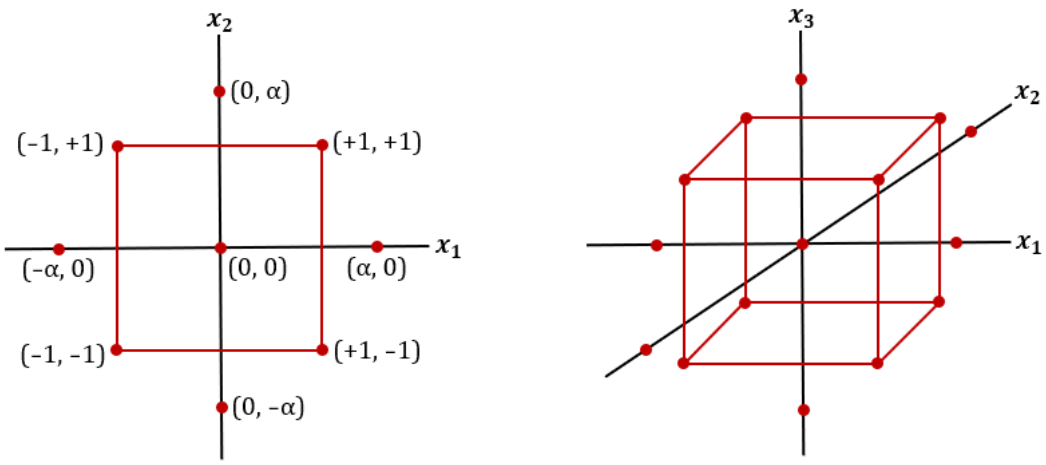

Figure 3-5. Central composite designs for two factors (left) and three factors (right), adapted from [81]

3.3.2 EXPERIMENTAL SETUP

The electrostatic precipitation experiments were conducted on a laboratory-scale demonstration unit of a wire-plate electrostatic precipitator (ESP), as illustrated in Figure 3-6. The ESP walls were manufactured from plexiglass – an electrical insulative material – and lined with grounded wires to confine the electrostatic field within the system for safety purposes. The ESP channel consists of an inlet section, an ESP section (1) with a diverging front end and converging rear end, and an outlet section. The ESP section contains two parallel collection plates (2) and an assembly of one to four discharge electrodes (3), situated between the plates. The collection plates have adjustable positions across the width of the ESP chamber, whereas the discharge electrodes can be placed at different distances along the length of the overhead support bar.

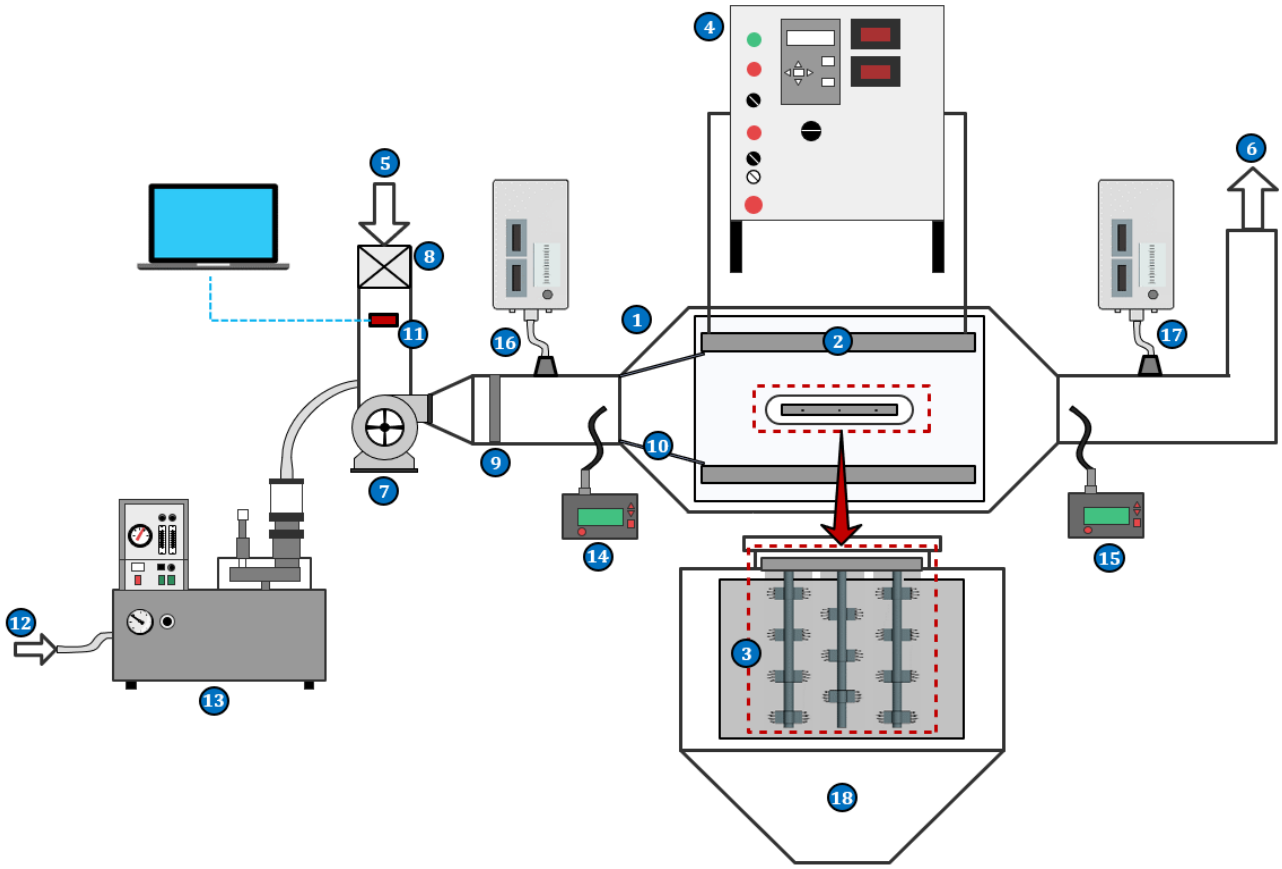

1	ESP chamber	7	Centrifugal fan	13	Dust feeder
2	Collection plates	8	HEPA filter	14	Inlet PM monitor
3	Discharge electrodes	9	Baffles	15	Outlet PM monitor
4	DC power supply	10	Guide plates	16	Upstream thimble
5	Inlet air supply	11	Humidity sensor	17	Downstream thimble
6	Exhaust air	12	Compressed air	18	Hopper bin

Figure 3-6. Laboratory-scale setup used for electrostatic precipitation experiments

A high-voltage direct current (DC) power source (4) with a voltage range of 0 – 50 kV was applied over the discharge electrode assembly to supply the electrodes with a negative polarity. On the other hand, the collection plates were electrically grounded and automatically adapted the positive polarity – opposite that of the discharge electrodes. This produced the potential gradient required to generate an electric field in the region between the collection plates. The voltage set point was manually increased on the control panel of the power supply unit until the sparkover voltage limit for a specific experimental run was reached.

Ambient air was circulated through the ESP setup from the inlet point (5) to the exhaust point (6), using a centrifugal fan (7) in the front of the ESP channel. A HEPA (high-efficiency particulate absorbing) filter (8) was used at the ESP entrance to remove foreign particulates from the incoming air supply. This was to prevent cross-contamination with the fly ash particles and minimise interference with the particulate matter (PM) concentration measurements. A variable speed drive (Movitrac LT model from Sew Eurodrive) was connected to the centrifugal fan to regulate its motor speed, and an input frequency of 23 Hz was specified to maintain the air velocity in the ESP close to 1.0 $m.s^{-1}$.

Baffles (9) were positioned in the channel upstream of the ESP section to create a uniform air velocity profile at the inlet to the electrode region. A set of guide planes (10) were used at the ESP inlet to direct the air stream between the collection plates. This ensured that most of the particle-laden air flowed across the discharge electrodes instead of passing through the space at the back of the plates. The instantaneous temperature and relative humidity of the air in the ESP channel were recorded on a continuous basis using an in-line humidity sensor (11) with a data logging system.

Fly ash was fed to the ESP by means of a DF-3 model dust feeder (13) from Sibata Scientific Technology Ltd with a compressed air supply (12). The ash injection point was situated on the pipeline leading to the centrifugal fan, which aided in evenly distributing ash particles throughout the air stream. The fly ash loading was controlled by manually adjusting the rotational speed of the dust feeder turntable.

Two DustTrak DRX particulate monitors (TSI Incorporated) were used to measure the mass fractions of ash particles in the air at the entrance (14) and exit (15) of the ESP chamber. The DustTrak technology employs advanced laser diffraction techniques to determine the total concentrations of airborne particles. In addition, two thimbles were placed approximately 2 m upstream (16) and downstream (17) of the ESP section to gravimetrically determine the PM concentrations at the front and back of the channel. Suspended ash was sampled from the air stream by external pumps connected to the thimbles and collected on glass fibre filters in the thimble compartments. The DustTrak and thimble data processing procedures are discussed in Appendix A-2.3 – A-2.4.

The DustTrak units and thimble systems were each equipped with specialised in-line sampling tubes featuring seven adjustable nozzle heads of diameters ranging from 4 – 10 mm. The ash concentration data were used to calculate the particle collection efficiencies for different experimental runs. Fly ash deposits on the collection plates were removed with a cloth at the end of every experiment to clear the plate surfaces for subsequent runs. Dislodged and settled dust was discarded in a hopper (18) situated underneath the ESP chamber to prevent re-entrainment in the following experiments. Table 3-4 provides a summary of the settings used in the ESP experiments.

Table 3-4. Electrode settings and fly ash conditions used for ESP experiments

Electrode geometry	Plate spacing (mm)	Electrode spacing (mm)	No. of electrodes	Dust loading ($mg.m^{-3}$)	Dust resistivity (Ω.cm)	Particle size range (μm)
Sawtooth	160, 220 & 280	57, 101 & 164	2, 3 & 4	3 – 30	$\sim 10^{10} - 10^{11}$	-75 & -150+75
Threaded rod	160, 220 & 280	57, 101 & 164	2, 3 & 4	3 – 30	$\sim 10^{10} - 10^{11}$	-75 & -150+75
G-spike	160, 280 & 400	112, 144 & 175	1, 2 & 3	3 – 30	$\sim 10^{10} - 10^{11}$	-75 & -150+75

The different combinations of ESP settings used in the experimental runs are listed in Table A. 3 in Appendix A-2.6, as well as Tables C. 3, C. 4, and C. 5 in Appendix C-2.

3.3.3 DATA ACQUISITION

The power supply control panel for the ESP setup in Figure 3-6 was used to determine the onset voltages for the different electrode configurations. The voltage over the discharge electrodes was then ramped-up from the onset point in increments of 1 kV or 2 kV after every 2 minutes. The power was increased up to a voltage that instigated a sparkover in the ESP section. This was considered to be the maximum voltage for a specific electrode combination in the ESP. The voltage set-points for every 2-minute interval were manually recorded during each experimental run.

The corresponding current outputs of the electrodes were simultaneously measured on a continuous basis with a digital Keithley multimeter Model DMM6500 6½ from Tektronix Incorporated. The current data was retrieved in a .csv (comma-separated variable) file through a USB cable and further processed in Excel. The electrical current readings were averaged for a specific supply voltage, and these values were used to construct current-voltage relationship plots for the different ESP runs.

The DustTrak monitors continuously measured the total particle concentrations at the inlet and outlet of the ESP section every 2 seconds, using laser diffraction technology. The DustTrak DRX units have a 0.001 $mg.m^{-3}$ resolution (0.1 % of the lowest particle concentration measured in this study), a 5% flow variance, and a maximum concentration limit of 150 $mg.m^{-3}$. Furthermore, these instruments have temperature and relative humidity operating ranges of 0 – 50 ºC and 0 – 95%, respectively, which complies with the ambient conditions in the ESP setup.

The PM concentration data were exported as .csv files with the use of the TrakPro data analysis software from TSI Incorporated. Similar to the current data, average values were calculated for the particle concentrations across the 2-minute time-interval for each applied voltage. These concentration measurements were used to determine the collection efficiencies of different ESP runs using procedures discussed in Section 4.2.6.

During each experimental run, an AM2302 digital temperature and humidity sensor (DHT22) was used to measure the temperature and relative humidity in the ESP channel. The sensor was connected to an Arduino

controller to establish a data logging system that recorded the temperature and humidity readings after every 2 seconds in a .csv file. The Arduino code for the DHT22 sensor is provided in Appendix A-2.2.

A Testo 440 hot wire anemometer kit was used to measure the average air velocities at the respective sampling points (14 – 17 in Figure 3-6). Each velocity measurement was logged in 1-second intervals for 1-minute periods and averaged. This was repeated three times and averaged again for 5 cm, 10 cm, and 15 cm distances from the top of the ESP duct at each sampling point. The velocities measured at the different heights were also averaged for every sampling point, and these values were designated to the corresponding sampling tubes.

The sampling flow rates and nozzle diameters required for isokinetic flow conditions were calculated for the local air velocities and applied accordingly. Isokinetic flow conditions entail equal flow velocities through the main ESP channel and the sampling tubes. Isokinetic sampling is crucial to prevent the over-sampling or under-sampling of particle-laden air, which can significantly reduce the accuracy of PM concentration readings [83]. The isokinetic sampling calculation is presented in Eq. 3.2:

$$Q_{Air} = A_{Nozzle} \times v_{Air} = \frac{\pi}{4} D_{Nozzle}^2 \times v_{Air} \qquad \text{E 3.2}$$

In Eq. 3.2, Q_{Air} is the air sampling flow rate $[m^3.s^{-1}]$, which was manually specified for the external pumps of the thimbles and factory-set for the internal pumps of the DustTrak monitors. Furthermore, A_{Nozzle} is the cross-sectional area of the sampling nozzle $[m^2]$, which was determined from the nozzle diameter, D_{Nozzle} $[m]$. Lastly, v_{Air} is the air velocity through the sampling tube $[m.s^{-1}]$, which, as previously mentioned, should be equal to the air velocity through the ESP duct.

4. MODEL DEVELOPMENT

The following section covers the procedure followed and the description of how the models in this study were set up.

4.1 RESPONSE SURFACE MODELLING

The response surface methodology (RSM) is commonly implemented in the optimisation of a response that is simultaneously affected by a number of different factors. In this study, the particle collection efficiency is the response that needs to be maximised by selecting the best combination of settings for the various ESP factors. The relationships between two factors and the response variable are represented by a response surface plot with axes in three dimensions. The response surface can be projected on a two-dimensional plane, called a contour plot, where each contour portrays the shape of the surface at a particular height [81]. Examples of contour and surface plots are given in Figure A. 7, Appendix A-2.7.

Since the relationships between the different ESP factors and the collection efficiency response are complex, a first-order RSM model was first developed to obtain an initial estimation of these effects. The first-order model was based on the linear equation given by Eq. 4.1, which was obtained from Montgomery (2013) [81].

$$y = \beta_0 + \beta_1 x_1 + \beta_2 x_2 + \cdots + \beta_k x_k + \boldsymbol{\epsilon} \qquad \text{E 4.1}$$

where y represents the response variable (in this case, collection efficiency) and the β-values are the model coefficients for the corresponding k number of factors. Furthermore, ϵ is the error term that describes the difference between the modelled response value and the actual value that was measured during the screening experiments. The model coefficients were separately solved for runs with fly ash A and B as feeds. This was achieved with the use of the regression analysis tool in the Minitab software.

The linear RSM models that describe the collection efficiencies of fly ash A and B are given in Eq. 4.2 and Eq. 4.3, respectively.

$$\eta_A = 41.49 - 10.98\, x_1 + 5.20\, x_2 + 7.03\, x_3 + 1.56\, x_4 + 4.51\, x_5 \qquad \text{E 4.2}$$

$$\eta_B = 46.57 - 10.98\, x_1 + 5.20\, x_2 + 7.03\, x_3 + 1.56\, x_4 + 4.51\, x_5 \qquad \text{E 4.3}$$

where x_1, x_2, x_3, x_4, and x_5 represent the high or low-level settings of the collection plate spacing, discharge electrode spacing, number of electrodes, ash loading, and electrode geometry. These expressions were used to better understand the relationships between ESP variables and the collection efficiency outcomes. This was to identify the preliminary direction in which to move to improve ESP efficiency. The resulting information allowed a more directed analysis of the ESP process to further optimise the factor settings for maximum collection rates.

Based on the negative signs of the β-coefficients for the collection plate spacing, it was deduced that increased plate-to-plate distances generally lead to decreased collection efficiencies. On the contrary, the positive signs of the remaining model coefficients indicated that larger electrode spacings, numbers of electrodes, and fly ash loadings increased the collection efficiency. Furthermore, the G-spike electrode generally exhibited higher collection efficiencies than the threaded rod electrodes. These conclusions were taken into consideration for the selections of ESP settings in the subsequent CCD experiments.

The collection efficiencies that were calculated with the models in Eq. 4.2 and Eq. 4.3 showed fairly good correlations with the experimental screening data, with an R^2-value of 73.1% (see regression plot in Figure A. 6, Appendix A-2.5). However, the determined fit was not as good as desired for ensuring accurate collection efficiency predictions and implicated second-order rather than first-order behaviour for the ESP variables. Therefore, a quadratic RSM model was employed to describe the collection efficiencies that were measured for different electrode configurations and ash feeds in the actual (CCD) ESP experiments.

The general expression for the second-order RSM model was also obtained from [81]:

$$y = \beta_0 + \sum_{i=1}^{k} \beta_i x_i + \sum_{i=1}^{k} \beta_{ii} {x_i}^2 + \sum_{j=2} \sum_{i<j} \beta_{ij} x_i x_j + \boldsymbol{\epsilon} \qquad \text{E 4.4}$$

In this case, β_i and β_{ii} are the model coefficients for the linear and quadratic effects of factor i, and β_{ij} represents the effect of interactions between two different factors (i and j). More information regarding the RSM modelling procedure is given in Appendix A-2.7. The final RSM model and the corresponding results are further discussed in Section 5.2.

4.2 COMPUTATIONAL FLUID DYNAMIC (CFD) MODELLING

The Simcenter STAR-CCM+ software was used to develop a computational fluid dynamic (CFD) model that describes the coupled air flow, electrostatic field, and particle trajectories in the electrostatic precipitator (ESP). The construction of 3-D geometries and model setup for different collection and discharge electrode settings in the ESP are explained in Section 4.2.1. Furthermore, the mathematical laws and the model parameters related to the electrostatic precipitation of fly ash particles are discussed in Sections 4.2.2 – 4.2.6.

4.2.1 MODEL SETUP

Three-dimensional (3-D) geometries of the discharge electrode and collection plate settings for each ESP assembly were created with the use of the Siemens NX-12 software. Figure 4-1 illustrates an example of such an ESP assembly with three G-spike electrodes.

Additional details regarding the geometric models are provided in Appendix B-2. The constructed geometries were exported to the Parasolid file format (*.x_t) and subsequently imported to the STAR-CCM+ software for further processing.

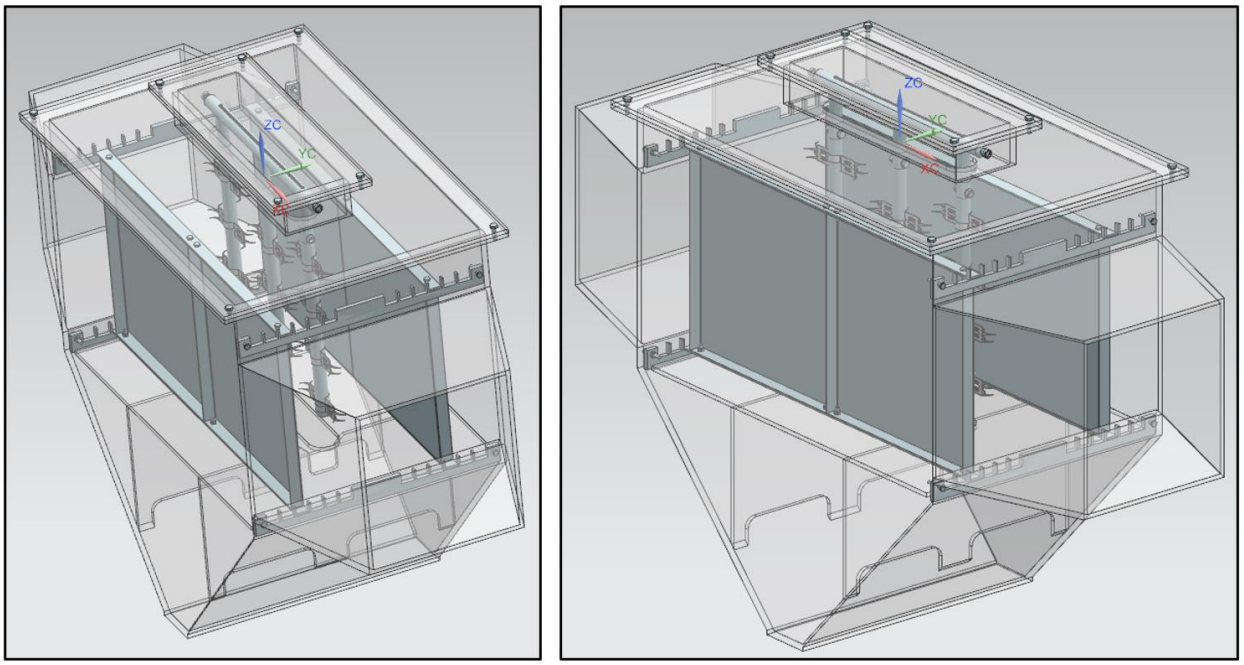

Figure 4-1. Isometric views of entire ESP section assembly – example with three G-spike electrodes

The various parts of the ESP geometry were assigned to separate regions – each with its own specified boundary type, as listed in Table 4-1. The properties of the different types of boundaries are summarised in Table B. 1, Appendix B-1.

Table 4-1. Specified boundaries for ESP regions

ESP part region	**Boundary type**
Inlet	Velocity Inlet
Outlet	Pressure Outlet
Discharge electrodes	Wall
Collection plates	Wall
Top plane	Symmetry Plane
Bottom plane	Wall

The 3-D geometries of the sawtooth, threaded rod, and G-spike electrodes used in this study are shown in Figure 4-2.

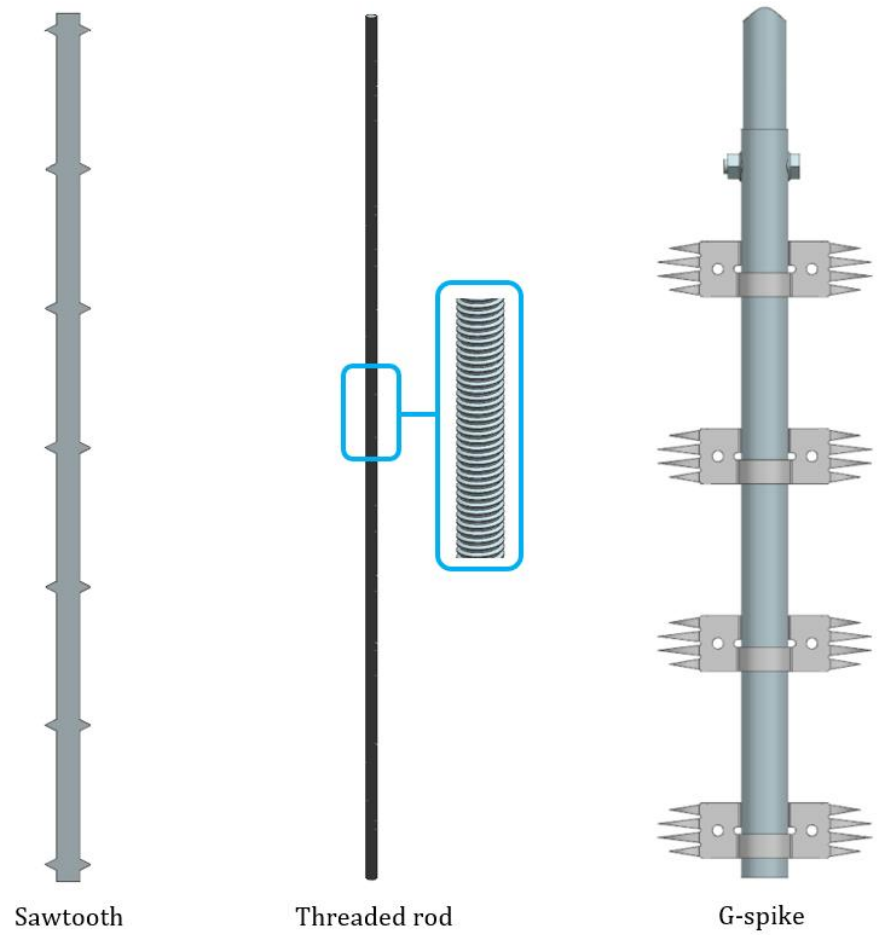

Figure 4-2. Discharge electrode geometries created in NX-12

Each geometry was discretised into a mesh containing many polyhedral cells, using the *Polyhedral Mesher* model in STAR-CCM+. In addition, the *Prism Layer Mesher* and *Surface Remesher* models were used to create a more structured mesh at the electrode surfaces. Volume-based meshing was also applied through volumetric controls to generate a sufficiently fine mesh near the electrodes while maintaining a reasonably coarse mesh throughout the rest of the geometry to minimise the solution time of the model. Figure 4-3 shows an example of an ESP geometry discretised into a mesh.

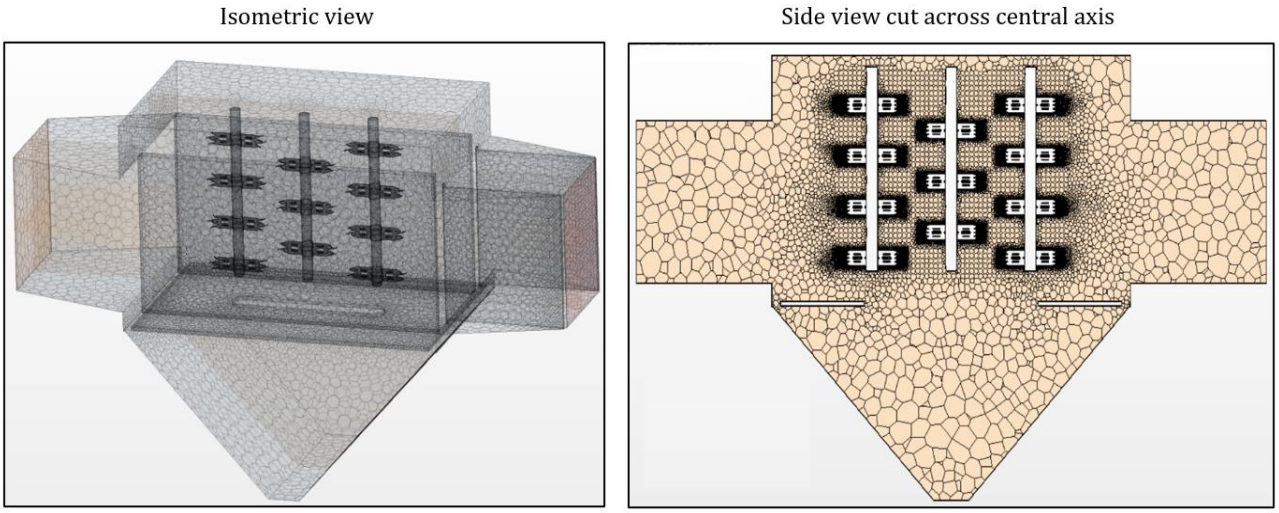

Figure 4-3. Example of an ESP geometry mesh

The grid structure at the electrode interface needs to be appropriately defined to ensure mesh independence, which is a crucial aspect of model accuracy. The mesh quality of the models was evaluated and verified with mesh independence analyses, which are further discussed in Appendix B-1.1.

The computational model was solved using the finite volume (FV) approach. For the FV method, the model values are calculated at the central point of every cell, as opposed to the finite element (FE) method, which performs the calculations at the cell edges. The physical phenomena involved in the ESP process were simulated with a selection of physics and numerical models integrated into the STAR-CCM+ software, as well as the corresponding user-specified input parameters required for the models. The description of the relevant physical processes in the CFD model is explained in the subsequent sections.

4.2.2 FLUID DYNAMIC FIELD

The air in the ESP is the continuous phase that serves as a carrier medium for the particles (dispersed phase). Steady-state, incompressible, and turbulent flow conditions were assumed for the entire ESP system. The airflow through the ESP section is governed by the principles of conservation of mass and momentum [36]:

Conservation of mass

$$\frac{\partial \rho_f}{\partial t} + \nabla \cdot (\rho_f \boldsymbol{u}) = 0 \qquad \text{E 4.5}$$

where ρ_f is the air density $[\mathrm{kg.\,m^{-3}}]$ and u is the air velocity $[\mathrm{m.\,s^{-1}}]$. At steady-state, Eq. 4.5 reduces to:

$$\nabla \cdot \boldsymbol{u} = 0 \qquad \text{E 4.6}$$

Conservation of momentum

$$\rho_f \left[\frac{\partial \boldsymbol{u}}{\partial t} + \boldsymbol{u} \cdot \nabla \boldsymbol{u}\right] = -\nabla P + \mu_f \nabla^2 \boldsymbol{u} \qquad \text{E 4.7}$$

where μ_f represents the dynamic viscosity $[\mathrm{kg.\,(m.\,s)^{-1}}]$ of air, and P is the absolute pressure [Pa]. If an electric potential difference is applied over the collection plates and discharge electrodes, an electric field develops, and a third body force term is added to the right-hand side of Eq. 4.7:

$$\rho_f \left[\frac{\partial \boldsymbol{u}}{\partial t} + \boldsymbol{u} \cdot \nabla \boldsymbol{u}\right] = -\nabla P + \mu_f \nabla^2 \boldsymbol{u} + \rho_c \boldsymbol{E} \qquad \text{E 4.8}$$

where ρ_c is the space charge density $[\mathrm{C.\,m^{-3}}]$ and E is the magnitude of the electric field $[\mathrm{V.\,m^{-1}}]$. The term $\rho_c \boldsymbol{E}$ represents the Coulomb forces produced during corona discharge that induce secondary electrohydrodynamic (EHD) flow patterns in the continuous phase [74].

The standard K-Epsilon model was used to describe the turbulent eddy currents in the ESP since it is the most robust among the turbulence models in terms of mesh coarseness [84].

4.2.3 ELECTROSTATIC FIELD

As discussed in Section 3.3.2, when the discharge electrodes are negatively charged with a high-voltage power supply, it creates an electric potential gradient between the electrodes and grounded collection plates. This generates an electric field, which, when large enough, produces corona discharge from the electrodes to the surrounding air. A space charge develops in the region between the collection plates due to the ionisation of air molecules that pass through the corona fields. The resulting electric potential distribution is described by the Poisson equation [85]:

$$\nabla^2 \phi = -\frac{\rho_c}{\varepsilon_0} \qquad \text{E 4.9}$$

where

$$\rho_c = \rho_i + \rho_d \qquad \text{E 4.10}$$

In Eq. 4.9, ϕ is the electric potential [V] and ε_0 is the permittivity of free space (8.85×10^{-12} F.m^{-1}). Furthermore, ρ_i and ρ_d in Eq. 4.10 denote the ion space charge and particle space charge [C.m^{-3}], respectively. Considering that only small fly ash loadings were used in this study (< 30 mg.m^{-3}), the effects of particle charge on the electric potential are deemed negligible [86]:

$$\rho_c = \rho_i \qquad \text{E 4.11}$$

The electric field that forms upon the introduction of a potential gradient is expressed as follows [15]:

$$\boldsymbol{E} = -\nabla \phi \qquad \text{E 4.12}$$

Coulomb forces attract the air ions near the discharge electrodes to the collection plates, producing a flow of electric current. The current density (J) is defined as:

$$\boldsymbol{J} = \rho_c K_i \boldsymbol{E} + \rho_c \boldsymbol{u} - D_i \nabla \rho_c \qquad \text{E 4.13}$$

where J is in A.m^{-2}, K_i is the ion mobility [m^2.(V.s)$^{-1}$], and D_i is the ion diffusivity [m^2.s^{-1}]. The terms $\rho_c K_i \boldsymbol{E}$, $\rho_c \boldsymbol{u}$, and $D_i \nabla \rho_c$ represent the effects of ion drift, convection, and diffusion on the current distribution, respectively [67]. The air velocity in the direction of the collection plates is considerably lower than the ion drift velocity, hence making the convective current insignificant [77] and yielding:

$$\boldsymbol{J} = \rho_c K_i \boldsymbol{E} - D_i \nabla \rho_c \qquad \text{E 4.14}$$

The ion diffusivity and mobility are related through the Nernst-Einstein equation [87]:

$$K_i = \frac{F z_i D_i}{RT} \qquad \text{E 4.15}$$

where F is Faraday's constant [C.mol^{-1}], z_i is the charge number (assumed to be 1 for singular ionic species), R is the universal gas constant [J.(mol.K)$^{-1}$], and T is the temperature [K]. However, the diffusive

current is typically several orders of magnitude smaller than the drift current [15] and can, therefore, be omitted from Eq. 4.14 to obtain the generalised form of Ohm's law [88]:

$$\boldsymbol{J} = \rho_c K_i \boldsymbol{E} = \sigma \boldsymbol{E} \qquad \text{E 4.16}$$

where σ is the conductivity of air $[\mathrm{S.m^{-1}}]$. At steady-state, the current density must satisfy the law of charge conservation [79]:

$$\boldsymbol{J} = 0 \qquad \text{E 4.17}$$

Eq. 4.9, 4.12, 4.16, and 4.17 were simultaneously solved with the *Electromagnetism* and *Electrostatic Potential* models in STAR-CCM+ to simulate the electric potential, electric field, and current density profiles in the ESP.

A threshold electric field strength is needed to initiate corona discharge – which is essential for particle charging and collection. Therefore, a sufficient electric potential flux must be provided to reach this minimum required field strength. The smallest applied voltage at which the system is able to generate corona discharge is known as the onset voltage. This value depends on the electrode geometry, electrode spacing, and the properties of the carrier medium [63].

For cylindrical electrodes such as the threaded rods used in this study, the electric field at the onset voltage can also be estimated with Peek's law [26]:

$$E_0 = g_0 m \left(\delta + 0.0308 \sqrt{\frac{\delta}{r_e}} \right) \qquad \text{E 4.18}$$

where E_0 is the onset electric field strength $[\mathrm{V.m^{-1}}]$, g_0 is the dielectric breakdown strength of atmospheric air $(32.15 \times 10^5\ \mathrm{V.m^{-1}})$, m is a roughness factor (typically 0.55 for threaded rods), and r_e is the equivalent radius of the threaded rod electrode [m], calculated as the average of the inner and outer thread radii [69]. The factor, δ, is the air density at any temperature (T) and pressure (P) relative to standard conditions [36]:

$$\delta = \frac{T_S P}{T P_S} \qquad \text{E 4.19}$$

In this case, T_S and P_S represent the standard temperature and pressure (STP) – 273.15 K and 101 325 Pa, respectively. Peek's law is, however, limited to cases where the electric field is constant across the entire electrode. For complex electrode geometries, like the G-spike and sawtooth electrodes, the current is concentrated on the spike tips, resulting in uneven field distributions on the electrode surfaces. Therefore, Eq. 4.18 could not be applied to these geometries [85]. Instead, the model was fitted to the experimentally measured voltage-current (V-I) data for the different assemblies of G-spike and sawtooth electrodes.

The current density on an electrode spike (J_s) was obtained from the V-I data with Eq. 4.20 [26]:

$$J_s = \frac{I}{A_s} \qquad \text{E 4.20}$$

where I is the current on the electrode [A], measured experimentally at a specified voltage, and A_s is the spike surface area [m^2]. An initial guess was given for the space charge density (ρ_c) to predict the current density on the electrode spikes in STAR-CCM+, using Eq. 4.16. The original value specified for ρ_c was subsequently amended until the modelled current density was close to the experimental value. In the case of threaded rod electrodes, the model accuracy was additionally tested by comparing the calculated electric field on the electrode to the Peek law estimate from Eq. 4.18.

4.2.4 PARTICLE DYNAMIC FIELD

The fly ash particles in the dispersed phase were assigned to the Lagrangian framework. STAR-CCM+ predicts a particle's motion by applying a force balance and the law of conservation of momentum on the particle [84]:

$$m_p \frac{d\boldsymbol{u}_p}{dt} = \boldsymbol{F}_d + \boldsymbol{F}_p + \boldsymbol{F}_g + \boldsymbol{F}_c \qquad \text{E 4.21}$$

where m_p is the particle mass [kg] and $\boldsymbol{u}_p$ is the particle velocity [$\mathrm{m}.s^{-1}$]. On the right-hand side of Eq. 4.21, $\boldsymbol{F}_d$, $\boldsymbol{F}_p$, $\boldsymbol{F}_g$, and $\boldsymbol{F}_c$ are the drag, pressure gradient, gravitational, and Coulomb forces acting on the particle [N]. Each force term can be expanded into its respective components as shown in Eq. 4.22 [27]:

$$m_p \frac{d\boldsymbol{u}_p}{dt} = \frac{1}{2} C_D \rho_f A_p |\boldsymbol{v}_s| \boldsymbol{v}_s - V_p \nabla P_s + \boldsymbol{g} \rho_p V_p + q_p \boldsymbol{E} \qquad \text{E 4.22}$$

where A_p, V_p, ρ_p, and q_p represent the projected area [m^2], volume [m^3], density [$\mathrm{kg}.\mathrm{m}^{-3}$], and charge [C] of the particle. Furthermore, C_D is the drag coefficient, $\boldsymbol{v}_s$ is the particle slip velocity (the velocity of the particle relative to that of the continuous phase) in $\mathrm{m}.\mathrm{s}^{-1}$, ∇P_s is the static pressure drop across the ESP section [Pa], and $\boldsymbol{g}$ is the gravitational acceleration constant ($9.81\ \mathrm{m}.\mathrm{s}^{-2}$).

Assuming that the particles are spherical [37], the drag coefficient was calculated using the Schiller-Naumann correlation [89]:

$$C_D = \begin{cases} \frac{24}{Re_p}\left(1 + 0.15 Re_p^{\,0.687}\right) & Re_p \leq 10^3 \\ 0.44 & Re_p > 10^3 \end{cases} \qquad \text{E 4.23}$$

where Re_p is the particle Reynolds number, expressed as:

$$Re_p = \frac{\rho_f |\boldsymbol{v}_s| d_p}{\mu_f} \qquad \text{E 4.24}$$

In Eq. 4.24, d_p is the particle diameter [m], and ρ_f and μ_f represent the air density [$\mathrm{kg}.\mathrm{m}^{-3}$] and dynamic viscosity [$\mathrm{kg}.(\mathrm{m}.\mathrm{s})^{-1}$], respectively [27].

4.2.5 PARTICLE CHARGING

The particles at the ESP chamber entrance were considered electrically neutral and to move at a velocity equal to that of the inlet air stream. Particles that flow through the ESP acquire a negative charge from surrounding air ions and are subsequently attracted to the grounded collection plates by Coulomb forces. The charge on each particle determines the strength of the attraction force acting on the particle and its migration velocity toward the collection plate. Particle charging is controlled by two mechanisms – field charging and diffusion charging [36].

In the case of field charging, particles gain charge through collisions with negatively charged air ions that travel under the influence of the electric field. The air ions continue to impinge on a particle and transfer charge to it until the charge on the particle reaches its saturation point. A particle's saturation charge is defined as [15]:

$$q_s = \frac{3\pi\varepsilon_c\varepsilon_r}{\varepsilon_r + 2}|E|d_p^2 \qquad \text{E 4.25}$$

where q_s is the saturation charge $[\mathrm{C}]$, ε_c is the air permittivity $[\mathrm{F.m^{-1}}]$, ε_r is the relative particle permittivity, E is the magnitude of the electric field $[\mathrm{V.m^{-1}}]$, and d_p is the particle diameter $[\mathrm{m}]$.

Diffusion charging occurs when particles are charged upon bombardment with air ions whose movements are governed by Brownian forces. This is primarily related to air velocity as a function of temperature. Therefore, diffusion charging becomes more significant at higher temperatures, for which the Brownian motions occur at higher speeds [36]. Field charging dominates when a particle's charge is below its saturation level, whereas diffusion charging is dominant for electrically saturated particles [67]. The rate of particle charging is defined as [84]:

$$\frac{dq_p}{dt} = \frac{q_s}{\tau_q}\left(1 - \frac{q_p}{q_s}\right)^2 \qquad \text{E 4.26}$$

where q_p is the particle charge $[\mathrm{C}]$, which can be calculated at the time, t, using Eq. 4.27 [25]:

$$q_p(t) = q_s\left(\frac{t}{t + \tau_q}\right) \qquad \text{E 4.27}$$

Equations 4.25 – 4.27 were solved in STAR-CCM+. The *Field Charging* model in the Lagrangian reference frame was used to calculate the field charging rate. The *Turbulent Dispersion* model and *Two-Way Coupling* with the electric field were used to account for the Brownian motion of the particles for the calculation of the diffusion charging rate. For the *Field Charging* model, the time constant, τ_q $[\mathrm{s}]$, is defined as [67]:

$$\tau_q = \frac{4\varepsilon_c}{\rho_c K_i} \qquad \text{E 4.28}$$

For the *Turbulent Dispersion* model, an alternative time constant, τ_c [s], is used in Eq. 4.26 and 4.27 [84]:

$$\tau_c = \begin{cases} \infty & \tau_v \leq \dfrac{l_e}{|\boldsymbol{v}_s|} \\ -\tau_v \ln\left(1 - \dfrac{l_e}{\tau_v |\boldsymbol{v}_s|}\right) & \tau_v > \dfrac{l_e}{|\boldsymbol{v}_s|} \end{cases} \qquad \text{E 4.29}$$

where τ_v is the momentum relaxation time scale, given by Eq. 4.30:

$$\tau_v = \frac{2m_p}{C_D \rho_f A_p |\boldsymbol{v}_s|} \qquad \text{E 4.30}$$

In Eq. 4.29, l_e is the eddy length-scale [m], expressed as:

$$l_e = \sqrt{6}\frac{\tau_t \mu_t}{\rho_f l_t} \qquad \text{E 4.31}$$

where μ_t is the turbulent viscosity [kg. (m. s)$^{-1}$], and l_t and τ_t are the turbulence length and time-scales, calculated with the K-Epsilon turbulence model.

4.2.6 MODEL PARAMETERS

Additional details related to the input parameters that were used for the fluid dynamics, particle dynamics, and electrostatic models presented in Sections 4.2.2 – 4.2.5 are provided in this section. The boundary conditions used for the CFD model in STAR-CCM+ are summarised in Tables 4-2, and 4-3.

Table 4-2. Fluid boundary conditions

ESP part region	Air conditions	Turbulence	Electric potential	Phase condition
Inlet	Inlet velocity (0.86 m. s^{-1})	Intensity (~5 %) + length scale	$\frac{\partial \boldsymbol{D}_\phi}{\partial n} = 0$	Inject
Outlet	Gauge pressure ($P = 0$)	Default	$\frac{\partial \boldsymbol{D}_\phi}{\partial n} = 0$	Escape

Table 4-3. Wall boundary conditions

ESP part region	Shear stress	Surface condition	Electric potential	Phase condition
Electrodes	No-slip	Smooth	Applied voltage (15–42 kV)	Reflect
Plates	No-slip	Smooth	$\phi = 0$	Composite: Escape (Default) + Rebound
Bottom	Slip	None	$\frac{\partial \boldsymbol{D}_\phi}{\partial n} = 0$	Composite: Escape (Default) + Rebound

Air properties

The average air velocity at the ESP entrance was measured to be 0.86 $\mathrm{m.s^{-1}}$ and was specified as such in the CFD model. Physical properties of air, like density and viscosity, are used to calculate the Reynold's number to establish whether the airflow is in the laminar, transition, or turbulent regime. This is essential for the modelling of flow profiles for the continuous and dispersed phases in the ESP [11].

Air density is a function of temperature and pressure, described by the following relation [90]:

$$\rho_f(T,P) = \frac{P}{R_S T} \qquad \text{E 4.32}$$

where P and T denote the absolute pressure [Pa] and temperature $[K]$ in the ESP, respectively, and R_S is the specific gas constant of air ($287.05\ \mathrm{J.kg^{-1}.K^{-1}}$). The air dynamic viscosity (μ_f) was also obtained at different values of T and P through interpolation of empirical data provided by Green & Perry (2008) [11].

The K-Epsilon model further described the turbulent airflow with initial conditions defined in terms of turbulence intensity and length scale. The turbulence at the ESP inlet was calculated with Eq. 4.33 [91]:

$$I_t = 0.16\left(Re_{D_H}\right)^{-1/8} \qquad \text{E 4.33}$$

where I_t is the turbulence intensity [%] and Re_{D_H} is the Reynolds number for the hydraulic diameter (D_H):

$$Re_{D_H} = \frac{\rho_f u_0 D_H}{\mu_f} \qquad \text{E 4.34}$$

In Eq. 4.34, u_0 is the inlet air velocity $[\mathrm{m.s^{-1}}]$ and D_H [m] is defined as:

$$D_H = \frac{4A_{Duct}}{P_w} = \frac{4L_x S_y}{P_w} \qquad \text{E 4.35}$$

The rectangular duct area, A_{Duct} $[\mathrm{m^2}]$, was obtained from the product of the horizontal length of the collection plates (L_x) and the plate spacing (S_y). The term, P_w, is the "wetted" perimeter, which represents the perimeter of the duct cross-section that comes into contact with the air:

$$P_w = 2\left(L_x + S_y\right) \qquad \text{E 4.36}$$

The inlet turbulence intensity was determined to be close to 5% for all the ESP runs relevant to this study (see Table 4-2). The turbulent length scale (l_t) at the ESP inlet was estimated with Eq. 4.37 [91].

$$l_t = 0.07 D_H \qquad \text{E 4.37}$$

In Section 4.2.2, it was explained that the electrostatic field also controls the airflow. The EHD flow term in Eq. 4.8 was included in the model with the use of the *Electrochemistry* and *Electrochemical Species* models in STAR-CCM+. The air was represented as plasma with a large concentration of negatively charged air ions. The molar concentration of the air ions was obtained from the space charge density (ρ_c) by applying the following equation [92]:

$$c = \frac{\rho_c}{F} \qquad \text{E 4.38}$$

where c is the molar concentration $[\mathrm{mol.\,m^{-3}}]$ and F is the Faraday constant, with a value of 96 485 $\mathrm{C.\,mol^{-1}}$. Another parameter of interest for the *Electrochemical* and *Electromagnetic* models is ion mobility (K_i) from Eq. 4.16, whose dependence on T and P was described by Kallio (1987) [54]:

$$K_i = 1.768 \times 10^{-4} \left(\frac{T}{T_S}\right)^{1.51} \left(\frac{P_S}{P}\right) \qquad \text{E 4.39}$$

In Eq. 4.39, K_i is defined in $[\mathrm{m^2.(V.s)^{-1}}]$, and T_S and P_S are the STP conditions in SI units. The *Electrochemical Species* model was solved for two-way coupling between the continuous and dispersed phases, which considers the air and particle flow profiles as interdependent.

With reference to Table 4-3, the 'no-slip' condition was selected for the shear stress at the electrode and collection plate surfaces, corresponding to a zero air velocity at these interfaces due to shear forces. On the other hand, the bottom section of the ESP was defined as a slip wall, where the air velocity is equal to the tangential velocity component in the absence of shear forces. The smooth surface condition was specified for the collection plates and discharge electrodes since both were manufactured from stainless steel, with a negligible surface roughness height of approximately 0.015 mm [11].

Electrostatic properties

The electric flux in Tables 4-2 and 4-3 is a function of the electric field ($\boldsymbol{E}$) and is described by Eq. 4.40 [84]:

$$\boldsymbol{D}_\phi = \varepsilon_c \boldsymbol{E} \qquad \text{E 4.40}$$

where $\boldsymbol{D}_\phi$ is the electric flux density $[\mathrm{C.\,m^{-2}}]$, and ε_c is the permittivity of the medium (in this case, air) $[\mathrm{F.\,m^{-1}}]$. The specific electric flux is the normal component of $\boldsymbol{D}_\phi$, and was assumed to be zero across the ESP inlet, outlet, and the bottom of the ESP section. This assumption is supported by the fact that the ESP body was constructed from plexiglass, which is an electrically insulating material.

The initial electric potential on the discharge electrodes was set to the onset voltage for the corresponding ESP run. This value ranged from 15 kV to 42 kV, depending on the type of electrode used, the electrode settings, and the fly ash conditions in the ESP (listed in Table 3-4). An electric potential of 0 kV was assigned to the collection plates to introduce the potential gradient required for generating an electric field (see Table 4-3). The voltages were specified in STAR-CCM+ by means of custom field functions, which accommodated small deviations from the provided values to make the model more flexible. Furthermore, experimentally measured current values for each voltage set point were used as input to the CFD model to compute the space charge density, electric field strength, and current distribution in the ESP.

Particle properties

The *Material Particles* model was applied to compute the solid particles' mass and volume. The particle density was measured experimentally for each type of ash and specified accordingly as input parameters for the abovementioned model. The relative particle permittivity (ε_r) was adjusted between 1.6 and 2.1 based on the temperature and relative humidity conditions, type of ash, and best fit between modelled and actual collection efficiencies for a specific ESP run.

Particles were injected at the inlet boundary using a *Part Type Injector*, which produces a group of injection points that are spread across the entire boundary region. The particle mass flow rate at the injection region was defined according to the fly ash loading for the corresponding ESP run. In addition, based on the assumption at the beginning of Section 4.2.5, the initial particle velocity was set to be the same as the inlet air velocity. The particle charge was described by Eq. 4.26 with the built-in *Particle Charge* field function in STAR-CCM+. Lastly, the particles were considered to be polydispersed, and having particle-size distributions (PSDs) that are well represented by the Rosin-Rammler model.

The phase conditions listed for the different boundaries in Tables 4-2 and 4-3 describe how each boundary interacts with the dispersed phase. By default, the particles enter and exit the simulation at the velocity inlet and pressure outlet boundaries, respectively. Furthermore, particles were assumed to be reflected upon impingement on the discharge electrodes. This is equivalent to a particle rebounding with no loss of kinetic energy to the electrode surface. To achieve this in STAR-CCM+, the *Rebound* interaction mode was selected, and a value of 1 was specified for the tangential and normal restitution coefficients, which imitates elastic collisions between the particles and electrode boundary.

The *Composite* option was used for the collection plates and ESP bottom section to define the boundary-particle interactions as a combination of *Escape* and *Rebound* modes. The main interaction mode was set to *Escape* for both boundaries, describing the removal of particles from the computational domain due to electrostatic deposition on the plates and gravitational settling through the bottom plane. The *Rebound* mode was specified for the secondary interaction to account for efficiency losses resulting from particle re-entrainment.

A standard STAR-CCM+ field-function was used to determine the average particle volume fractions at the inlet and outlet boundaries, with which the modelled collection efficiency could be calculated as follows:

$$\eta_C = \frac{(\varphi_p)_{in} - (\varphi_p)_{out}}{(\varphi_p)_{in}} \times 100\% \qquad \text{E 4.41}$$

where $(\varphi_p)_{in}$ and $(\varphi_p)_{out}$ are the volume fractions of particles at the ESP inlet and outlet, respectively, and η_C is the particle collection efficiency predicted by the CFD model [%].

Finally, the particle trajectories in the presence of eddy currents, gravity, and electrostatic fields in the ESP were portrayed with the use of *Track Files* in STAR-CCM+.

4.3 EMPIRICAL MODELLING

Several empirical relations have been used to design industrial-scale ESPs that can economically attain high particle collection efficiencies. Two of the most well-known empirical models, the Deutsch-Anderson equation and its derivative – the Matts-Öhnfeldt equation [24], were applied and evaluated in this study.

4.3.1 DEUTSCH-ANDERSON MODEL

The Deutsch-Anderson equation is commonly used in industry and relates an ESP's collection efficiency to its effective collection area with respect to the airflow rate [93]:

$$\eta_D = \{1 - \exp[-\boldsymbol{w}(A_P/Q_f)]\} \times 100\% \qquad \text{E 4.42}$$

In Eq. 4.42, η_D, is the particle collection efficiency [%], where the subscript, 'D' denotes that it is predicted by the Deutsch-Anderson model. Furthermore, A_P is the effective collection plate area $[\mathrm{m}^2]$ and Q_f is the volumetric flow rate of air through the ESP section $[\mathrm{m}^3.\mathrm{s}^{-1}]$. The term $\boldsymbol{w}$ represents the particle migration velocity $[\mathrm{m}.\mathrm{s}^{-1}]$, which is the velocity at which a particle travels to the collection plate. A more comprehensive discussion of this concept is given in Section 4.3.4.

Despite its widespread application to date, the Deutsch-Anderson equation was reported to overestimate the collection efficiencies of ESPs, especially for larger particles. As a result, ESPs are often undersized and unable to meet the desired efficiencies in the industry. The lack of accuracy in the Deutsch-Anderson model can be attributed to the many assumptions on which it is based, including uniform distributions of the air flow, particle flow and electric field in the ESP, constant air and particle velocities, monodispersed particles, and, most importantly, that no re-entrainment occurs after collection [94].

4.3.2 MATTS-ÖHNFELDT MODEL

Matts & Öhnfeldt (1964) addressed this issue with a simple modification to the Deutsch-Anderson equation [24]:

$$\eta_M = \left\{1 - \exp\left[-\boldsymbol{w}_k\left(A_P/Q_f\right)^k\right]\right\} \times 100\% \qquad \text{E 4.43}$$

Eq. 4.43 reduces the predicted collection efficiency by a factor k – a value between 0 and 1 – to account for the effects of ash properties and particle re-entrainment that were not included in the Deutsch-Anderson model. The value of k was solved by minimising the root mean square error (RMSE) between the average experimental collection efficiency and the efficiency calculated with the Matts-Öhnfeldt relation (η_M). In this case, the subscript, 'M', signifies the Matts-Öhnfeldt model.

4.3.3 PARTICLE CHARGE

The mathematical equations and assumptions pertaining to the particle charging model in this study were elaborated in Section 4.2.5. As previously mentioned, field and diffusion charging mechanisms govern the particle charging rate. However, the extent to which each mechanism affects the overall charging rate

depends on the particle size since it is directly related to the maximum charge that the particle can bear (see Eq. 4.25). Diffusion charging is reportedly negligible for particles with diameters > 0.2 μm [20]. The fly ash samples used in this study had minimum particle diameters of 0.46 μm (0.01 & 0.08 vol%) and 2.13 μm (0.07 & 0.11 vol%) for the -75 μm and -150+75 μm size fractions, respectively. Therefore, diffusion charging was assumed to be negligible, and the particle charge was approximated by its saturation charge [25]:

$$q_p = q_{max} = \pi \varepsilon_0 K d_p^2 \boldsymbol{E} \qquad \text{E 4.44}$$

where ε_0 is the vacuum permittivity $[\mathrm{F.m^{-1}}]$, q_p is the charge on the particle $[\mathrm{C}]$, $\boldsymbol{E}$ is the electric field $[\mathrm{V.m^{-1}}]$, and d_p is the particle diameter [m]. The factor, K, represents the term:

$$K = \frac{3\varepsilon_r}{\varepsilon_r + 2} \qquad \text{E 4.45}$$

where ε_r is the particle dielectric constant (relative permittivity).

4.3.4 PARTICLE MIGRATION VELOCITY

The probability of a particle depositing on the collection plates in an ESP is primarily dependent on the particle's migration velocity toward the collection plates. Coulomb attraction promotes a charged particle's acceleration toward the plates and allows it to be removed from the air stream when it reaches the plate interface. For small particles in an electric field, gravitational forces are typically insignificant and were, therefore, neglected in the empirical models [95]. A force balance on a particle in the ESP yields:

$$m_p \frac{d\boldsymbol{w}}{dt} = q_p \boldsymbol{E} - 3\pi \mu_f d_p \boldsymbol{w} \qquad \text{E 4.46}$$

where $\boldsymbol{w}$ is the particle migration velocity $[\mathrm{m.s^{-1}}]$, m_p is the particle mass [kg], and μ_f is the air dynamic viscosity $[\mathrm{kg.(m.s)^{-1}}]$. The terms $q_p \boldsymbol{E}$ and $3\pi \mu_f d_p \boldsymbol{w}$ in Eq. 4.46 respectively describe the electrostatic (Coulomb) and aerodynamic drag forces [N] acting in opposite directions on the particle. The latter is defined by Stoke's law under the assumption of laminar flow in the ESP chamber [25].

Through integration and rearrangement of Eq. 4.46, an expression for the migration velocity at time t was obtained, which is given by Eq. 4.47:

$$\boldsymbol{w} = \left(\frac{q_p \boldsymbol{E}}{3\pi \mu_f d_p}\right)\left[1 - \exp\left(-\frac{3\pi \mu_f d_p t}{m_p}\right)\right] \qquad \text{E 4.47}$$

The exponential term becomes insignificant after $t = 0.01$ s and was, consequently, omitted from Eq. 4.47:

$$\boldsymbol{w} = \frac{q_p \boldsymbol{E}}{3\pi \mu_f d_p} \qquad \text{E 4.48}$$

Equation 4.44 was substituted for particle charge (q_p) in Eq. 4.48 to obtain:

$$\boldsymbol{w} = \frac{\varepsilon_c d_p P \boldsymbol{E}^2}{3\mu_f} \qquad \text{E 4.49}$$

The average electric field between a discharge electrode and collection plate was estimated as:

$$\boldsymbol{E} = \frac{\phi}{L} \qquad \text{E 4.50}$$

where ϕ is the voltage applied over the discharge electrodes [V] and L is the distance between the centre of the electrode to the surface of the collection plate [96].

5. RESULTS & DISCUSSION

The following section provides and discusses the results obtained from the ash analyses, ESP experiments, and the different modelling methods.

5.1 FLY ASH PROPERTIES

The fly ash samples used as feed to the ESP channel were analysed for different physical and chemical properties. The results provided information that was useful for both the modelling process and understanding the ESP experiments' outcomes.

5.1.1 PARTICLE SIZE DISTRIBUTION

The particle size distributions (PSDs) of the -75 µm and -150+75 µm size fractions for fly ash A and B are shown in Figure 5-1.

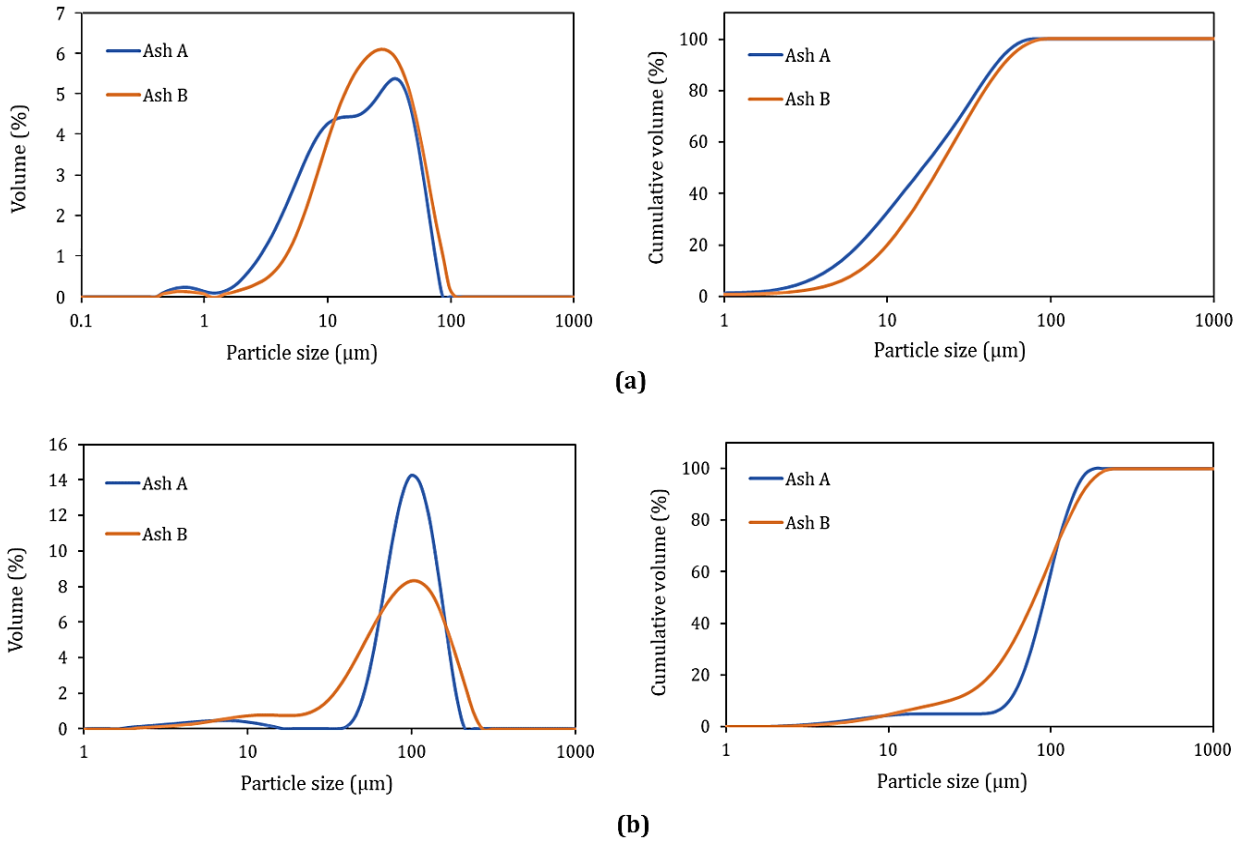

Figure 5-1. Particle size distribution of fly ash A and fly ash B in (a) the -75 µm size fraction and (b) the -150+75 µm size fraction

The plots in Figure 5-1 (a) indicate that the PSDs of the -75 µm size fraction ash samples are very similar, with fly ash A and B having peak volume fractions at the 35 µm and 27 µm particle sizes, respectively. Furthermore, both of these samples predominantly consist of particles with diameters smaller than -75 µm (≥ 99%), confirming that the sieving process was executed effectively.

The -150+75 μm size fraction of fly ash A and B also exhibit analogous distributions, as shown in Figure 5-1 (b). For this size group, ash A and B have the largest volume fractions for particles with diameters close to 98 μm. However, only 64% and 43% of particles lie within the -150+75 μm size range for fly ash A and B, respectively. More specifically, ±10% of particles are larger than 150 μm for both ash samples, while ±30% and ±40% of the particles are smaller than 75 μm for ash A and B, respectively. The coarse particles in the samples could have resulted from cross-contamination between the different particle size fractions. On the other hand, the fraction of undersized particles retained in the -150+75 μm ash could be due to particle segregation during sieving. Segregation is a problem often encountered with vibrating sieves, where fine lightweight particles move to the powder surface, preventing these particles from being screened [97].

The D_{10}, D_{50}, and D_{90} percentile values and the volumetric mean ($D_{[4,3]}$) for the different fly ash samples are summarised in Table 5-1.

Table 5-1. Percentile values and volumetric mean of ash A and B

Ash sample	D_{10} (μm)	D_{50} (μm)	D_{90} (μm)	$D_{[4,3]}$ (μm)
-75 μm				
Fly ash A	4.85	18.6	52.0	24.1
Fly ash B	7.64	23.5	58.1	28.7
-150+75 μm				
Fly ash A	62.4	104	158	106
Fly ash B	26.3	89.8	176	96.6

When considering the -75 μm size fraction, ash A consists of finer particles than ash B, since the D_{10}, D_{50}, D_{90}, and $D_{[4,3]}$ values of ash A are all smaller than that of ash B. According to the D_{10} percentiles in Table 5-1, 10% of the particles in ash A are smaller than 4.9 μm, while ash B contains 10% of particles with diameters below the 7.6 μm size. Furthermore, the D_{50} and D_{90} values indicate that 50% of the particles are smaller than 18.6 μm and 23.5 μm, and 90% of the particles are smaller than 52.0 μm and 58.1 μm in ash A and B, respectively. In addition, volume means of 24.1 μm and 28.7 μm were reported for ash A and B.

For the -150+75 μm size fraction, ash B has smaller D_{10}, D_{50}, and $D_{[4,3]}$ values than ash A – corresponding to finer ash particles for at least 50% of the sample volume. However, the D_{90} percentile of ash B is in the 176 μm size group, whereas that of ash A is in the 158 μm size, indicating coarser particles for the 90% cumulative volume of ash B compared to A. The large gap between the D_{50} and D_{90} values of ash B in this study could be due to the insufficient sieving previously observed for this sample, resulting in a wider distribution of particle sizes in the ash. This is evident from the first plot in Figure 5-1 (b), displaying a flatter, wider curve for ash B, as opposed to the sharp, narrow curve representing ash A.

The $D_{[4,3]}$ value of each type of ash in Table 5-1 was used for the average particle diameter in the relevant calculations for the empirical Deutsch-Anderson and Matts-Öhnfeldt models from Section 4.3. For the CFD model discussed in Section 4.2, the particle diameters of the various ashes were described with the corresponding Rosin-Rammler distribution functions that were fitted to the relevant ash PSDs. A general

procedure for the derivation of a Rosin-Rammler distribution from experimental PSD data is explained in Appendix A-1.1 and Figure A. 1. The Rosin-Rammler plots are depicted in Figure 5-2, and the related fitting parameters are listed in Table 5-2.

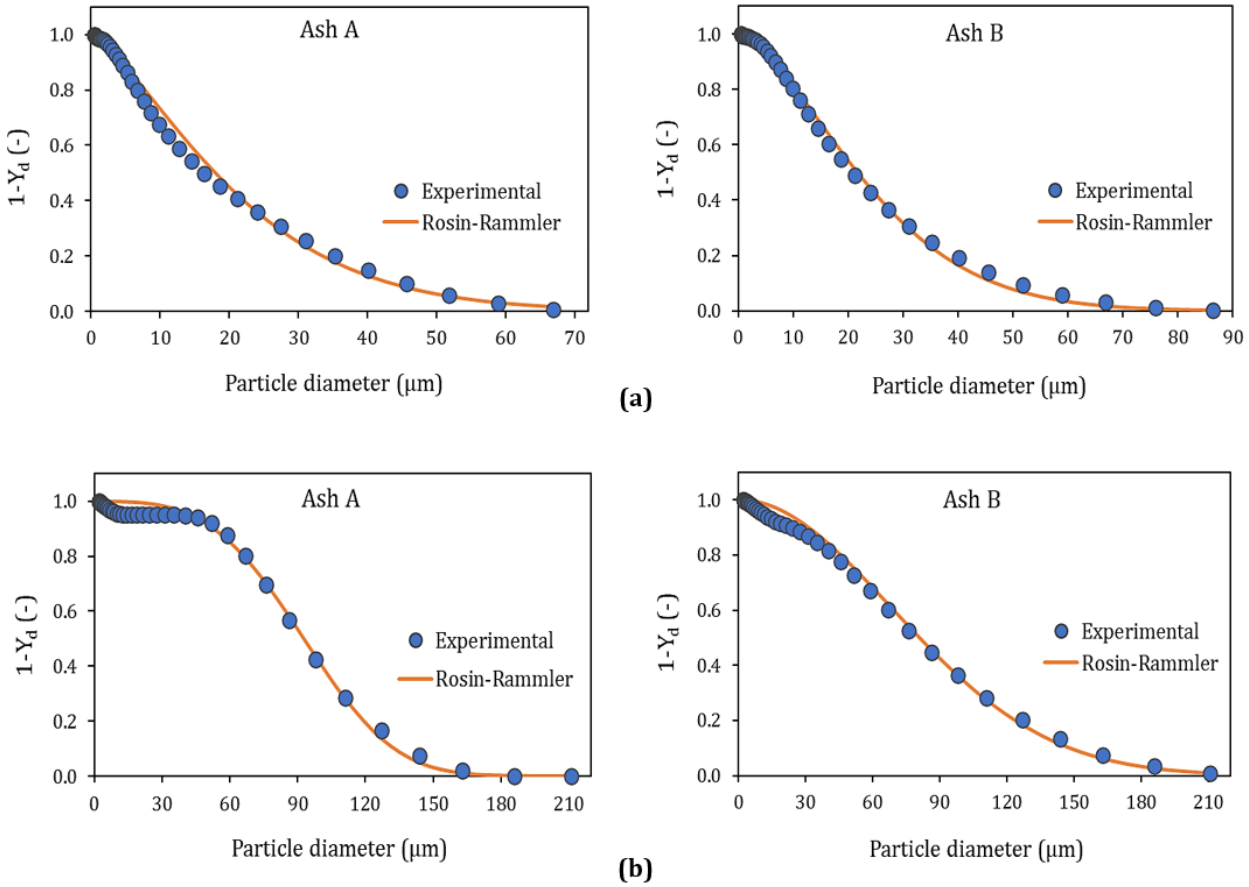

Figure 5-2. Rosin-Rammler and experimental size distribution plots for particles in (a) -75 µm and (b) -150+75 µm size fractions of fly ash A and B

As seen in Figure 5-2, the Rosin-Rammler distribution is a good fit for the PSDs of the fly ash used in this study and was, therefore, suitable for predicting the sizes of the polydispersed particles in the CFD model. The parameters used to describe the PSD of a specific fly ash according to the Rosin-Rammler approach include the minimum particle diameter (d_{min}), the maximum diameter (d_{max}), the reference diameter (d_0) for which 63.2% of the particles are smaller in comparison and the distribution coefficient (n) [Table 5-2].

Table 5-2. Rosin-Rammler fitting parameters for ash A and B

Ash sample	d_0 (µm)	d_{min} (µm)	d_{max} (µm)	n
-75 µm				
Fly ash A	23.6	0.46	76.0	1.36
Fly ash B	27.4	0.46	86.4	1.56
-150+75 µm				
Fly ash A	103	1.88	211	3.36
Fly ash B	97.5	2.13	240	1.98

The Rosin-Rammler parameters for the different ash samples in Table 5-2 were used as input for the particle injector in the CFD model discussed in Section 4.2.6.

5.1.2 PARTICLE DENSITY

The skeletal densities that were measured for the -75 µm and -150+75 µm size fractions of fly ash A and B are provided in Table 5-3.

Table 5-3. Particle density for -75 µm and -150+75 µm sizes of ash A & B

Ash sample	**Fly ash A**		**Fly ash B**	
	-75 µm	**-150+75 µm**	**-75 µm**	**-150+75 µm**
Density (kg.m^{-3})	2213	2124	2222	2145

These values were used to specify the particle density of each type of ash to model the particle flows for the corresponding ESP runs in STAR-CCM+ [see Section 4.2.4 and *Particle properties* in Section 4.2.6].

5.1.3 CHEMICAL COMPOSITION

The mineralogical compositions of fly ash A and B were determined with X-ray fluorescence (XRF) analyses. The XRF results for the species of interest are presented in Table 5-4 and compared to the results obtained by Ribberink (2018) for the same fly ash samples [41]. Note that the compositions in Table 5-4 are given in weight fractions (wt%). Additional components and the corresponding contents in fly ash A and B are listed in Table C. 2, Appendix C-1.

Table 5-4. XRF results for major and trace elements in fly ash A and B

Major elements					
		This study		**Ribberink**	
Species	**wt**	**Fly ash A**	**Fly ash B**	**Fly ash A**	**Fly ash B**
Al_2O_3	**%**	30.2	26.6	30.4	27.2
SiO_2	**%**	57.3	59.1	57.2	58.5
$Al_2O_3 + SiO_2$	**%**	87.5	85.7	87.6	85.7
Trace elements					
		This study		**Ribberink**	
Species	**wt**	**Fly ash A**	**Fly ash B**	**Fly ash A**	**Fly ash B**
CaO	**%**	4.4	3.5	4.3	3.4
Fe_2O_3	**%**	3.6	6.6	3.6	6.5
MgO	**%**	1.0	1.1	1.0	1.0
Na_2O	**%**	0.2	nd*	0.4	<0.1

*nd = Not detected

In general, the chemical composition of major and trace elements in the ash samples from this study are similar to that of Ribberink (2018). Firstly, the measured contents of alumina (Al_2O_3) and silica (SiO_2) deviate from Ribberink's data by 0.1 – 0.2% and 0.6% for ash A and B, respectively. Furthermore, the trace element composition measurements in this study differ by less than 0.2% from the values of Ribberink [41].

The compositions of the fly ash samples were also compared to Indian and American coal fly ash samples from the studies of Chandra (2013) and Bickelhaupt (1979), respectively. The results are given in Table 5-5. The fly ash used in this study and the study of Ribberink (2018) were sampled from the same South African coal-fired power plants. The XRF results show that South African fly ash generally resembles Indian fly ash [44] but differs from American ash [43].

Table 5-5. Composition of South African ash compared to Indian & American fly ashes [43], [44]

		This study		**Ribberink**		**India**	**America**
Species	**wt.**	**Fly ash A**	**Fly ash B**	**Fly ash A**	**Fly ash B**		
Al_2O_3	**%**	30.2	26.6	30.4	27.2	29.8	22.8
CaO	**%**	4.4	3.5	4.3	3.4	2.1	8.2
Fe_2O_3	**%**	3.6	6.6	3.6	6.5	5.8	9.1
K_2O	**%**	0.7	0.8	0.7	0.8	0.9	1.9
MgO	**%**	1.0	1.1	1.0	1.0	0.6	2.7
Na_2O	**%**	0.2	nd*	0.4	<0.1	0.1	1.4
P_2O_5	**%**	0.4	0.4	0.3	0.4	0.3	0.4
SiO_2	**%**	57.3	59.1	57.2	58.5	58.1	50.5
TiO_2	**%**	1.5	1.3	1.5	1.3	2.1	1.9
SO_3	**%**	0.2	0.3	0.3	0.5	0.3	1.6

*nd = Not detected

While the Al and Si contents of all the ashes listed in Table 5-5 are reasonably close, the Fe, Na, K, and SO_3 fractions of South African and Indian ashes are considerably smaller than that of American ash. As these species are known to improve conduction (see Section 2.6.1), South African and Indian ashes are expected to have higher resistivities than American ash.

On the contrary, resistivity-enhancing species such as CaO and MgO also exist in lower quantities in South African and Indian ash compared to American ash (see Table 2-2). However, based on observations made in previous research, the difference in alkali metal and SO_3 compositions should outweigh the effects of CaO and MgO on ash resistivity [45]. Therefore, lower resistivities are still anticipated for American ash with respect to ash sourced from South African and Indian power plants.

The compositions of phosphorous pentoxide (P_2O_5) and titania (TiO_2) are also given in Table 5-5 for comparison, and vary by less than 0.1% and 0.8% for the different ash samples.

5.1.4 FLY ASH RESISTIVITY

The fly ash resistivity was measured at ambient temperature and relative humidity conditions for a range of voltages and the results are illustrated in Figure 5-3.

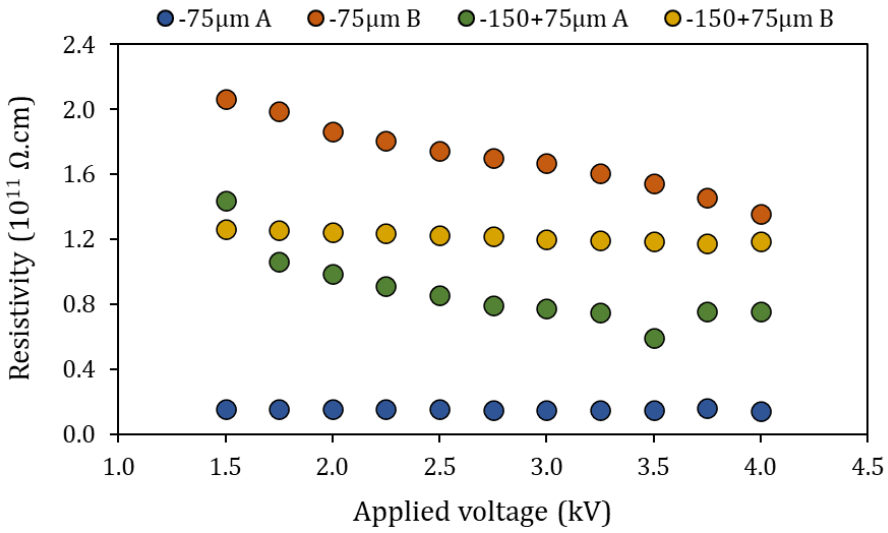

Figure 5-3. Resistivity of fly ash A and B at 1.5 – 4.0 kV

The resistivity values of fly ash A and B are in the order of 10^{10} – 10^{11} Ω.cm, which, according to the criteria listed in Table 2-3 are regarded as medium to high resistivities for electrostatic precipitation. High resistivity is a common observation for South African fly ash and is, reportedly, one of the main reasons for the low efficiencies obtained by most industrial-scale ESPs [50].

The resistivity of the -75 µm size fraction of ash B appears to be a stronger function of the electric field than that of ash A, whereas ash A in the -150+75 µm size range exhibits a stronger resistivity dependence on the electric field than the corresponding size fraction of ash B. This is shown more clearly in Figure C. 1, Appendix C-1. In general, the fly ash resistivity decreases with increased applied voltage. This relates to the increase in electric field intensity, which promotes current flow in the ash through the Schottky effect [47] (see Section 2.6.1). The average resistivities of fly ash A and B in the -75 µm and -150+75 µm size fractions, calculated from the plots in Figure A. 2, using Eq. 3.1 in Section 3.2.2, are provided in Table 5-6.

Table 5-6. Average resistivity of ash A and B

Ash sample	**Average resistivity (Ω.cm)**
-75 µm	
Fly ash A	1.66×10^{10}
Fly ash B	1.18×10^{11}
-150+75 µm	
Fly ash A	5.38×10^{10}
Fly ash B	1.30×10^{11}

The data in Figure 5-3 and Table 5-6 show that ash B has a higher resistivity than ash A for both the -75 μm and -150+75 μm particle size fractions. This could be due to the presence of Na-ions in ash A, as opposed to ash B, which contains undetectable quantities of Na_2O (see Tables 5-4 and 5-5).

As discussed in Section 2.6.1 – 2.6.2, the sodium ions are responsible for charge transport through the ash, which improves conduction and decreases fly ash A's resistivity. The same observation was made in the study of Ribberink (2018) [41]. It was previously stated that the Na content is the determining factor for the resistivity of fly ash in terms of its chemical composition. This is especially true for surface conduction – the prevalent conduction mechanism at ambient conditions relevant to this study.

The resistivities for the -75 μm fractions of ash A and B differ by almost an order of magnitude. On the other hand, the resistivity for the -150+75 μm fraction of ash B is only two times higher than that of ash A. Therefore, ash A exhibits a more drastic increase in resistivity between the -75 μm and -150+75 μm sizes than ash B. This corresponds to the larger variance in the PSDs of ash A, with an average diameter change of ~80 μm between the undersize and oversize fractions, compared to a ~70 μm change for that of ash B.

The increase in resistivity from the -75 μm to the -150+75 μm size range could suggest a dependence of ash resistivity on particle size at low temperatures. A logical explanation could be that the finer particles in the -75 μm ash provide a larger surface area for electron transport, resulting in a lower resistivity relative to the -150+75 μm ash. This statement is supported by Ribberink (2018) [41] and Qi & Yuan (2013) [98], whose research concluded that particles in the -75 μm size fraction exhibit considerably lower volume resistivities than -150+75 μm size particles.

5.2 RESPONSE SURFACE MODELLING

A generalised RSM model was developed to calculate the collection efficiencies for various combinations of ESP settings, based on the statistics of the experimental results. This model can be used to generate additional data for the ESP process in an artificial manner, which is a much less tedious alternative to physical experimentation. Two additional RSM models were derived from the general equation: one specifically focused on the ash particle size distribution (PSD) and the other on ash resistivity.

5.2.1 GENERAL RSM MODEL EQUATION

The quadratic RSM model derived from experimental data was used to predict the effects of different ESP variables (factors) on particle collection efficiency. The RSM model has the general form presented by Eq. 5.1, according to the method provided by Montgomery (2017) [81]:

$$\eta_{RSM} = \beta_0 + \sum_{i=1}^{5} \beta_i x_i + \sum_{i=1}^{5} \beta_{ii} {x_i}^2 + \sum_{j=2} \sum_{i<j} \beta_{ij} x_i x_j + X_k + \boldsymbol{\epsilon} \qquad \text{E 5.1}$$

In Eq. 5.1, the term x_i represents the standardised factor level for a particular variable (i) used in the experimental run of interest. The parameters β_i, β_{ii}, and β_{ij} are model coefficients that describe the corresponding first-order, second-order, and interactive effects of the various factors on collection efficiency. Furthermore, the coefficient, β_0, is a model constant for all the variables, and $\boldsymbol{\epsilon}$ denotes the error term for the modelled collection efficiency (η_{RSM}) relative to the measured value for a specific run.

The experiments were subdivided into three blocks, based on the discharge electrode geometry. An additional constant, X_k, was added to the model equation to account for the effect of the electrode geometry on particle collection efficiency. Every block group was assigned different settings (levels) for the experimental factors, depending on the practicality associated with the relevant electrode geometry. The five factors (each with four levels), three block variables, and respective numbering are listed in Table 5-7.

Table 5-7. Model blocks and factors

Block	$\boldsymbol{k}$	$\boldsymbol{X_k}$
G-spike	I	X_I
Threaded rod	II	X_{II}
Sawtooth	III	X_{III}
Factor	$\boldsymbol{i}$	$\boldsymbol{x_i}$
Plate spacing	1	x_1
Electrode spacing	2	x_2
Ash loading	3	x_3
Number of electrodes	4	x_4
Type of ash	5	x_5

Table 5-8 provides the corresponding first-order and second-order response coefficients for the blocks and factors from Table 5-7. The -75 µm ash A, -75 µm ash B, -150+75 µm ash A, and -150+75 µm ash B samples are denoted as *a*, *b*, *c*, and *d* in that order for the type of ash ($i = 5$) in Table 5-8.

Table 5-8. Model coefficients for response surface methodology

First-order response							
β_1	β_2	β_3	β_4	β_5			
				a	b	c	d
-3.18	1.28	5.13	1.26	-3.76	3.33	-2.20	2.63
Constant	**Block response**						
β_0	X_I	X_{II}	X_{III}				
87.2	10.1	-10.9	0.784				
Second-order response							
Interaction-1							
β_{11}	β_{12}	β_{13}	β_{14}	β_{15}			
				a	b	c	d
-0.585	0.057	-1.15	2.07	0.50	3.70	-0.75	-3.46
Interaction-2							
	β_{22}	β_{23}	β_{24}	β_{25}			
				a	b	c	d
	-3.25	-0.657	-2.29	1.12	-2.69	3.80	-2.23
Interaction-3							
		β_{33}	β_{34}	β_{35}			
				a	b	c	d
		-1.99	1.85	-0.54	-2.52	1.55	1.52
Interaction-4							
			β_{44}	β_{45}			
				a	b	c	d
			-1.14	0	0	0	0

The signs of the model coefficients indicate whether higher values for the corresponding terms in the model equation have positive or negative effects on the collection efficiency. A regression analysis concluded an R^2-value of 99.44% and a standard deviation of 1.34 for the RSM model (see Figure C. 2 in Appendix C-2). This shows a good fit between the RSM and experimental data, which proves the model's reliability for calculating the collection efficiencies of several kinds of ash with various ESP configurations. Tables C. 3 – C. 5 in Appendix C-2 provide all the RSM model results and the respective experimental efficiencies for different ESP settings.

An analysis of variance (ANOVA) study was performed to determine how – and to what extent – the different ESP factors affect the collection efficiency. Firstly, the contribution of the respective terms in Eq. 5.1 to the variability in average collection efficiency was analysed with the use of the Pareto chart in Figure 5-4. The relative sizes of the first-order, quadratic, and interactive effects of each variable are illustrated in

descending order on the chart. The reference line in red specifies a standard size of 2.11, beyond which an effect is considered significant at the corresponding significance level (α) of 5%. In this case, electrode spacing and its interactions with plate spacing and ash loading demonstrate negligible effects on collection efficiency. The remaining linear and quadratic terms have absolute effect sizes larger than the 2.11 reference point and are regarded as influential parameters in the RSM model.

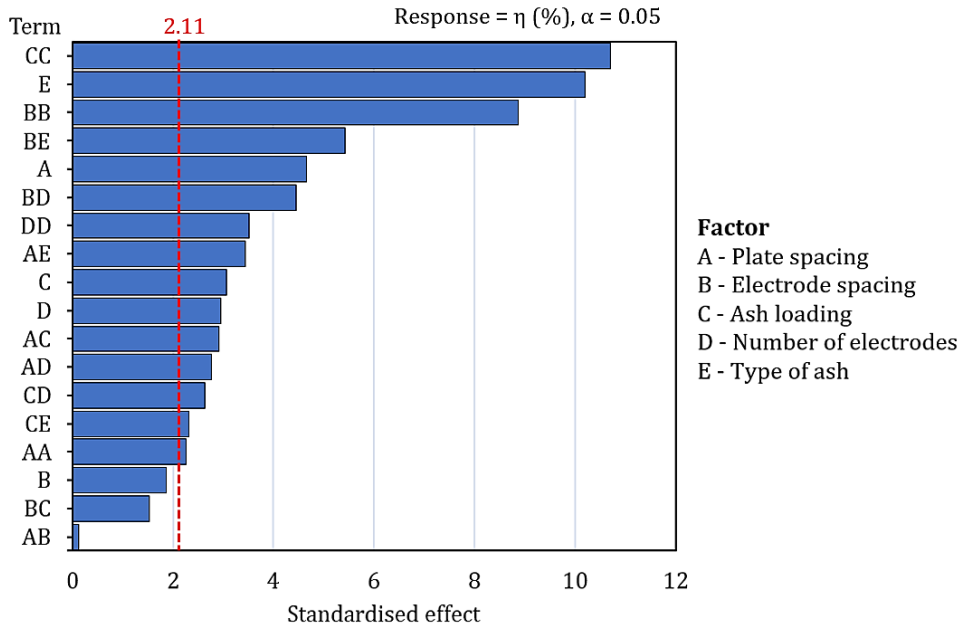

Figure 5-4. Pareto chart for the standardised effects on particle collection efficiency (η), with reference line at 2.11 for a significance level (α) of 0.05

It is also evident from Figure 5-4 that the type of ash (E) has the largest primary effect on collection efficiency, followed by that of collection plate spacing (A). These are the factors that one would typically consider for alteration when ESP efficiencies are very low and require drastic improvement. The fly ash loading (C) and the number of electrodes (D) have primary effects of similar magnitudes. The effects of factors C and D are smaller than that of factors A and E, though still detectable for some ESP configurations, like those involving threaded rod electrodes.

In terms of secondary effects, factors C and B seem to be the most notable in size, especially concerning the type of ash and the number of electrodes, as indicated by the relative sizes of the corresponding interactive effects (CC, BB, BE, and BD). The second-order and interactive effects are important when the collection efficiency is already high, and the ESP performance needs only to be refined. At this stage, the settings of the major contributing factors have already been optimised. The additional modification involves minor adjustments to the secondary effect variables to maximise the particle collection efficiency.

For a more detailed analysis of the second-order interactions, the F-statistic and P-value of each were determined and are given in Table 5-9. The F-value of a specific effect was calculated from the ratio of the effect's mean squared error (MS_F) to the combined mean squared error of all effects (MS_E). The size of this parameter relative to the critical F-value indicates the extent to which each term in the model is associated

with the output – in this case, collection efficiency [81]. An F-critical value of 2.54 was obtained for the 60 experimental runs at a probability level of 5% ($\alpha = 0.05$).

Table 5-9. Analysis of variance (ANOVA) table for RSM model

Term	F-value	P-value	Significant? (Yes/No)
AA	5.09	3.76E-02	Y
BB	78.7	8.70E-08	Y
CC	115	5.65E-09	Y
DD	12.4	2.65E-03	Y
AB	0.02	8.96E-01	N
AC	8.49	9.68E-03	Y
AD	7.69	1.30E-02	Y
AE	6.87	3.09E-03	Y
BC	2.33	1.46E-01	N
BD	19.8	3.51E-04	Y
BE	15.2	4.60E-05	Y
CD	6.98	1.71E-02	Y
CE	3.66	3.36E-02	Y

As seen in Table 5-9, the F-values of the AB and BC interactions are 0.02 and 2.33, respectively, which are both smaller than $F_{crit} = 2.54$. This suggests that these terms have little to no significance in the collection efficiency result. Furthermore, the probability statistics (P-values) of the AB and BC effects are both larger than the reference value of $\alpha = 0.05$, confirming that the conclusion drawn from the F-test is correct (with a 95% probability). The remaining effects all have F-values higher than 2.54 and P-values below 0.05, which indicates the importance of the corresponding terms in the RSM model.

Considering the high degree of statistical significance observed for the type of ash through the ANOVA review, a more comprehensive examination was performed on this factor. This was to establish whether the sizeable effect is predominantly related to the ash particle size or the fly ash resistivity.

5.2.2 RSM MODEL FOR PARTICLE SIZE OF ASH

To analyse the involvement of ash PSD in the effect of factor E (type of ash) on collection efficiency, a separate RSM model was developed for the ESP runs involving only ash A in the -75 µm and -150+75 µm size fractions. The parameters approximated for the model are provided in Table C. 6, Appendix C-2. Good accuracy was confirmed for the PSD-related RSM model with a high R^2-value of 99.87% (see Figure C. 3 in Appendix C-2) and a small standard deviation of 1.01.

The significance of fly ash particle size for collection efficiency was evaluated with experimental data from runs S_{-75} and S_{+75}. The ESP settings for S_{-75} and S_{+75} in uncoded units include three sawtooth electrodes situated 101 mm apart between two collection plates with a spacing of 160 mm. Fly ash feed concentrations of 15 $mg.Nm^{-3}$ and 13 $mg.Nm^{-3}$, and ash with PSDs of -75 µm and -150+75 µm were used for S_{-75} and S_{+75},

respectively. The collection efficiencies were averaged for the total voltage ranges of the corresponding runs, and the results are indicated in Table 5-10.

Table 5-10. Results from S_{-75} and S_{+75} for comparison of PSD effect on efficiency

Run	Ash PSD (μm)	Voltage range (kV)	η_{EXP} (%)	η_{RSM} (%)
S_{-75}	-75	23 – 37	84.8	84.7
S_{+75}	-150+75	23 – 38	82.8	82.8

As seen in Table 5-10, S_{-75} with the smaller -75 μm particle size fraction achieved higher average collection efficiencies across the 23 – 37 kV voltage range than S_{+75} with the larger -150+75 μm ash. This is also depicted in the collection efficiency plots in Figure 5-5 for the 75 μm undersize and oversize ash fractions.

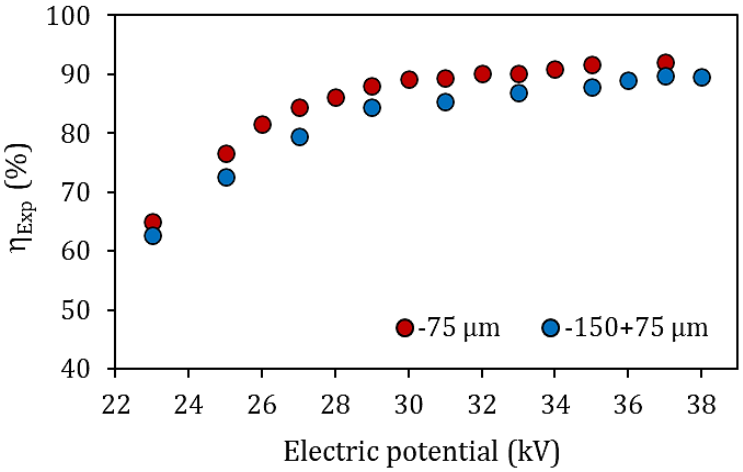

Figure 5-5. Collection efficiency of -75 μm compared to -150+75 μm ash

Considering the larger size of the particles in the -150+75 μm fraction, the gravitational, drag, and electrostatic body forces (see Eq. 4.22) acting on these particles should be larger relative to that of smaller particles. Therefore, larger ash particles are expected to exhibit faster charging, migration, and settling rates and to show higher collection efficiencies than finer ash as a consequence. This theory was confirmed by the studies of Kim *et al.* (2001), Chengfeng *et al.* (2004), and Sarkar *et al.* (2012), as discussed in Section 2.5. However, the collection efficiencies determined from the experimental measurements show otherwise.

Since the experimental data, in this case, contradict the fundamental principles of electrostatic precipitation, the only logical explanation is that the DustTrak monitors provided inaccurate concentration readings for the coarse fly ash samples. As a result, the information obtained from the experimental and RSM results was insufficient for a final conclusion to be made regarding the effect of ash PSD on collection efficiency. Therefore, this matter is further investigated with the outcomes of the CFD model (Section 5.3.2).

5.2.3 RSM MODEL FOR FLY ASH RESISTIVITY

The fly ash resistivity contribution to the type of ash (E) effect on efficiency was also investigated independently from ash PSD. This was achieved with a third RSM model, accounting only for the ESP runs that used the -75 μm size samples of ash A and B. The corresponding coefficients determined for this RSM model are listed in Table C. 7 of Appendix C-2.

According to the R^2-value shown on the regression plot in Figure C. 4, Appendix C-2, a 99.36% correlation was obtained between the RSM predictions and experimental data. In addition, the model exhibits a small standard deviation of 1.18 from measured values, which indicates a satisfactory degree of accuracy.

In an evaluation of the results from runs S_{H-1} and S_{L-1}, runs S_{H-2} and S_{L-2}, and runs G_H and G_L, the difference in particle collection efficiency was examined for fly ash of medium and high resistivity. The ESP settings and collection efficiency versus voltage plots for the relevant runs are given in Figure 5-6.

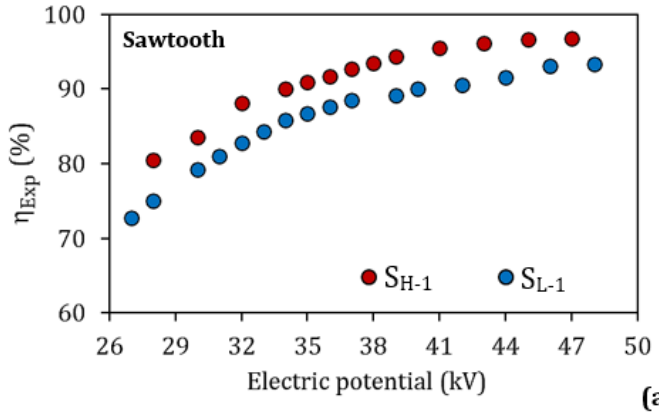

Run	S_{H-1}	S_{L-1}
Plate spacing (mm)	220	220
Electrode spacing (mm)	101	101
Ash loading (mg.Nm^{-3})	22	34
No. of electrodes	3	3
Ash resistivity (Ω.cm)	1.2E+11	1.7E+10
η_{EXP} (%)	91.6	85.7
η_{RSM} (%)	91.9	86.6

(a)

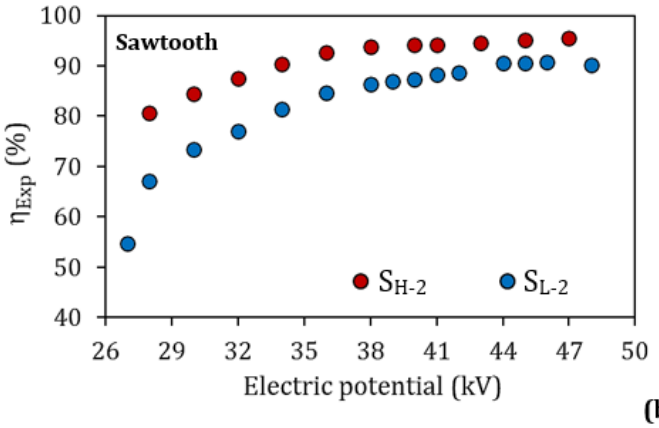

Run	S_{H-2}	S_{L-2}
Plate spacing (mm)	220	220
Electrode spacing (mm)	101	101
Ash loading (mg.Nm^{-3})	16	14
No. of electrodes	3	3
Ash resistivity (Ω.cm)	1.2E+11	1.7E+10
η_{EXP} (%)	91.2	82.5
η_{RSM} (%)	90.5	82.5

(b)

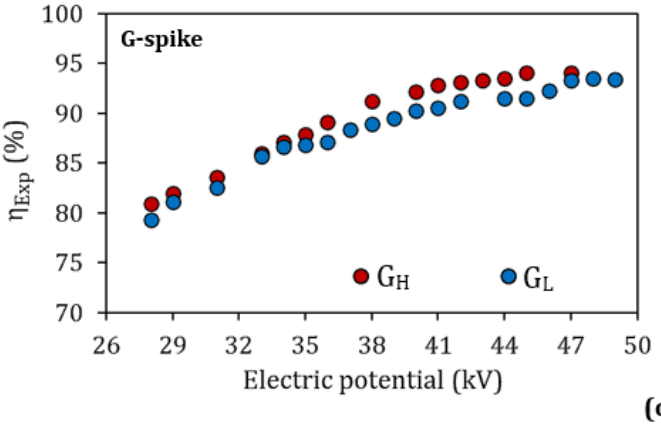

Run	G_H	G_L
Plate spacing (mm)	280	280
Electrode spacing (mm)	144	144
Ash loading (mg.Nm^{-3})	16	16
No. of electrodes	2	2
Ash resistivity (Ω.cm)	1.2E+11	1.7E+10
η_{EXP} (%)	89.4	88.6
η_{RSM} (%)	90.4	86.8

(c)

Figure 5-6. Collection efficiency comparison of S_{H-1}, S_{L-1}, S_{H-2}, S_{L-2}, G_H, and G_L for resistivity effect

In S_{H-1} and S_{L-1}, the collection efficiencies of high and medium resistivity fly ash (ash B and A in Table 5-6) are compared for large ash loadings (>20 mg.Nm^{-3}), using three sawtooth electrodes at a 101 mm spacing with a 220 mm plate-plate distance. The RSM results in Figure 5-6 (a) are in good agreement with

experimental data, having small deviations of 0.3% and 0.9% from the average collection efficiencies of S_{H-1} and S_{L-1}, respectively.

The efficiency plots in Figure 5-6 (a) further indicate a higher onset voltage (28 kV) for S_{H-1} with high resistivity ash (B), relative to that of S_{L-1} (27 kV) with medium resistivity ash (A). This corresponds with the increased difficulty experienced by particles from ash B to acquire charge due to its higher characteristic resistance to the flow of current. For such high resistivity ash, a larger threshold electric field is required for particle charging to commence, necessitating a steeper voltage gradient between the electrodes and collection plates. The higher relative current for the lower resistivity ash in S_{L-1} compared to S_{H-1} at equivalent voltages is also portrayed in the current-voltage plots for the respective runs in Figure C. 5, Appendix C-2.

In addition, dielectric breakdown in the collected dust layer occurs at a lower voltage (47 kV) for the high resistivity ash from S_{H-1}, compared to the 48 kV sparkover voltage for medium resistivity ash in S_{L-1}. This can be attributed to the increased tendency of high resistivity ash (B) to retain charge, as opposed to medium resistivity ash (A) that gradually loses charge upon collection. As a result, back-corona initiates at lower voltages for high-resistivity ash due to excessive charge build-up in the deposited dust (see Section 2.6.2).

Nevertheless, an average collection efficiency of 91.6% was reported for the 28 – 47 kV voltage range of S_{H-1} with the higher resistivity ash. This is almost 6% higher than the average efficiency of 85.7% observed for the medium resistivity ash from S_{L-1} at 27 – 48 kV. As listed in Table 2-3 from Section 2.6.2, fly ash in the 10^8 – 10^{11} Ω.cm resistivity range is categorised as medium resistivity ash. Therefore, from a technical point of view, ash A and B in the -75 μm size range fall within the medium resistivity class. This was also confirmed by Mizuno (2000) and Roberts *et al*. (2018), who associated ash resistivities of ~10^5 – 10^{11} Ω.cm with normal ESP operating conditions and high collection efficiencies (see Figure 2-2, Section 2.6.2).

In such circumstances, the higher relative resistivity of ash B could improve collection efficiency as its sustained particle attraction to the collection plates can prevent re-entrainment. Furthermore, since the ESP process was closely monitored and immediately stopped once arcing occurred, the efficiency losses due to back-corona were minimised for each experimental run.

Runs S_{H-2} and S_{L-2} present a comparison of the collection efficiencies for the same high and medium resistivity ash samples and electrode configuration from S_{H-1} and S_{L-1}, but with intermediate ash loadings (10 – 20 mg.Nm^{-3}). In Figure 5-6 (b), the average collection efficiencies calculated with the RSM model are close to the actual measurements for S_{H-2} and S_{L-2}, with corresponding differences of 0.7% and < 0.01%.

Analogous to runs S_{H-1} and S_{L-1}, run S_{H-2} with the higher resistivity ash (B) exhibits a shorter voltage span (28 – 47 kV) than that of S_{L-2} (27 – 48 kV) with the lower resistivity ash (A). This is also attributed to the fact that identical electrode settings were used for S_{H-1}, S_{L-1}, S_{H-2}, and S_{L-2}. However, in this case, the average particle collection efficiency determined for the high resistivity ash in S_{H-2} is 9% higher than that of the lower resistivity ash from S_{L-2}. The efficiency difference between runs S_{H-2} and S_{L-2} is 3% larger than that

between runs S_{H-1} and S_{L-1}. This shows that, for lower fly ash loadings, the ash resistivity plays a more significant role in the collection efficiency outcome than for higher fly ash loadings.

In an assessment of the data from G_H and G_L, the collection efficiency dependence on ash resistivity was investigated for two G-spike electrodes with electrode and plate spacings of 144 mm and 280 mm, respectively. The medium and high resistivity ash from runs S_{H-1} and S_{L-1}, and S_{H-2} and S_{L-2} were also used in runs G_H and G_L, both with a moderate ash loading of 16 mg.Nm^{-3}. Figure 5-6 (c) shows that the modelled and experimental average collection efficiencies differ by 1.0% for G_H and 1.8% for G_L. These deviations – although larger than for S_{H-1}, S_{L-1}, S_{H-2}, and S_{L-2} – are still in good order for application in this study.

Unlike the former ESP assemblies from Figure 5-6 (a) and (b), runs G_H and G_L have almost identical current-voltage characteristics (see Figure C. 5, Appendix C-2) and the same onset voltage of 28 kV. On the other hand, G_H with the higher resistivity ash demonstrates arcing at a voltage of 47 kV, which is 2 kV lower than the 49 kV sparkover voltage of G_L with the medium resistivity ash. This is consistent with the previous findings for runs S_{H-1} and S_{L-1}, and S_{H-2} and S_{L-2}.

In contrast to the ESP configurations involving sawtooth electrodes, the G-spikes exhibit almost identical collection efficiencies across the 27 – 49 kV voltages for both ash B in G_H and ash A in G_L. The average collection efficiencies for the higher and medium resistivity ash from G_H and G_L vary by only 0.8%. This is considerably smaller than the 6% and 9% variations observed for the sawtooth assemblies in Figure 5-6 (a) – (b). Based on these findings, it can be deduced that the collection efficiency has a more negligible dependence on ash resistivity for G-spikes than for sawtooth electrodes.

A general conclusion on this topic is that the collection efficiency outcome has a variable sensitivity toward the fly ash resistivity for different electrode geometries, fly ash loadings and other ESP settings. Another common observation among all of the runs considered for this evaluation is that the ash with the higher 1.2×10^{11} Ω.cm resistivity showed higher collection efficiencies than the 1.7×10^{10} Ω.cm resistivity ash.

Additional data for the ash resistivity effect on collection efficiency were generated with the general RSM model from Section 5.2.1. The model plots for the collection efficiencies of sawtooth, G-spike, and threaded rod electrodes as functions of ash resistivity are illustrated in Figure 5-7. The sawtooth, G-spike, and threaded rod electrodes with constant ESP settings (summarised in the table in Figure 5-7) show similar trends in collection efficiencies for the 1.6×10^{10} – 1.3×10^{11} Ω.cm resistivity range.

Overall, the G-spikes show the highest, the sawtooth electrodes the second-highest, and the threaded rods have the lowest collection efficiencies across the 1.6×10^{10} – 1.3×10^{11} Ω.cm resistivity range for identical ESP settings. Three distinct resistivity regions were identified for the efficiency plots in all cases. These include resistivities of 0.16 – 0.5 $\times10^{11}$ Ω.cm, 0.5 – 1.2 $\times10^{11}$ Ω.cm, and 1.2 – 1.3 $\times10^{11}$ Ω.cm, which are indicated by the dotted lines with orange markers on the graph in Figure 5-7. The collection efficiencies increase with increased ash resistivities up to 0.5×10^{11} Ω.cm, after which the efficiencies remain relatively constant for a further increase in resistivity to 1.2×10^{11} Ω.cm. Above 1.2×10^{11} Ω.cm, the plots demonstrate sharp declines in collection efficiency for increased ash resistivities up to 1.3×10^{11} Ω.cm.

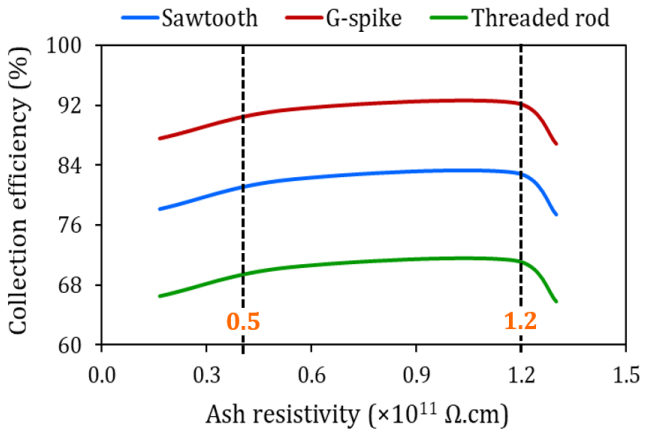

ESP Setting	Specification
Plate spacing	280 mm
Electrode spacing	164 mm
Number of electrodes	2
Ash loading	14 mg.m^{-3}
Ash resistivity	1.6×10^{10} – 1.3×10^{11} Ω.cm

Figure 5-7. Ash resistivity effect on collection efficiency as predicted by the RSM model

According to the plot in Figure 2-2 (Section 2.6.2), which closely resembles the plot in Figure 5-7, this behaviour is consistent with high re-entrainment, normal operation, and high arcing resistivity ranges in ESPs. Initially, the efficiencies increase due to a decreased susceptibility to re-entrainment for the collected dust when the ash resistivity increases from 0.16×10^{11} Ω.cm to 0.5×10^{11} Ω.cm. Ashes with resistivities between 0.5×10^{11} Ω.cm and 1.2×10^{11} Ω.cm sustain normal ESP operating conditions, where the highest particle collection rates are typically achieved. An additional increase in ash resistivity above 1.2×10^{11} Ω.cm instigates back-corona of increasing intensity in the ESP, resulting in severe efficiency losses (see Section 2.7.3).

The collection efficiency generally changes by a maximum of 5% within the measured range of resistivities for a specific electrode geometry. Conversely, a 9 – 12% difference in efficiency is observed for the various types of electrodes. Therefore, a change in ash resistivity from 1.6×10^{10} Ω.cm to 1.3×10^{11} Ω.cm presents a much smaller effect on the collection efficiency than other ESP variables, such as the electrode shape.

5.2.4 PREDICTION OF ASH LOADING EFFECT WITH RSM MODEL

The effect of ash loading on the ESP collection efficiency was further investigated using data that was generated with the general RSM model (Section 5.2.1). The predicted plots for the collection efficiencies of sawtooth, G-spike, and threaded rod electrodes at various ash loadings are given in Figure 5-8. The same ESP settings were used in the RSM model for the three types of discharge electrodes and are summarised in the table on the right in Figure 5-8.

Similar to the plots in Figure 5-7, the sawtooth, G-spike, and threaded rod electrodes demonstrate analogous trends in collection efficiencies for ash loadings of 3 – 31 mg.m^{-3} in Figure 5-8. Once again, the G-spike, sawtooth, and threaded rod electrodes show decreased collection efficiencies in the corresponding order. An increase in ash loading from 3 mg.m^{-3} to 25 mg.m^{-3} produces a 9.7% increase in particle collection efficiency. This efficiency change is comparable in size to the 9 – 12% efficiency difference between the threaded rod, sawtooth, and G-spike electrode geometries. Therefore, ash loading plays a significant role in the overall ESP performance.

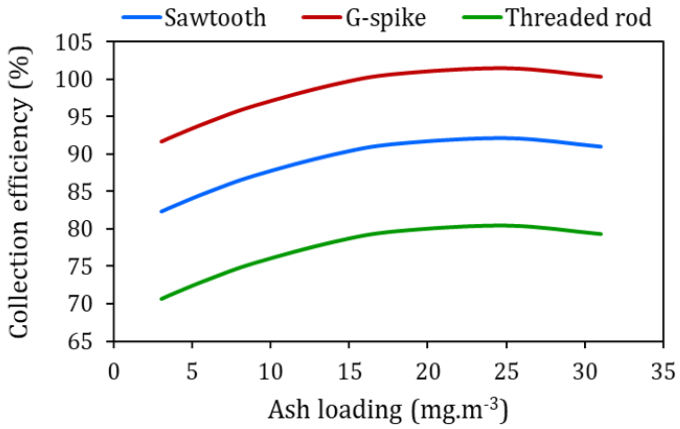

ESP Setting	Specification
Plate spacing	160 mm
Electrode spacing	112 mm
Number of electrodes	3
Ash type	Ash A
Ash PSD	-75 µm
Ash loading	3 – 31 mg.m^{-3}

Figure 5-8. Ash loading effect on collection efficiency as predicted by the RSM model

In general, the particle collection efficiencies gradually increase for increased ash loadings up to approximately 16 mg.m^{-3}. This is consistent with the results in Section 5.2.3, which indicated increased levels of difficulty and complexity for particle collection with decreased ash concentrations in the ESP. The collection efficiencies start to plateau with ash loadings approaching 26 mg.m^{-3} and reach maximum values near this point. A further increase in ash loading up to 31 mg.m^{-3} finally leads to decreased collection efficiencies, which can be attributed to an excessive accumulation of ash in the dust layers on the collection plates. This leads to weakened electrostatic attraction forces between the plates and charged particles, which results in slow particle charging and migration rates, together with high levels of ash re-entrainment.

5.3 COMPUTATIONAL FLUID DYNAMIC (CFD) MODELLING

A computational fluid dynamic model was developed to describe the ESP process. The CFD model outcomes provided insight into the fundamental operation of the ESP, which was useful for interpreting the collection efficiency results from the ESP experiments.

5.3.1 MODEL VALIDATION

STAR-CCM+ uses acknowledged numerical models to compute the relevant physics at each node in the mesh. Therefore, the model's accuracy is justified by the quality of the geometries and meshes used in the computational models. The 3-D ESP geometries created in Siemens NX-12 had the exact dimensions of the actual electrodes, collection plates, and other significant components. This ensured that the simulated domains resembled the real ESP setup used in the experiments. Secondly, the mesh of each model was refined to the greatest extent practically possible and verified with mesh independence studies, proving its ability to obtain accurate solutions [see Appendix B-1.1].

The air flow CFD model was tested with a configuration that included three G-spike discharge electrodes and a 280 mm plate-to-plate distance. The average air flow velocities across the ESP inlet and outlet were measured experimentally and compared with model values. Figure 5-9 shows the modelled air flow distribution through the ESP section.

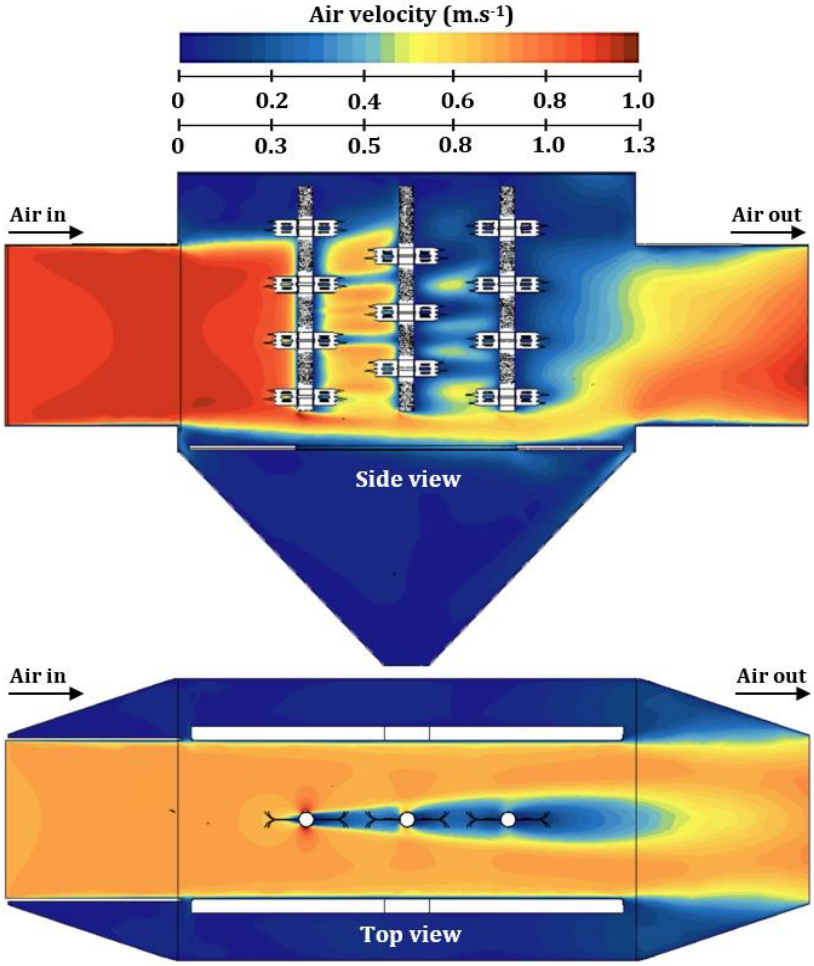

Figure 5-9. Modelled air flow profile through ESP setup

The upper and lower air velocity scales indicated in the figure correspond to the side-view and top-view flow profiles, respectively. The model predicted average velocities of 0.90 $m.s^{-1}$ and 0.73 $m.s^{-1}$ at the ESP entrance and exit. Experimental measurements provided an average value of 0.86 $m.s^{-1}$ for the inlet air velocity and 0.72 $m.s^{-1}$ for the outlet air velocity, which confirms that the CFD model accurately projects the air flow in the ESP.

As demonstrated in Figure 5-9, the guide plates at the front of the ESP fulfilled their purpose of maintaining the air flow within the space between the collection plates so that no particles bypass at the back of the plates. Furthermore, the floor plate at the bottom of the ESP serves as a shield to prevent stirring in the hopper bin, which can cause settled particles to re-enter the gas stream. The low flow velocities at the electrode and plate surfaces correspond to the 'no-slip' condition implemented at these boundaries in the model description (see Section 4.2.6). In addition, the discharge electrodes caused a slight drop in the air velocity across the ESP, hence the lower velocity values at the outlet region.

The computational model was further validated by comparing the simulated voltage-current (V-I) relationships for different ESP settings with experimental data. The V-I characteristics for a single G-spike electrode (see geometries and components in Figure B. 7 – Figure B. 10 in Appendix B-2) with a collection plate spacing of 160 mm, as predicted by the model and measured experimentally, are presented in Figure 5-10.

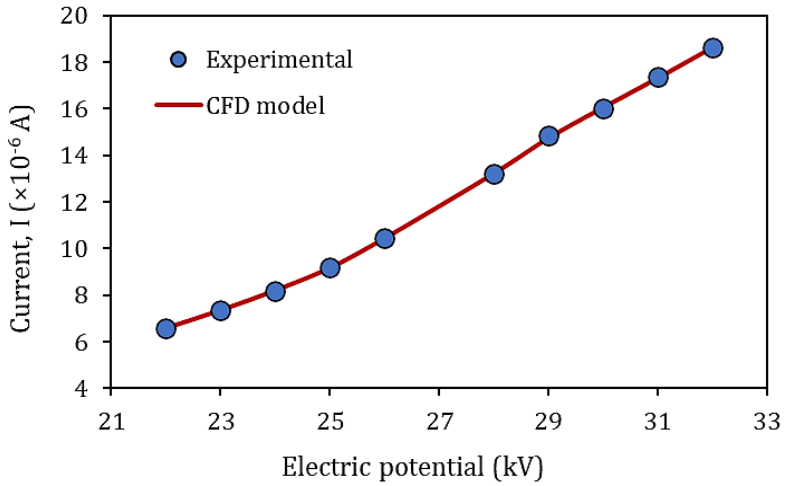

Figure 5-10. Modelled and experimental V-I curves for G-spike electrode

The V-I characteristics of three sawtooth electrodes (see geometry in Figure B. 6, Appendix B-2) with an electrode spacing of 101 mm and a plate spacing of 160 mm were modelled and fitted to experimental data, as shown in Figure 5-11.

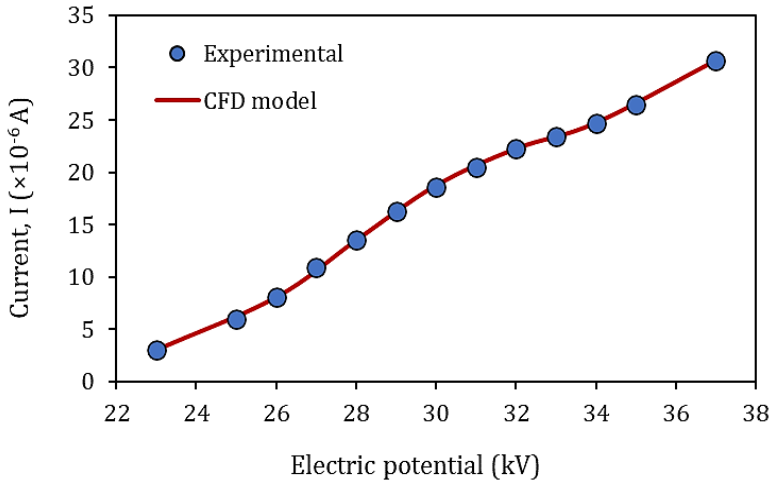

Figure 5-11. Modelled and experimental V-I curves for sawtooth electrode

The current across two threaded rods (geometry shown in Figure B. 11, Appendix B-2), situated 57 mm apart, with a 160 mm plate spacing, was modelled and compared to measured values at voltages of 36 – 44 kV. The results are illustrated in Figure 5-12.

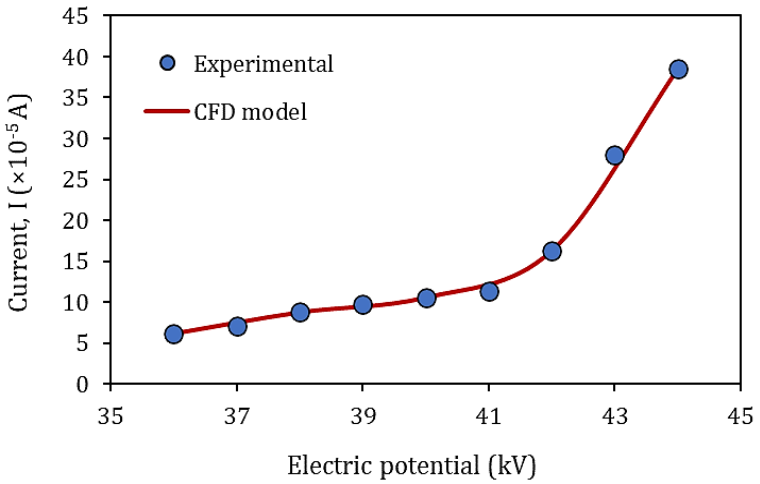

Figure 5-12. Modelled and experimental V-I curves for threaded rod electrode

A high degree of accuracy could be obtained for the electric current distribution across the discharge electrodes and in the ESP. The current was recorded for each electrode assembly at different voltages during the ESP experiments. The electrodes were connected in parallel; therefore, the total current was evenly divided among the electrodes – or electrode spikes in the case of G-spike and sawtooth electrodes. The current density was calculated from the current measurement per square meter of electrode. The respective electrode and spike surface areas were obtained from the geometries in NX-12.

The space charge density was manually adjusted in STAR-CCM+ until the average current density on each electrode predicted by the model differed by less than 0.1% from the experimental data. Furthermore, the

applied voltage was specified to be the same at every point on all the electrodes (parallel connection), while the potential on the plate was set close to zero. With the current density, electric potential, and electrode geometries being fitted to experimental values, the simulated electric fields would automatically distribute in a manner representative of the actual ESP conditions.

The simulation results in Figure 5-10 – 5-12 exhibit close correlations with experimental V-I data for the G-spike, sawtooth, and threaded rod electrodes. This confirms the computational model's accuracy and suitability to predict the V-I relationships of different electrode setups in this study.

The CFD model from this study was further tested with a base case from Neimarlija *et al.* (2009) [79] of an elementary wire-plate ESP setup. This entailed a 2-D geometry of a single wire discharge electrode with a radius of 0.152 mm taken from an assembly with a 152.4 mm wire-to-wire distance and a 114.3 mm wire-to-plate distance. The model of Neimarlija *et al.* (2009) was developed for experimental data from Penney and Matick (1960) [99] and found a good agreement between modelled and measured values. The current density at the collection plate (J_0), ion mobility (K), and electric potential (ϕ) obtained from the model in this study and that of [79] are given in Table 5-11.

Table 5-11. Comparison of model values from [79] and this study

Parameter	This study	Neimarlija
J_0 (A.m^{-2})	3.78×10^{-4}	3.77×10^{-4}
K (m^2.V^{-1}.s^{-1})	2.0×10^{-4}	2.0×10^{-4}
ϕ (kV)	25.0	25.0

The model compares very well with the model of Neimarlija *et al.* (2009), which is a proven model, indicating that this model can be trusted and applied to the ESP system in this study.

5.3.2 GRAVITATIONAL SETTLING

Several ESP runs were conducted in the absence of an electric field. This was to determine the percentage of ash particles that exited the air stream in the ESP due to gravitational settling. Each computational model was initially run without electrostatics to acquire settling efficiencies close to the experimentally measured values for the related ash feed. The electrode assemblies and corresponding settling rates for the gravitational runs are shown in Table 5-12. Additional information on the results obtained from the gravitational settling experiments is given in Appendix C-3.1.

Table 5-12. Gravitational runs settings and settling rates of particles in the -75 µm size fraction

Run	Electrode shape	Plate spacing (mm)	Electrode spacing (mm)	No. of electrodes	Ash PSD (µm)	Settling rate (%)
GR-1	None	N/A	N/A	N/A	-75	36.7
GR-2	Sawtooth	400	164	2	-75	28.5
GR-3	G-spike	160	112	3	-75	21.6

Settling rates were compared for minimum obstruction (no collection plates or electrodes in run GR-1), medium obstruction (flat sawtooth electrodes and a wide plate spacing of 400 mm in run GR-2), and maximum obstruction (three large G-spikes and a narrow plate spacing of 160 mm in run GR-3). According to the thimble values, the settling rates for -75 µm particles decrease with an increased extent of obstruction in the ESP due to a lower pressure drop and higher turbulence. Therefore the settling of the particles from the -75 µm ash is governed by the ESP's gravitational, pressure gradient and fluid drag forces.

The average particle settling rates for runs GR-2 and GR-3 were calculated with the CFD model and compared to the gravimetric thimble measurements. These results are given in Table 5-13. The modelled settling rates in Table 5-13 show small deviations of 0.3% and 1.5% from experimental data for GR-2 and GR-3, respectively. This indicates a good correlation between the CFD model and thimble measurements for the settling efficiencies of runs GR-2 and GR-3.

Table 5-13. Modelled settling rates versus measured values in GR-2 and GR-3

Run	Average settling rate (%)	
	Thimble measurement	**CFD model**
GR-2	28.5	28.8
GR-3	21.6	20.1

The air flow patterns and turbulence were modelled for the two ESP assemblies used in the gravitational runs, and the results are shown in Figure 5-13 and Figure 5-14. The "**v** →" sign in the diagrams indicates the direction in which the particle-laden air flows. An investigation of the flow fields reveals that the extent of obstruction in the ESP significantly affects the air turbulence, which indirectly influences the particle dispersion and settling rates.

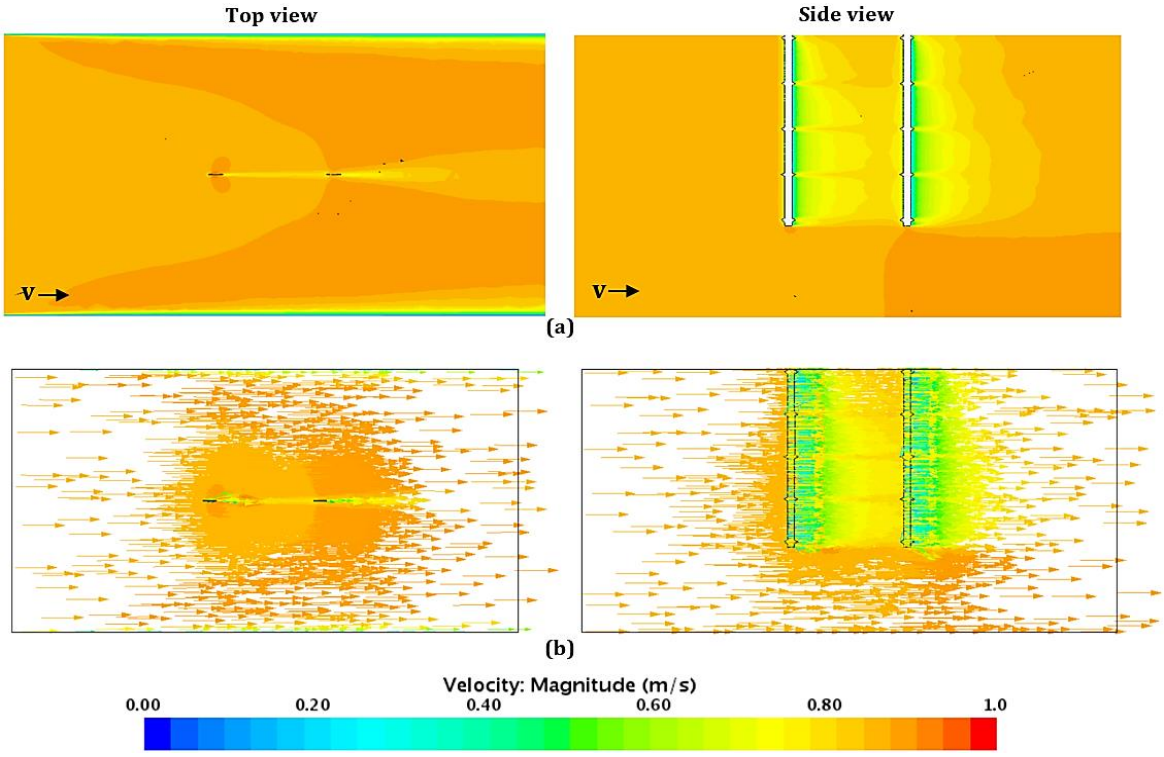

Figure 5-13. Velocity profile for run GR-2, represented in **(a)** scalar and **(b)** vector scenes

For the less-obstructed setup used in run GR-2 (Figure 5-13), the flow is laminar, and the air velocity remains relatively constant, with a minimal variation of approximately 0.2 $m.s^{-1}$ throughout the ESP chamber. The air maintains momentum and enters and exits the ESP at similar velocities. The velocity vectors indicate linear flow patterns across the sawtooth electrodes and between the collection plates.

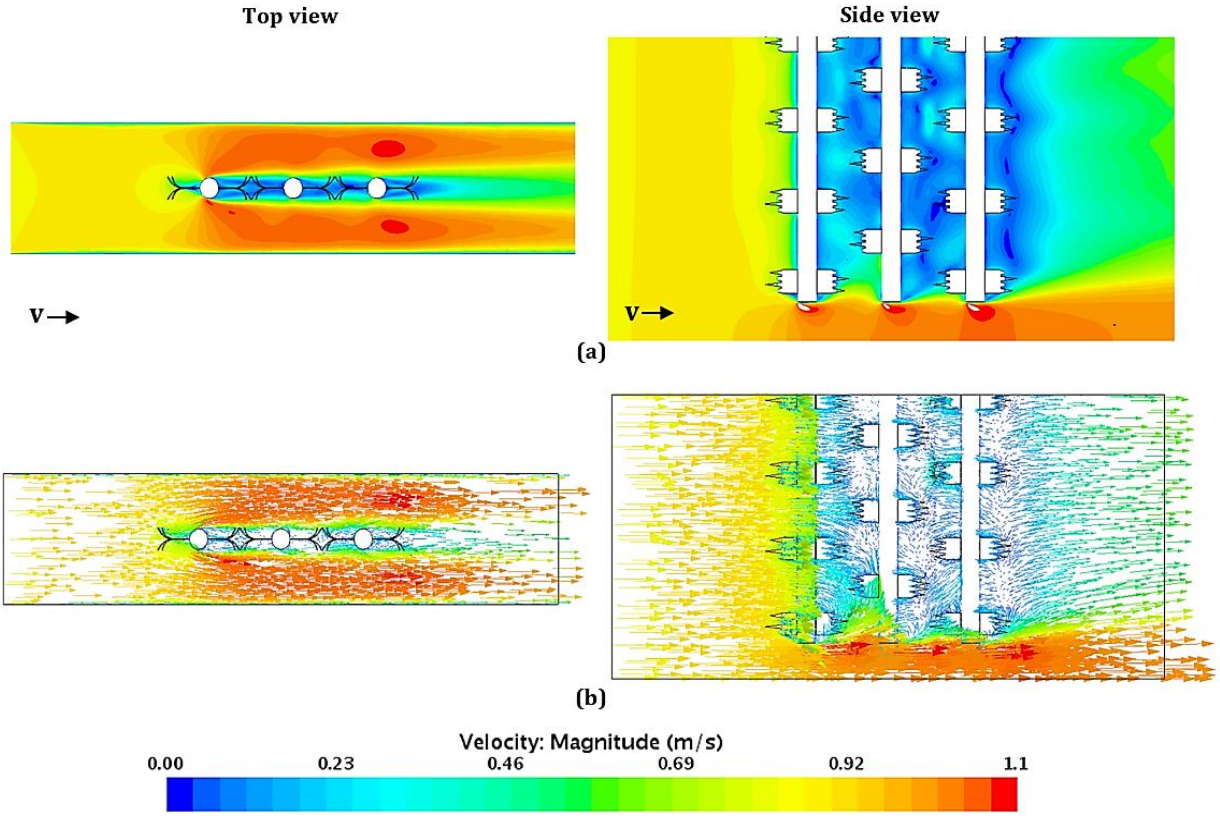

Figure 5-14. Velocity profile for runs GR-3, represented in **(a)** scalar and **(b)** vector scenes

The air flow for the setup in run GR-3, where the flow path is more obstructed, exhibits a higher degree of turbulence. This is evident from the difference in size and direction of the arrow vectors in Figure 5-14 (b), which illustrates non-linear flow patterns, caused by eddy currents in-between and around the G-spike electrodes. A larger variance in air velocity (>1 $m.s^{-1}$) is observed for this electrode configuration. In this case, the overall air velocity drops from 0.86 $m.s^{-1}$ at the ESP inlet to around 0.6 $m.s^{-1}$ at the outlet. This facilitates longer particle residence times in the ESP, which is expected to increase settling rates. However, the high-velocity region at the bottom of the ESP promotes the re-entrainment of settled particles on the floor plane, potentially resulting in decreased settling rates.

The modelled particle trajectories for the gravity runs were represented by track fields, which are shown in Figure 5-15 and Figure 5-16. For the spacious assembly in run GR-2 (Figure 5-15), the particle tracks portray distinct, segregated flow lines, as opposed to run GR-3 (Figure 5-16), which exhibits more evenly distributed particle-laden flows across the ESP section. Air turbulence is, therefore, required for sufficient dispersion of suspended particles in the air stream, which can increase the collection efficiencies of such particles. However, this is rather the case for the electrostatic precipitation of particles on the collection plate surfaces and is less important for gravitational settling. Instead, excessive turbulent intensities can result in large efficiency losses due to particle re-entrainment in the absence of an electric field.

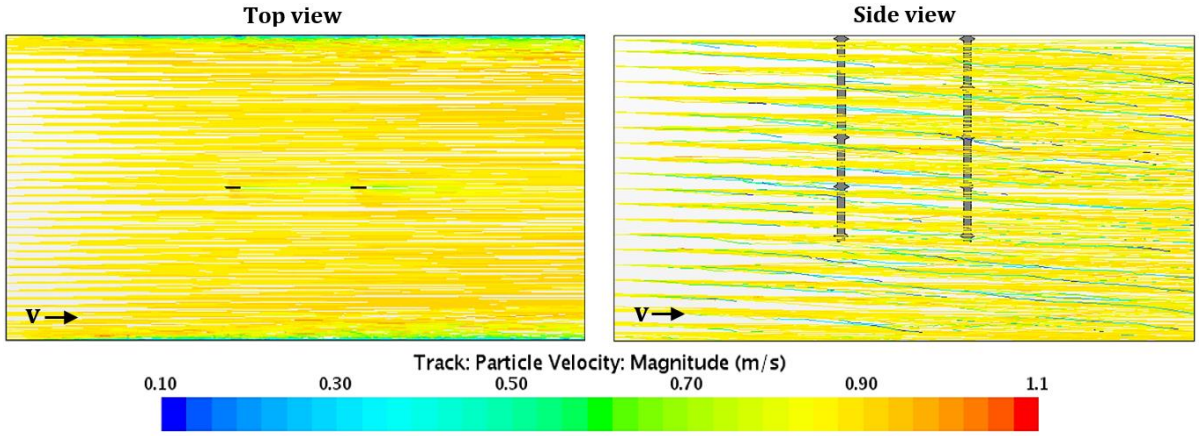

Figure 5-15. Particle track velocities for run GR-2

The flow paths of the small particles in the -75 µm size fraction show a strong correlation to air flow patterns in the ESP. The trajectories of these particles are governed by drag, buoyancy, pressure gradient, and turbulent forces imposed by the surrounding air [17]. This can be seen in the particle tracks, where the particles follow straight paths in the laminar flow from Figure 5-15, contrary to the irregular particle paths observed in the turbulent flow from Figure 5-16. The high susceptibility of fine particulates to turbulent currents was previously pointed out by White (1977) [17]. Therefore, factors such as the structural design of the ESP and air conditions generally play a significant role in the collection of particles from fine ash.

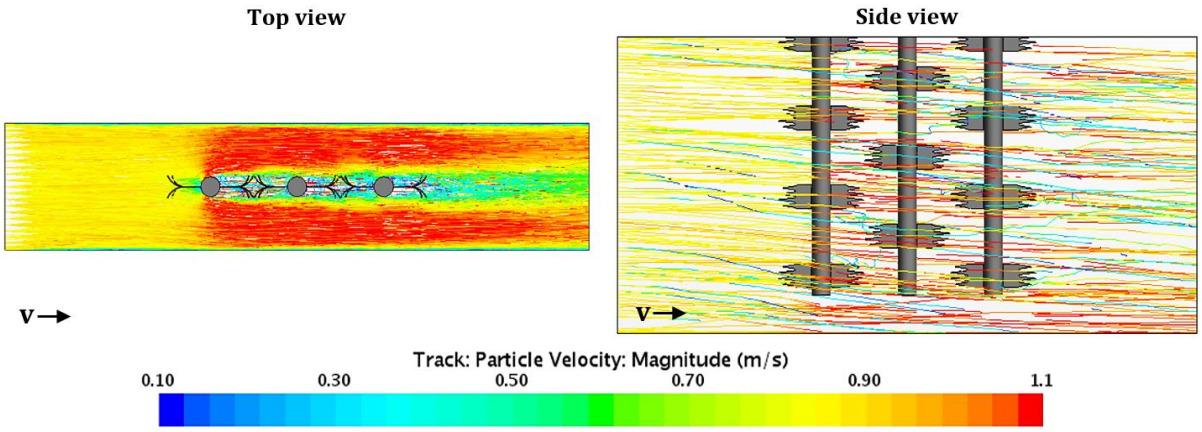

Figure 5-16. Particle track velocities for runs GR-3

5.3.3 ELECTRODE GEOMETRY AND ELECTRIC FIELD DISTRIBUTION

The electric field distributions across the sawtooth, threaded rod and G-spike electrode geometries were modelled. The models were fitted to experimental data from runs S-3, T-2 and G-1, for which the settings are summarised in Table 5-14.

Table 5-14. Electrode settings and voltages used for S-3, T-2 and G-1

Run	Electrode shape	Plate Spacing (mm)	No. of electrodes	Voltage range (kV)
S-3	Sawtooth	160	3	23 – 37
T-2	Threaded rod	160	2	36 – 44
G-1	G-Spike	160	1	22 – 32

The shapes of the electric fields generated by each electrode geometry were evaluated and compared qualitatively. Figure 5-17 shows the electric field and current density distributions for three sawtooth electrodes and a 160 mm plate spacing at an applied voltage of 23 kV.

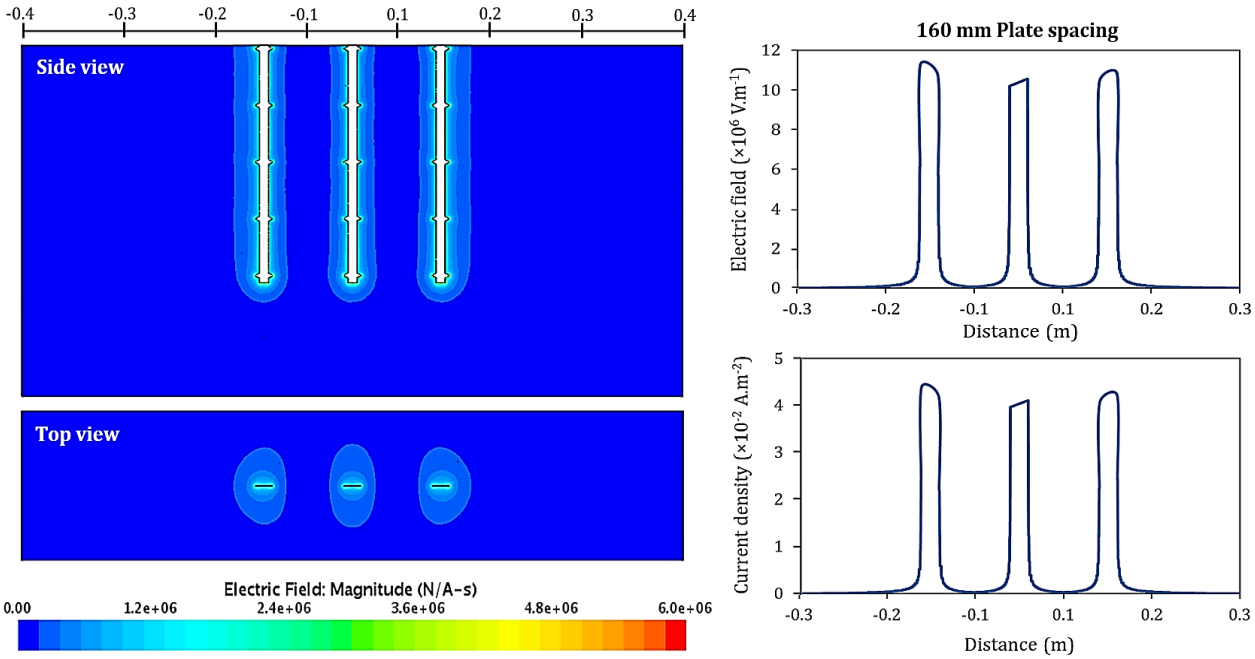

Figure 5-17. Electric field and current density across ESP section for three sawtooth in S-3 at 23 kV

The electric field and current density distributions across a single G-spike electrode with a 160 mm plate spacing and an applied voltage of 23 kV are presented in Figure 5-18.

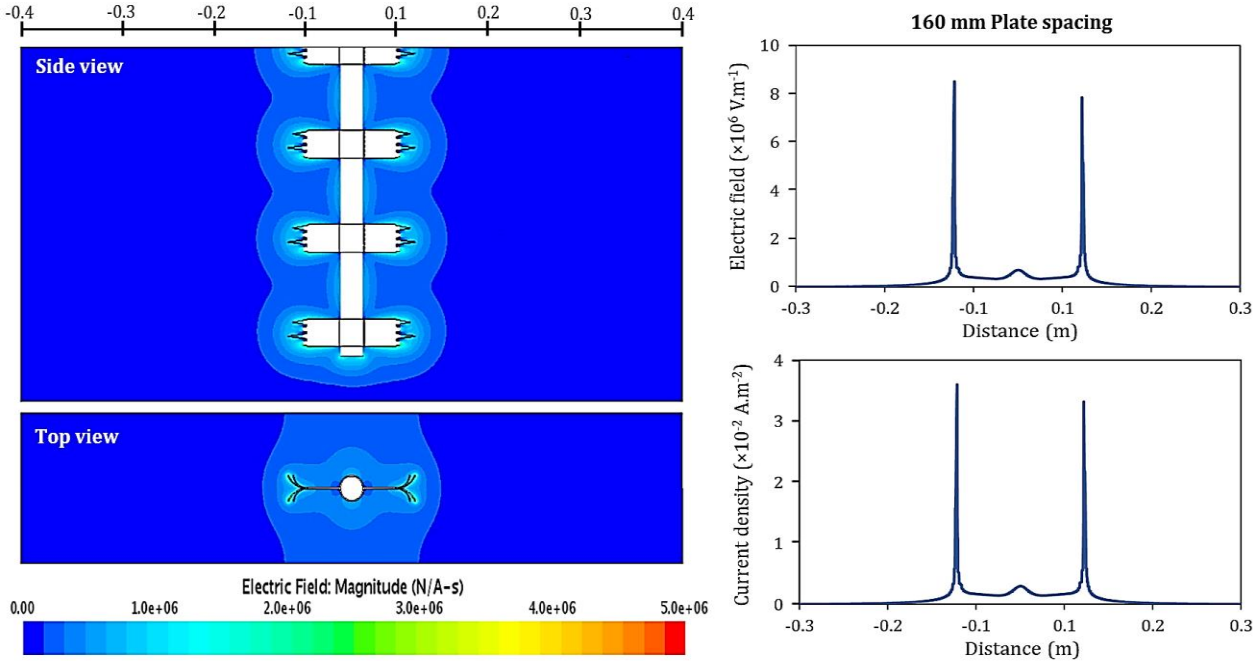

Figure 5-18. Electric field and current density across ESP section for one G-spike in G-1 at 23 kV

From the scalar scenes on the left-hand sides of Figures 5-17 and 5-18, it can be seen that the size of the electric field varies for different regions on the sawtooth and G-spike electrodes. This implies that irregular electrode geometries, like sawtooth and, especially G-spikes, have non-uniform electric field and current

density distributions. The electric field and current density on an electrode are inverse functions of the electrode length and surface area, respectively. As a result, sharp points with small surface areas will have higher electric field intensities and current densities than flat or smooth surfaces on the electrode body.

The three double-edged peaks in the current density distribution plot from Figure 5-17 represent the current densities at the spikes on both sides of the three sawtooth electrodes. The current density remains relatively constant across the electrode width between the spikes, suggesting that the concentration of current on the spikes relative to the electrode body is minimal for sawtooth electrodes.

The current density plot in Figure 5-18 exhibits two sharp peaks and a small central peak corresponding to the current densities on the spike tips and the shaft of a single G-spike electrode. Therefore, it is clear that, unlike the sawtooth electrodes, the G-spike electrode has a high concentration of current on the spike tips relative to the current on the rest of the electrode body. Arif *et al.* (2018) also noted highly concentrated fields around the G-spike tips with negligible field intensities and current densities across the electrode shaft [15]. The smaller current density peak observed for the spike on the right-hand side of the electrode indicates the complexity of the G-spike structure. The spikes of this geometry alternate in size and direction along the electrode length, and the field and current profiles conform to the G-spike shape.

Figure 5-19 and Figure 5-20 show the vector field patterns for the sawtooth and G-spike electrodes, respectively. As illustrated in the scalar scene from Figure 5-17 and the vector arrows in Figure 5-19, individual sawtooth electrodes generate elliptical-shaped electric fields. The field lines follow linear outward paths from the electrode faces and edges in all directions. Blanchard *et al.* (2002) identified similar elliptical field profiles for discharge electrodes with cylindrical spikes [100]. The fields on the sides closest to neighbouring sawtooth electrodes are flattened, and the field lines are bent due to shielding effects that are discussed later on in this chapter.

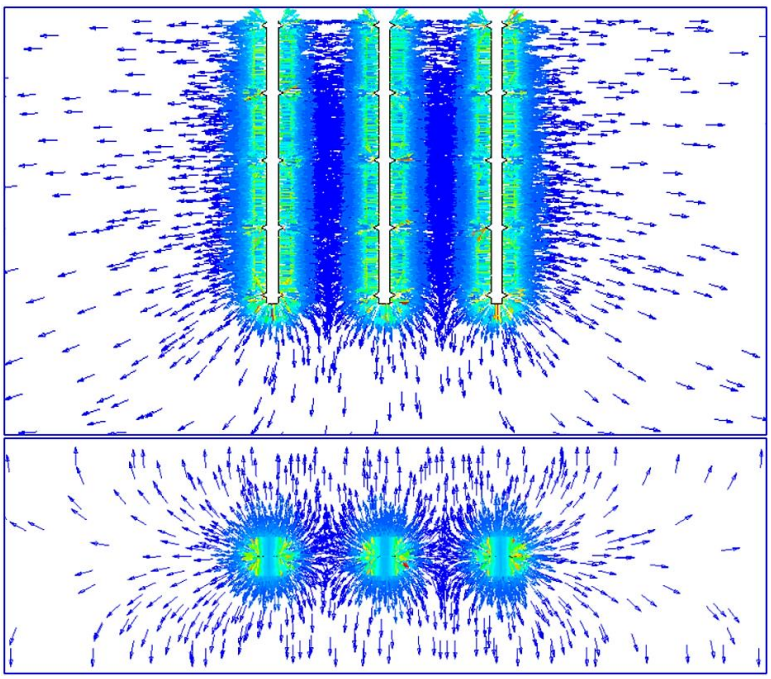

Figure 5-19. Electric vector field lines for sawtooth electrodes

According to the scalar scene from Figure 5-18 and the vectors in Figure 5-20, G-spike electrodes produce teardrop-shaped electric fields at the curved spike tips, and semi-circular fields around the cylindrical electrode body. The vector tracks in Figure 5-20 depict overlapping fin-like electric field lines at each spike group on the G-spike electrode. In addition, the central bar comprising the G-spike shaft generates radial field patterns. Some linear field lines also appear to emerge from the edges and faces of the flat vanes to which the spikes are attached. This leads to an overall irregular field shape, similar to the G-spike geometry.

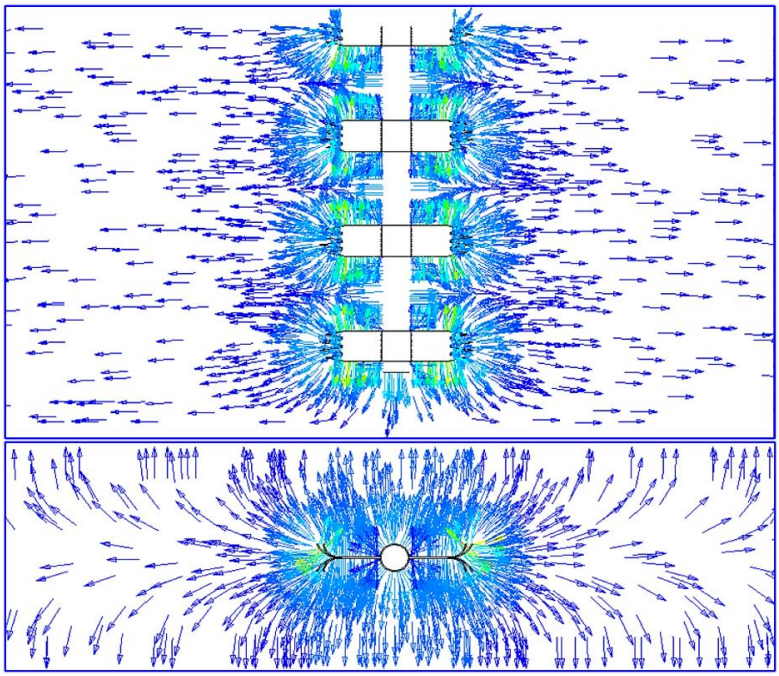

Figure 5-20. Electric vector field lines for G-spike electrode

The images and plots in Figure 5-21 portray the electric field and current density along two threaded rod electrodes with a 160 mm plate spacing for a supply voltage of 36 kV.

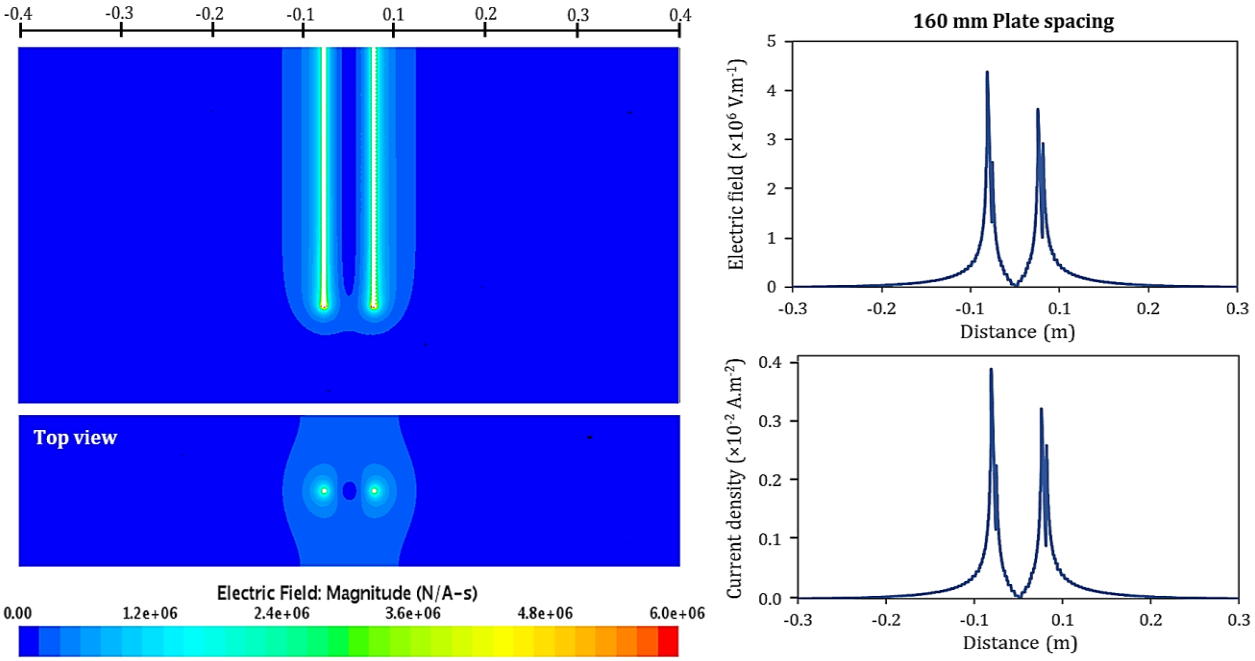

Figure 5-21. Electric field and current density across ESP section for two threaded rods in T-2 at 36 kV

The current density plot in Figure 5-21 shows a series of two peak pairs at the crossing points on the two ends of each threaded rod. A single peak pair indicates the current densities on the thread at opposite sides of an individual electrode. The peaks vary in height, corresponding to the variation in current densities at different positions on the thread. Current density is highest at the sharp edges of the thread, and decreases inward along the depth of the thread. The current density is at its lowest at the inner thread shaft.

Threaded rod electrodes have higher tip-to-body current density ratios than sawtooth electrodes. However, due to the small thread pitch (0.8 mm), the fields of subsequent thread tips combine to form a uniform electric field and current density distribution along the electrode body. This is also visible on the electric field and current density plots in Figure 5-21, which have very narrow distances between each set of peaks. Instead, the electric field accumulates at the bottom ends of the threaded rods, as illustrated by the red regions in the scalar scene of Figure 5-21.

From the vector scene in Figure 5-22, it is clear that threaded rods generate circular-shaped electric fields with radial tracks. Furthermore, the field vectors point upward or downward, depending on the angle of the thread. Subsequent field lines face in opposite directions to ultimately produce resultant field vectors in the direction normal to the central axes of the electrode bodies. With an increased distance from the origin at the electrodes, the field lines demonstrate a descending tendency toward the elevated field region at the bottom ends of the electrodes.

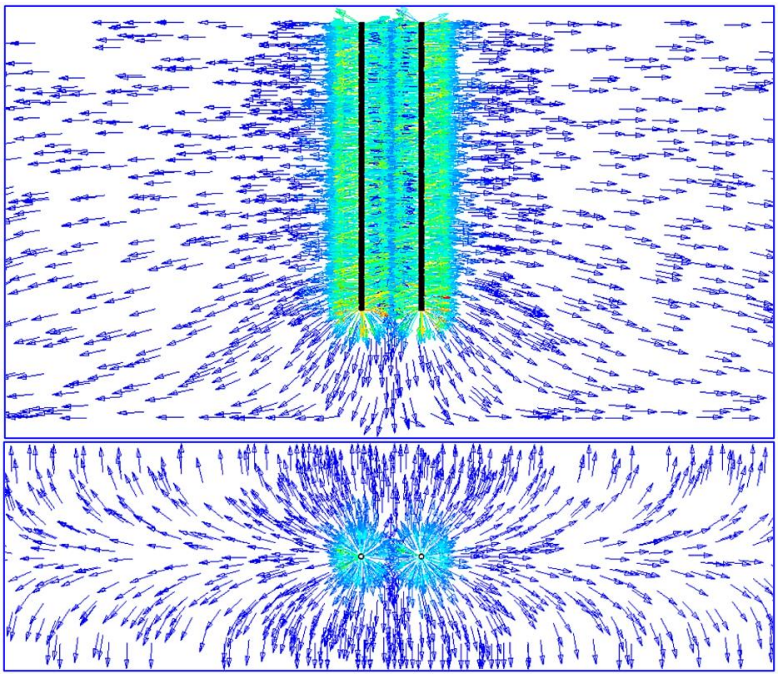

Figure 5-22. Electric vector field lines for threaded rod electrodes

5.3.4 EFFECT OF ELECTRODE GEOMETRY ON PARTICLE COLLECTION

During the ESP experiments, it was frequently observed that ash deposits on the collection plates formed patterns that resembled the electric fields produced by a particular electrode geometry. The shapes of the ash patterns on the collection plates for different discharge electrode geometries are shown in Figure 5-23.

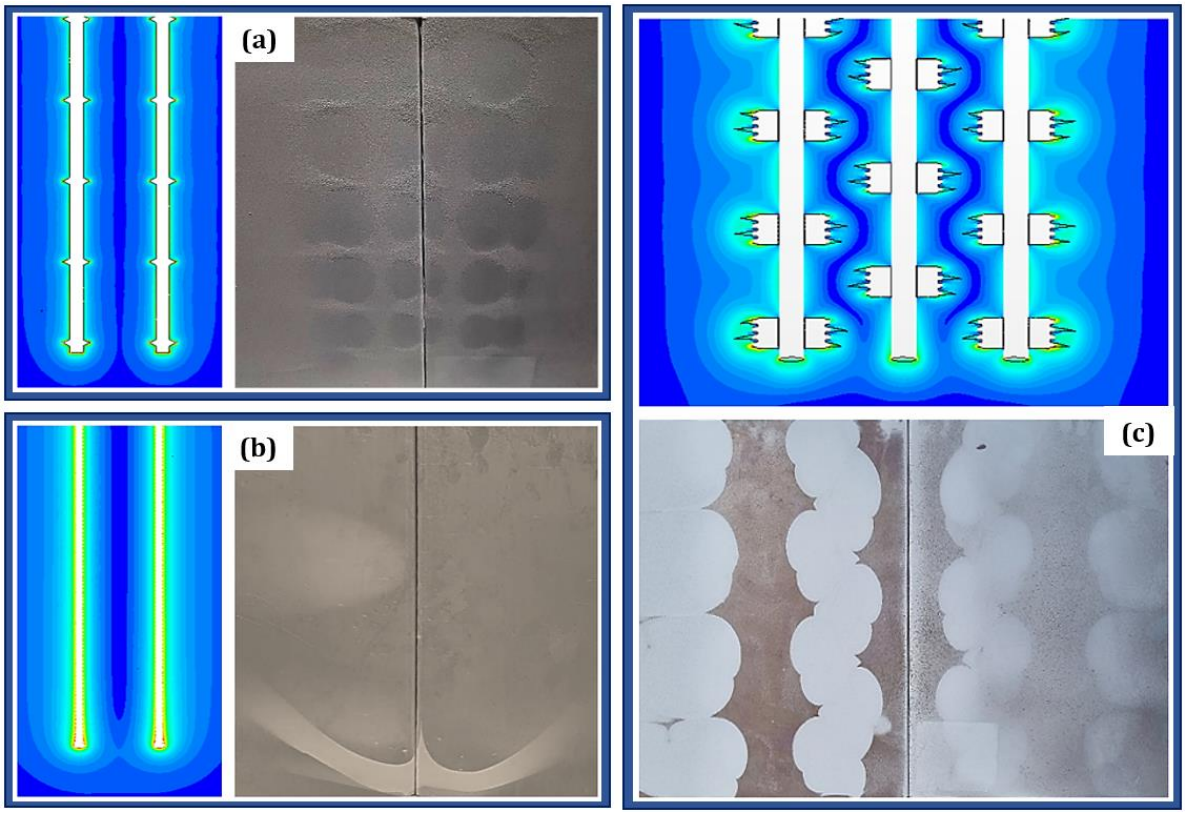

Figure 5-23. Fly ash patterns on collection plates for **(a)** sawtooth, **(b)** threaded rod, and **(c)** G-spike electrode geometries

This discovery led to the theory that the particle collection efficiency is predominantly related to the type of discharge electrode used and its current density profile in the ESP. During the experiments of Blanchard *et al.* (2002), they also noted specific dust patterns on the collection surfaces of a laboratory ESP. Blanchard *et al.* attributed this to a strong correspondence between dust deposition and current distribution, and identified regions of high and low field intensities based on the local dust layer thickness [100].

Further investigations on the effect of electrode geometry on the collection efficiency were conducted through a comparison of runs $S_{A\text{-}3}$ and $G_{A\text{-}3}$, and runs $T_{B\text{-}3}$ and $G_{B\text{-}3}$. The settings for the relevant runs are listed in Table 5-15.

Table 5-15. Electrode settings, ash samples, and voltages used for $S_{A\text{-}3}$, $T_{B\text{-}3}$, $G_{A\text{-}3}$, and $G_{B\text{-}3}$

Run	Electrode shape	Plate spacing (mm)	Electrode spacing (mm)	No. of electrodes	Type of ash (-75 µm)	Voltage range (kV)
$S_{A\text{-}3}$	Sawtooth	160	101	3	Ash A	23 – 37
$T_{B\text{-}3}$	Threaded rod	160	164	3	Ash B	34 – 40
$G_{A\text{-}3}$	G-Spike	160	112	3	Ash A	19 – 36
$G_{B\text{-}3}$	G-Spike	160	112	3	Ash B	20 – 36

The electric field and potential distributions for three G-spike and sawtooth electrodes in $S_{A\text{-}3}$ and $G_{A\text{-}3}$, respectively, with a constant plate spacing of 160 mm, are displayed in Figure 5-24.

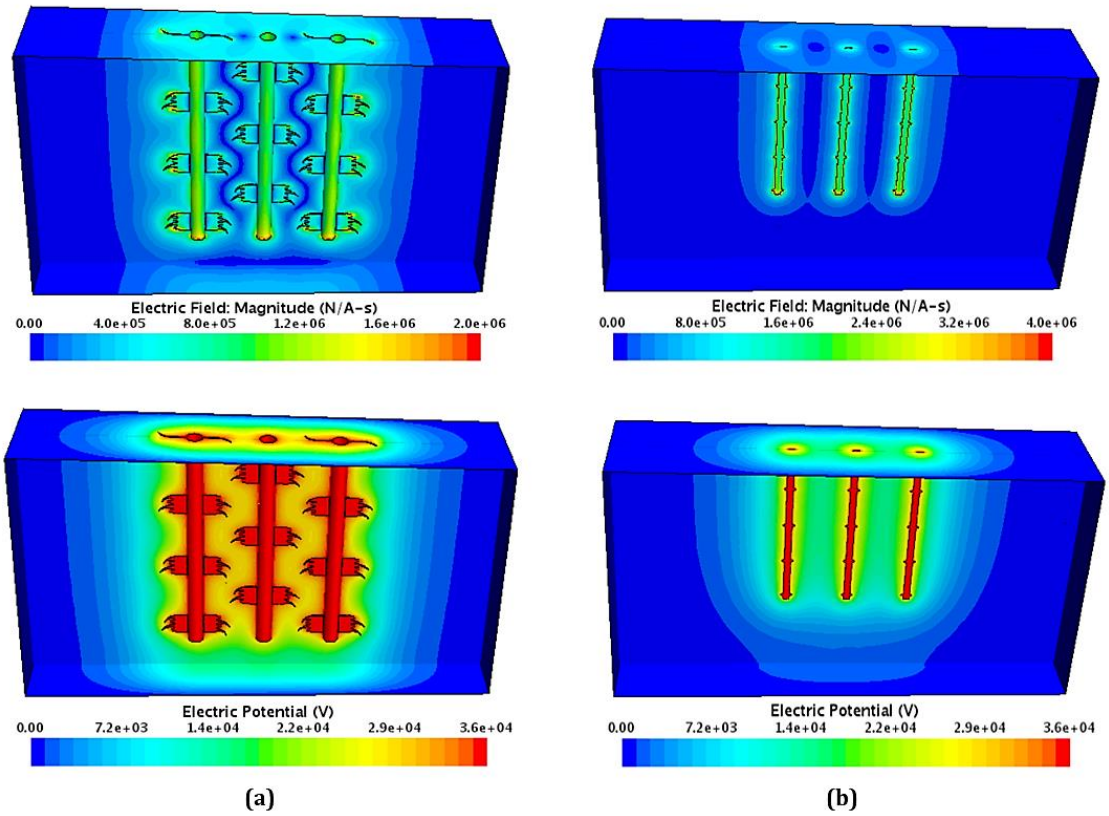

Figure 5-24. Electric field and potential magnitudes for **(a)** G-spike and **(b)** sawtooth electrodes

At first glance, the electric field on the sawtooth electrodes in Figure 5-24 (b) appears stronger than that of the G-spikes in Figure 5-24 (a) for the same applied voltage. However, this is misleading as the fields on G-spikes predominantly accumulate at the spike tips, whereas sawtooth electrodes present more evenly spread electric fields across the electrode faces.

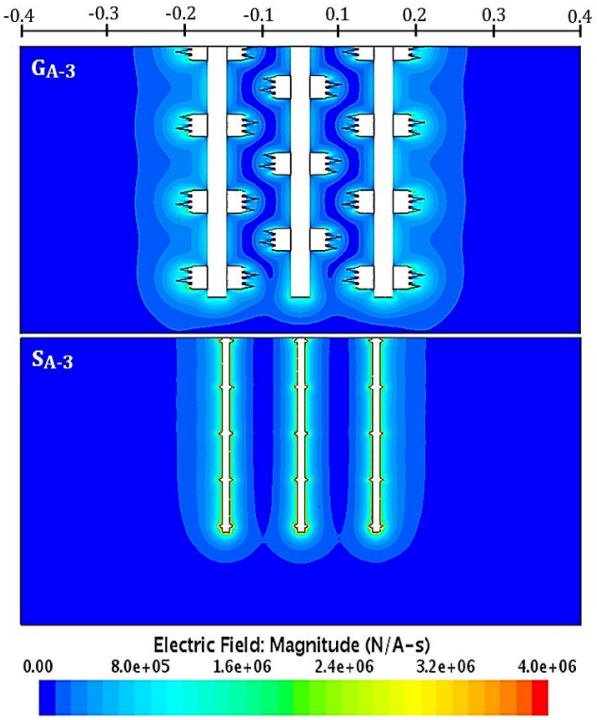

Run	S_{A-3}	G_{A-3}
Electrode shape	Sawtooth	G-spike
No. of electrodes	3	3
Electrode spacing (mm)	101	112
Plate spacing (mm)	160	160
Type of ash (-75 µm)	A	A
Applied voltage (kV)	36	36

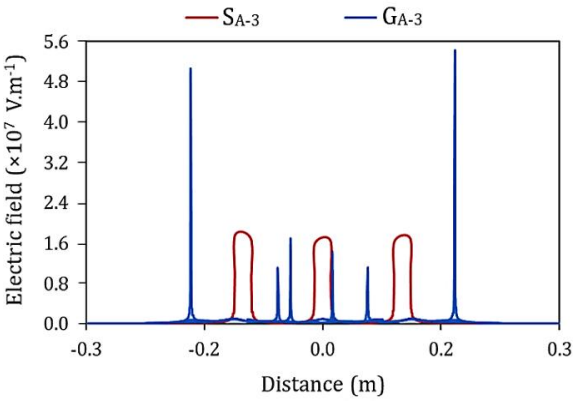

Figure 5-25. Comparison of electric fields at 36 kV for sawtooth electrodes in S_{A-3} and G-spikes in G_{A-3}

As discussed in Section 5.3.3, the G-spike geometry obtains higher electric field concentrations at the spike tips relative to the electrode body than the sawtooth geometry. Figure 5-25 shows that the G-spikes (G_{A-3}) produced a maximum electric field of 5.4×10^{7} V.m^{-1}, which is three times higher than the maximum field of 1.7×10^{7} V.m^{-1} for the sawtooth electrodes (S_{A-3}) at 36 kV. Also, the G-spike electrodes are larger in size and produce a resultant electric field of higher magnitude compared to the sawtooth electrodes.

The current density, space charge density, total current, and electric field generated by the sawtooth and G-spike electrodes at the corresponding voltage ranges of 23 – 37 kV for S_{A-3} and 19 – 36 kV for G_{A-3} are given in Figure 5-26 (a) – (d). The experimental data points are indicated with dots, while the modelled relationships are represented as lines. S_{A-3} and G_{A-3} involve three sawtooth and G-spike electrodes, respectively, with a constant plate spacing of 160 mm.

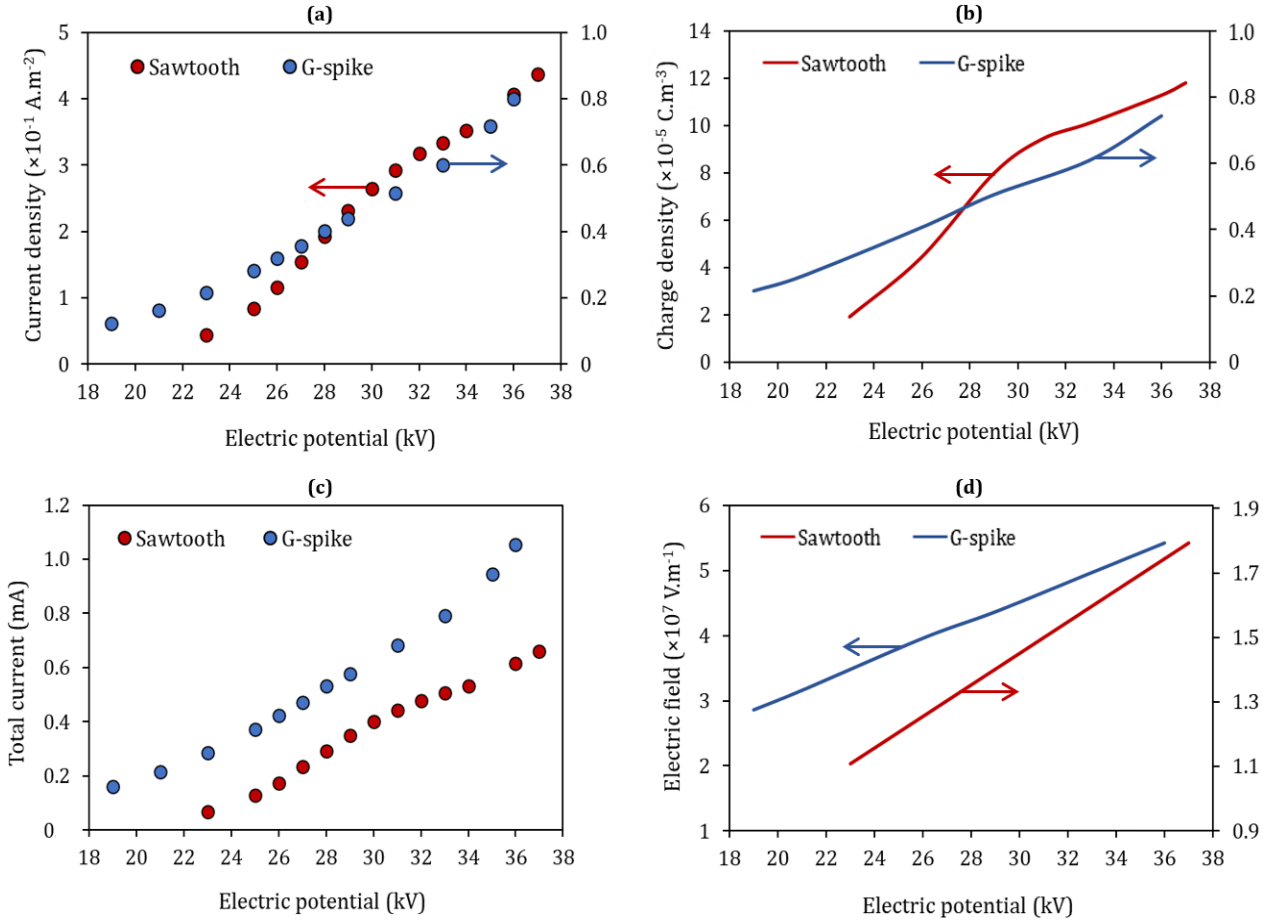

Figure 5-26. Modelled [—] and experimental [●] values for **(a)** current density, **(b)** space charge density, **(c)** total current, and **(d)** electric field of sawtooth and G-spike electrodes at various voltages

According to the data in Figure 5-26 (a), a single sawtooth spike generates a current density 3 – 5 times the magnitude of the current density on a single spike of the G-spike electrode for the same applied voltage. This is due to the difference in spike sizes for the two electrode geometries. G-spikes produce lower peak current densities since the average surface area for individual spikes on a G-spike electrode is four times larger than that of the sawtooth spikes.

Figure 5-26 (b) shows that the resulting space charge density at a specific voltage is significantly higher for the sawtooth electrodes than for the G-spikes. Therefore, the localised current discharge increases for a decrease in the surface area of an emitting point on the electrode. This statement agrees with Kasdi (2016), who reported higher current intensities for a discharge wire with a smaller radius (0.2 mm), compared to that of a discharge wire with a larger radius (0.4 mm) at equivalent voltages [63].

Nevertheless, Figure 5-26 (c) – (d) indicates that the G-spikes' total current and electric field strength are still 2 – 3 times higher than the related values for the sawtooth electrodes. One G-spike electrode comprises 24 or 32 spikes, giving a total of 88 spikes for the electrode assembly in G_{A-3}, whereas the three sawtooth electrodes in S_{A-3} constitute only 42 spikes. Consequently, G-spikes acquire larger overall currents and electric fields than sawtooth electrodes for equal voltages.

Further inspection of the plots in Figure 5-26 shows that the sawtooth electrodes have an onset voltage of 23 kV, which is higher than the 19 kV starting voltage for the G-spike electrodes. This suggests that a higher electric potential is required to produce a sufficient electric field for the initiation of corona discharge from sawtooth electrodes, compared to G-spikes. Correspondingly, G-spike electrodes exhibit a stronger electric field dependence on applied voltage than that observed for sawtooth electrodes in Figure 5-26 (d).

Figure 5-27 illustrates the collection efficiencies obtained at the 23 – 37 kV and 19 – 36 kV voltage spans for the sawtooth and G-spike electrodes in S_{A-3} and G_{A-3}, respectively.

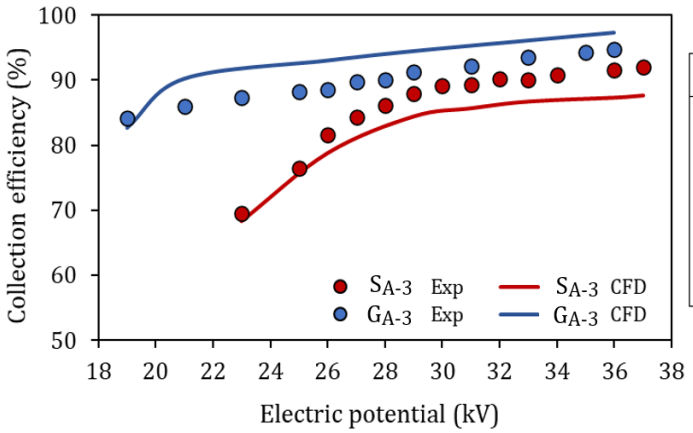

Run	S_{A-3}	G_{A-3}
Electrode shape	Sawtooth	G-spike
No. of electrodes	3	3
Electrode spacing (mm)	101	112
Plate spacing (mm)	160	160
Type of ash (-75 µm)	Ash A	Ash A

Figure 5-27. Modelled (CFD) and experimental (Exp) efficiencies for S_{A-3} and G_{A-3} at 19 – 37 kV

As opposed to the electrostatic model in Figure 5-26, which presents an exact fit to experimental measurements, some deviation is observed between the modelled and experimental particle collection efficiencies in Figure 5-27. The collection efficiencies determined by the computational model differ from the actual efficiencies recorded for S_{A-3} and G_{A-3} by 1 – 4%.

For G-spike electrodes, the model overpredicts the efficiency by more than 2% over the complete voltage range, with the exception of 19 kV at the start of the run. At this voltage, the computed efficiency is 1% lower than the measured value. For the sawtooth electrodes in S_{A-3}, the model accuracy decreases from 99% to 96% with an increase in voltage from 23 kV to 37 kV. In this case, the model underpredicts the experimental efficiencies for the entire range of voltages. This corresponds with the studies of Arif *et al.*

(2018) and Farnoosh *et al*. (2011), where the CFD models calculated collection efficiencies lower than experimental efficiencies for sawtooth electrodes [15], [101]. Therefore, the CFD particle dynamic model shows lower general compatibility with the sawtooth geometry than with the G-spike geometry and requires some amendment in this regard.

The G-spikes and settings used for G_{A-3} (listed in Figure 5-27) resulted in collection efficiencies as high as 95% at 36 kV. Similar settings for the sawtooth electrodes in S_{A-3} (Figure 5-27) provided a maximum efficiency of 92% at 36 – 37 kV. The sawtooth electrodes obtained an initial efficiency of 70%, demonstrating a sharp increase with each voltage increment up to 29 kV, followed by a more gradual increase between 30 – 37 kV. This corresponds with the change in current and space charge densities for the sawtooth electrodes, which follow analogous trends along the 23 – 37 kV voltage range. An overall rise in efficiency of 22% was achieved for a 14 kV potential change with the sawtooth electrodes. On the other hand, the G-spike electrodes showed high collection efficiencies across the entire voltage range, starting at 84% and increasing by approximately 10% between 19 – 36 kV.

The higher collection efficiencies recorded for the G-spike electrodes can be attributed to its higher current and electric field intensities relative to that of sawtooth electrodes. Furthermore, due to the large size of G-spike electrodes, with spikes bending toward the collection plates, the electrode-plate distance for this geometry is much shorter than for flat sawtooth electrodes with equal plate-plate spacing. A smaller distance between the G-spike tips and collection plates provides a steeper potential gradient to form a strong electric field for better particle collection. The narrow electrode-plate spacing for G-spikes also facilitates higher particle collection rates by minimising the distance that charged particles travel to reach the collection plates.

The threaded rod electrode geometry's effectiveness in electrostatic precipitation was also examined through a comparison of T_{B-3} and G_{B-3} with settings as listed in Table 5-15. The scalar scenes in Figure 5-28 depict the modelled 3-D electric field and potential distributions for three G-spike electrodes (a) and threaded rod electrodes (b) with a plate spacing of 160 mm.

Owing to the large size of the G-spike geometry and the small inter-electrode spacing, the electric potential fields of the G-spike electrodes in Figure 5-28 (a) span wider areas than that of the threaded rods in Figure 5-28 (b). However, in both cases, a constant electric potential of 34 kV is attained across the electrode surfaces. Correspondingly, the two electrode geometries in Figure 5-28 generate electric fields with the same order of magnitude but different distributions. In accordance with former observations, the electric field of the G-spikes accumulates at the spike tips. In contrast, the threaded rods present a more uniform field with a slight concentration at the bottom ends.

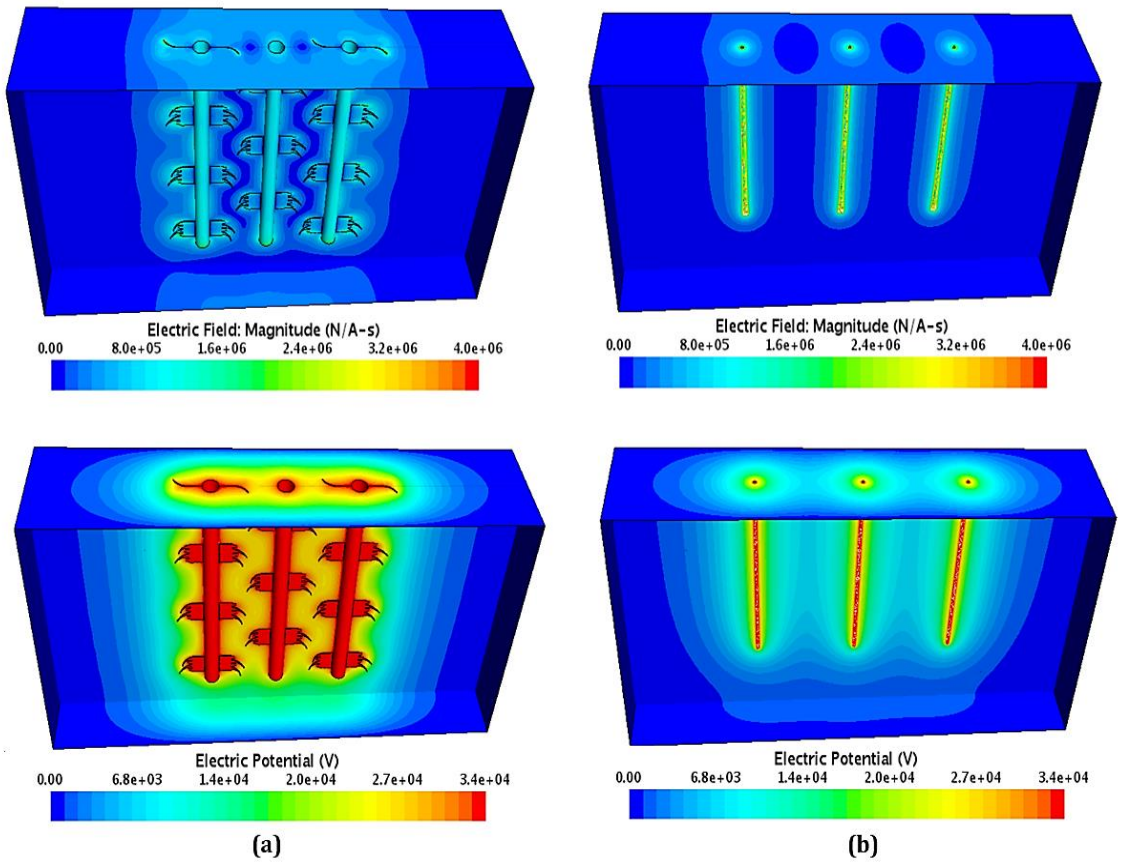

Figure 5-28. Electric field and potential magnitudes for **(a)** G-spike and **(b)** threaded rod electrodes

Figure 5-29 shows the electric field profiles across the three G-spike electrodes (G_{B-3}) and threaded rod electrodes (T_{B-3}) from Figure 5-28 at a supply voltage of 34 kV.

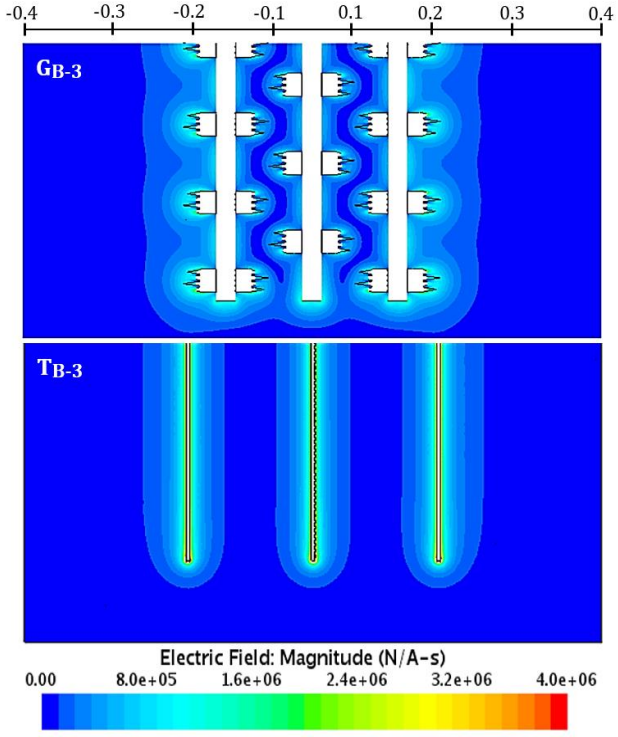

Run	T_{B-3}	G_{B-3}
Electrode shape	Threaded rod	G-Spike
No. of electrodes	3	3
Electrode spacing (mm)	164	112
Plate spacing (mm)	160	160
Type of ash (-75 µm)	B	B
Applied voltage (kV)	34	34

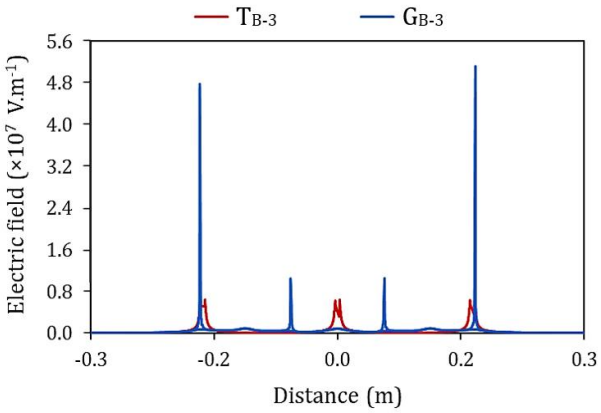

Figure 5-29. Comparison of electric fields at 34 kV for threaded rods in T_{B-3} and G-spikes in G_{B-3}

Figure 5-29 accentuates the contrast in electric field intensities at the G-spike tips and threaded rod bottom edges for the same applied voltage of 34 kV. While the three G-spike electrodes from G_{B-3} obtained a maximum electric field of 5×10^7 V.m^{-1}, the highest field intensity recorded for the threaded rod electrodes in T_{B-3} is 6×10^6 V.m^{-1}. This corresponds to a factor difference of 8 for the peak electric field of the G-spikes relative to that of the threaded rods at 34 kV.

An onset electric field intensity of 4.4×10^6 V.m^{-1} was calculated for the cylindrical threaded rod electrodes, using Peek's formula in Eq. 4.18 and $m = 1$. The Peek's law estimate is close to the average field of 4.2×10^6 V.m^{-1} measured on the inside thread diameters of the threaded rod electrodes.

The electric fields for the associated current-voltage relationships of the threaded rod and G-spike electrodes were modelled and evaluated at the respective voltage ranges for T_{B-3} and G_{B-3}. The results are illustrated in Figure 5-30, where the experimental data are indicated as dots, and the modelled trends are portrayed with lines.

In Figure 5-30, it can be seen that the electric fields of both the threaded rod and G-spike electrodes exhibit strictly linear relations to the applied voltage. In contrast, the current and charge density trends indicate exponential increases for each voltage increment.

The relative slopes of the plots in Figure 5-30 suggest that the electrostatic properties of threaded rods demonstrate stronger dependences on the applied voltage compared to that of G-spike electrodes. This could be attributed to the difference in sizes of the two electrode geometries, and the variation in electrode spacings between the two runs. The bigger G-spike electrodes with a smaller inter-electrode distance of 112 mm are expected to experience a higher degree of shielding than the small threaded rod electrodes with a 164 mm electrode distance. This is also evident from the overlapped electric fields for the G-spikes, as opposed to the separated fields observed for the threaded rods in Figure 5-29. Nonetheless, the G-spike electrodes produce larger field intensities and current densities in the ESP than the threaded rod electrodes for all the corresponding voltages. This is discussed in more detail later on in this section.

Furthermore, the plots in Figure 5-30 demonstrate a small operating voltage range of Δ6 kV (34 – 40 kV) for the threaded rods, which is 10 kV less than the Δ16 kV range (20 – 36 kV) for the G-spikes. This is due to the uniformly distributed field and lack of charge concentration on the threaded rods, making it difficult for these electrodes to produce local high current densities like the G-spike electrodes. As a result, ESP configurations with threaded rods experience faster rates of charge build-up in the air surrounding the electrodes, leading to quicker sparkovers. This significantly decreases the overall efficiency of the threaded rod electrode geometry.

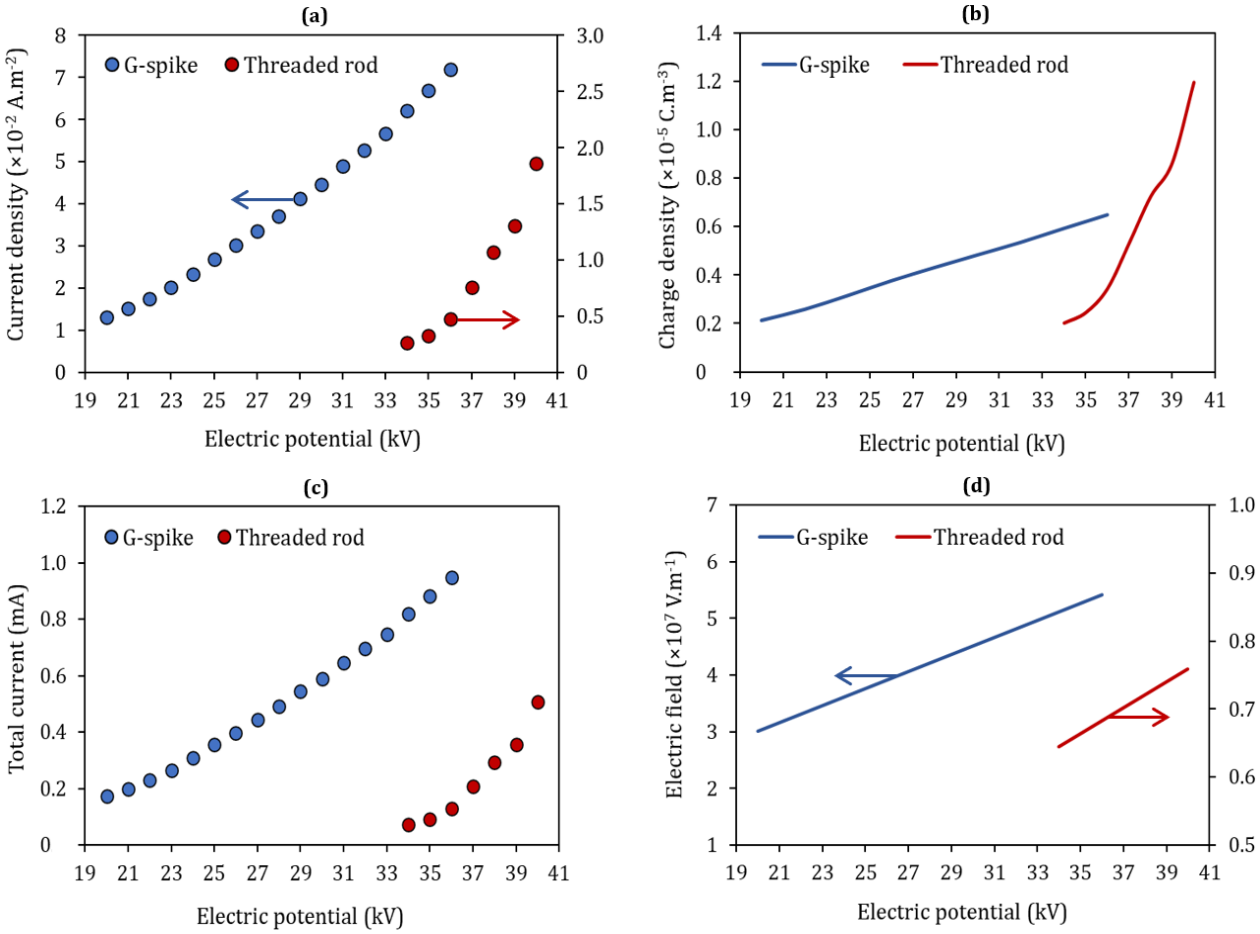

Figure 5-30. Modelled [—] and experimental [●] values for **(a)** current density, **(b)** space charge density, **(c)** total current, and **(d)** electric field of sawtooth and G-spike electrodes at various voltages

The collection efficiencies obtained during the experiments and computed by the CFD model for different voltages in T_{B-3} and G_{B-3} are given in Figure 5-31. The model exhibits a poor predictive ability in terms of the collection efficiency across the 34 – 40 kV voltage range for the threaded rod electrodes in T_{B-3}. The modelled values deviate from the actual efficiencies in T_{B-3} by up to 9%. On the other hand, a reasonably good correlation was achieved between the efficiencies obtained from the CFD model and experimental measurements at 20 – 36 kV for the G-spikes in G_{B-3}. The difference between the modelled and experimental values ranged from 0.05% to 2.7%, with the highest deviations corresponding to the minimum and maximum voltages for G_{B-3}.

This could be indicative of a large experimental error, as well as the neglection of some ESP parameters that could have a larger impact on collection efficiency at the lower field intensities of T_{B-3}. Weaker electric fields result in increased effects of flow turbulence on the particles, whereas for high field intensities, particles are less subjected to air flow profiles and follow more definite paths in the ESP. As a result, particle trajectories should be more difficult to predict for ESP configurations, such as T_{B-3}, with lower field and discharge current intensities.

In the research conducted by Yang *et al*. (2019) [86], it was discovered that the turbulence effects on particle flow became more prominent with a decrease in current density following weakened field intensities. This caused the particles to lose some of their charge to the carrier fluid. Therefore, the actual particle charges

were lower than expected for a specific current density, leading to smaller particle migration velocities toward the collection plates. Consequently, the collection efficiencies of the particles were lower than that predicted by the numerical model in [86], which validates the reasoning behind the model error for T_{B-3} in the present study.

Run	Electrode shape	No. of electrodes	Electrode spacing (mm)	Plate spacing (mm)	Type of ash (-75 µm)
T_{B-3}	Threaded rod	3	164	160	Ash B
G_{B-3}	G-Spike	3	112	160	Ash B

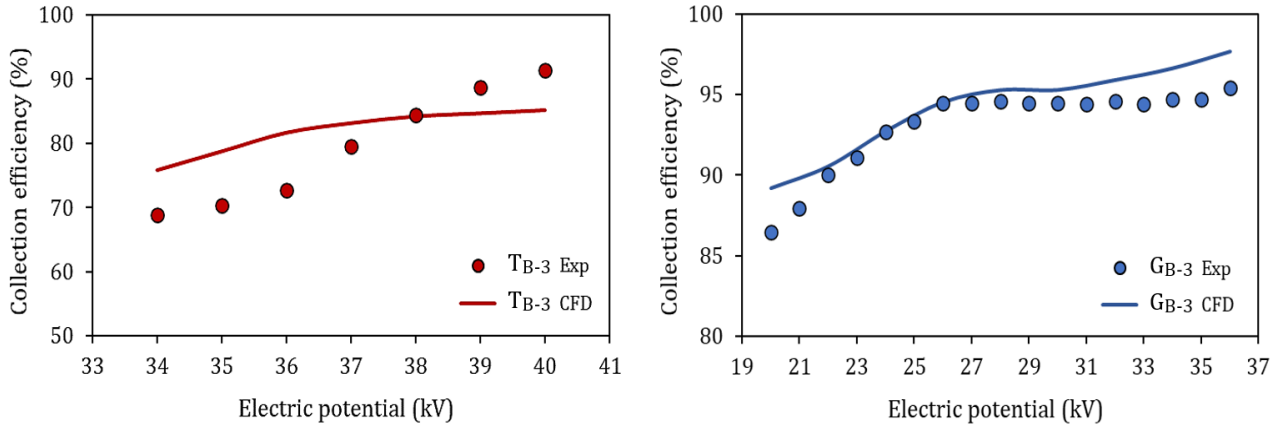

Figure 5-31. Modelled (CFD) and experimental (Exp) efficiencies for T_{B-3} and G_{B-3} at 20 – 40 kV

According to the modelled and experimental data, the G-spike electrodes in G_{B-3} obtained up to 26% higher efficiencies than the threaded rod electrodes in T_{B-3} for the same applied voltages. This corresponds to the significant difference in electrostatic properties for the two electrode geometries. The G-spikes have current densities of approximately two orders of magnitude larger than the threaded rods at voltages 34 – 36 kV. The G-spikes are, therefore, more effective in producing larger electric currents and stronger fields at lower onset voltages (19 kV), compared to the threaded rod electrodes, with an onset voltage of 34 kV.

Furthermore, average current densities of 7.2×10^{-2} A.m^{-2} and 1.8×10^{-2} A.m^{-2} were recorded for the G-spike and threaded rod electrodes at the corresponding sparkover voltages of 36 kV and 40 kV, respectively. This shows that, despite the lower arcing voltage reported for G_{B-3}, the G-spike electrodes' maximum current density still exceeds that of the threaded rods by a factor of four.

Based on the observations from runs S_{A-3} and G_{A-3}, and runs T_{B-3} and G_{B-3}, it is clear that the current and electric fields are the strongest for the G-spike electrodes, followed by the sawtooth electrodes and, lastly, the threaded rods. The G-spikes and sawtooth electrodes exhibit electric fields of similar magnitudes, whereas the threaded rods show considerably weaker fields than the other two geometries. Analogous trends are visible for the collection efficiencies of the different electrode geometries, suggesting a strong relationship between electric field strength and particle collection rate. Collection efficiencies are higher than 90% for the G-spike and sawtooth electrodes and lower than 73% for the threaded rods at 33 – 36 kV.

These results are consistent with that of previous studies. Brocilo *et al.* (2003, 2008) concluded higher particle collection efficiencies for sawtooth electrodes than simple wire and threaded rod electrodes with

the same applied voltages and electrode settings [53], [69]. Arif *et al*. (2018) later investigated the performances of G-spike and wire electrodes and found that the G-spikes produced significantly higher current densities and particle collection efficiencies than the wire electrodes [15].

5.3.5 EFFECT OF NUMBER OF ELECTRODES ON PARTICLE COLLECTION

According to the ANOVA results for the experimental variables in this study, the number of discharge electrodes used in the ESP configuration showed a significant contribution to the change in particle collection efficiency. To further investigate this matter, the electrostatic properties and collection efficiencies for one G-spike electrode were compared to that of three G-spike electrodes at a fixed collection plate spacing of 160 mm. A constant ~ 4 mg.Nm^{-3} feed of fly ash B was used for this evaluation.

The measured current-voltage relationships in Figure 5-32 (b) were used as input to the CFD model, and therefore the electric field intensities for a single G-spike and three G-spike electrodes could be successfully computed. The modelled field results are given in Figure 5-32 (a). For the plots in Figure 5-32, "Exp" indicates experimental data points, and "CFD" indicates model trends.

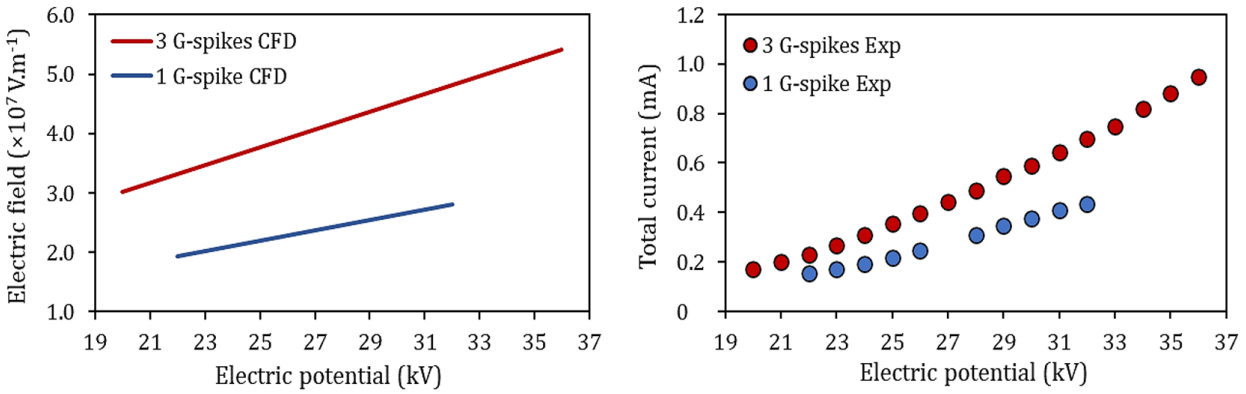

Figure 5-32. Modelled (CFD) and experimental (Exp) plots for the electric field **(a)** and total current **(b)** of 1 G-spike and 3 G-spike electrodes at different voltages

For three G-spike electrodes, the current starts to emerge from the spike tips at a corresponding onset voltage of 20 kV, and increases up to 36 kV, at which the ESP system exhibits an electric sparkover. The single G-spike electrode demonstrates a smaller current with a more gradual increase from the start of corona discharge at 22 kV to the sparkover point at 32 kV. While the single G-spike shows a linear increase in current with increasing voltage, an exponential current-voltage relationship is illustrated for the three G-spike electrodes in Figure 5-32 (b).

Based on this observation, a further increase in the number of electrodes should enhance the exponential behaviour of the current-voltage curves, due to the increased dependence of current output on the applied voltage. This was confirmed in the research of Kasdi (2016), which showed increasingly steeper current-voltage curves for an increased number of discharge wires from 1 to 5 across the same voltage range [63].

Furthermore, the combined field of the three G-spike electrodes is almost two times stronger than the electric field on the single G-spike electrode. This is smaller than the factor 3 increase in field intensity

expected for adding two extra G-spikes to the assembly, which could be indicative of shielding effects for this particular configuration. Shielding is discussed in more detail in the subsequent sections. The resulting current increased by a factor of 1.5 at 22 kV, and by a factor of 1.6 at 32 kV for an increase in the number of G-spike electrodes from 1 to 3. Therefore, the variation in current between 1 and 3 electrodes becomes more prominent at higher voltages, corresponding to the stronger current-voltage relationship for the larger electrode count.

Although changes in current and field intensities for different electrode quantities are seemingly trivial compared to other ESP variables, two additional G-spikes expanded the operating voltage range by Δ6 kV. This can drastically improve the ESP operation if proper electrode and plate spacings are used. Furthermore, the current fields of three G-spike electrodes are more stable [15] since larger voltages can be applied over the electrode assembly before dielectric breakdown occurs than in the case of one G-spike electrode.

Figure 5-33 illustrates the electric field profiles and intensities at 28 kV, and the corresponding particle tracks and collection efficiency plots for the three G-spikes and the single G-spike electrode. The field for the three G-spikes develops dead regions across the electrode in the middle, resulting in weakened fields on the central electrode spikes, with intensities almost 5 times lower than the outside field intensities. Even then, the maximum electric field intensity on the outer sides of the three G-spike electrodes is 1.7 times higher than that on the single G-spike electrode.

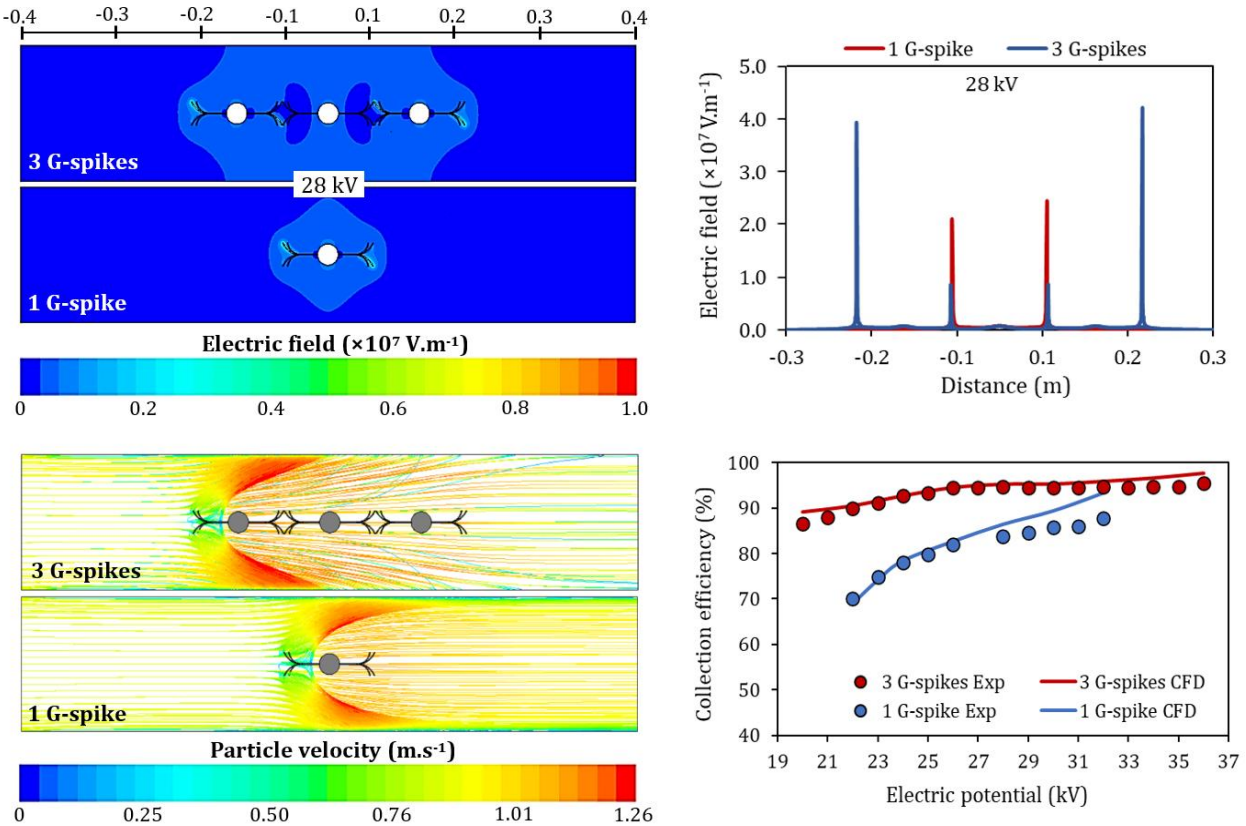

Figure 5-33. Electric field distributions, particle track velocities, and collection efficiencies of 1 G-spike and 3 G-spike electrodes

The field profile for the three electrodes has a high-intensity region with a large cross-sectional area that far exceeds the 160 mm distance between the collection plates. On the other hand, a single G-spike produces a smaller high-intensity field region with a width of approximately 145 mm (~ 15 mm shorter than the 160 plate-to-plate distance). Since the three G-spikes form high field line densities at the collection plates, charged particles travel almost exclusively under the influence of the electrostatic field for this electrode assembly.

Therefore, more particles are carried up to the collection plate surfaces, resulting in higher particle collection efficiencies for three G-spike electrodes. In the case of one G-spike electrode, particle trajectories are governed by the electric field and thermal diffusion forces. As a consequence, the particle paths are more susceptible to changes in the air flow patterns [86], making particle collection more difficult with a single G-spike electrode.

These observations were made from the relative particle track velocities of the two cases in Figure 5-33. For three G-spikes, the particles show high migration velocities from the deflection point at the first electrode. These velocities are maintained up to the collection point at the particle-plate interface. The particle tracks for the single G-spike show high initial migration velocities that gradually decrease toward the plate surface. As a result, more particles glide along the plates and escape with the air at the ESP outlet for one electrode, while the majority of the particles exit the air stream via the collection plates when three electrodes are used.

Furthermore, the particle tracks for three G-spike electrodes show linear-shaped paths toward the collection plates, while the tracks for the single G-spike electrode have curved deflection paths. This indicates stronger tendencies for charged particles to the collection plate surfaces with three electrodes, due to stronger electrostatic attraction forces acting on the particles relative to that of one electrode. Also observed in the particle tracks for both cases are higher particle concentrations at the bottom of the ESP compared to the top of the ESP. This indicates that a fraction of the particles settles out of the air stream under the influence of gravity. Settling appears to show a larger contribution to the ESP process for one G-spike than for three since the stronger electrostatic field of the latter counteracts the effect of gravity to a greater extent.

The plots give the collection efficiencies obtained with one and three discharge electrodes in the bottom right corner of Figure 5-33. The modelled (CFD) plot for the single G-spike electrode shows a good agreement with experimentally measured (Exp) collection efficiencies, with a small average deviation of 0.75% up to 26 kV. The model error increases to 2.6 – 5.6% across the rest of the voltage range (28 – 32 kV). Therefore, the CFD model estimates the actual collection efficiencies at the lower voltage range and overestimates the efficiencies at higher voltages.

This could be due to a charge build-up in the ash layer on the collection plates, resulting in weakened electrostatic attraction forces that were not accounted for in the CFD model. Another reason may be that the average particle diameter decreases with time. Larger particles have higher migration and settling velocities and are, therefore, collected first, thereby leaving behind smaller particles that are more difficult to collect (see Section 2.5). This is also not taken into account in the CFD model.

When considering the collection efficiencies of the three G-spike electrodes, the model maintains a high level of accuracy across the entire voltage range. The deviations between modelled and experimental data vary from 0.05% at the intermediate voltage range to 2.7% at the lower and upper voltage limits. This shows that the electric field for the three discharge electrodes is strong enough to outweigh the negative impacts of the aforementioned factors on the particle collection efficiency.

For one G-spike electrode, the efficiency increases from 70% to 88% for a voltage increase from 22 kV to 32 kV. On the other hand, the three G-spikes already show a high efficiency (> 86%) from the start at 20 kV, with a smaller increase to 95% at the 36 kV sparkover point. This relates to the stronger electric field and current density for the three G-spikes, resulting in faster particle charging and migration rates at lower voltages compared to a single G-spike electrode. Furthermore, the three electrodes generated double the current obtained with one electrode (see Figure 5-32), which raised the maximum collection efficiency from 87.7% to 95.4%. Therefore, the collection efficiency increased by almost 8% for the addition of two more G-spike electrodes to the ESP assembly.

5.3.6 EFFECT OF PLATE SPACING ON PARTICLE COLLECTION

The collection efficiencies for two different plate spacings in runs S_{160} and S_{280} were compared to analyse the impact of this variable on the ESP performance. The remaining electrode settings and fly ash samples were identical for S_{160} and S_{280}, as given in Table 5-16.

Table 5-16. Electrode settings, ash samples, and voltages used for S_{160} and S_{280}

Run	Electrode shape	Plate spacing (mm)	Electrode spacing (mm)	No. of electrodes	Type of ash (-75 µm)	Voltage range (kV)
S_{160}	Sawtooth	160	101	3	Ash A	23 – 37
S_{280}	Sawtooth	280	101	3	Ash A	33 – 49

The electrostatic properties of the 160 mm and 280 mm plate spacings corresponding to S_{160} and S_{280} are shown in Figure 5-34 (a) – (d). Modelled data trends are once again displayed as lines, whereas experimental data are indicated with dots.

As seen in Figure 5-34, the current and electric field intensities are inversely proportional to the distance between the collection plates. The average current density obtained with the same electrode assembly increased by a factor of 4 – 5 between 33 – 37 kV for a decrease in plate spacing from 280 mm to 160 mm. The associated space charge densities determined for the 160 mm plate spacing are 4 – 6 times larger than for the 280 mm plate spacing across the 33 – 37 kV voltage range.

Therefore, current discharge started at a low voltage of 23 kV for the smaller 160 mm plate spacing and at a significantly higher voltage of 33 kV for the larger 280 mm plate spacing. Correspondingly, the 160 mm plate spacing demonstrates a low sparkover limit of 37 kV, yet with current two times higher than that produced at the 49 kV sparkover voltage for the 280 mm plate spacing. The significant difference between the onset and sparkover voltages for the 160 mm and 280 mm plate-to-plate distances indicates the sizeable effect of this variable on the electrostatic properties and performance of the ESP.

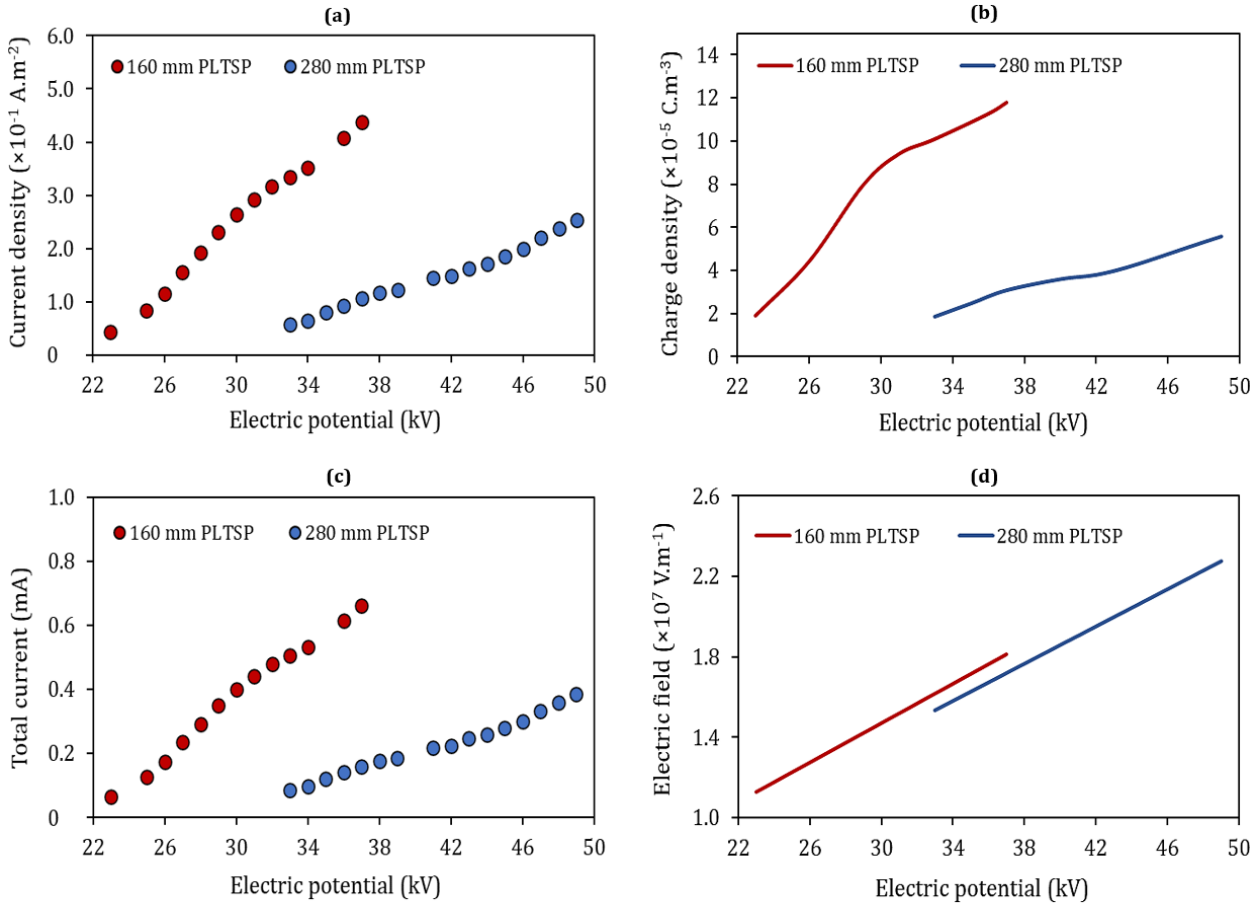

Figure 5-34. Modelled [—] and experimental [●] values for **(a)** current density, **(b)** space charge density, **(c)** total current, and **(d)** electric field of sawtooth electrodes at 160 and 280 mm plate spacings (PLTSP)

The current and charge density plots in Figure 5-34 (a) – (c) for the 160 mm plate spacing show stronger relations with applied voltage compared to the 280 mm plate spacing plots. This corresponds with these parameters' second and third-order dependences on the electrode-plate distance. On the other hand, the electric field plots in Figure 5-34 (d) have equal slopes, suggesting an equivalent linear increase in field strength with applied voltage for both plate spacings. As a result, the electric field magnitude of the 160 mm plate spacing exceeds that of the 280 mm plate spacing by a constant factor of 1.05 at all voltages.

The particle tracks at 33 kV and collection efficiencies across the relevant voltage spans for the sawtooth electrodes with 160 mm and 280 mm plate spacings are illustrated in Figure 5-35.

The model plots in Figure 5-35 follow similar trends to experimental collection efficiency data for S_{160} and S_{280}. For the 33 kV onset voltage of S_{280}, the modelled and experimental values differ by only 0.5%. However, at 35 – 49 kV, the model accuracy drastically drops, and predicted values deviate by approximately 4% from the measured efficiencies of the three sawtooth electrodes with a plate spacing of 280 mm. For S_{160}, the model accuracy gradually decreases from 99% to 96% along the 23 – 37 kV voltage range of the 160 mm plate spacing.

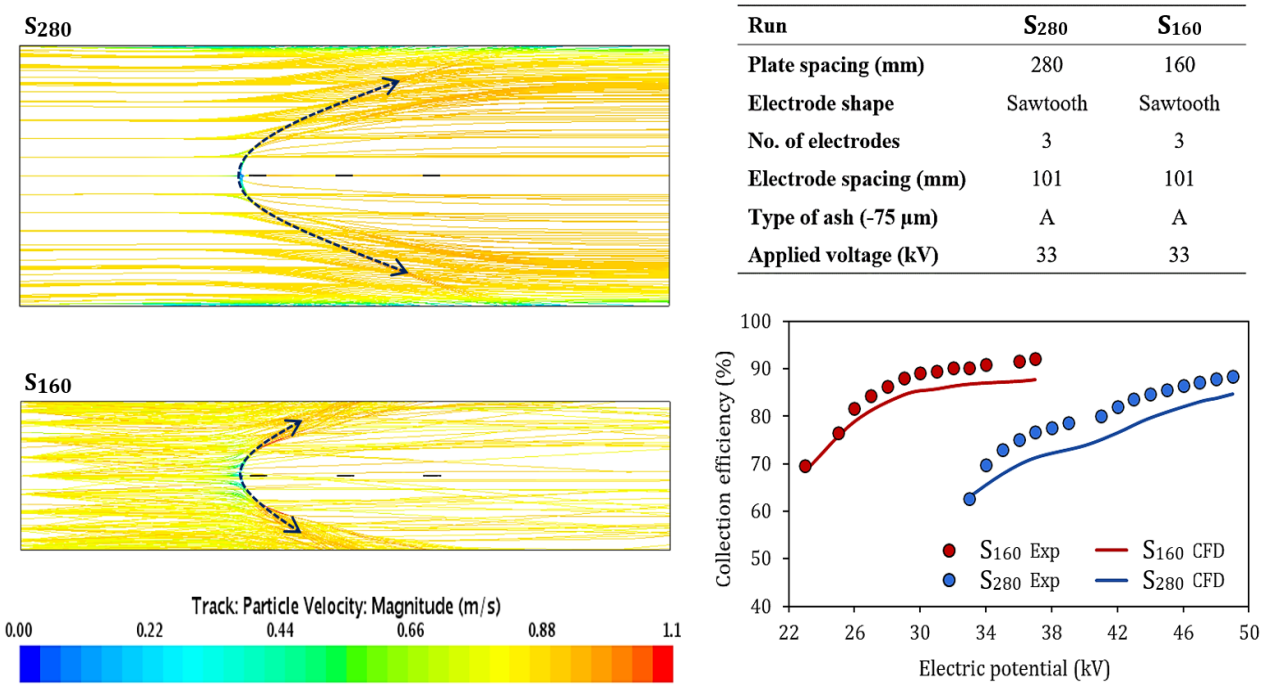

Run	S_{280}	S_{160}
Plate spacing (mm)	280	160
Electrode shape	Sawtooth	Sawtooth
No. of electrodes	3	3
Electrode spacing (mm)	101	101
Type of ash (-75 µm)	A	A
Applied voltage (kV)	33	33

Figure 5-35. Modelled (CFD) and experimental (Exp) collection efficiencies and modelled particle tracks for S_{160} with 160 mm plate spacing and S_{280} with 280 mm plate spacing

Average collection efficiencies of 80% and 86% were determined for the 280 mm and 160 mm plate spacings in S_{280} and S_{160}, respectively. Furthermore, according to the results in Figure 5-35, the change in plate spacing from 280 mm to 160 mm increased the collection efficiency from 63 – 77% to 90 – 92% at voltages 33 – 37 kV. This corresponds to a 15 – 28% rise in collection efficiency for a 120 mm decrease in plate-plate distance. Therefore, the smaller 160 mm plate spacing yielded considerably higher efficiencies than the 280 mm plate spacing for the same electrode settings and applied voltages.

The significant impact of the plate-plate distance on collection efficiency was also observed during the ANOVA analysis on the RSM model from Section 5.2. The higher efficiency for the narrow plate spacing of 160 mm is related to the larger current density and electric field obtained with this setting, compared to the 280 mm plate spacing (see Figure 5-34). The stronger electric field for the 160 mm plate spacing corresponds to the larger voltage gradient between the discharge electrodes and collection plates, resulting from the decreased electrode-plate distance.

Charged particles in the ESP travel to the plates at rates proportional to the strength of the electrostatic attraction forces that develop due to the electric field. Therefore, the particles in S_{160} with the higher field intensity show higher migration velocities to the plates. In addition, larger current densities between the plates promote higher particle charging rates that, in effect, improve particle collection efficiencies. This is evident from the particle tracks in Figure 5-35, indicating wider deflection paths for the 160 mm plate spacing (S_{160}) with higher current and electric field intensities relative to the 280 mm plate spacing (S_{280}).

The shorter migration distances for charged particles between the discharge electrodes and collection plates in S_{160} also contributed to the increased collection efficiencies of the 160 mm plate spacing. This is demonstrated by the relative lengths of the dotted lines in Figure 5-35. The particles have much longer

distances to travel before reaching the collection plates for the 280 mm plate spacing (S_{280}) compared to the 160 mm plate spacing (S_{160}). Consequently, the ESP configuration with the larger 280 mm plate-plate distance has slower particle collection rates and lower collection efficiencies than the 160 mm alternative.

Some turbulence effects could also have been involved in the collection efficiency outcomes of S_{160} and S_{280}. As mentioned earlier in Section 5.3.2, the increase in turbulence intensity observed for a smaller plate spacing of 160 mm enhances the degree of particle dispersion through the air between the plates. This maximises the probability of particle-electrode interactions for higher particle charging and collection rates.

5.3.7 INVESTIGATION OF SHIELDING EFFECTS

Shielding effects were compared for different supply voltages, electrode spacings, plate spacings, and electrode geometries in the ESP.

Shielding as a function of applied voltage

The shielding degree was examined at different voltage supplies for an assembly of three G-spike electrodes with a 112 mm electrode-to-electrode distance and a constant plate spacing of 160 mm. The current density values at the G-spike tips were compared for voltages of 20 kV, 24 kV, 30 kV, 34 kV, and 36 kV, and the results are shown in Figure 5-36.

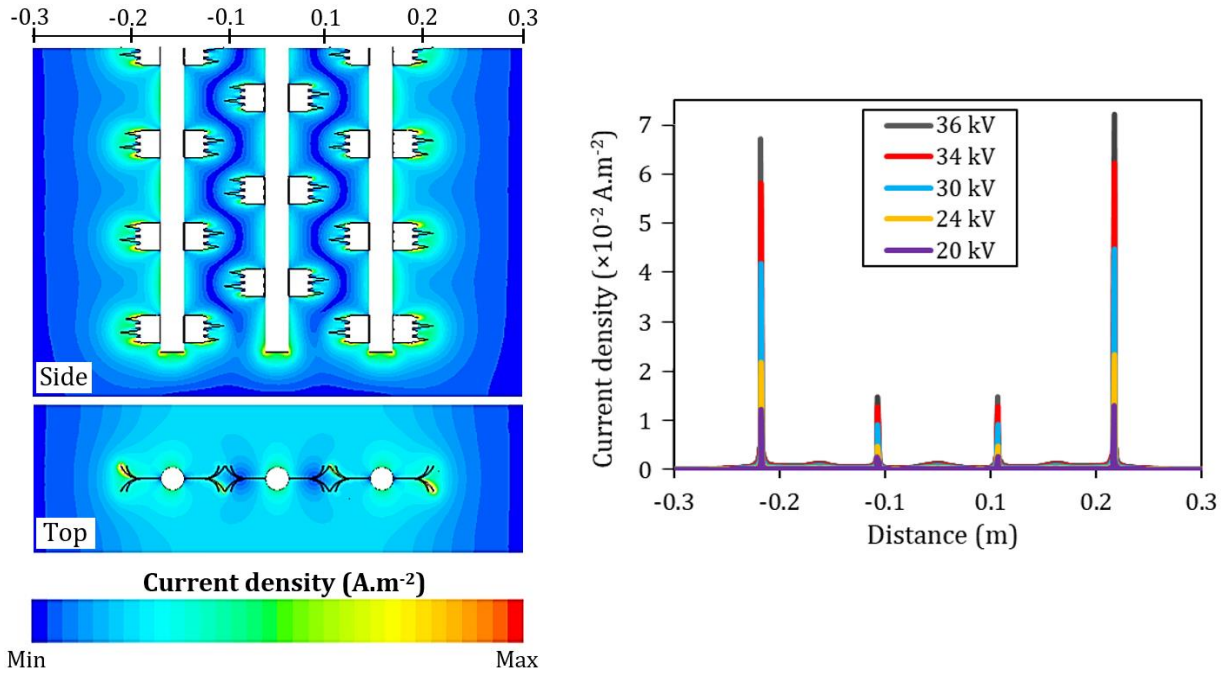

Figure 5-36. Current density distribution across three G-spike electrodes at different voltages

According to Figure 5-36, the current density on the electrodes increased with an increase in the voltage supply. The current density plots show maxima at the spike tips and small current densities at the cylindrical shafts of each G-spike electrode. Based on the relative sizes of the peaks in the current density plots, it is clear that the current densities on the spikes of the central electrode are significantly smaller than that of the outer electrode spikes. This is also evident from the current density scalar scene on the left, indicating negligible current regions between each pair of electrodes, with a suppressed current profile on the electrode

in the centre. The information in Figure 5-36 above confirms that shielding effects were present for the particular combination of electrode settings under consideration.

The ratios between the maximum current densities at the spikes on the adjacent sides of the central and outside electrodes were calculated. These values are provided in Table 5-17 and were used to quantify the degree of shielding for the electrodes at each voltage supply.

Table 5-17. Shielding degree at various supply voltages

Applied voltage (kV)	Current density ratio 1	Current density ratio 2
20	4.54	4.83
24	4.55	4.85
30	4.55	4.85
34	4.57	4.86
36	4.54	4.83

As seen in Table 5-17, the current density ratios between the outer and centre electrodes remain relatively constant across the entire voltage range. This indicates that the degree of shielding is not significantly affected by a change in applied voltage, which is consistent with the findings of Arif *et al.* (2018) [15] and Chen *et al.* (2022) [62], previously mentioned in Section 2.7.4. However, where results from Chen (2022) show a slight decrease in shielding effects with an increased voltage supply [62], the shielding degree in this case follows no particular trend from 20 kV to 36 kV. This could be attributed to the different nature of the electric fields generated by wire electrodes in [62] compared to that of the G-spike electrodes in this study.

As discussed in Section 5.3.3, G-spike electrodes generate uneven electric field distributions and attain considerably higher current densities than threaded rods, whose electrostatic characteristics resemble typical wire electrodes. Therefore, more notable changes in shielding effects should be observed for wire electrodes since the shielding degree shows a stronger dependence on ESP settings at lower current densities, according to Arif *et al.* (2018) [61].

In addition, shielding between spikes on the same G-spike electrode is reduced by the alternating directions and sizes of the spikes. Inter-electrode shielding for an assembly containing three G-spike electrodes is further alleviated by using electrodes with four spike groups on the outer ends and an electrode with three spike groups in the centre. The electrodes are designed to align the spike groups and open spaces of neighbouring electrodes to minimise field intersection.

Shielding as a function of electrode spacing

The current density profiles for three G-spike electrodes with different electrode-to-electrode distances were compared to determine the change in the shielding degree for a change in electrode spacing. For this comparison, a fixed plate spacing of 160 mm was used, and the electrode spacing was adjusted from 112

mm to 175 mm. The current density distributions for the two G-spike configurations at 20 kV are illustrated in Figure 5-37.

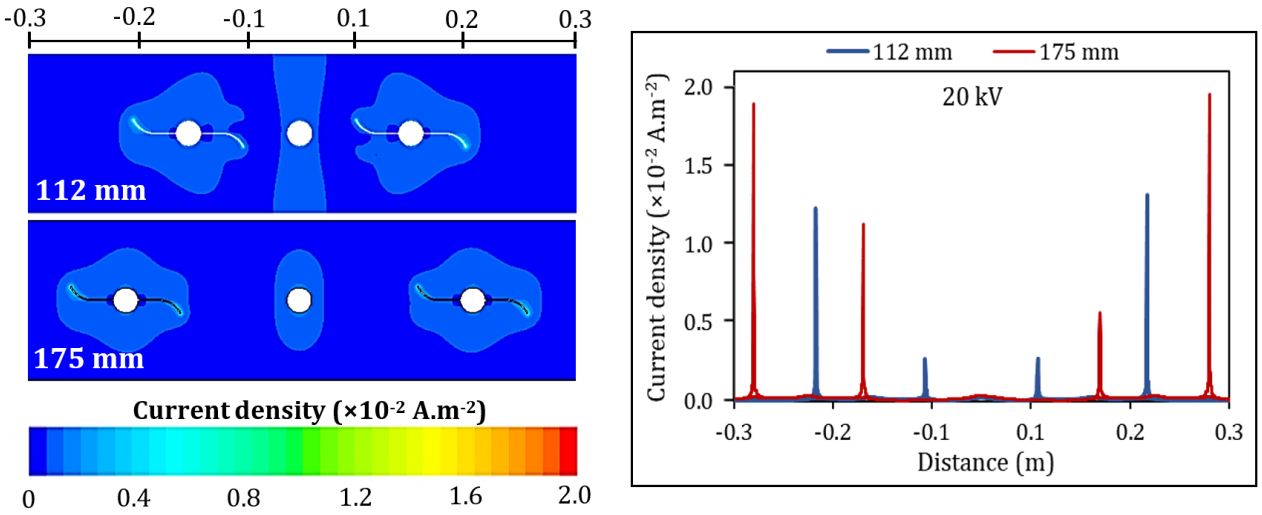

Figure 5-37. Current density profiles for G-spike electrodes with 112 mm and 175 mm electrode spacings

The G-spikes with the 112 mm electrode spacing show disformed current profiles on the inner electrode sides, while a more uniform current distribution is depicted for the 175 mm electrode spacing. This suggests that shielding effects are present for the 112 mm electrode distance as can be seen in the images on the left in Figure 5-37. The current density plots indicate a drastic decrease in current density for a decrease in electrode spacing from 175 mm to 112 mm. This corresponds to enhanced shielding effects for the smaller 112 mm electrode distance, which considerably reduces the current density over the central electrode region. The shielding degree (ratios of current densities on outside spikes to that on inside spikes of the electrodes) for the 112 mm and 175 mm electrode spacings are provided in Table 5-18.

Table 5-18. Shielding degree at various electrode spacings

Electrode spacing (mm)	Current density ratio 1	Current density ratio 2
112	4.54	4.83
175	1.67	3.40

The results in Table 5-18 also show a larger degree of shielding for the 112 mm electrode distance than for the 175 mm electrode distance. The change in shielding degree between the 112 mm and 175 mm electrode spacings is more notable at the first electrode pair (current density ratio 1) compared to the second electrode pair (current density ratio 2). Therefore, the irregular-shaped field of the G-spike geometry causes random variations in shielding effects at different positions across the G-spike electrodes.

Based on the relative sizes of the two current density ratios for the 112 mm and 175 mm electrode spacings, the overall change in shielding degree can be small or significant, depending on the electrode geometry. Nevertheless, the shielding degree inevitably increases for decreased electrode spacings at a constant plate spacing. Arif *et al.* (2018) [15] and Chen *et al.* (2022) [62] also observed increased shielding effects for smaller electrode-to-electrode distances (see Section 2.7.4). Therefore, the electrode spacing – though

seemingly insignificant for particle collection in general – can be an important ESP parameter when shielding occurs.

Shielding as a function of plate spacing

The shielding degree was studied as a function of collection plate spacing by comparing the current density distributions for three sawtooth electrodes with 160 mm and 280 mm plate-to-plate distances. The discharge electrode spacing was kept constant at 101 mm. Figure 5-38 depicts the current density profiles for the two cases at a fixed voltage of 37 kV.

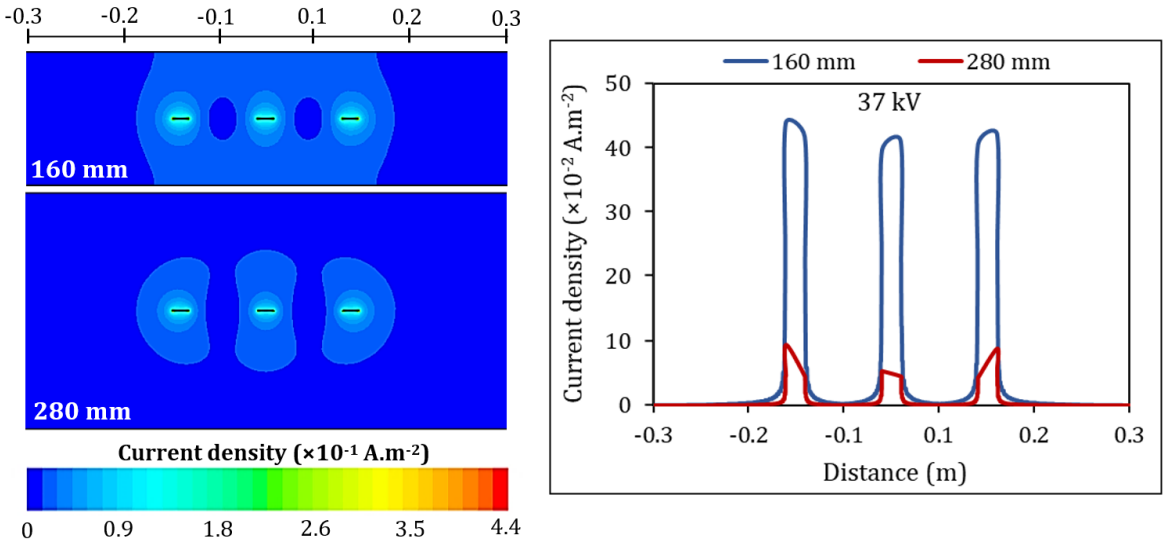

Figure 5-38. Current density profiles for sawtooth electrodes with 160 mm and 280 mm plate spacings

The current density scalar scenes on the left-hand side of Figure 5-38 show flattened field profiles for the 280 mm plate spacing with larger vacant regions between the discharge electrodes relative to that of the 160 mm plate spacing. These results are reproduced in the current density plots on the right, which indicate a sharper current decline from the outer electrode edges toward the central electrode with the 280 mm plate spacing. Therefore, the 280 mm plate spacing exhibits a larger degree of shielding across the three sawtooth electrodes compared to the 160 mm plate spacing. This is further explained in Section 2.7.4.

The current density is also significantly lower for the 280 mm plate spacing than for the 160 mm plate spacing. This is mostly due to an increase in electric field intensity for the latter (see Section 5.3.6) and the contributing effects of shielding. In order to quantitively investigate the change in shielding degree for an adjusted plate spacing of 160 mm to 280 mm, the current density ratios between the outer and central electrodes were calculated and compared. These ratios are presented in Table 5-19.

Table 5-19. Shielding degree at various plate spacings

Plate spacing (mm)	Current density ratio 1	Current density ratio 2
160	1.11	1.03
280	1.79	1.96

The larger current density ratios for the 280 mm plate distance confirm the previously noted increased shielding effects at wider plate-to-plate spacings for a particular electrode geometry and electrode spacing. This is in agreement with the findings from Arif *et al.* (2018) [15] and Chen *et al.* (2022) [62], which are discussed in Section 2.7.4. However, contrary to the abovementioned studies that concluded the plate spacing demonstrates the largest effect on the shielding degree, the ratios in Table 5-19 suggest relatively small shielding changes between the 160 mm and 280 mm plate distances.

Compared to the ratios for different electrode spacings in Table 5-18, the changed plate spacing appears to exhibit a less notable influence on the shielding degree. This could be due to the sawtooth electrodes experiencing smaller shielding effects than the G-spike electrodes from the former section in general. If this is the case, shielding effects would be less prone to alterations in ESP settings for sawtooth electrodes than in the case of G-spike electrodes. To confirm this, the electrostatic shielding characteristics of each electrode geometry needed to be investigated.

Shielding as a function of electrode geometry

Shielding effects were evaluated as a function of electrode size and geometry in a comparison of sawtooth and G-spike electrodes. Three discharge electrodes were used with a fixed plate spacing of 160 mm. The current density and corresponding field distributions across the G-spike and sawtooth electrodes at an applied voltage of 36 kV are illustrated in Figure 5-39.

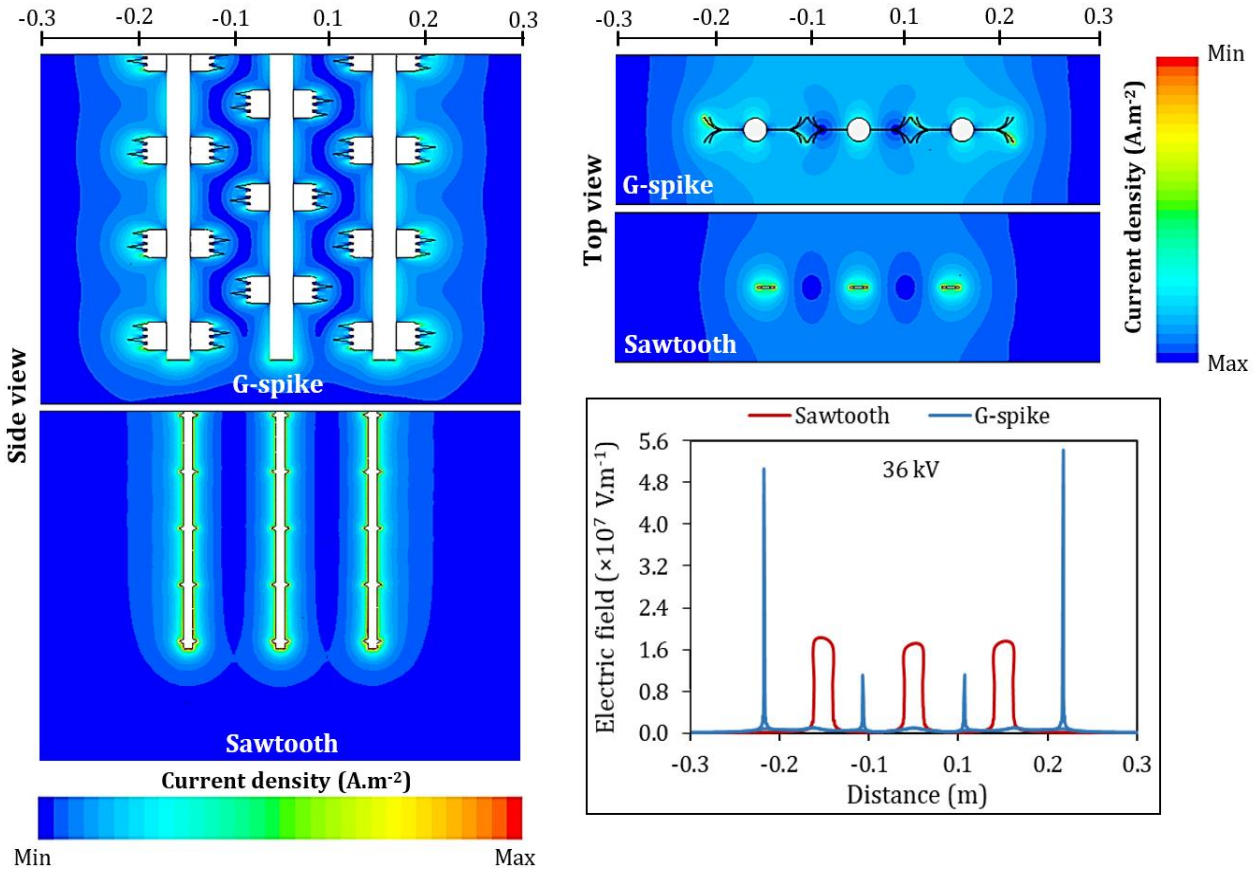

Figure 5-39. Current density and electric field distributions for sawtooth and G-spike electrodes at 36 kV

With reference to the electric field plots in Figure 5-39, the G-spike electrodes demonstrate much larger field intensities at 36 kV, compared to sawtooth electrodes. This confirms again the phenomenon that field intensities are higher for G-spike electrodes (see Section 5.3.4). However, the field intensities are approximately equal across all three sawtooth electrodes, whereas in the case of G-spike electrodes, the field on the central electrode is considerably smaller than that on the outer electrodes.

Therefore, shielding effects are much more prominent for G-spike electrodes as the fields of this geometry show a higher degree of overlapping than the fields of sawtooth electrodes with the same electrode and plate spacings. This is due to the G-spike geometry's larger size and complex design, leading to electric fields that cover larger distances, with concentrated regions at the extended spikes. The resulting decrease in current density on the central G-spike electrode, where shielding is at a maximum, is evident from the corresponding current profiles in Figure 5-39.

For a more detailed comparison of the shielding effects for the G-spike and sawtooth geometries, the current densities on individual electrodes in the three-electrode assembly of each were evaluated. The shielding degree between each electrode pair was calculated as the ratio of the current densities on the outer electrode spikes relative to that of the central electrode spikes. The current density ratios for the sawtooth and G-spike electrode geometries are given in Table 5-20.

Table 5-20. Shielding degree for sawtooth and G-spike electrodes

Electrode geometry	Current density ratio 1	Current density ratio 2
Sawtooth	1.02	1.03
G-spike	4.56	4.84

The current density ratios for the sawtooth electrodes are close to one. This shows that the current densities on the three sawtooth electrodes are almost identical in size and that the shielding degree is practically negligible. For G-spikes, on the other hand, the current densities on the outermost sides of the external electrodes are almost five times higher than that on both sides of the central electrode.

This indicates a significant degree of shielding for the G-spike geometry. Therefore, the shielding degree predominantly depends on the electric field profiles for different discharge electrode geometries. Furthermore, shielding effects are the most pronounced for assemblies of the bulky G-spike electrodes.

No shielding compared to shielding

The current density distribution for a single G-spike electrode in the absence of shielding effects was compared to that of three G-spike electrodes with a high degree of shielding. This was to investigate the effect of shielding on the current generation in the ESP. The same 160 mm plate spacing was used in both cases, and the current profiles for shielding versus no shielding are shown in Figure 5-40.

The individual G-spike electrode with no shielding effects exhibits a symmetrical distribution of current across the diagonal of the electrode. Conversely, the three G-spike electrodes indicate uneven current

density profiles with weakened intensities toward the inner sides. The corresponding current density plots show maximum current densities for the single G-spike that are almost double the size of the maximum current densities on the group of three G-spike electrodes.

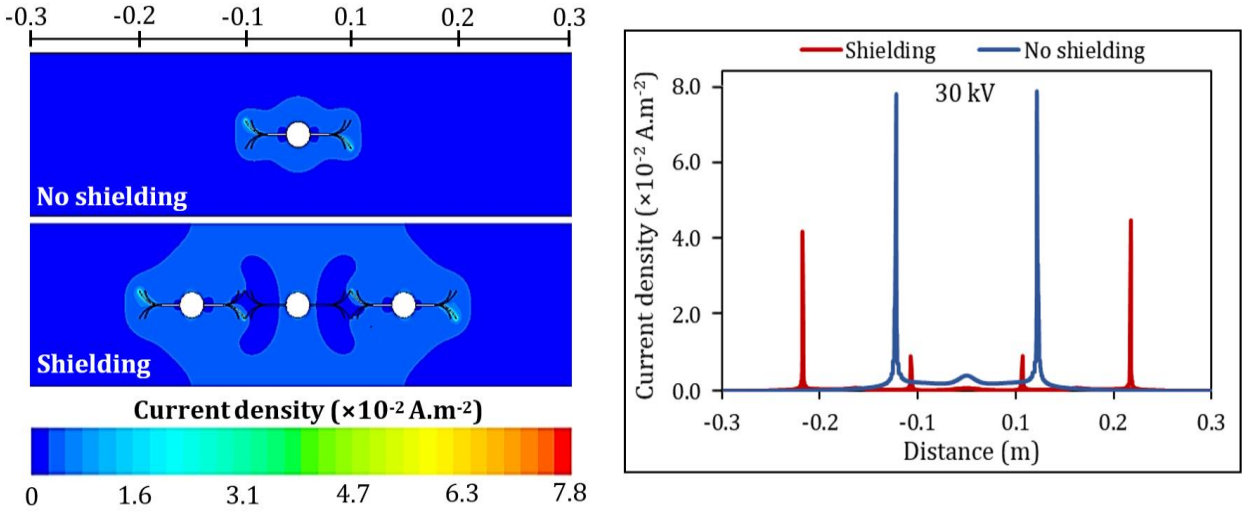

Figure 5-40. Current density profiles for G-spike electrodes with and without shielding effects

The current densities on the G-spike in the absence of shielding are more than four times larger than the corresponding current densities on the central G-spike electrode where shielding is present. Therefore, in this case, the shielding effects for the three G-spike electrodes were so extreme that the current densities of this assembly could not even reach that of one G-spike electrode. This shows the significant extent to which shielding can affect the current generation in the ESP.

As previously noted in Sections 5.3.3 – 5.3.5 and confirmed by [61] and [62], higher current densities lead to faster particle charging rates and migration velocities, which results in higher particle collection efficiencies. The inhibition of current caused by shielding effects in this study, as well as in earlier studies, is shown to decrease collection efficiency, thereby impeding the overall performance of the ESP. However, some degree of shielding will unavoidably occur for ESP configurations with good field-producing abilities.

Therefore, to optimise particle collection rates, different electrode and plate settings should be combined as such to maximise electric field intensities while preventing excessive shielding effects in the ESP as far as possible.

5.3.8 EFFECT OF FLY ASH LOADING ON COLLECTION EFFICIENCY

Since the RSM model showed the ash loading to play a significant role in the ESP performance, this factor was further investigated with the CFD model. Two ESP runs with identical electrode and plate settings were repeated for 4 mg.Nm^{-3} and 30 mg.Nm^{-3} feed concentrations of fly ash B. The ESP configuration used for these runs included one G-spike electrode with a plate-to-plate distance of 160 mm.

The peak current densities for the high (30 mg.Nm^{-3}) and low (4 mg.Nm^{-3}) ash loadings were compared across the voltage operating range for the specific ESP settings. Furthermore, the current density

distributions for the different ash feeds were evaluated at the 22 kV onset voltage and 32 kV maximum voltage, and the results are shown in Figure 5-41.

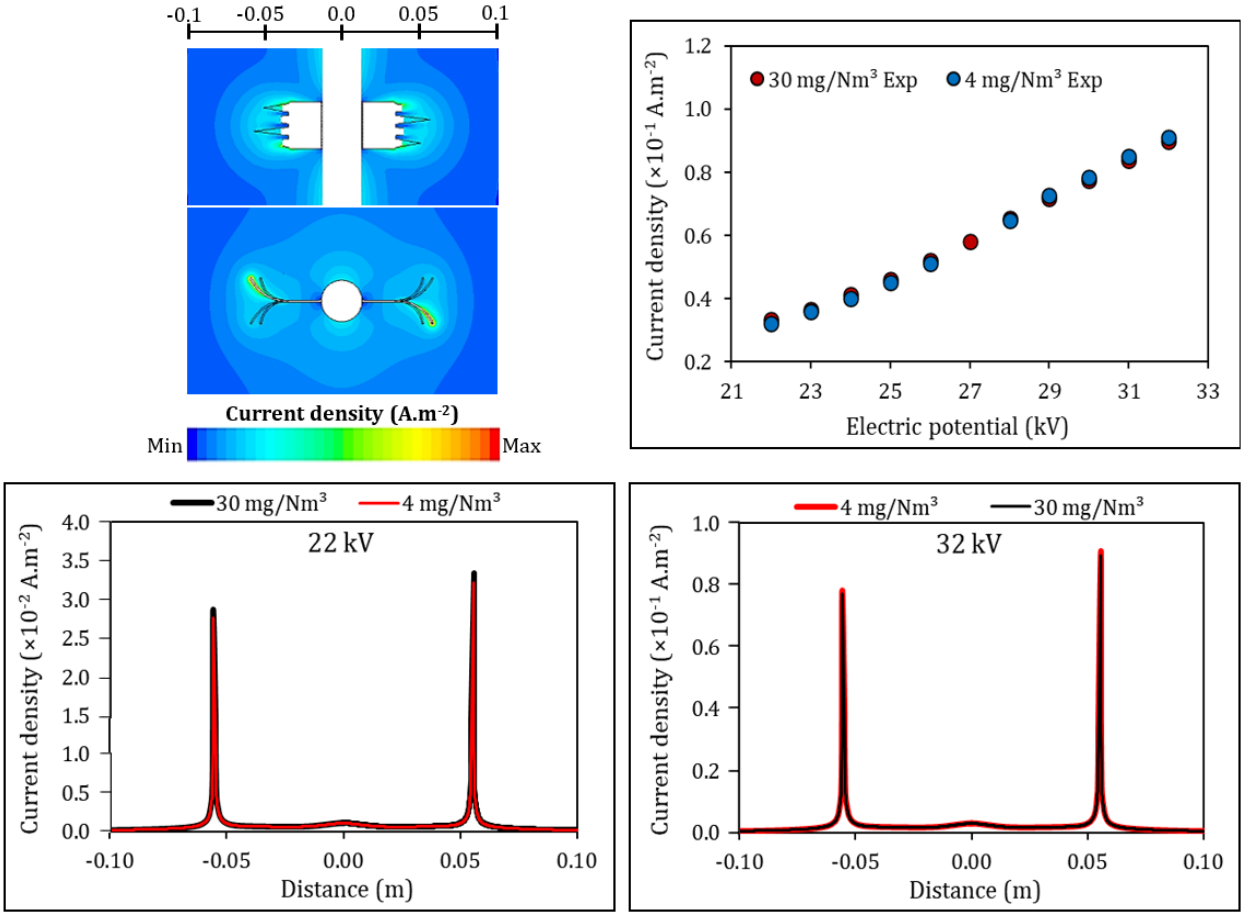

Figure 5-41. Current densities for 4 mg.Nm^{-3} and 30 mg.Nm^{-3} feeds of fly ash B at different voltages

The CFD model was fitted to the current-voltage measurements taken during the ESP experiments, which are shown on the plot at the top right corner of Figure 5-41. The CFD-modelled V-I relationships were subsequently used to reproduce the actual electrostatic field properties for the corresponding runs, from which the current density distributions at the bottom of Figure 5-41 could be obtained.

The G-spike electrode exhibits almost identical current densities across the 22 – 32 kV voltage range for the 4 mg.Nm^{-3} and 30 mg.Nm^{-3} fly ash loadings. However, the peak current densities show slightly higher values for the 30 mg.Nm^{-3} ash feed than the 4 mg.Nm^{-3} ash feed at 22 kV, and vice versa at 32 kV. Therefore, changes in the fly ash loading do cause some alterations to the current-voltage characteristics of a particular ESP setup, but to a minimal extent.

The particle collection efficiencies were measured experimentally and subsequently computed with the CFD model for the 4 mg.Nm^{-3} and 30 mg.Nm^{-3} ash feed rates at voltages between 22 kV and 32 kV. The plots in Figure 5-42 illustrate the experimental (Exp) and model (CFD) results. The collection efficiencies calculated with the CFD model show deviations of 0.01 – 1.5% from experimentally measured efficiencies for the high 30 mg.Nm^{-3} ash loading. Therefore, the model presents accurate predictions for the actual collection rates of particles in large concentrations from the passing air stream. Though an equivalent

goodness-of-fit was obtained between the modelled and experimental efficiencies for the 4 mg.Nm^{-3} feed at 22 – 26 kV, the model error increases by 4% for the remaining voltages in the range.

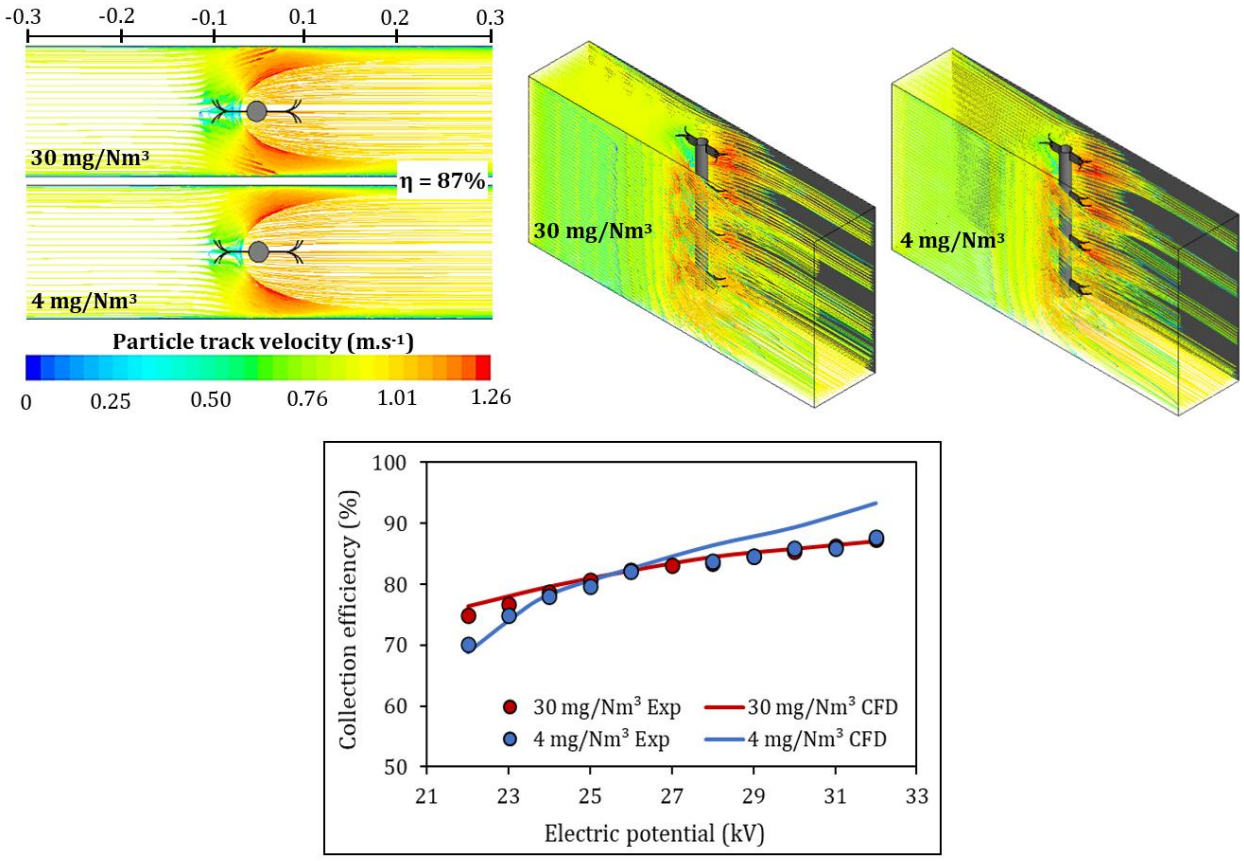

Figure 5-42. Particle tracks and collection efficiencies at 22 – 32 kV for one G-spike with 4 mg.Nm^{-3} and 30 mg.Nm^{-3} fly ash loadings

Following a similar comparison of the collection efficiencies for different ash loadings in Sections 5.2.3 and 5.2.4, it was deduced that the complexity of the ESP process is inversely related to the size of the ash feed. Factors typically regarded as insignificant for the effective collection of particles in large volumes can demonstrate rather sizeable impacts on the collection rates of individual particles in smaller quantities. Therefore, while the exclusion of several parameters from the CFD model generally shows negligible effects on the model accuracy for high ash concentrations, such simplifications can significantly reduce the model quality for low ash concentrations.

The results in Figure 5-42 indicate initial ESP collection efficiencies of 70% and 75% for the 4 mg.Nm^{-3} and 30 mg.Nm^{-3} ash loadings, respectively. Therefore, the collection efficiency for the 30 mg.Nm^{-3} ash feed is 5% higher than that of the 4 mg.Nm^{-3} feed at 22 kV. The lower particle collection rates for the smaller ash loading relate to the increased difficulty associated with particle collection on a more detailed level, as opposed to the bulk removal of particles. This is also portrayed in the particle tracks (Figure 5-42). Particles from the 4 mg.Nm^{-3} feed show stronger migration tendencies, less sneakage at the plates, and smaller concentrations at the ESP exit, but still delivered the same 87% efficiency as the 30 mg.Nm^{-3} feed.

On the contrary, at 32 kV, the G-spike obtained maximum collection efficiencies of 87.7% and 87.5% for the 4 mg.Nm^{-3} and 30 mg.Nm^{-3} feed, respectively. These efficiencies are very close but slightly higher for

the smaller ash feed. Therefore, where smaller ash loadings necessitate more optimal ESP conditions for sufficient collection at low voltages, molecular-level effects are dampened by increased field intensities at higher voltages. Furthermore, larger volumes of ash in the ESP cause a faster build-up of dust on the collection plates, followed by faster charge accumulation in the dust deposits and increased susceptibility to particle re-entrainment losses. As a result, the ESP exhibits a plateau in collection efficiency at an earlier stage for higher ash feed concentrations than in the case of small ash loadings.

The shift in the efficiency offset between the 4 mg.Nm^{-3} and 30 mg.Nm^{-3} ash loadings is also partly related to the relative current densities for the two feeds at 22 kV and 32 kV. At 22 kV, the higher current density for the 30 mg.Nm^{-3} feed promoted faster particle charging and migration rates, resulting in increased collection efficiencies. At 32 kV, the higher current density for the 4 mg.Nm^{-3} feed improved the corresponding particle collection efficiencies, in the same manner, to balance out the efficiency advantage of the 30 mg.Nm^{-3} feed.

In general, the ESP is more robust in terms of particle collection when high ash feed concentrations are used, whereas collection rates show a higher degree of sensitivity to ESP conditions when low ash feed concentrations are used.

5.4 EMPIRICAL MODELLING

The average collection efficiencies obtained from the ESP experiments, RSM model, and computational (CFD) model were further evaluated with the empirical Deutsch-Anderson and Matts-Öhnfeldt equations from Section 4.3.

Two ESP runs with different configurations of each electrode geometry were considered for validation against the empirical data. These include runs ST_1 and ST_2 for sawtooth electrodes (Saw), runs TR_1 and TR_2 for threaded rod electrodes (Thread), and runs GS_1 and GS_2 for G-spike electrodes (G-spike), with settings as given in Table 5-21.

Table 5-21. ESP settings for runs used in empirical model validation

Run	**ST_1**	**ST_2**	**TR_1**	**TR_2**	**GS_1**	**GS_2**
Electrode geometry	Saw	Saw	Thread	Thread	G-spike	G-spike
No. of electrodes	3	3	2	3	2	3
Electrode spacing (mm)	101	101	57	164	144	112
Plate spacing (mm)	280	160	280	280	280	160
Type of ash (-75 µm)	A	A	B	B	A	B
Ash loading (mg.Nm^{-3})	29	15	23	29	16	4.3

The Deutsch-Anderson and Matts-Öhnfeldt relations were used to estimate the average collection efficiencies of the runs in Table 5-21, and the outcomes were compared to the respective experimental and RSM model values of each. Table 5-22 shows the measured efficiencies (η_{Exp}) and predicted efficiencies from the RSM model (η_{RSM}), Deutsch-Anderson model (η_{D}), and Matts-Öhnfeldt model (η_{M}) for the

relevant runs. The corresponding model parameters, including particle migration velocity (w) and the corrective k-factor from Eqs. 4.42 and 4.43 are also given in Table 5-22. The empirical model results for the remaining ESP runs are tabulated in Appendix C-4.

Table 5-22. Empirical model parameters and efficiencies, compared to experimental and RSM data

Run	η_{Exp} (%)	η_{RSM} (%)	η_D (%)	η_M (%)	k	ε_r	w (m.s^{-1})
ST_1	82.2	82.4	96.8	82.6	0.64	2.0	0.52
ST_2	84.8	84.2	99.4	85.0	0.44	2.0	0.85
TR_1	63.1	63.5	99.1	63.1	0.21	1.8	0.66
TR_2	71.1	72.2	99.2	71.0	0.31	1.8	0.68
GS_1	88.6	87.9	94.9	90.0	0.85	2.0	0.47
GS_2	93.1	92.5	99.0	93.2	0.68	1.8	0.83

Constant relative permittivity values (ε_r) of 2.0 and 1.75 (~1.8) were used in Eq. 4.45 for ash A and B, respectively. These quantities were determined during the CFD modelling process by iterative adjustment for the closest correlation between the modelled and experimental efficiencies of a particular run. Despite the variation in temperature and humidity conditions, a constant relative permittivity of 2.0 provided the best model fits for all ESP runs with fly ash A. Conversely, runs involving fly ash B had amended relative permittivity values in the range of 1.7 – 1.8, hence the averaged value of 1.75 used in the empirical models.

Chan *et al.* (2005) [102] reported dielectric constant (relative permittivity) values between 2 and 5 for different fly ash samples. Arif *et al.* (2018) [15] also measured relative permittivity values between 1.0 and 4.0 for South-African fly ash samples similar to the ones used in this study and used a constant relative permittivity of 2.5 in all of their CFD models. Furthermore, Arif *et al.* (2018) [15] found high-resistivity ash particles to have smaller permittivity values compared to that of low-resistivity ash particles with better charging abilities. This corresponds to the larger relative permittivity of 2.0 obtained for the lower resistivity ash (A) and the smaller relative permittivity of 1.75 assigned to the higher resistivity ash (B) in the current study.

As seen in Table 5-22, the Deutsch-Anderson model obtained collection efficiency values between 95% and 100% for all the ESP runs. These values exceed the actual collection efficiencies by 6 – 36%, whereas the RSM model calculated efficiencies within a 0.2 – 1.1% offset from the experimental measurements. This shows the poor predictive ability of the Deutsch-Anderson equation for the ESP experiments and the corresponding RSM model under consideration. The large variance in the model error for the different ESP runs further indicates that the Deutsch-Anderson relation demonstrates little to no correlation with experimental data. This could be due to the negligence of particle polydispersity and re-entrainment, as well as changes in flow patterns and physical conditions during the ESP process [24].

These shortcomings were accounted for using the Matts-Öhnfeldt equation with dampening k-factors in the range of 0.2 – 0.9, as determined for the runs in Table 5-22. The Matts-Öhnfeldt relation yielded modelled collection efficiencies with an average deviation of 0.4% from the experimental data in Table 5-22. This is

smaller than the average deviation of 0.6% obtained with the RSM model for the same ESP runs. Therefore, the modified Matts-Öhnfeldt equation significantly improved the accuracy of the Deutsch-Anderson predictions, rendering the model suitable for use in the ESP system of this study.

Kim *et al.* (2001) determined k-values of 0.3 – 0.44 for fly ash from pulverised coal combustion and 0.3 – 0.53 for fly ash from fluidised bed combustion [37]. Furthermore, k-values of 0.4 – 0.6 are typically used for ESPs in industrial applications [19]. This confirms that the 0.2 – 0.9 k-factor range for the controlled ESP conditions from this study is a reasonable approximation.

The size of the k-factor depends on the extent of variability in ash properties and flow profiles and the relative electric field strength for a specific ESP configuration. A k-factor of 1 represents an ideal scenario of optimum ESP operation and therefore changes the Matts-Öhnfeldt equation to the Deutsch-Anderson equation. Accordingly, runs with k-values close to 1 demonstrate good ESP performance with high collection efficiencies, whereas runs with k-values closer to 0 indicate unsatisfactory particle removal rates [24]. The largest k-values were calculated for the G-spike assemblies, followed by that of the sawtooth electrodes, and the k-values determined for the threaded rods are the smallest.

G-spikes generate the strongest electric fields and typically obtain the best efficiencies, while threaded rods prove to be the least efficient among the three electrode geometries. This relates the error between the Deutsch-Anderson model and experimental data for the respective electrode geometries, which is the lowest for G-spikes (~ 6%), second-lowest for sawtooth (~ 15%), and the highest for threaded rods (~ 30%). Small k-factors (0.2 – 0.3) were required for runs with threaded rod electrodes to provide a sufficient degree of dampening such that accurate predictions can be made with the Matts-Öhnfeldt model. Intermediate k-values (0.4 – 0.6) were used for the sawtooth electrodes to correct the ~ 15% efficiency overestimate in the Matts-Öhnfeldt model. Finally, large k-factors (0.7 – 0.9) are applied to the runs with G-spike electrodes, which necessitated only small adjustments to the Deutsch-Anderson values.

Further investigation of the data in Table 5-22 shows smaller k-values for runs with narrow electrode and collection plate spacings. This is true for all electrode geometries and could be attributed to shielding effects between adjacent electrodes and collection plates, resulting in weaker electric fields than expected. Nevertheless, the particle migration velocities and collection efficiencies are higher for G-spike and sawtooth assemblies with smaller electrode and plate distances, due to the increased electrostatic field strength associated with such configurations.

For the threaded rod electrodes, run TR_2 with the larger 164 mm electrode spacing shows a higher migration velocity and collection efficiency than TR_1 with a 57 mm electrode spacing. This corresponds with the three electrodes used in TR_2, as opposed to the two electrodes used in TR_1. Therefore, the smaller electrode spacing advantage in TR_1 was overruled by the larger number of electrodes in TR_2. This indicates that the number of electrodes plays a more significant role in the ESP performance than the electrode spacing.

6. CONCLUSION & RECOMMENDATIONS

The main conclusions made with regard to the ESP operation are summarised in this section. A list of recommendations is subsequently provided for further research on this topic.

6.1 CONCLUSION

The following conclusions were derived from the results obtained in this study:

1. Based on the analysis of variance (ANOVA) results, the fly ash resistivity, fly ash loading, electrode geometry, electrode count, and collection plate spacing all demonstrate significant effects on the collection efficiency outcome. The electrode spacing, on the other hand, only shows a notable impact on the collection efficiency response in the case of shielding effects.
2. Respective average resistivities of 1.66×10^{10} Ω.cm, 1.18×10^{11} Ω.cm, 5.38×10^{10} Ω.cm, and 1.30×10^{11} Ω.cm were determined at ambient conditions for the -75 μm and -150+75 μm size fractions of ash A and B from two separate South-African power stations. The ESP generally exhibits shorter effective voltage spans but higher collection efficiencies for the higher resistivity ash, compared to the lower resistivity ash in this study. Furthermore, variations in ash resistivity within the 1.6×10^{10} – 1.3×10^{11} Ω.cm range from this study show relatively insignificant effects on the ESP performance.
3. Smaller ash feed concentrations present a higher level of difficulty for effective particle collection in the ESP than larger ash feed concentrations. Therefore, the ESP collection efficiency decreases with a decrease in the fly ash loading.
4. Each discharge electrode geometry produces unique electric field and current discharge profiles in the ESP, which determine the particle deposition patterns on the collection plate surfaces. G-spike electrodes generate the strongest electric fields with the highest particle collection rates, followed by sawtooth electrodes and threaded rod electrodes.
5. The electric field strength and associated current discharge increases for an increased number of discharge electrodes in the ESP, which results in higher collection efficiencies.
6. Shielding occurs for narrow electrode spacings and wide plate spacings in the ESP and reduces the electric field intensity on the central parts of the electrode assemblies. Shielding effects are the most prominent for G-spike electrodes and, in some cases, inhibit the corona fields to such an extent that ESP collection efficiencies are significantly reduced. The relative contributions of different ESP factors to shielding are directly related to the corresponding effect size on the collection efficiency.
7. A decreased collection plate spacing enhances electric field and current density and increases ESP collection efficiency. Small adjustments to the plate-to-plate distance cause drastic changes in the collection efficiency, which indicates a strong positive correlation between the ESP performance and collection plate spacing.
8. The Deutsch-Anderson relation is only suitable for ideal ESP conditions since this model calculates collection efficiencies significantly higher than the actual efficiencies of various electrode

configurations. The agreement between modelled and experimental collection efficiency data is better for the Matts-Öhnfeldt model with empirical k-values in the range of 0.2 – 0.9.

9. The RSM, CFD, and Matts-Öhnfeldt models show good correlations with experimental data and can be used for future research purposes.

6.2 RECOMMENDATIONS

The following recommendations are given for future studies on electrostatic precipitation:

1. Perform the ESP experiments in temperature and humidity-controlled conditions to alleviate variability in the ash resistivity between successive trials.
2. Devote an entire study to investigate the effects of different factors on particle rebound velocities and re-entrainment probabilities and the contributions of each phenomenon to collection efficiency losses.
3. Conduct additional research on the relationship between gravitational settling rates and the electric field intensity.
4. Experimentally measure the fly ash particle permittivity at ambient conditions to use as input in the CFD model for more accurate descriptions of the particle trajectories.
5. Evaluate the field distributions and collection efficiencies for the G-spike, sawtooth, and threaded rod electrode designs with different geometric dimensions, like rotation angles, electrode lengths, spike curve diameters, thread pitches, and tip areas.
6. Expand the computational domain for the CFD model from the ESP section to the entire ESP channel. This can provide more representative predictions of the air and particle flow patterns by introducing factors such as upstream turbulence and particle settling rates to the ESP simulation.
7. Complete ESP experiments at constant supply voltages for a particular run.
8. Install in-line air velocity measurement equipment to track the air flow at the entrance and exit of the ESP section continuously, as variations in air flow can significantly affect the ESP operation.
9. Modify the ESP setup to facilitate higher temperatures and SO_3/NH_3 injection to replicate industrial-scale ESP conditions.
10. Investigate pulsed-energy supply systems for back-corona prevention in ESPs.

BIBLIOGRAPHY

[1] World Coal Association, “Coal & Electricity,” 2020. https://www.worldcoal.org/coal-facts/coal-electricity/ (accessed Mar. 26, 2021).

[2] International Energy Agency, “Energy and Air Pollution,” 2016. doi: 10.1016/B978-0-12-809597-3.00127-9.

[3] N. M. Odhiambo, “Coal consumption and economic growth in South Africa: An empirical investigation,” *Energy and Environment*, vol. 27, no. 2, pp. 215–226, 2016, doi: 10.1177/0958305X15627535.

[4] Department of Energy, “The South African Energy Sector Report 2019,” vol. 44, no. 18. p. 9, 2019.

[5] Eskom Holdings SOC Ltd, “Coal Power,” *Electricity Technologies*, 2021. https://www.eskom.co.za/AboutElectricity/ElectricityTechnologies/Pages/Coal_Power.aspx (accessed Mar. 26, 2021).

[6] IQAir, “2020 World Air Quality Report,” 2020. https://www.iqair.com/ (accessed Mar. 26, 2021)

[7] K. E. Langerman and C. J. Pauw, “A critical review of health risk assessments of exposure to emissions from coal-fired power stations in South Africa,” *Clean Air Journal*, vol. 28, no. 2, pp. 68–79, 2018, doi: 10.17159/2410-972X/2018/v28n2a19.

[8] B. L. Garnham and K. E. Langerman, “Mercury emissions from South Africa’s coal-fired power stations,” *Clean Air Journal*, vol. 26, no. 2, pp. 14–20, 2016, doi: 10.17159/2410-972x/2016/v26n2a8.

[9] DEA, “National Environmental Management: Air Quality Act, 2004 (Act No. 39 of 2004),” *Government Gazette*. 2010.

[10] J. Speight, “Processing gas from tight formations,” in *Shale Oil and Gas Production Processes*, United States: Elsevier Inc., 2020, pp. 451–518.

[11] D. W. Green and R. H. Perry, *Perry’s Chemical Engineer’s Handbook*, 8th ed., vol. 59, New York: McGraw-Hill, 2008.

[12] I. Pretorius, S. Piketh, R. Burger, and H. Neomagus, “A perspective on South African coal fired power station emissions,” *Journal of Energy in Southern Africa*, vol. 26, no. 3, pp. 27–40, 2015, doi: 10.17159/2413-3051/2015/v26i3a2127.

[13] I. Pretorius, S. J. Piketh, and R. P. Burger, “Impacts and control of coal-fired power station emissions in South Africa,” North-West University, Natural and Agricultural Sciences, no. 2417, 2015.

[14] L. Sloss, “Emissions from coal-fired utilities in South Africa and neighbouring countries and potential for reduction,” *IEA Clean Coal Centre*. 2018.

[15] S. Arif, D. Branken, R. Everson, and H. Neomagus, "A computational model for the description of

electrostatic precipitator performance," North-West University, Engineering, no. 1343, 2018.

[16] C.-S. J. Yuan and T. T. Shen, "Electrostatic Precipitation," in *Handbook of Environmental Engineering*, vol. 1. Totowa, NJ: Humana Press, 2004, doi: 10.1007/978-1-59259-778-9_4.

[17] H. J. White, "Electrostatic Precipitation Of Fly Ash," *Journal of the Air Pollution Control Association*, vol. 27, no. 1, pp. 15–22, 1977, doi: 10.1080/00022470.1977.10470386.

[18] B. G. Miller, "Particulate Formation and Control Technologies," in *Clean Coal Engineering Technology*, 2nd ed., Oxford, US: Elsevier, 2017.

[19] J. R. Richards, "Control of Particulate Matter Emissions," in *APTI Course 413,* 3rd ed., ICES Ltd., 2000.

[20] H. J. Lowe and D. H. Lucas, "The physics of electrostatic precipitation," *British Journal of Applied Physics*, vol. 4, no. 2, 1953, doi: 10.1088/0508-3443/4/S2/317.

[21] R. F. Weiner and A. A. Matthews, "Air Pollution Control," in *Environmental Engineering*, 2nd ed., Butterworth-Heinemann, 2003, pp. 385–409.

[22] J. H. Turner *et al.*, "Sizing and costing of electrostatic precipitators," *Journal of the Air Pollution Control Association*, vol. 38, no. 4, pp. 458–471, 1988, doi: 10.1080/08940630.1988.10466396.

[23] V. Behjat, A. Rezaei-Zare, I. Fofana, and A. Naderian, "Concept design of a high-voltage electrostatic sanitizer to prevent spread of covid-19 coronavirus," *Energies*, vol. 14, no. 22, 2021, doi: 10.3390/en14227808.

[24] A. Bäck, "Some observations regarding the Matts-Öhnfeldt equation," *International Journal of Plasma Environmental Science and Technology*, vol. 8, no. 1, pp. 1–8, 2014.

[25] C.-S. J. Yuan and T. T. Shen, "Electrostatic Precipitation," in *Air Pollution Control Engineering*, Totowa NJ: Humana Press, 2010.

[26] C. Zheng *et al.*, "Current density distribution and optimization of the collection electrodes of a honeycomb wet electrostatic precipitator," *RSC Advances*, vol. 8, no. 54, pp. 30701–30711, 2018, doi: 10.1039/C8RA04765K.

[27] S. M. E. Haque, M. G. Rasul, and M. M. K. Khan, "Modelling and Simulation of Particle Trajectory Inside an Electrostatic Precipitator," in *BSME-ASME International Conference on Thermal Engineering*, 2008, no. 4, pp. 648–657.

[28] G. Gai, A. Hadjadj, S. Kudriakov, and O. Thomine, "Particles-induced turbulence: A critical review of physical concepts, numerical modelings and experimental investigations," *Theoretical and Applied Mechanics Letters*, vol. 10, no. 4, pp. 241–248, 2020, doi: 10.1016/j.taml.2020.01.026.

[29] J. D. Kulick, J. R. Fessler, and J. K. Eaton, "Particle response and turbulence modification in fully developed channel flow," *Journal of Fluid Mechanics*, vol. 277, pp. 109–134, 1994, doi: 10.1017/S0022112094002703.

[30] Y. Yamamoto, M. Potthoff, T. Tanaka, T. Kajishima, and Y. Tsuji, “Large-eddy simulation of turbulent gas-particle flow in a vertical channel: Effect of considering inter-particle collisions,” *Journal of Fluid Mechanics*, vol. 442, September, pp. 303–334, 2001, doi: 10.1017/S0022112001005092.

[31] Y. Tsuji, Y. Morikawa, and H. Shiomi, “LDV measurements of an air-solid two-phase flow in a vertical pipe,” *Journal of Fluid Mechanics*, vol. 139, pp. 417–434, 1984, doi: 10.1017/S0022112084000422.

[32] R. A. Gore and C. T. Crowe, “Effect of particle size on modulating turbulent intensity,” *International Journal of Multiphase Flow*, vol. 15, no. 2, pp. 279–285, 1989, doi: 10.1016/0301-9322(89)90076-1.

[33] G. Hetsroni, “Particles-turbulence interaction,” *International Journal of Multiphase Flow*, vol. 15, no. 5, pp. 735–746, 1989, doi: 10.1016/0301-9322(89)90037-2.

[34] J. Kussin and M. Sommerfeld, “Experimental studies on particle behaviour and turbulence modification in horizontal channel flow with different wall roughness,” *Experiments in Fluids*, vol. 33, no. 1, pp. 143–159, 2002, doi: 10.1007/s00348-002-0485-9.

[35] B. S. Choi and C. A. J. Fletcher, “Turbulent particle dispersion in an electrostatic precipitator,” *Applied Mathematical Modelling*, vol. 22, no. 12, pp. 1009–1021, 1998, doi: 10.1016/S0307-904X(98)10034-3.

[36] W. Gao *et al.*, “A Numerical Investigation of the Effect of Dust Layer on Particle Migration in an Electrostatic Precipitator,” *Aerosol and Air Quality Research*, vol. 20, pp. 166–179, 2020, doi: 10.4209/aaqr.2019.11.0609.

[37] B. H. Kim, K. C. Ahn, and Y. S. Jang, “Electrostatic precipitability of the coal fly-ash by the pilot scale test,” *KSME International Journal*, vol. 15, no. 5, pp. 602–612, 2001, doi: 10.1007/BF03184376.

[38] Z. Chengfeng, Y. Qiang, and S. Junming, “Characteristics of particulate matter from emissions of four typical coal-fired power plants in China,” *Fuel Processing Technologies*, vol. 86, no. 7, pp. 757–768, 2005, doi: 10.1016/j.fuproc.2004.08.006.

[39] A. Sarkar, S. Vishwakarma, H. Banichul, K. K. Mishra, and S. S. Roy, “A comprehensive analysis of the particle size and shape of fly ash from different fields of ESP of a super thermal power plant,” *Energy Sources, Part A: Recovery, Utilization and Environmental Effects*, vol. 34, no. 5, pp. 385–395, 2012, doi: 10.1080/15567031003614649.

[40] C. R. Mohanty, A. K. Swar, B. C. Meikap, and J. N. Sahu, “Studies on factors influencing fly ash resistivity from electrostatic precipitator with reference to India,” *Journal of Scientific and Industrial Research (India)*, vol. 70, no. 9, pp. 795–803, 2011.

[41] J. Ribberink, “Influence of moisture on the resistivity of selected South African fly ashes,” North-

West University, Engineering, no. 1343, 2018.

[42] H. J. White, “Resistivity Problems in Electrostatic Precipitation,” *Journal of the Air Pollution Control Association*, vol. 24, no. 4, pp. 313–338, 1974, doi: 10.1080/00022470.1974.10469923.

[43] R. E. Bickelhaupt, “Effect of chemical composition on surface resistivity of fly ash,” in *Environmental Protection Technology Series*, United States: N., 1975.

[44] A. Chandra, “Some Investigations on Fly Ash Resistivity Generated in Indian Power Plants,” *Electrostatic Precipitation*, pp. 399–405, 2009, doi: 10.1007/978-3-540-89251-9_81.

[45] C. Zheng *et al.*, “Measurement and prediction of fly ash resistivity over a wide range of temperature,” *Fuel*, vol. 216, December 2017, pp. 673–680, 2018, doi: 10.1016/j.fuel.2017.12.047.

[46] O. Tassicker, Z. Herceg, and K. McLean, “The Electrical Resistivity of Precipitator Fly-Ash,” *Wollongong University: College Bulletin*, no. 7, 1966.

[47] Y. Aleksin, A. Vora, and U. Riebel, “A new understanding of electric conduction in highly resistive dusts and bulk powders,” *Powder Technologies*, vol. 294, pp. 353–364, 2016, doi: 10.1016/j.powtec.2016.02.031.

[48] O. J. Tassicker, Z. Herceg, and K. Mclean, “Mechanism of Current Conduction through Precipitated Fly-Ash Mechanism of Current Conduction through Precipitated Fly-Ash,” *Wollongong University: College Bulletin*, no. 17, 1966.

[49] W. E. Bucher, “A Study of the Bulk Electrical Resistivity Characteristics of Fly Ash from Lignite and Other Western Coals,” University of North Dakota, no. 460, 1970.

[50] S. M. Lloyd, “The Control of Air Pollution at South African Coal-Fired Power Stations,” *The Clean Air Journal*, vol. 7, no. 4, pp. 20 - 24, 1987, ISSN 0379-8849.

[51] A. Mizuno, “Electrostatic precipitation,” *IEEE Transactions on Dielectrics and Electrical Insulation*, vol. 7, no. 5, pp. 281–300, 2000, doi: 10.1201/noe0849398438.ch20.

[52] L. J. Roberts, P. E. Mason, J. M. Jones, W. F. Gale, A. Williams, and C. Ellul, “Investigating the impact of an Al-Si additive on the resistivity of biomass ashes,” *Fuel Processing Technologies*, vol. 178, pp. 13–23, 2018, doi: 10.1016/j.fuproc.2018.05.018.

[53] D. Brocilo, J. Podlinski, S. Chang, J. Mizeraczyk, and D. Findlay, “Electrode geometry effects on the collection efficiency of submicron and ultra-fine dust particles in spike-plate electrostatic precipitators,” *Journal of Physics: Conference Series*, vol. 142, pp. 0–6, 2008, doi: 10.1088/1742-6596/142/1/012032.

[54] C. L. Chang and H. Bai, “Effects of some geometric parameters on the electrostatic precipitator efficiency at different operation indexes,” *Aerosol Science and Technology*, vol. 33, no. 3, pp. 228–238, 2000, doi: 10.1080/027868200416222.

[55] X. Zhang, L. Wang, and K. Zhu, “Particle tracking and particle-wall collision in a wire-plate

electrostatic precipitator," *Journal of Electrostatics*, vol. 63, no. 11, pp. 1057–1071, 2005, doi: 10.1016/j.elstat.2005.02.002.

[56] Y. Zamrodah, "A Model of Particle Re-entrainment in Electrostatic Precipitators," *Aerosol Science and Technology*, vol. 26, no. 2, pp. 227–239, 1995.

[57] G. N. Popa, S. loan Deaconu, I. Popa, and C. M. Dinis, "New Trends in Detection of Back - Corona Discharges in Plate-Type Electrostatic Precipitators," *Acta Technica Corviniensis - Bulletin of Engineering*, vol. 5, no. 2, pp. 93–96, 2012.

[58] P. A. Lawless and L. E. Sparks, "A mathematical model for calculating effects of back corona in wire-duct electrostatic precipitators," *Journal of Applied Physics*, vol. 51, no. 1, pp. 242–256, 1980, doi: 10.1063/1.327416.

[59] G. Bacchiega, I. Gallimberti, V. Arrondel, N. Caraman, and M. Hamlil, "Back-Corona Model for Prediction of Esp Efficiency and Voltage-Current Characteristics," in *The International Conference on Electrostatic Precipitation*, 2006, June, pp. 1–11.

[60] Z. Al-hamouz, "Numerical and experimental evaluation of fly ash collection efficiency in electrostatic precipitators," *Energy Conversion and Management*, vol. 79, pp. 487–497, 2014, doi: 10.1016/j.enconman.2013.11.047.

[61] S. Arif, D. J. Branken, R. C. Everson, H. W. J. P. Neomagus, and A. Arif, "The influence of design parameters on the occurrence of shielding in multi-electrode ESPs and its effect on performance," *Journal of Electrostatics*, vol. 93, October 2017, pp. 17–30, 2018, doi: 10.1016/j.elstat.2018.03.001.

[62] B. Chen, S. Li, Y. Guo, H. Li, W. Zhou, and B. Liu, "Research on electrostatic shielding characteristics of electrostatic precipitator," *Journal of the Air and Waste Management Association*, vol. 72, no. 4, pp. 331–345, 2022, doi: 10.1080/10962247.2021.2017374.

[63] A. Kasdi, "Computation and measurement of corona current density and V–I characteristics in wires-to-plates electrostatic precipitator," *Journal of Electrostatics*, vol. 81, pp. 1–8, 2016, doi: 10.1016/j.elstat.2016.02.005.

[64] A. Back, "Relation between gas velocity profile and apparent migration velocity in electrostatic precipitators," *International Journal of Plasma Environmental Science and Technology*, vol. 11, no. 1, pp. 104–111, 2017.

[65] L. Zhao, K. Adamiak, and S. Member, "Numerical Simulation of the Electrohydrodynamic Flow in a Single Wire-Plate Electrostatic Precipitator," *IEEE Transactions on Dielectrics and Electrical Insulation*, vol. 44, no. 3, pp. 683–691, 2008.

[66] G. Cooperman, "A unified efficiency theory for electrostatic precipitators," *Atmospheric Environment*, vol. 18, no. 2, pp. 277–285, 1984, doi: 10.1016/0004-6981(84)90101-X.

[67] N. Farnoosh, K. Adamiak, and G. S. P. Castle, "3-D numerical analysis of EHD turbulent flow and

mono-disperse charged particle transport and collection in a wire-plate ESP," *Journal of Electrostatics*, vol. 68, no. 6, pp. 513–522, 2010, doi: 10.1016/j.elstat.2010.07.002.

[68] M. Robinson, "Turbulent gas flow and electrostatic precipitation," *Journal of the Air Pollution Control Association*, vol. 18, no. 4, pp. 235–239, 1968, doi: 10.1080/00022470.1968.10469120.

[69] D. Brocilo, J. Podlinski, S. Chang, J. Mizeraczyk, and D. Findlay, "Electrode geometry effects on the collection efficiency of submicron and ultra-fine dust particles in wire-plate electrostatic precipitators," *Journal of Physics: Conference Series*, vol. 142, 2003, doi: 10.1088/1742-6596/142/1/012032.

[70] M. Feldkamp, M. Dickamp, and C. Moser, "CFD simulation of Electrostatic Precipitators and Fabric Filters State of the Art and Applications," in *Electrostatic Precipitation : 11th International Conference on Electrostatic Precipitation*, Heidelberg: Springer, 2010, pp. 141–150.

[71] M. Jedrusik and A. Świerczok, "The correlation between corona current distribution and collection of fine particles in a laboratory-scale electrostatic precipitator," *Journal of Electrostatics*, vol. 71, no. 3, pp. 199–203, 2013, doi: 10.1016/j.elstat.2013.01.002.

[72] K. Adamiak, "Numerical models in simulating wire-plate electrostatic precipitators: A review," *Journal of Electrostatics*, vol. 71, no. 4, pp. 673–680, 2013, doi: 10.1016/j.elstat.2013.03.001.

[73] B. Y. Guo, J. Guo, and A. B. Yu, "Simulation of the electric field in wire-plate type electrostatic precipitators," *Journal of Electrostatics*, vol. 72, no. 4, pp. 301–310, 2014, doi: 10.1016/j.elstat.2014.05.005.

[74] J. Guo, X. Ye, S. Wang, B. Guo, C. Zhang, and Y. Su, "The influence of electrohydrodynamic secondary flow on the collection efficiency and deposition pattern in ESP," *Mathematical Problems in Engineering*, vol. 10, pp. 1 - 7, 2019, doi: 10.1155/2019/8923030.

[75] J. Podliński, A. Niewulis, and J. Mizeraczyk, "Electrohydrodynamic flow and particle collection efficiency of a spike-plate type electrostatic precipitator," *Journal of Electrostatics*, vol. 67, pp. 99–104, 2009, doi: 10.1016/j.elstat.2009.02.009.

[76] M. Dong, F. Zhou, Y. Shang, and S. Li, "Numerical study on electrohydrodynamic flow and fine-particle collection efficiency in a spike electrode-plate electrostatic precipitator," *Powder Technology*, vol. 351, pp. 71–83, 2019, doi: 10.1016/j.powtec.2019.03.046.

[77] H. Fujishima, Y. Ueda, K. Tomimatsu, and T. Yamamoto, "Electrohydrodynamics of spiked electrode electrostatic precipitators," *Journal of Electrostatics*, vol. 62, no. 4, pp. 291–308, 2004, doi: 10.1016/j.elstat.2004.05.006.

[78] G. Skodras, S. P. Kaldis, D. Sofialidis, O. Faltsi, P. Grammelis, and G. P. Sakellaropoulos, "Particulate removal via electrostatic precipitators — CFD simulation," *Fuel Processing Technologies*, vol. 87, pp. 623–631, 2006, doi: 10.1016/j.fuproc.2006.01.012.

[79] N. Neimarlija, I. Demirdžić, and S. Muzaferija, “Finite volume method for calculation of electrostatic fields in electrostatic precipitators,” *Journal of Electrostatics*, vol. 67, no. 1, pp. 37–47, 2009, doi: 10.1016/j.elstat.2008.10.007.

[80] “IEEE Standard Criteria and guidelines for the laboratory measurement and reporting of fly ash resistivity,” New York: Institute of Electrical and Electronics Engineers, 1984, doi: 10.1109/IEEESTD.1984.81767.

[81] D. C. Montgomery, *Design and Analysis of Experiments*, 8th ed, Hoboken, NJ: John Wiley & Sons, Inc., 2013.

[82] K. Dunn, *Process Improvement Using Data*. 2021. https://learnche.org/pid/contents (accessed Apr. 09, 2022).

[83] J. D. Wilcox, “Isokinetic flow and sampling,” *Journal of the Air Pollution Control Association*, vol. 5, no. 4, pp. 226–245, 1956, doi: 10.1080/00966665.1956.10467715.

[84] CD-adapco, *STAR CCM+ User Guide*, 4.02. 2008.

[85] K. Adamiak and P. Atten, “Simulation of corona discharge in point-plane configuration,” *Journal of Electrostatics*, vol. 61, no. 2, pp. 85–98, 2004, doi: 10.1016/j.elstat.2004.01.021.

[86] D. Yang, B. Guo, X. Ye, A. Yu, and J. Guo, “Numerical simulation of electrostatic precipitator considering the dust particle space charge,” *Powder Technology*, vol. 354, pp. 552–560, 2019, doi: 10.1016/j.powtec.2019.06.013.

[87] A. Marquard, J. Meyer, and G. Kasper, “Unipolar Field and Diffusion Charging in the Transition Regime—Part II: Charging Experiments,” *Aerosol Science and Technology*, vol. 41, no. 6, pp. 611–623, 2007, doi: 10.1080/02786820701272061.

[88] B. V. Somov, “The Generalized Ohm’s Law in Plasma,” *Plasma Astrophysics: Astrophysics and Space Science Library*, vol. 391, pp. 223–236, 2012.

[89] S. S. Karunarathne and L.-A. Tokheim, “Comparison of the influence of drag models in CFD simulation of particle mixing and segregation in a rotating cylinder,” *Proceedings of the 58th Conference on Simulation and Modelling (SIMS 58)*, Reykjavik, Iceland, Sept. 25th – 27th, 2017, vol. 138, pp. 151–156, 2017, doi: 10.3384/ecp17138151.

[90] M. Koretsky, “Engineering and Chemical Thermodynamics,” *Journal of Chemical Information and Modelling*, vol. 53, no. 9, p. 287, 2008, doi: 10.1017/CBO9781107415324.004.

[91] Fluent Inc., *Fluent 6.3 User Guide*, September, 2006.

[92] L. Deng, L. Shi, T. Zhou, X. Zhang, and S. W. Joo, “Charge properties and electric field energy density of functional group-modified nanoparticle interacting with a flat substrate,” *Micromachines*, vol. 11, no. 12, pp. 1–15, 2020, doi: 10.3390/mi11121038.

[93] J. P. Reynolds, L. Theodore, and J. Marino, “Calculating Collection Efficiencies for Electrostatic

Precipitators," *Journal of the Air Pollution Control Association*, vol. 25, no. 6, pp. 610–616, 1975, doi: 10.1080/00022470.1975.10470116.

[94] G. Y. Lin, T. M. Chen, and C. J. Tsai, "A modified Deutsch-Anderson equation for predicting the nanoparticle collection efficiency of electrostatic Precipitators," *Aerosol and Air Quality Research*, vol. 12, no. 5, pp. 697–706, 2012, doi: 10.4209/aaqr.2012.04.0085.

[95] N. Gajbhiye, V. Eswaran, A. K. Saha, and A. Kumar, "Numerical calculation of particle collection efficiency in an electrostatic precipitator," *Sadhana - Academy Proceedings in Engineering Sciences*, vol. 40, no. 3, pp. 863–873, 2015, doi: 10.1007/s12046-015-0342-1.

[96] J. H. Turner, P. A. Lawless, T. Yamamoto, and D. W. Coy, "Particulate Matter Controls: Electrostatic Precipitators," U.S. Environmental Protection Agency, Research Triangle Park NC 27711, 1999, EPA/452/B-02-001.

[97] M. L. Jansen and J. R. Glastonbury, "The size separation of particles by screening," *Powder Technology*, vol. 1, no. 6, pp. 334–343, 1968, doi: 10.1016/0032-5910(68)80016-6.

[98] L. Qi and Y. Yuan, "Mechanism of the effect of alkali metal on the electrostatic precipitability of fly ash," *Fuel*, vol. 107, pp. 848–851, 2013, doi: 10.1016/j.fuel.2013.02.004.

[99] G. W. Penney and R. E. Matick, "Potentials in D-C Corona Fields," *Transactions of the American Institute of Electrical Engineers*, vol. 79, pp. 91–99, 1960, doi: 10.1109/TCE.1960.6368550.

[100] D. Blanchard, P. Atten, and L. M. Dumitran, "Correlation between current density and layer structure for fine particle deposition in a laboratory electrostatic precipitator," *IEEE Transactions on Industry Applications*, vol. 38, no. 3, pp. 832–839, 2002, doi: 10.1109/TIA.2002.1003437.

[101] N. Farnoosh, K. Adamiak, and G. S. P. Castle, "Numerical Calculations of Submicron Particle Removal in a Spike-plate Electrostatic Precipitator," *IEEE Transactions on Dielectrics and Electrical Insulation*, vol. 18, no. 5, 2011, doi: 10.1109/TDEI.2011.6032814.

[102] K. Chan, R. J. Weber, and R. C. Brown, "Characterization of Unburned Carbon Content in Coal Fly Ash with Dielectric Constant Measurement," in *American Institute of Physics: Conference Proceedings*, vol. 760, no. 1, pp. 327 - 342, 2005, doi: 10.1063/1.1916851.

[103] P. A. Vesilind, "The Rosin-Rammler particle size distribution," *Resource Recovery and Conservation*, vol. 5, no. 3, pp. 275–277, 1980, doi: 10.1016/0304-3967(80)90007-4.

APPENDIX

Supplementary information for different sections of this study is given in Appendix A – C.

APPENDIX A : EXPERIMENTAL PROCEDURES

Appendix A gives information relevant to Chapter 3.

APPENDIX A-1. FLY ASH PROPERTIES

Additional calculations applied for the characterisation of the fly ash samples used in this study are discussed in the subsequent text.

A-1.1. Particle size distribution analysis

The particle size distributions (PSDs) of the different ash samples were described as Rosin-Rammler distributions. A typical Rosin-Rammler distribution curve is defined as follows [103]:

$$Y_d = 1 - \exp\left(-\frac{d}{d_0}\right)^n \qquad \text{E A-1}$$

where Y_d [%] is the cumulative mass fraction of particles with diameters smaller than size d [µm], d_0 is the reference particle size (the diameter larger than 63.2% of the particles), and n is the size distribution coefficient. Eq. A-1 was linearised according to the following steps:

$$1 - Y_d = \exp\left(-\frac{d}{d_0}\right)^n \qquad \text{E A-2}$$

$$\frac{1}{1 - Y_d} = \exp\left(\frac{d}{d_0}\right)^n \qquad \text{E A-3}$$

$$\ln\left(\frac{1}{1 - Y_d}\right) = \left(\frac{d}{d_0}\right)^n \qquad \text{E A-4}$$

$$\ln\left[\ln\left(\frac{1}{1 - Y_d}\right)\right] = n \ln\left(\frac{d}{d_0}\right) \qquad \text{E A-5}$$

The linear Rosin-Rammler equation (Eq. A-5) was described, using a plot of $\ln[\ln(1/1 - Y_d)]$ versus $\ln(d/d_0)$. The magnitude of the constant, n, was calculated from the slope of the plot from Eq. A-5.

The linearised Rosin-Rammler plots and corresponding trendline equations for each ash sample used in this study are illustrated in Figure A. 1.

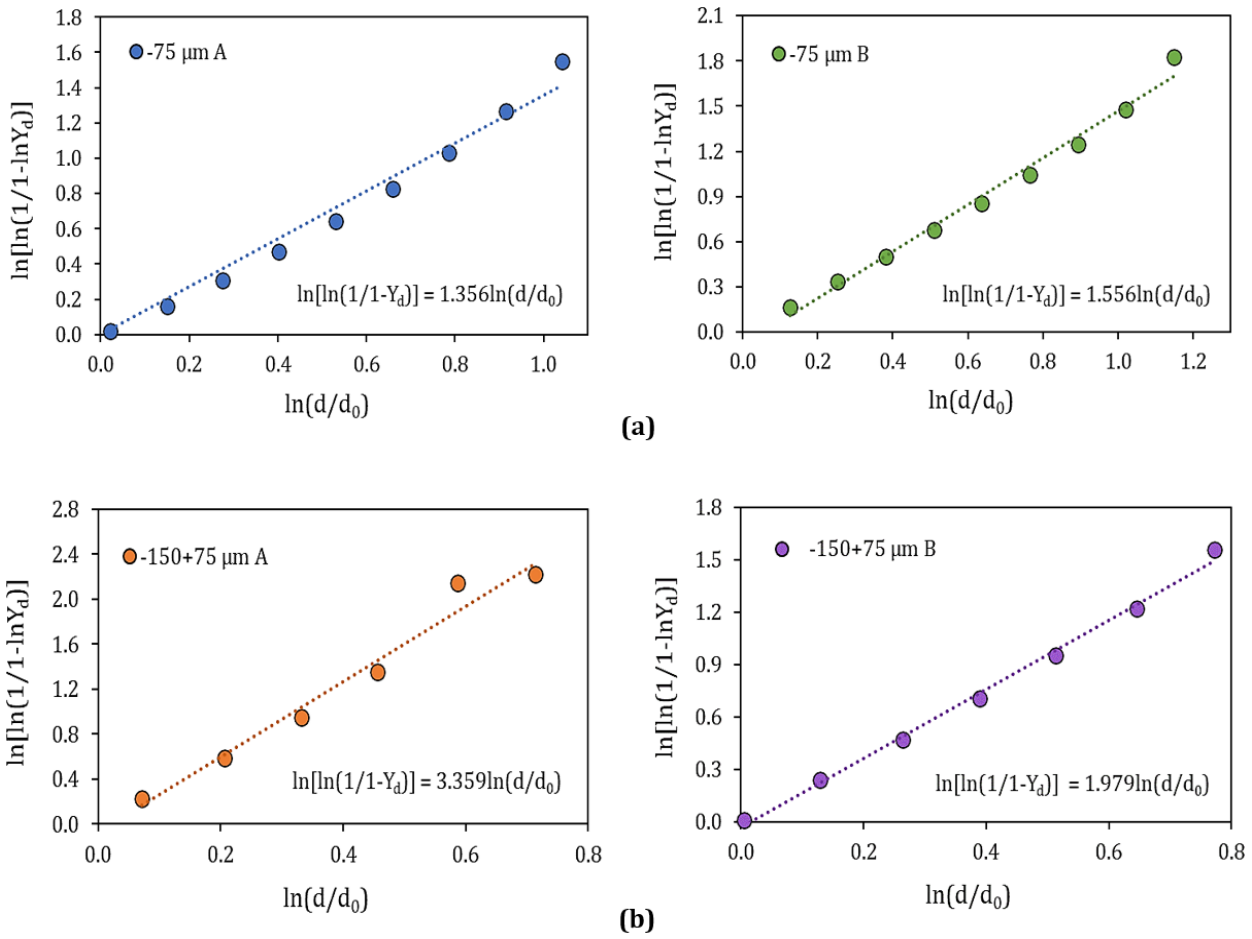

Figure A. 1. Rosin-Rammler calculations for size distributions of fly ash A and B in the (a) -75 µm and (b) -150+75 µm size fractions

The Rosin-Rammler parameters that were obtained from the plots in Figure A. 1 were substituted into Eq. A-1 for the different fly ash samples. The resulting cumulative volume functions as predicted by the Rosin-Rammler model were compared to the experimental measurements from the Malvern Mastersizer instrument. These plots are provided in Figure 5-2 and discussed in Section 5.1.1.

A-1.2. Resistivity

The resistivities of ash A and B in the -75 µm and -150+75 µm size fractions were calculated from the currents measured for applied voltages in the range of 1.5 – 4.0 kV. Figure A. 2 shows the current reading at each voltage set point for the different ash samples. These current-voltage plots were used for the fly ash resistivity calculation procedure discussed in Section 3.2.2.

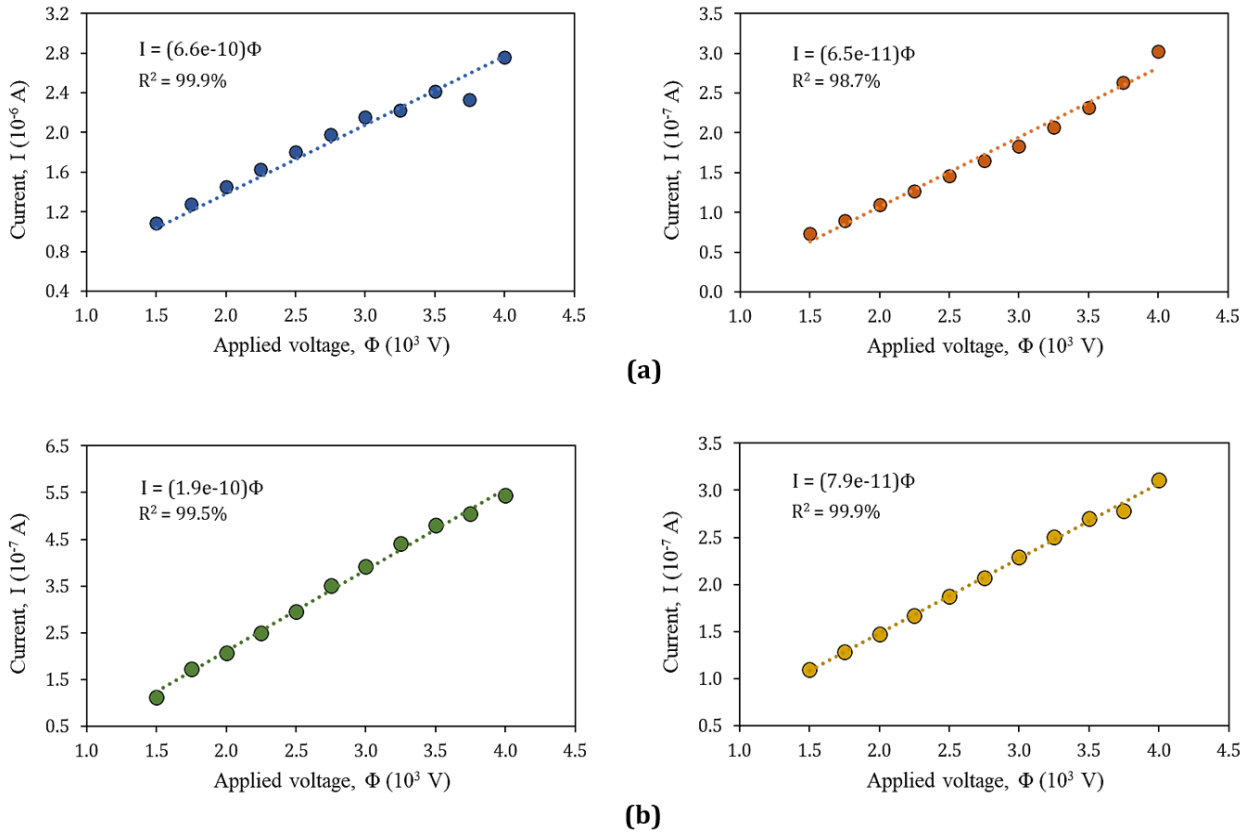

Figure A. 2. Current-voltage plots for resistivity calculation of -75 µm ash A (●) and ash B (●) in **(a)** and -150+75 µm ash A (●) and ash B (●) in **(b)**

The resistivity values that were determined from the inverse slopes of the plots in Figure A. 2, using Eq. 3.1, are summarised in Table 5-6, Section 5.1.4.

Linear trendline equations were fitted to the experimental current-voltage data and yielded R^2-values between 98.7% and 99.9% for all the ash samples. These high R^2-values are an indication of strong linear current-voltage relationships that, in effect, imply relatively constant resistivities across the range of voltages. Therefore, the effect of applied voltage on ash resistivity, if any, is small. This matter is further discussed in Section 5.1.4 and Appendix C-1.

APPENDIX A-2. ELECTROSTATIC PRECIPITATION

The following sections discuss some of the procedures followed during the ESP experiments and the processing of the data afterwards.

A-2.1. Screening experiments: Fractional factorial design

As explained in Section 3.3.1, the screening experiments were conducted according to a 2^{6-2} factorial design. The base '2' denotes that there are two levels (settings) for each factor, and '$6-2$' in the exponent indicates that there are six factors, two of which are determined from the product of the levels of the four main factors. In this case, plate spacing, electrode spacing, number of electrodes, and ash loading are the four main factors whose settings are used to determine the electrode geometry and type of ash used in the corresponding runs. This is shown in Table 3-2 and Table 3-3 in Section 3.3.1.

The settings for the screening runs are provided in Table A. 1, which shows the factor levels in brackets next to the actual settings. Furthermore, 'GS' denotes G-spike electrodes and 'TR' denotes threaded rod electrodes in Table A. 1.

Table A. 1. ESP settings for preliminary screening experiments

Run	Plate spacing (mm)	Electrode spacing (mm)	No. of electrodes	Ash loading ($mg.m^{-3}$)	Electrode geometry	Ash type
1	160 (**+1**)	80 (**+1**)	2 (**+1**)	3 (**+1**)	GS (**+1**)	A (**+1**)
2	400 (**−1**)	80 (**+1**)	2 (**+1**)	3 (**+1**)	TR (**−1**)	B (**−1**)
3	160 (**+1**)	175 (**−1**)	2 (**+1**)	3 (**+1**)	TR (**−1**)	B (**−1**)
4	400 (**−1**)	175 (**−1**)	2 (**+1**)	3 (**+1**)	GS (**+1**)	A (**+1**)
5	160 (**+1**)	80 (**+1**)	3 (**−1**)	3 (**+1**)	TR (**−1**)	A (**+1**)
6	400 (**−1**)	80 (**+1**)	3 (**−1**)	3 (**+1**)	GS (**+1**)	B (**−1**)
7	160 (**+1**)	175 (**−1**)	3 (**−1**)	3 (**+1**)	GS (**+1**)	B (**−1**)
8	400 (**−1**)	175 (**−1**)	3 (**−1**)	3 (**+1**)	TR (**−1**)	A (**+1**)
9	160 (**+1**)	80 (**+1**)	2 (**+1**)	18 (**−1**)	GS (**+1**)	B (**−1**)
10	400 (**−1**)	80 (**+1**)	2 (**+1**)	18 (**−1**)	TR (**−1**)	A (**+1**)
11	160 (**+1**)	175 (**−1**)	2 (**+1**)	18 (**−1**)	TR (**−1**)	A (**+1**)
12	400 (**−1**)	175 (**−1**)	2 (**+1**)	18 (**−1**)	GS (**+1**)	B (**−1**)
13	160 (**+1**)	80 (**+1**)	3 (**−1**)	18 (**−1**)	TR (**−1**)	B (**−1**)
14	400 (**−1**)	80 (**+1**)	3 (**−1**)	18 (**−1**)	GS (**+1**)	A (**+1**)
15	160 (**+1**)	175 (**−1**)	3 (**−1**)	18 (**−1**)	GS (**+1**)	A (**+1**)
16	400 (**−1**)	175 (**−1**)	3 (**−1**)	18 (**−1**)	TR (**−1**)	B (**−1**)

A-2.2. Arduino code for digital humidity and temperature (DHT) sensor

```
#include  <dht .h>
#include  <Time .h>
#include <DS1307RTC .h>

#define  dataPin 8
dht DHT;

void setup ( )
{
Serial .begin ( 9600 ) ;
}

void loop ( )
{
if (hour ( ) < 10) {
   Serial .print ( ' 0 ' ) ;
 }
Serial .print (hour ( ) ) ;
Serial .print ( ' : ' ) ;
if (minute ( ) < 10) {
   Serial .print ( ' 0 ' ) ;
 }
Serial .print (minute ( ) ) ;
Serial .print ( ' : ' ) ;
if (second ( ) < 10) {
   Serial .print ( ' 0 ' ) ;
 }
Serial .print (second ( ) ) ;
Serial .print ( ' , ' ) ;

int readData = DHT .read22 (dataPin) ;
float t  = DHT .temperature;
float h = DHT .humidity;

Serial .print ( t ) ;
Serial .print ( ' , ' ) ;
Serial. println ( h ) ;

delay (2000) ;
}
```

A-2.3. DustTrak measurements of particle concentration

The DustTrak monitors mentioned in Sections 3.3.2 and 3.3.3 generated sets of continuous particle concentration data for the air at the inlet and outlet of the ESP section. A typical DustTrak monitor with a specialised in-line sampling tube used for the ESP experiments in this study is shown in Figure A. 3.

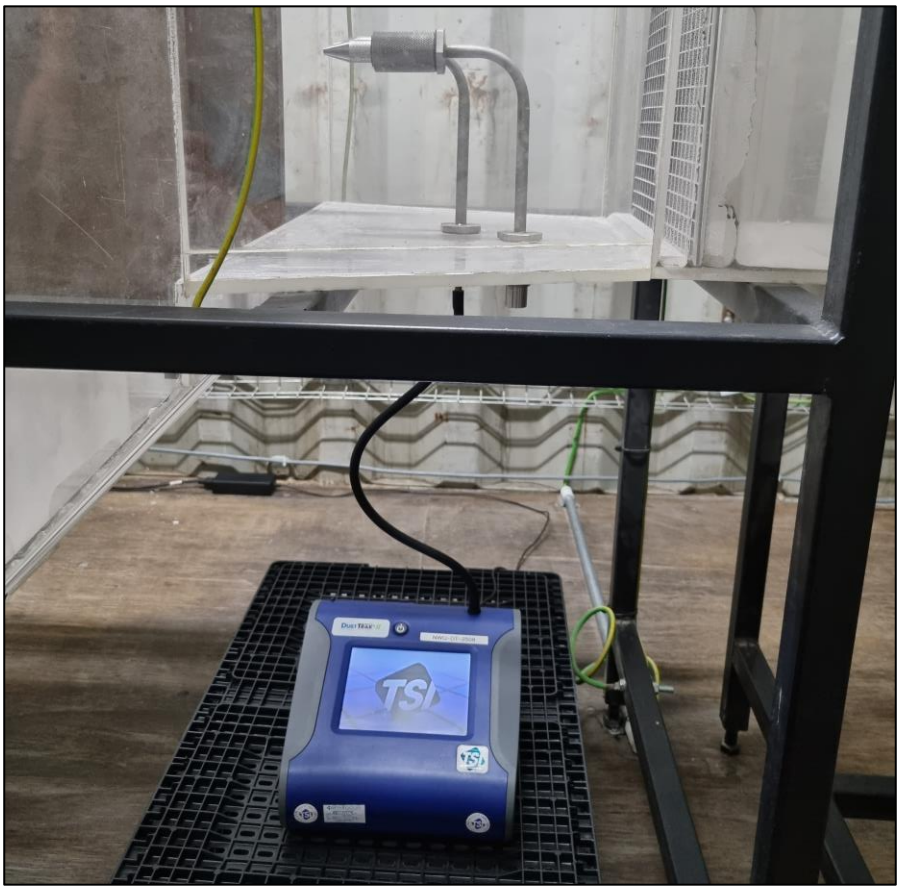

Figure A. 3. DustTrak monitor with specialised in-line sampling tube

The DustTrak concentration measurements were used to calculate the particle collection efficiencies for different ESP runs through the following relation:

$$\eta_{DT} = \frac{(n_{DT})_{in} - (n_{DT})_{out}}{(n_{DT})_{in}} \times 100\% \qquad \text{E A-6}$$

In Eq. A-6, η_{DT} is the particle collection efficiency calculated from DustTrak measurements [%], and $(n_{DT})_{in}$ and $(n_{DT})_{out}$ are the particle concentrations [mg.m^{-3}] measured by the DustTrak monitors at the ESP entrance and exit, respectively.

A-2.4. Gravimetric determination of particle concentration

As stated in Section 3.3.2, two thimbles with in-line sampling tubes were used to measure the total particle concentrations in the air upstream and downstream of the ESP section for each experimental run. Figure A. 4 shows the setup for the thimbles used in the ESP experiments.

Figure A. 4. Gravimetric thimble with specialised in-line sampling tube

The thimble measurements were conducted and processed on a gravimetric basis. The mass of each filter was determined before and after each ESP run, using an analytical-grade scale. The mass of the ash sampled on a filter during an experiment was then obtained from the difference between the final and initial filter masses, as demonstrated in Eq. A-7.

$$m_s = (m_f)_0 - (m_f)_i \qquad \text{E A-7}$$

where m_s is the total sample mass, $(m_f)_0$ is the filter mass after the ESP run, and $(m_f)_i$ is the filter mass before the ESP run [g]. Figure A. 5 shows the ash collected on the filters of the thimbles upstream (green) and downstream (purple) of the ESP section during an experimental run.

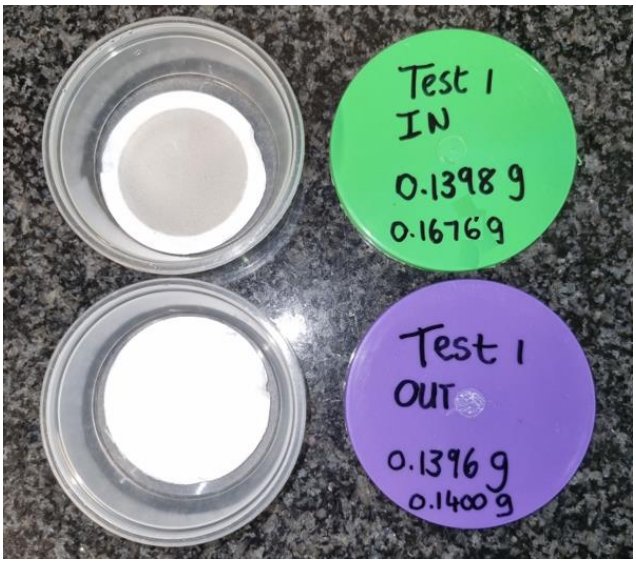

Figure A. 5. Glass-fibre filters with ash sampled from ESP channel

The sample mass was translated into the total mass of particulates across the ESP duct at the corresponding sampling point, using a volume ratio:

$$m_G = m_s \times \frac{V_T}{V_s} \qquad \text{E A-8}$$

where m_G is the total particle mass measured by a thimble and V_s is the volume of sampled particle-laden air [m^3], which was obtained from the volumetric sampling rate, as follows:

$$V_s = Q_s \times t_{Run} \qquad \text{E A-9}$$

In Eq. A-9, Q_s is the sampling flow rate [$m^3.s^{-1}$] and t_{Run} is the total time of the experimental run [s]. Similarly, V_T in Eq. A-8 is the total volume of particle-laden air across the ESP duct [m^3], defined as:

$$V_T = Q_T \times t_{Run} \qquad \text{E A-10}$$

In this case, Q_T is the total volume flow rate of particle-laden air in the ESP channel [$m^3.s^{-1}$], which was calculated, using Eq. A-11:

$$Q_T = A_{Duct} \times v_T \qquad \text{E A-11}$$

where A_{Duct} is the ESP duct cross-sectional area [m^2] and v_T is the average air-particle velocity at the point of sampling in the ESP channel [$m.s^{-1}$].

The total particulate mass, m_G from Eq. A-8 can be converted to the concentration of total particulates across the duct for a specific ESP run, using the following expression:

$$n_G = \frac{m_G}{V_T} \times 1000 \qquad \text{E A-12}$$

where n_G is the concentration of particulates measured by a gravimetric thimble [$mg.m^{-3}$].

The particle concentrations upstream and downstream of the ESP section were used to calculate the particle collection efficiencies for various ESP experiments gravimetrically, according to Eq. A-13:

$$\eta_G = \frac{(n_G)_{in} - (n_G)_{out}}{(n_G)_{in}} \times 100\% \qquad \text{E A-13}$$

For this equation, η_G is the particle collection efficiency computed with thimble data [%], while $(n_G)_{in}$ and $(n_G)_{out}$ are the particle concentrations [$mg.m^{-3}$] measured by the thimbles upstream and downstream of the ESP section, respectively. These efficiency values were compared with that of the DustTrak monitors (η_{DT} in Eq. A-6) as reference.

A-2.5. RSM first-order regression

The set of data generated through the screening experiments listed in Table A. 1 from Appendix A-2.1 was used to derive a first-order RSM model, according to Eq. 4.1 and the procedure discussed in Section 4.1. Figure A. 6 illustrates the regression plot for the first-order RSM model used in the screening process of the ESP experiments.

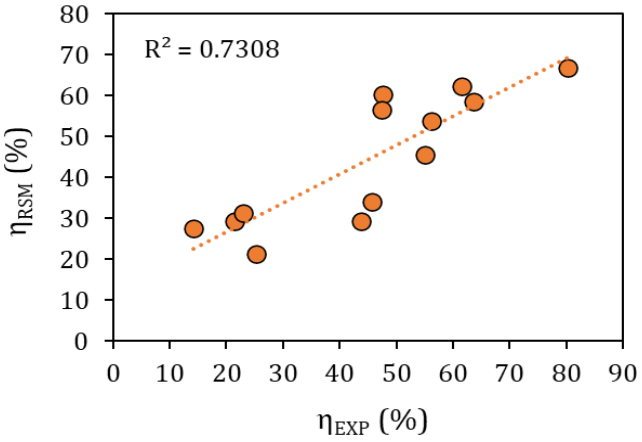

Figure A. 6. Regression plot for first-order RSM model

The resulting RSM models in Eq. 4.2 and Eq. 4.3 for ash A and B were used to select the most important variables in the subsequent central composite design (CCD) experiments. This procedure is explained in more detail in Section 4.1.

A-2.6. Setup of CCD plan

The actual ESP experiments were conducted according to a central composite design (CCD) methodology. This experimental design technique minimised the number of experimental runs required to generate useful data from a large set of interrelated variables. More information on the CCD plan followed for the ESP experiments in this study is provided in Section 3.3.1.

The CCD plan was developed with the use of the Minitab statistical software. This was achieved by using the Design of Experiments (DOE) function on the Statistics (Stat) tab. The DOE function provides several options for experimental design methodologies, including screening designs, factorial designs, Response Surface designs, Taguchi designs, or a mixture of the different designs. In this case, the Response Surface design was used by selecting the "Create Response Surface Design" option in Minitab.

The Response Surface method further distinguishes two types of designs: the central composite design, which suits experiments with 2 – 10 continuous factors, and the Box-Behnken design, which applies to cases where 3, 4, 5, 6, 7, 9, or 10 continuous factors are involved. The central composite design option was selected for the ESP experiments in this study. Four continuous factors were specified, which include the collection plate spacing, discharge electrode spacing, fly ash loading, and number of electrodes. These variables all have large numbers of possible settings, hence their classification as continuous factors. The type of ash, on the other hand, was defined as a categorical factor with four discrete settings: -75 µm ash A, -75 µm ash B, -150+75 µm ash A, and -150+75 µm ash B. This is summarised in Table A. 2.

Table A. 2. Classification of variables for central composite design of experiments

Blocks	Continuous factors				Categorical factor
	Plate spacing (mm)	Electrode spacing (mm)	Ash loading ($mg.m^{-3}$)	No. of electrodes	Type of ash
G-spike	100 – 400	57 – 164	3 – 35	1 – 6	✶-75 µm A ✶-75 µm B ✶-150+75 µm A ✶-150+75 µm B
Sawtooth	100 – 280	57 – 164	3 – 35	1 – 6	✶-75 µm A ✶-75 µm B ✶-150+75 µm A ✶-150+75 µm B
Threaded rod	100 – 280	112 – 175	3 – 35	1 – 3	✶-75 µm A ✶-75 µm B ✶-150+75 µm A ✶-150+75 µm B

As seen in Table A. 2, the settings for the G-spike, sawtooth, and threaded rod electrodes are different. Even though a large number of settings are possible for the different ESP variables, there are some limitations to the settings for the various electrode geometries.

These include structural limitations, such as a limited number of electrodes and sufficient electrode spacing that are required for the G-spikes, due to the large size of this electrode geometry. Another limiting factor is the electrostatic properties of the electrodes. While a G-spike electrode is able to generate a strong electric field, this is not the case for sawtooth and threaded rod electrodes. When spaced too far apart, the sawtooth and threaded rod electrodes produce electric fields that are too small for a stable voltage reading to be obtained on the high-voltage power unit. Therefore, these electrodes cannot be used in isolation or with electrode spacings larger than 164 mm.

Due to the variability in the properties of the different electrodes, it was considered more practical to perform the experiments separately for the G-spike, sawtooth, and threaded rod geometries and classify them as block variables. Table A. 3 shows the complete list of ESP experiments obtained from the CCD model in Minitab.

Table A. 3. ESP experiments from central composite design approach

Run	Electrode geometry	Plate spacing (mm)	Electrode spacing (mm)	Ash loading ($mg.m^{-3}$)	No. of electrodes	Ash type (µm)
1	Sawtooth	220	164	5	3	-75 B
2	Sawtooth	220	101	50	3	-75 B
3	Sawtooth	220	57	21	3	-75 A
4	Sawtooth	220	101	6	3	-75 A
5	Sawtooth	220	101	20	4	-75 A

6	Sawtooth	220	57	20	3	-75 B
7	Sawtooth	220	101	20	3	-75 B
8	Sawtooth	220	164	7	3	-150+75 A
9	Sawtooth	280	101	18	3	-75 B
10	Sawtooth	220	101	29	3	-75 A
11	Sawtooth	220	101	14	3	-75 B
12	Sawtooth	220	101	13	3	-75 A
13	Sawtooth	220	101	13	2	-75 B
14	Sawtooth	280	101	26	3	-75 A
15	Sawtooth	280	57	12	4	-75 A
16	Sawtooth	220	101	3	3	-150+75 B
17	Sawtooth	160	101	13	3	-75 A
18	Sawtooth	220	101	13	2	-75 A
19	Sawtooth	160	101	10	3	-150+75 A
20	Sawtooth	220	101	13	4	-75 B
21	Threaded	280	164	21	3	-75 A
22	Threaded	280	164	3	2	-150+75 B
23	Threaded	160	164	17	2	-75 B
24	Threaded	280	57	20	2	-75 B
25	Threaded	220	101	14	3	-75 B
26	Threaded	160	57	20	6	-75 B
27	Threaded	280	164	23	2	-75 B
28	Threaded	280	57	5	4	-75 A
29	Threaded	280	164	3	2	-150+75 A
30	Threaded	160	57	23	4	-75 A
31	Threaded	280	57	3	4	-75 B
32	Threaded	160	112	4	2	-75 B
33	Threaded	220	101	9	3	-150+75 B
34	Threaded	160	164	23	2	-75 A
35	Threaded	220	101	13	3	-75 A
36	Threaded	220	101	9	4	-75 A
37	Threaded	160	164	4	3	-75 A
38	Threaded	280	57	13	2	-150+75 A
39	Threaded	160	57	5	2	-75 A
40	Threaded	160	164	4	3	-75 B
41	G-spike	160	N/A	29	1	-75 A
42	G-spike	160	112	3	3	-75 A
43	G-spike	400	175	3	3	-150+75 B

44	G-spike	280	144	13	2	-75 B
45	G-spike	160	175	21	3	-75 B
46	G-spike	280	144	13	2	-75 A
47	G-spike	400	N/A	22	1	-75 B
48	G-spike	280	144	9	2	-150+75 B
49	G-spike	160	175	31	3	-75 A
50	G-spike	400	N/A	24	1	-75 A
51	G-spike	280	144	11	3	-75 A
52	G-spike	400	112	22	3	-75 B
53	G-spike	400	N/A	3	1	-150+75 A
54	G-spike	400	N/A	6	1	-75 B
55	G-spike	160	N/A	5	1	-75 A
56	G-spike	160	112	3.8	3	-75 B
57	G-spike	160	N/A	3	1	-75 B
58	G-spike	400	112	25	3	-75 A
59	G-spike	400	175	5	3	-75 A
60	G-spike	160	N/A	26	1	-75 B

A-2.7. Second-order RSM model

The experimental data obtained from the CCD experiments in Appendix A-2.6 were used to compute model coefficients for the second-order RSM model. The ESP settings and measured particle collection efficiencies for the runs in Table A. 3 were imported to a Minitab spreadsheet. The actual specifications for the factor settings (as listed in Table A. 3) were converted to comparable coded values, using the *Standardize* function in Minitab. This function computes the mean value of a factor's settings, subtracts this value from the corresponding setting value for each run, and divides the result by the standard deviation of the range of settings. The outcome is a set of normalised values that represent the respective settings of a specific ESP variable (factor) in the different experimental runs.

The normalised settings and collection efficiencies for the various ESP runs were subsequently used to calculate the RSM model coefficients. This was achieved by selecting the "Analyze Response Surface Design" option under DOE in Minitab and specifying the particle collection efficiency as the response variable (assigning the response variable to the collection efficiency column in the spreadsheet). The Minitab software automatically generates a list of model coefficients for the respective terms in the quadratic RSM model equation, as well as an ANOVA table, Pareto chart, normal probability plot, residual plots, contour plots, and surface plots.

Figure A. 7 shows an example of the contour (a) and surface (b) plots generated in Minitab for collection efficiency as a function of plate and electrode spacings in the ESP.

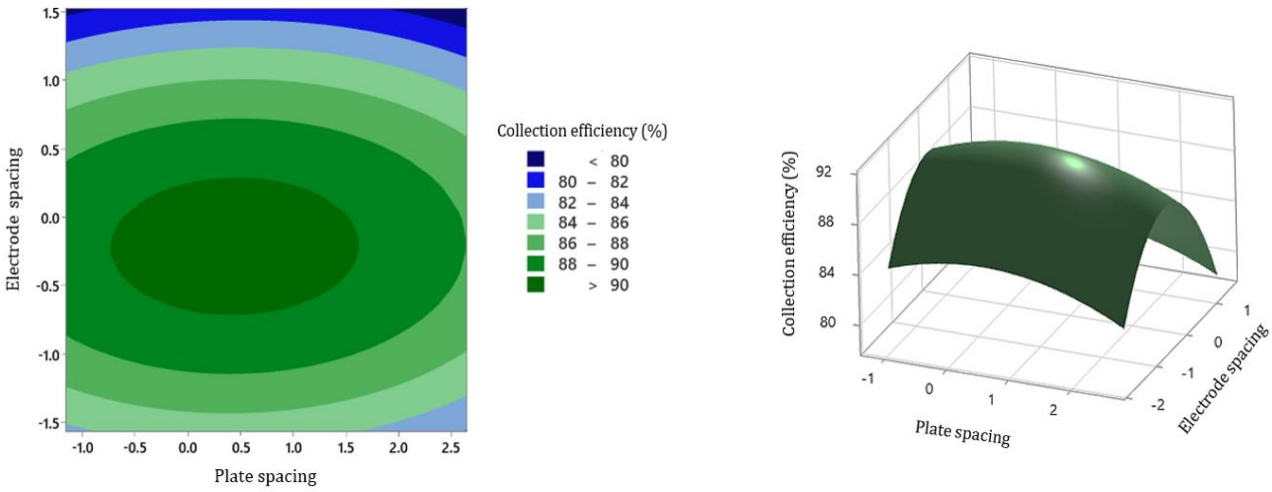

(a) **(b)**

Figure A. 7. Contour plot **(a)** and surface plot **(b)** for collection efficiency, plate spacing, and electrode spacing

Figure A. 8 shows the normal probability and residual plots given by Minitab for the ESP data imported to the CCD-RSM model.

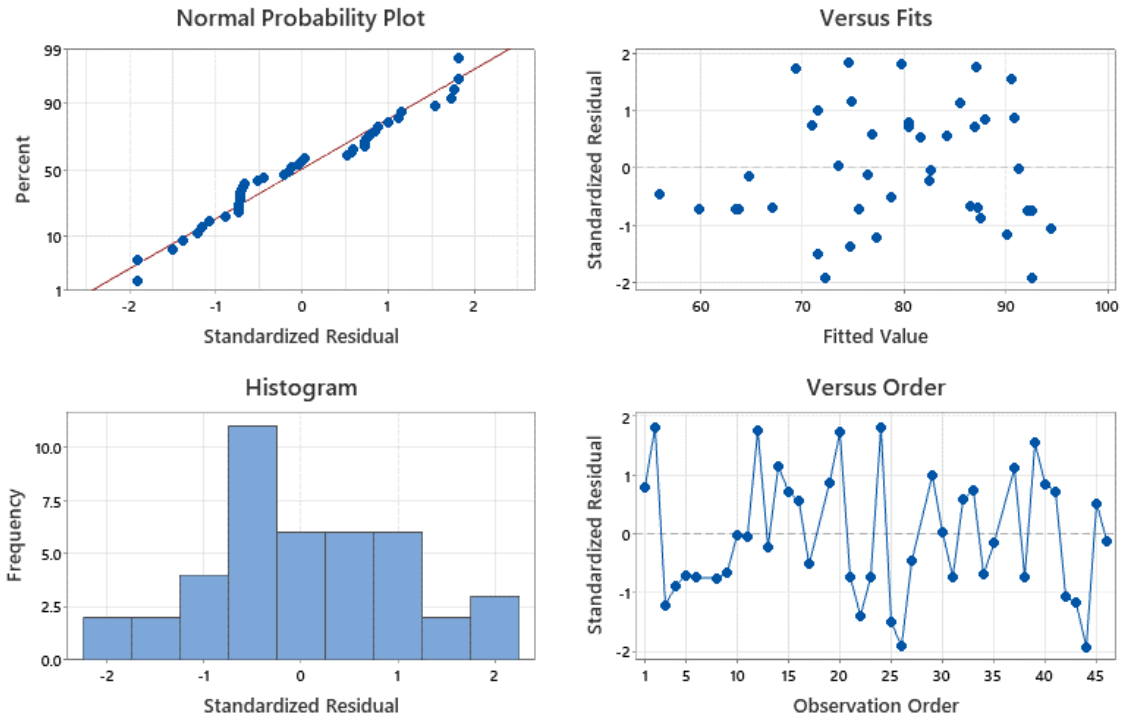

Figure A. 8. Normal probability and residual plots for ESP factors in RSM model

These plots present various methods of analysing the information from the RSM model. In this study, the Pareto chart (Figure 5-4) and ANOVA results (Table 5-9) were used to investigate the RSM model, which is discussed in Section 5.2.1.

The RSM coefficients and model outputs (computed efficiencies) were exported to Excel and replicated according to the model equation (Eq. 4.4) in Section 4.1. This yielded the model results from Section 5.2 and Appendix C-2.

A-2.8. Repeatability

Some of the ESP runs in Table A. 3 were performed two times to investigate the repeatability of the experiments. The run settings and numbers are provided in Table A. 4.

Table A. 4. ESP settings for repeated experimental runs

Run	Electrode geometry	Plate spacing (mm)	Electrode spacing (mm)	Ash loading ($mg.m^{-3}$)	No. of electrodes	Ash type (µm)
11	Sawtooth	220	101	15	3	-75 B
12	Sawtooth	220	101	10	3	-75 A
25	Threaded	220	101	13	3	-75 B
35	Threaded	220	101	13	3	-75 A
44	G-spike	280	144	17	2	-75 B
46	G-spike	280	144	10	2	-75 A

The results from the original and repeated runs with sawtooth electrodes are illustrated in Figure A. 9.

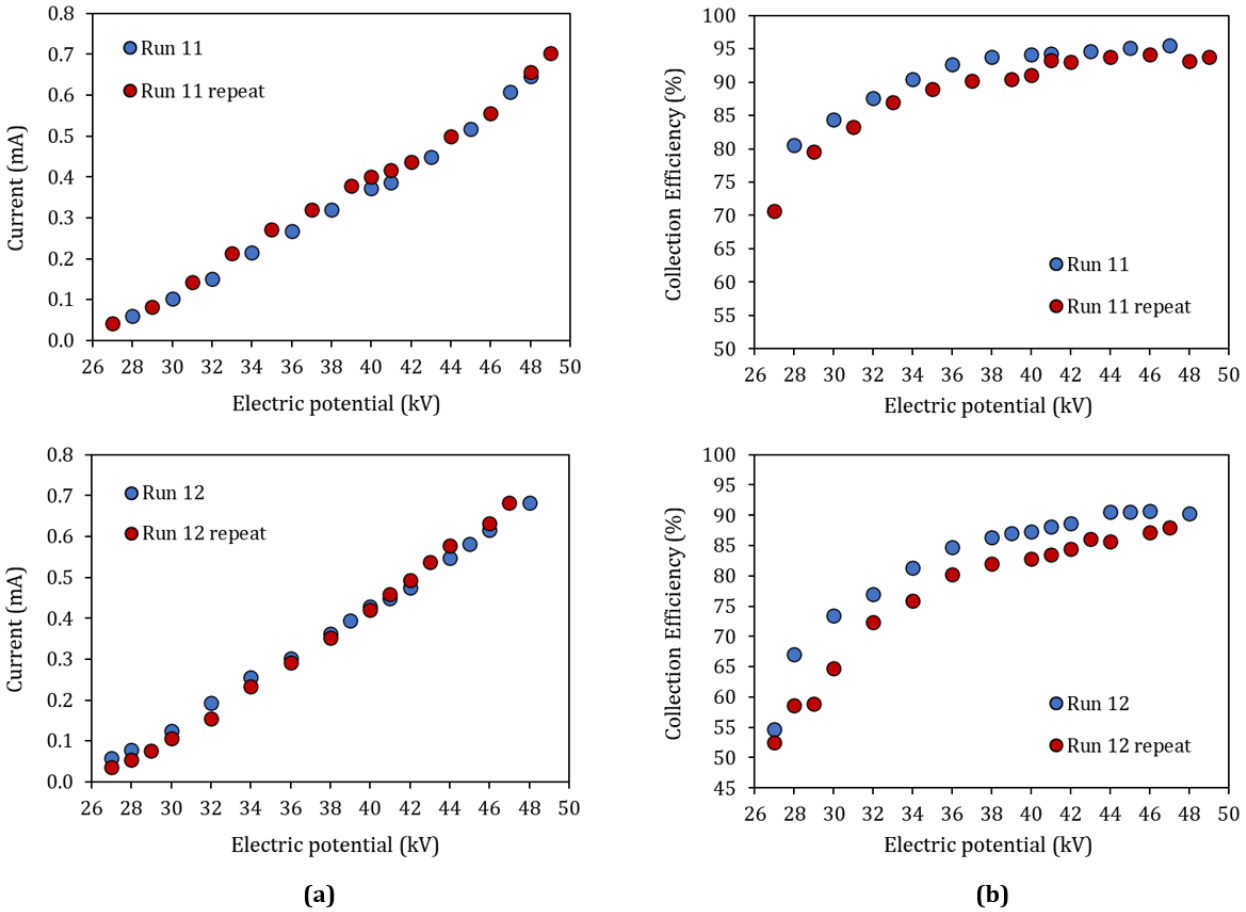

Figure A. 9. Comparison of current **(a)** and collection efficiency **(b)** as functions of applied voltage for identical ESP runs with sawtooth electrodes

The current-voltage data in Figure A. 9 (a) show an excellent correlation between the original and repeated runs, which indicates a high degree of stability for the multimeter current measurements with sawtooth electrode configurations. The collection efficiency data from the DustTrak monitors in Figure A. 9 (b) also demonstrate consistent results for the original and repeated runs. In both cases, the collection efficiencies

differ by less than 5% for the two repeated runs. Therefore, the data from the ESP experiments are repeatable for ESP configurations with sawtooth electrodes.

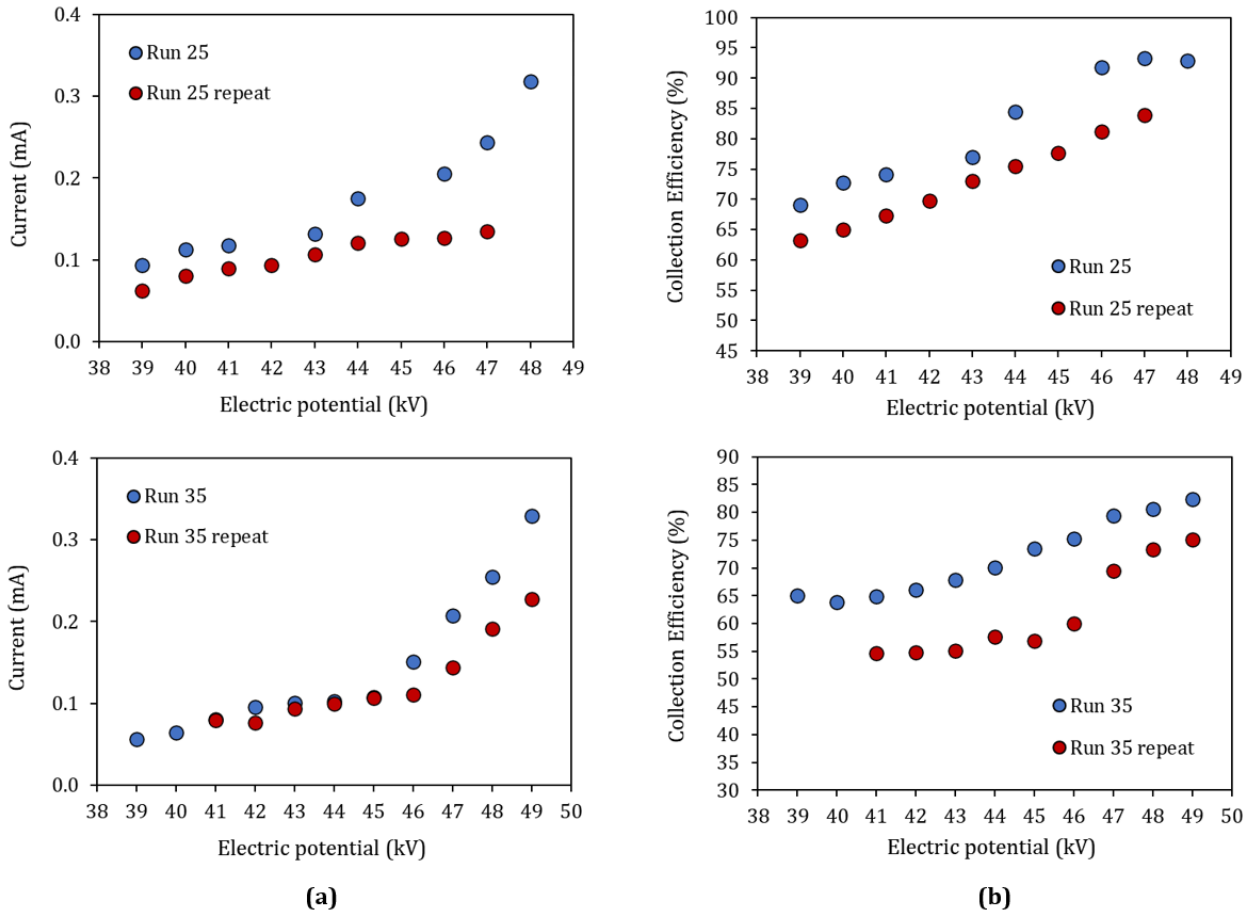

Figure A. 10. Comparison of current **(a)** and collection efficiency **(b)** as functions of applied voltage for identical ESP runs with threaded rod electrodes

Figure A. 10 shows the current-voltage and collection efficiency plots for the original and repeated experiments of two threaded rod electrode configurations. The current-voltage measurements in Figure A. 10 (a) show larger deviations between the original and repeated runs for threaded rods than that of sawtooth electrodes. In this case, the current readings differ by 19 – 45% for the two repeats of run 25 and by 0.7 – 31% for the two repeats of run 35. Therefore, the current readings are less stable for the threaded rod electrodes than for the sawtooth electrodes. This could be attributed to the weaker comparative electric fields of threaded rod electrodes, resulting in smaller current densities that are harder to detect by the multimeter. The smaller field intensities could also result in variable instantaneous currents across the electrodes themselves, which would then contribute to the unstable current readings from the multimeter.

The collection efficiency measurements in Figure A. 10 (b) also show a notable degree of variation between the original and repeated runs for threaded rods, yet to a smaller degree than the current readings. This is due to the larger scale of the particulate concentration readings, which have a lower associated sensitivity toward the measuring instrument accuracy, compared to the current readings. The efficiency values differ by 5 – 12% for the two repeats of run 25 and by 8 – 23% for the two repeats of run 35. This could partly be related to the unstable current densities generated by the threaded rod electrodes. Additional factors, such

as variable air velocities, uneven particle-air flow distributions, and inconsistent fly ash loadings could also be the cause of differences between the collection efficiencies of the original and repeated runs.

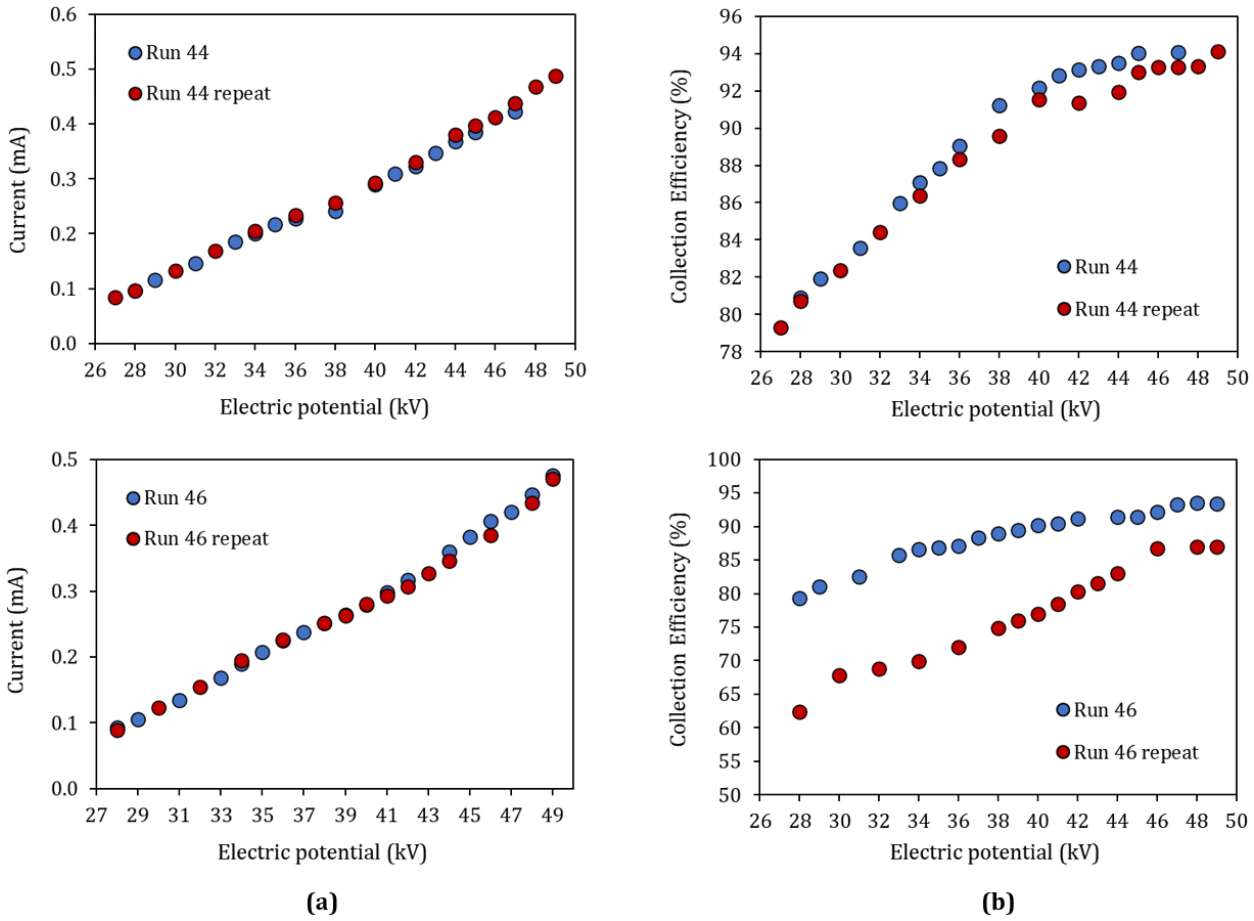

Figure A. 11. Comparison of current **(a)** and collection efficiency **(b)** as functions of applied voltage for identical ESP runs with G-spike electrodes

The current-voltage and collection efficiency plots for the original and repeat experiments with G-spike electrodes are provided in Figure A. 11. As in the case of sawtooth electrodes (even more so), the current-voltage plots in Figure A. 11 (a) for G-spike electrodes are almost identical for the two repeats of runs 44 and 46. Therefore, the multimeter readings show a high consistency for the G-spike geometry, which is known for its ability to produce high current densities. The large current discharge generated by the G-spike electrodes could have facilitated the excellent reproducibility of the current-voltage results.

The collection efficiency data for run 44 in Figure A. 11 (b) differ by less than 3% for the original and repeated runs. The efficiencies of the two repeats for run 46, however, differ by as much as 25%. This could be due to a defect in the outlet DustTrak monitor, resulting in higher than actual outlet particle concentration readings and lower corresponding collection efficiencies. Alternatively, the efficiencies measured during the repeat of run 46 could be lower, due to the smaller ash loading achieved in this run (10 $mg.m^{-3}$) than in the original run (13 $mg.m^{-3}$). As stated in Section 5.2.4, smaller ash feeds deliver lower collection efficiencies. This unanticipated lower ash loading could have resulted from fluctuations in the air velocity or the dust feeder injection rate. Nevertheless, this is not representative of the typical G-spike experimental results. Overall, the ESP runs show good repeatability for G-spike electrode configurations.

APPENDIX B : MODELLING PROCEDURES

Appendix B gives information relevant to Chapter 4.

APPENDIX B-1. CFD MODELLING

Table B. 1 lists the properties of the different types of boundaries used for the ESP domain in this study.

Table B. 1. Properties of boundary types

Boundary type	Properties
Velocity Inlet	Inlet where continuous and discreet phases enter solution domain Defines gas flow rate in terms of velocity Specify turbulence intensity and length scale
Pressure Outlet	Outlet where continuous and discreet phases exit solution domain Specify gauge pressure at boundary
Wall	Represents surface that interacts with continuous and discreet phases Specify slip or no-slip for shear force at wall surface Specify smooth or rough surface for no-slip condition
Symmetry Plane	Represents imaginary surface in solution domain Excluded from solution domain during computations

The boundaries specified for various ESP regions served different specialised purposes in the CFD model discussed in Section 4.2.

B-1.1. Mesh independence studies

Mesh independence studies were performed to test the quality of the generated meshes for each ESP setup used for the CFD model. A typical ESP configuration of three sawtooth electrodes is used as an example to explain the methodology followed in a mesh independence study. The properties and dimensions of the geometry used for this reference-case ESP setup are given in Table B. 2. Additional dimensions for the sawtooth electrode geometry are given in Appendix B-2 (Table B. 6 and Figure B. 6).

Table B. 2. Properties of base-case mesh independence geometry

Property	Specification
Electrode shape	Sawtooth
Number of electrodes	3
Electrode spacing	101 mm
Domain length	755 mm
Domain width	160 mm
Domain height	377 mm

The ESP geometry was discretised into four meshes with different degrees of coarseness, using the Polyhedral, Prism Layer, and Surface Remesher models in STAR-CCM+. A universal base size of 20 mm

was used for the cells in all of the meshes. As indicated in Figure B. 1, volumetric controls in the shapes of blocks around the electrode assembly (a) and individual electrodes (b) were used to refine the mesh near the electrode surfaces.

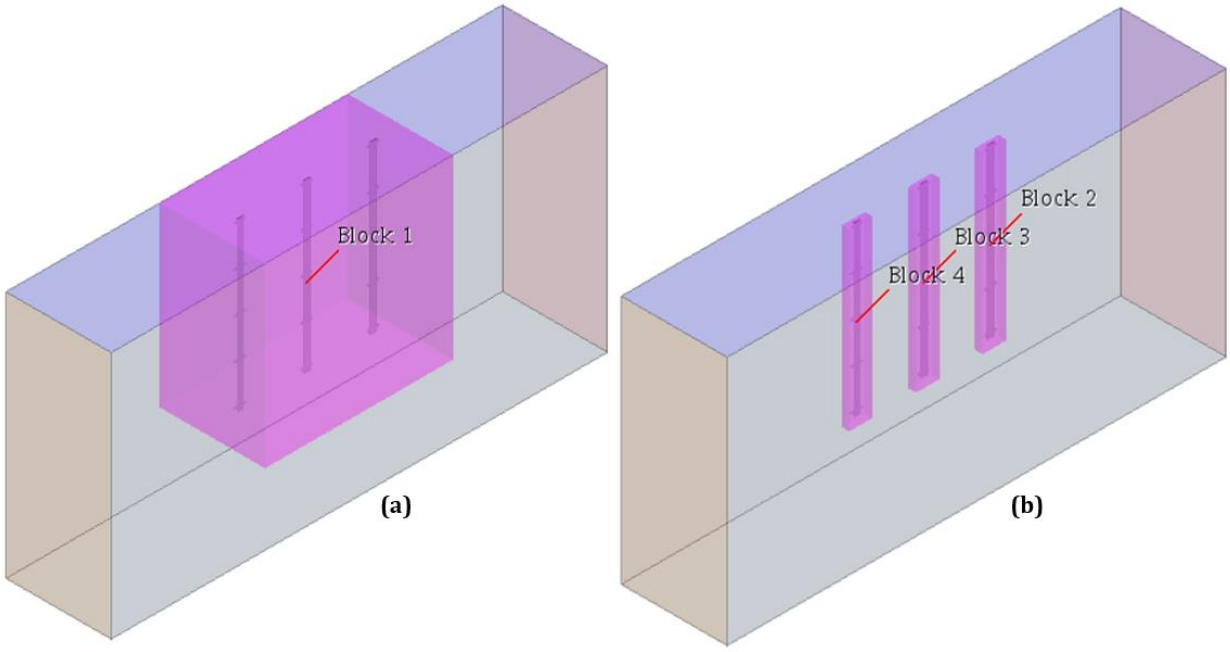

Figure B. 1. Volumetric control blocks used for mesh refinement around (a) electrode assembly and (b) individual electrodes

The base cell sizes of the block variables in Figure B. 1 for Mesh 1 – 4 are summarised in Table B. 3.

Table B. 3. Base cell sizes of volumetric controls for Mesh 1 to 4

Mesh number	Number of cells	Base size			
		Block 1	Block 2	Block 3	Block 4
1	405 170	12 mm	6 mm	6 mm	6 mm
2	939 317	8 mm	1.5 mm	1.5 mm	1.5 mm
3	1 646 627	8 mm	2 mm	2 mm	2 mm
4	1 966 844	5 mm	1 mm	1 mm	1 mm

Additional refinement was performed for the various meshes by specifying custom boundary mesh conditions for the electrode region in STAR-CCM+. The different mesh values are listed in Table B. 4.

Table B. 4. Electrode boundary mesh conditions for Mesh 1 to 4

Mesh number	Custom boundary mesh conditions				
	Number of prism layers	Prism layer stretching	Prism layer thickness	Min surface size	Max surface size
1	8	1.2	1.0 mm	0.01 mm	1.0 mm
2	8	1.4	1.0 mm	0.01 mm	0.8 mm
3	8	1.5	0.8 mm	0.005 mm	0.6 mm
4	8	1.5	0.8 mm	0.005 mm	0.6 mm

The resulting meshes, from coarsest to finest (1 to 4), comprised 405 170, 939 317, 1 646 627, and 1 966 844 cells (see Table B. 3). Figure B. 2 shows the coarsest mesh (405 170 cells) in (a) and the finest mesh (1 966 844 cells) in (b) for the ESP base-case geometry. The fine mesh presents a more organized arrangement of cells with an increasing level of precision toward the electrode surfaces. On the contrary, the cells in the coarse mesh have random shapes, sizes, and positions and the fine mesh near the electrodes meets a less gradual end than that in Figure B. 2 (b).

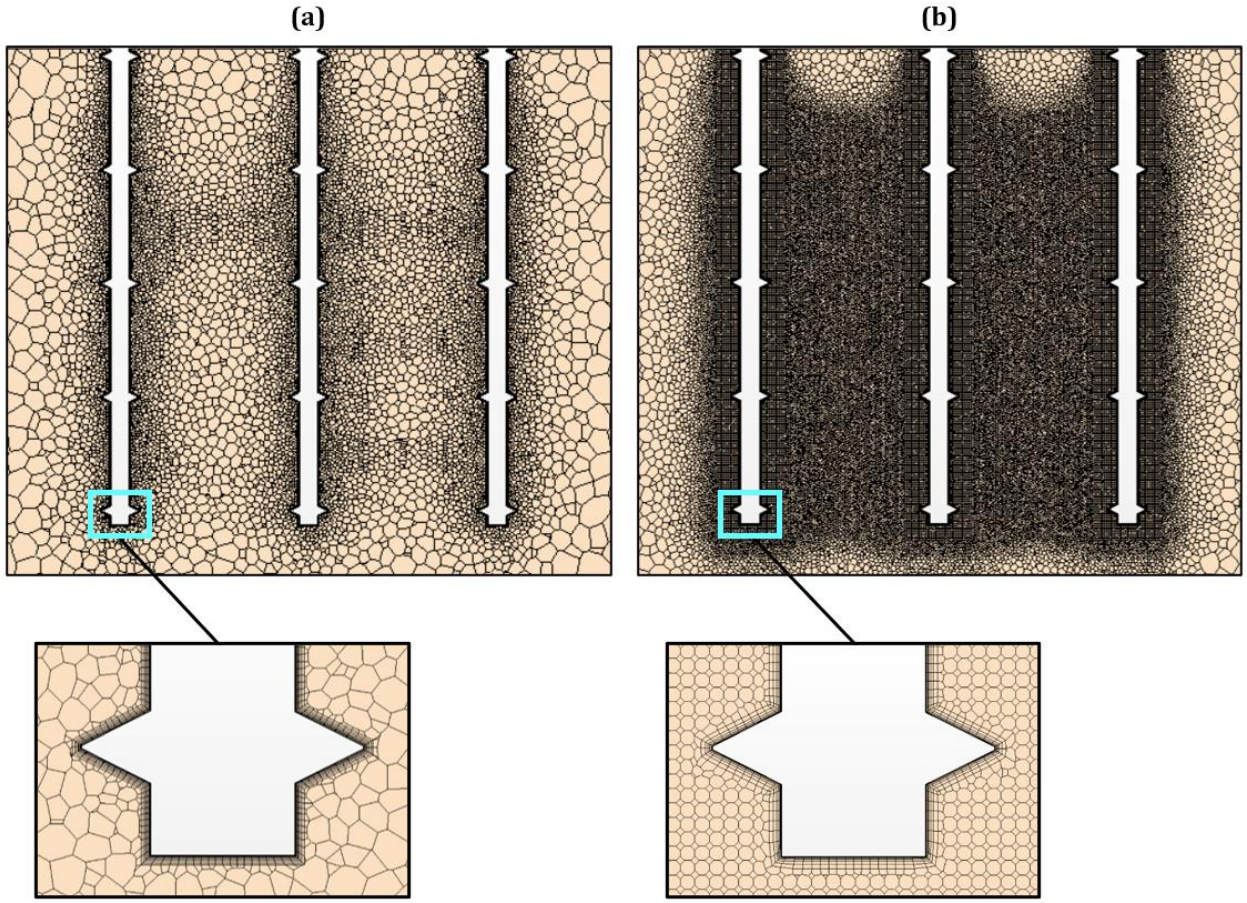

Figure B. 2. Sawtooth electrodes in the ESP base-case geometry discretised into (a) a coarse mesh of 405 170 cells and (b) a fine mesh of 1 966 844 cells

The air flow, electrostatics, and particle dynamics were simulated according to the modelling procedure discussed in Section 4.2, and applied to each of the four meshes. The collection efficiencies and average electric field intensities across the three sawtooth electrodes were calculated with the model for the different sized meshes. The results are illustrated in Figure B. 3.

The plots in Figure B. 3 show no significant changes in electric field intensity and collection efficiency between the meshes that comprise 1 646 627 and 1 966 844 cells. Therefore, the 1 646 627-cell mesh is equally effective in producing accurate model results as the 1 966 844-cell mesh, and so, 1 646 627 cells were used in the mesh for this particular ESP setup.

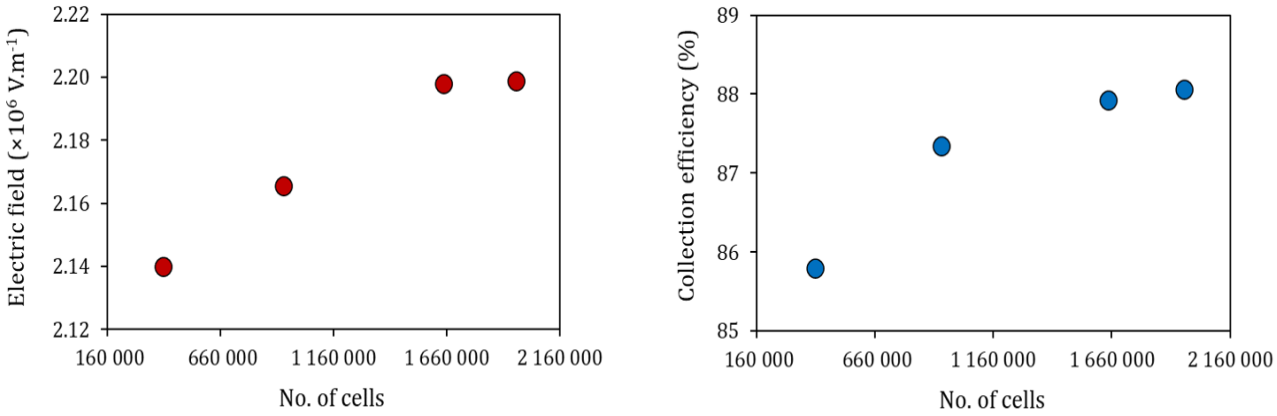

(a) **(b)**

Figure B. 3. Results for base-case mesh independence study to evaluate the effect of mesh quality on (a) the electric field and (b) the collection efficiency in the ESP

The electric field in Figure B. 3 shows a stronger dependence on the number of cells in the mesh compared to the particle collection efficiency. Therefore, the field distribution was further examined to test for mesh independence. A 3000 resolution line probe was applied from the inlet to the outlet of the ESP domain, across the spikes of the three sawtooth electrodes. The electric field distribution along the line probe was computed with the CFD model for the four different sized meshes. The field distribution plots along the probe length for each mesh is shown in Figure B. 4.

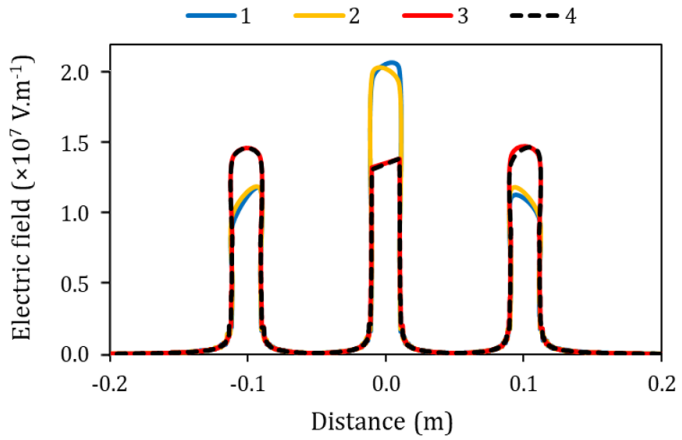

Mesh number	Number of cells
1	405 170
2	939 317
3	1 646 627
4	1 966 844

Figure B. 4. Electric field across three sawtooth electrodes in the base-case ESP geometry for the four different-sized meshes

From the red and dotted black plots in Figure B. 4, it is clear that the electric field exhibits no change for a 320 217 additional number of cells more than 1 646 627. This confirms that 1 646 627 cells are sufficient to obtain accurate model predictions of the electric field distribution in the ESP with this specific configuration. The same steps executed to test for mesh independence in this example were followed for the other ESP geometries used in the CFD model. In each case, the mesh with the fewest possible number of cells that delivered consistent model results was selected, since a higher cell count drastically increases the computation time – especially for complex models.

B-1.2. Model input parameters

Table B. 5 summarises the model parameters used for the ESP system in this study, compared to that of Arif *et al.* (2018) in [15]. The two studies used similar specifications for the model input parameters.

Table B. 5. CFD model input parameters for the ESP from this study compared to [15]

Model Parameter	**Value (This study)**	**Arif *et al.* (2018)**
Inlet air velocity	0.86 $m.s^{-1}$	1 – 2 $m.s^{-1}$
Inlet turbulence intensity	~ 5%	5%
Inlet turbulent length-scale	~ 15.7 mm	-
Temperature	290 – 310 K	293 K
Pressure	86 – 88 kPa	101.3 kPa
Air density	0.97 – 1.10 $kg.m^{-3}$	1.23 $kg.m^{-3}$
Air dynamic viscosity	(18 – 19) $\times 10^{-6}$ Pa.s	18×10^{-6} Pa.s
Air permittivity	8.85×10^{-12} $F.m^{-1}$	8.85×10^{-12} $F.m^{-1}$
Ion mobility	$\sim 2 \times 10^{-4}$ $m^2.(Vs)^{-1}$	2.6×10^{-4} $m^2.(Vs)^{-1}$
Relative particle permittivity	1.7 – 2.0	2.5
Particle density	2124 – 2222 $kg.m^{-3}$	2000 $kg.m^{-3}$
Fly ash loading	3 – 30 $mg.Nm^{-3}$	1.66×10^{-5} $kg.s^{-1}$
Particle size distribution	Rosin-Rammler	Log-normal

B-1.3.Model convergence

The CFD simulations were allowed to run until the model had reached convergence for the continuity, momentum, turbulence, and electric potential solver functions in STAR-CCM+. The condition of convergence was identified by a minimal change in the residuals with additional iterations for all of the abovementioned fields in the CFD model. For the continuity equation, the convergence criterion was a resolution of 10^{-5} in the residuals. The momentum and turbulence models were considered to have converged when the residuals had reached a 10^{-4} resolution. Finally, a resolution of 10^{-10} in the residuals was used as the condition of convergence for the electrostatic potential model solver. In the cases where a Lagrangian solver was included in the CFD model for the particulate phase dynamics, the simulation was continued up to the first two iterations after the latest set of sub-steps.

Depending on the complexity of the model – which varied for the different types of electrodes, ESP conditions, and in the absence or presence of fly ash and/or an electrostatic field – the model converged within 1 – 5 minutes after an input change was introduced. The solution time was also determined by the size of the input change and the type of parameter that was altered. A 1 kV change in potential would, for example, have a shorter solution time than a 10 kV change in potential. Alternatively, the model would have a much longer convergence time to adapt a change in the air inlet velocity or applied voltage, compared to a change in particle diameter, for instance. Nonetheless, the solution times were sufficiently short in all cases to implement the necessary iterative adjustments and reach a desirable outcome with the CFD model.

APPENDIX B-2. ESP GEOMETRIES

The computational domain used for the CFD simulations was the negative space between the collection plates and discharge electrodes in the ESP. This was obtained by subtracting the discharge electrode assembly geometries from a solid block with the collection plate dimensions (see Figure B. 5), using the *Assembly Cut* function in NX-12.

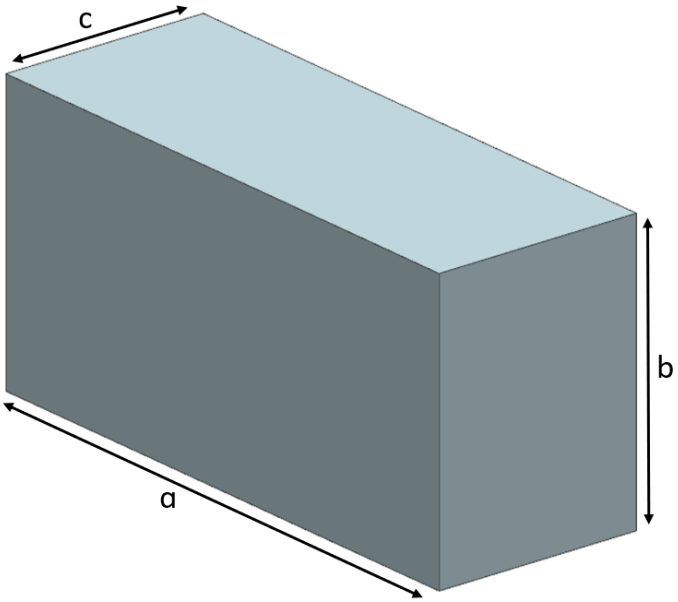

Figure B. 5. Negative space between collection plates

The labels **a**, **b**, and **c** in Figure B. 5 denote the horizontal and vertical lengths, and the distance between the collection plates in [mm], respectively.

The discharge electrode geometries used for the ESP experiments and modelling in this study include sawtooth, G-spike, and threaded rod electrodes. The dimensions for the sawtooth electrode design are listed in Table B. 6.

Table B. 6. Properties of sawtooth electrode geometry

Property	**Specification**
Electrode shape	Sawtooth
Number of spikes	14
Electrode length	380 mm
Electrode width (body)	10 mm
Electrode thickness	1 mm
Spike length	5 mm
Spike width	5 mm
Spike spacing	56 mm

The sawtooth electrode geometry dimensions in Table B. 6 are visually presented in Figure B. 6.

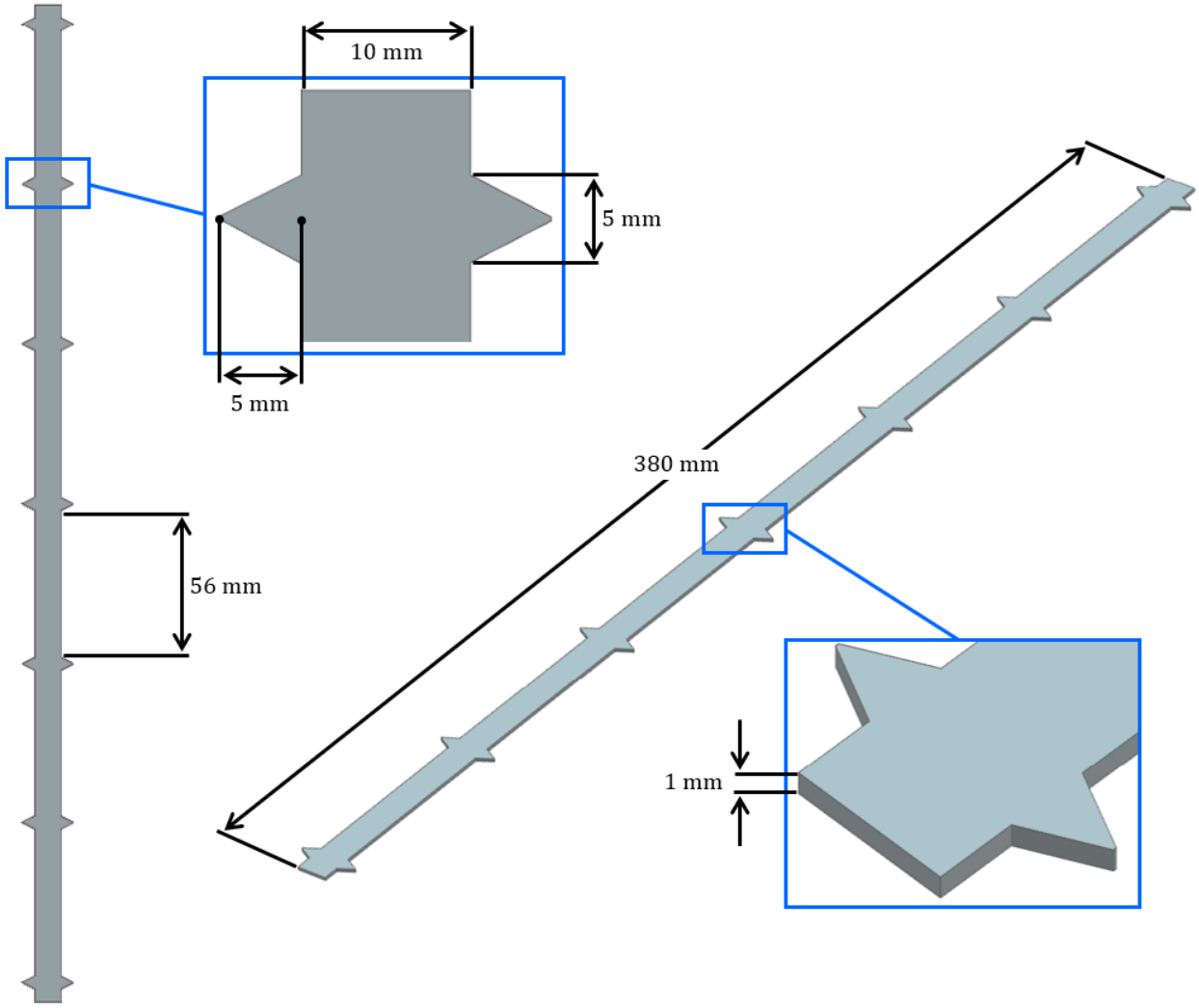

Figure B. 6. Dimensions for sawtooth electrode geometry

The G-spike electrode geometry dimensions are summarised in Table B. 7.

Table B. 7. Properties of G-spike electrode geometry

Property	Specification
Electrode shape	G-spike
Number of spike assemblies	3 or 4
Number of spikes	32 or 24
Electrode length	400 mm
Shaft outside diameter	25 mm
Shaft inside diameter	23 mm
Spike length	20 or 21 mm
Spike width	5.5 mm
Blade height	30 mm
Blade thickness	1 mm
Spike assembly spacing	70.4 mm

The dimensions given in Table B. 7 for a G-spike electrode with four spike assemblies are illustrated in Figure B. 7.

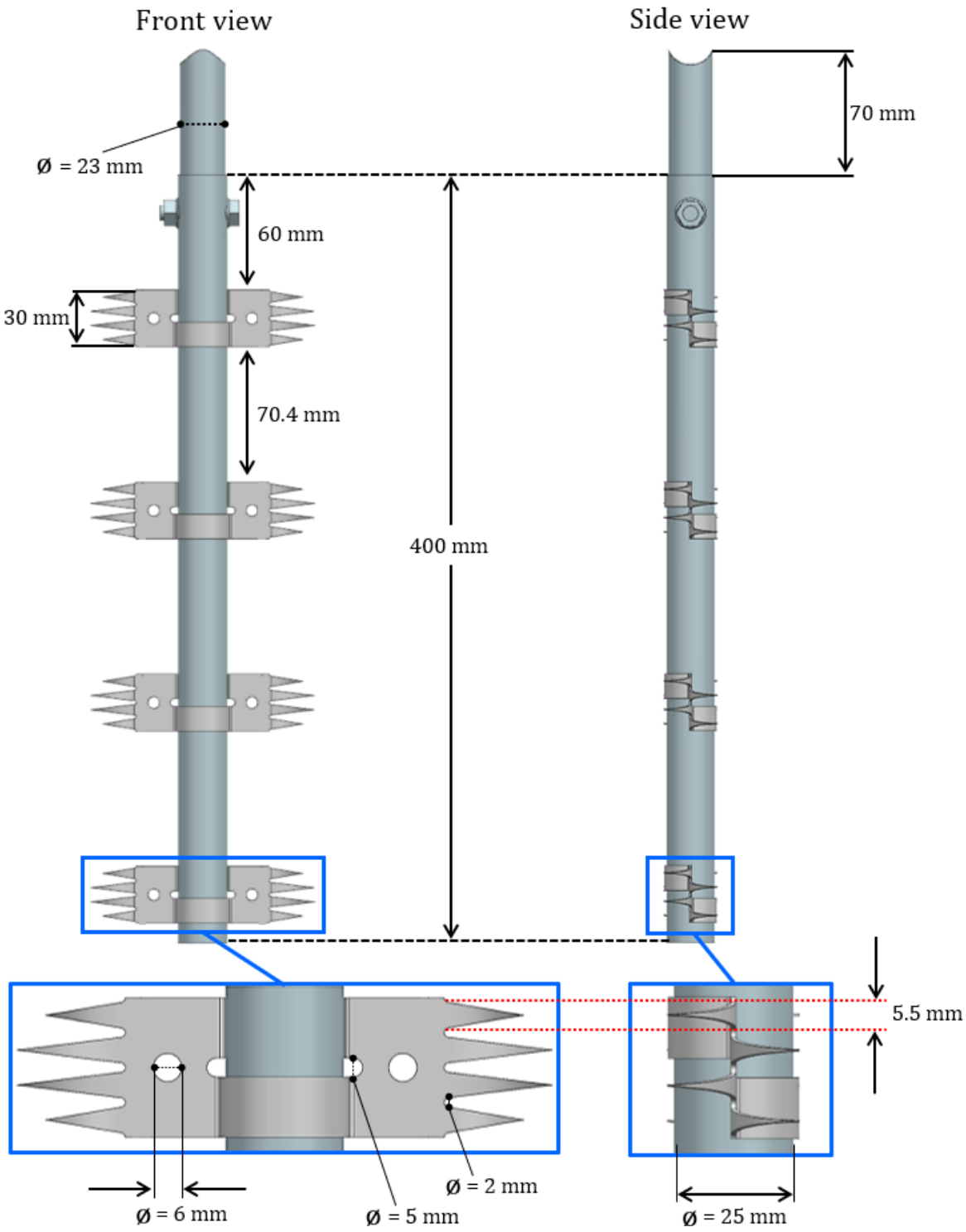

Figure B. 7. Dimensions for G-spike electrode with four spike assemblies

Figure B. 8 shows the dimensions of a G-spike electrode with three spike assemblies.

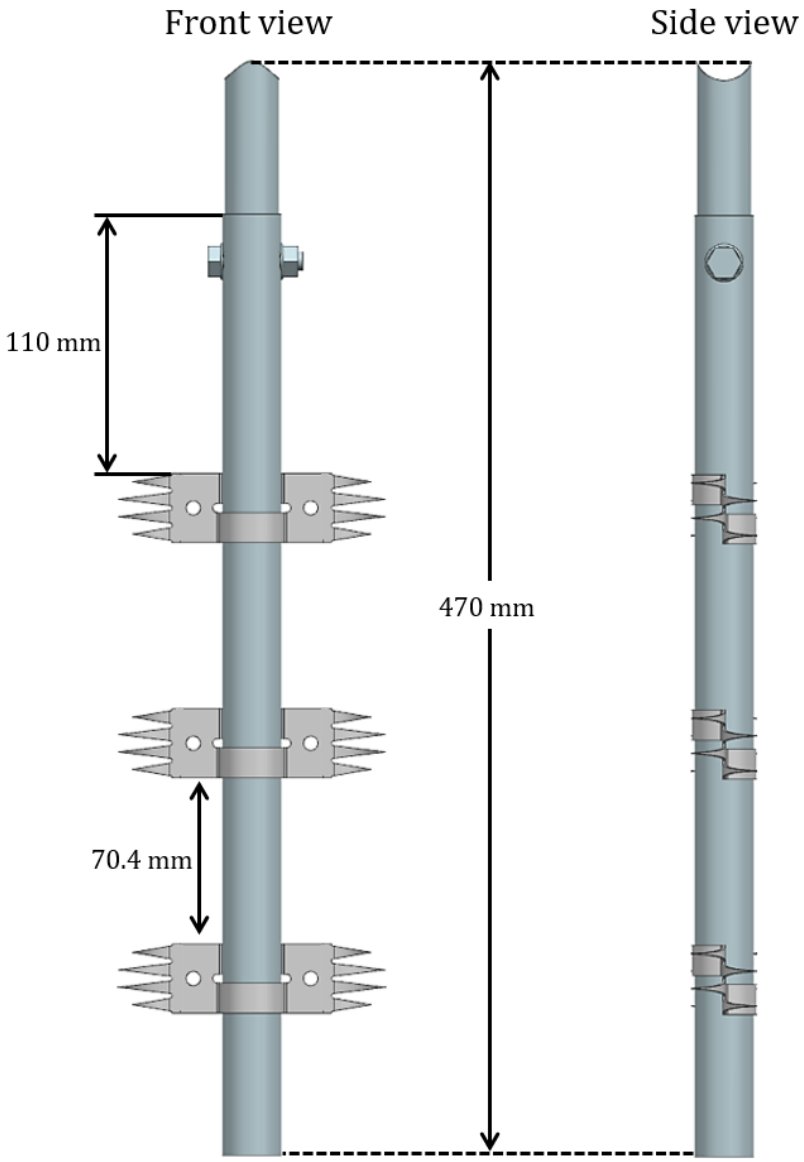

Figure B. 8. Dimensions for G-spike electrode with three spike assemblies

Figure B. 9 presents an isometric view of the G-spike electrodes with three and four spike assemblies.

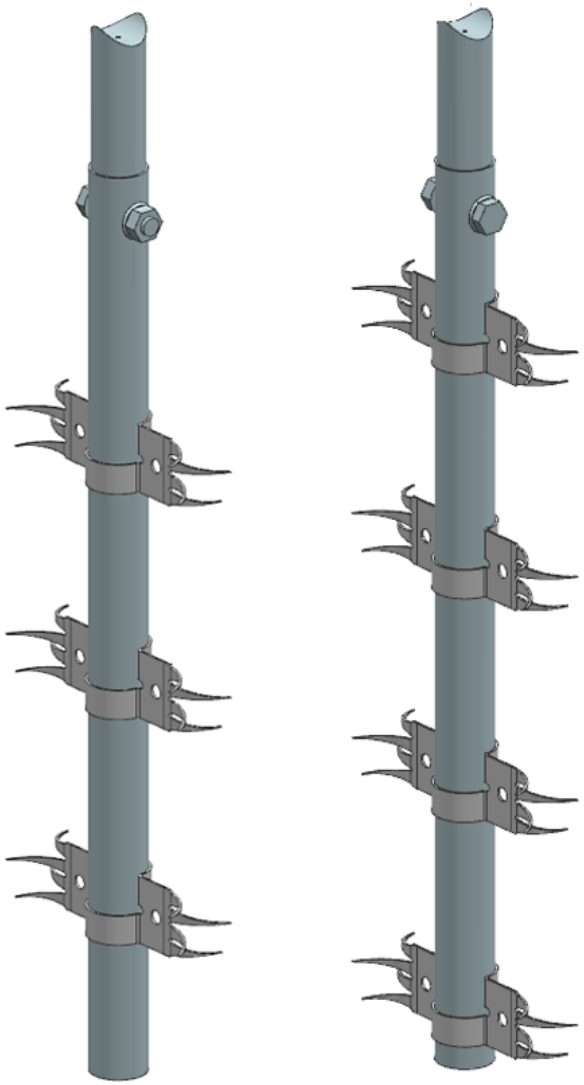

Figure B. 9. Isometric view of G-spike electrodes with (a) three spike assemblies and (b) four spike assemblies

The properties of a single spike assembly for the G-spike electrodes in Figures B. 7 – B. 9 are indicated in Figure B. 10.

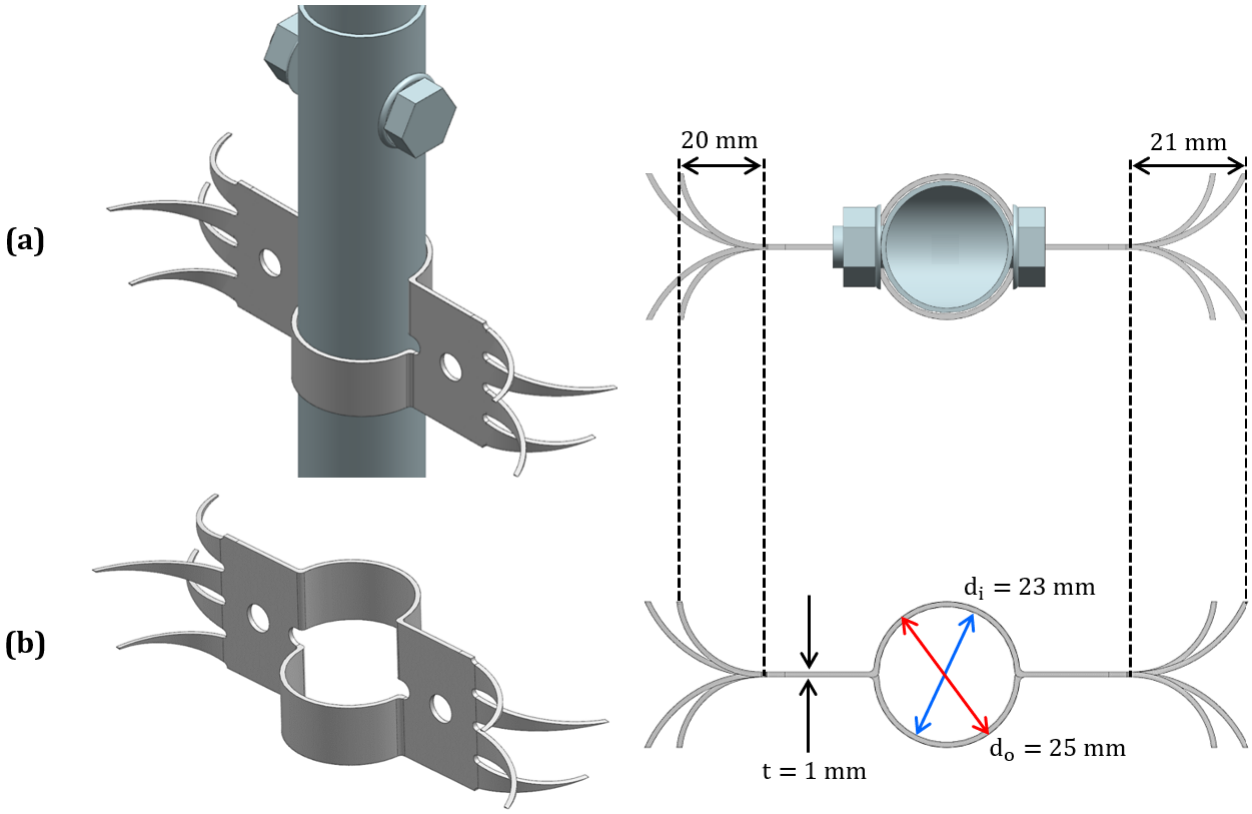

Figure B. 10. Dimensions for a single spike assembly of a G-spike electrode (a) on the electrode shaft and (b) without the electrode shaft

Table B. 8 provides the properties for the threaded rod electrode geometry.

Table B. 8. Properties of threaded rod electrode geometry

Property	Specification
Electrode shape	Threaded rod
Electrode length	400 mm
Thread diameter	5 mm
Thread pitch	0.8 mm

The threaded rod electrode dimensions in Table B. 8 are shown in Figure B. 11.

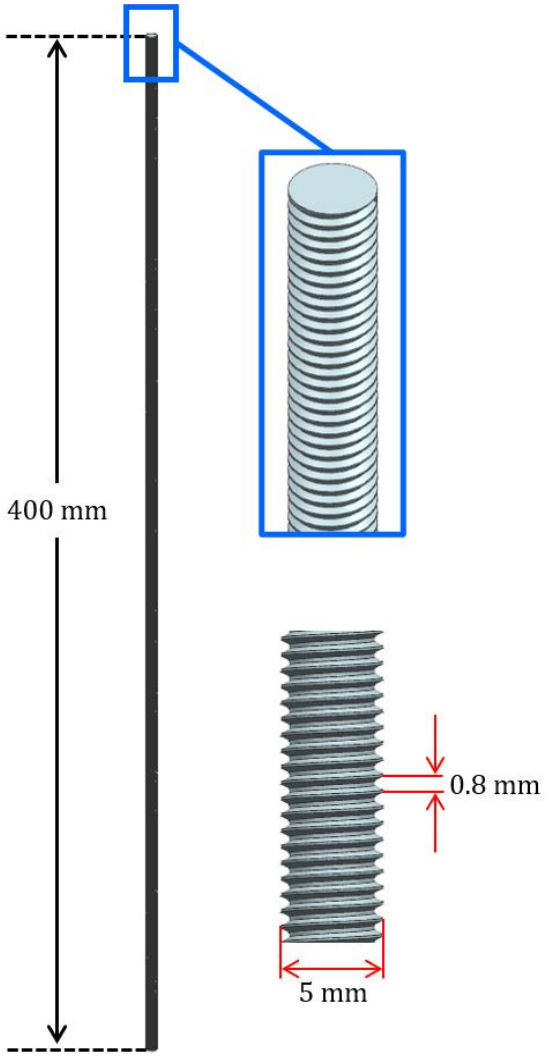

Figure B. 11. Dimensions for threaded rod electrode geometry

The ESP assembly presented in Figure 4-1 (Section 4.2.1) is shown from different points of view in Figure B. 12.

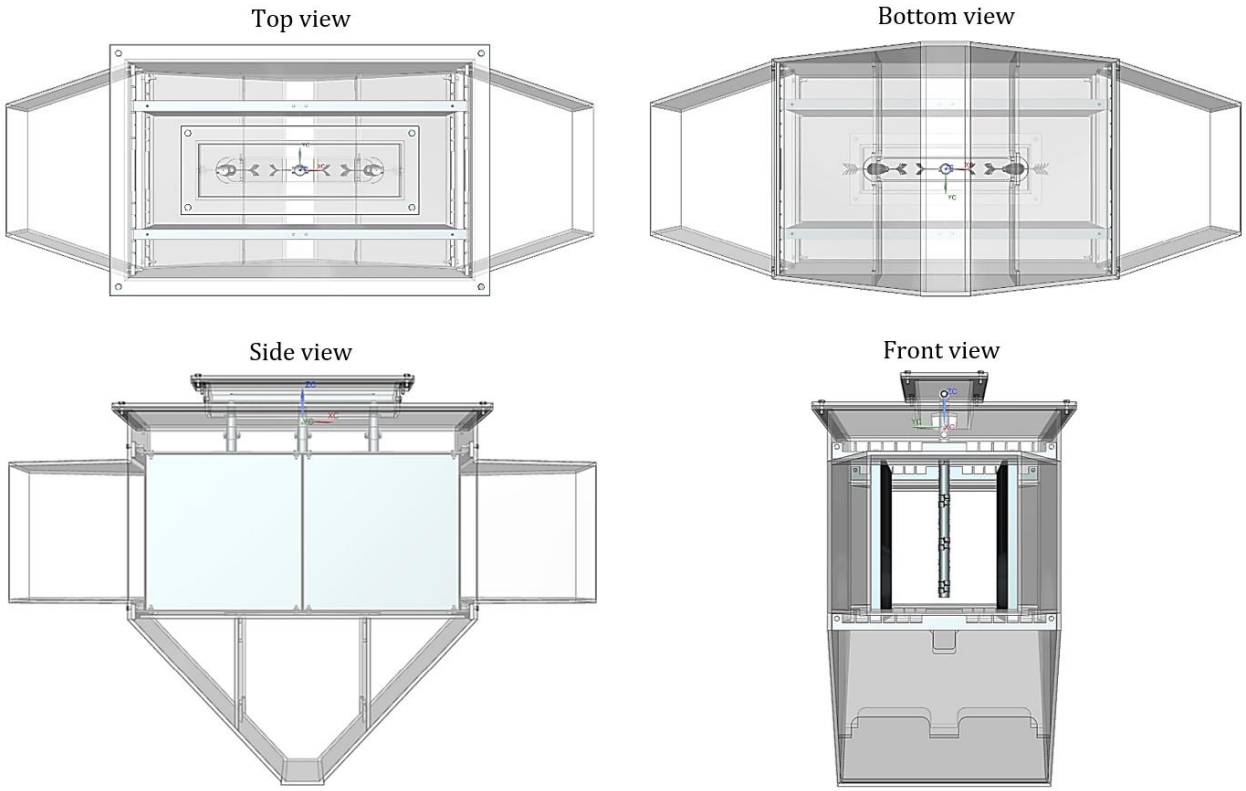

Figure B. 12. ESP section assembly from different viewpoints

The main dimensions for the ESP chamber are summarised in Table B. 9.

Table B. 9. Main dimensions for ESP chamber

Property	Specification
Material of construction	Plexiglass
Wall thickness	8 mm
Lid width	581 mm
Lid length	881 mm
Total lid height	102 mm
Chamber width	516 mm
Chamber length	816 mm
Chamber height	486 mm
Entrance / exit width	316 mm
Entrance / exit height	112 mm

The dimensions in Table B. 9 (and some additional dimensions) are indicated in Figure B. 13.

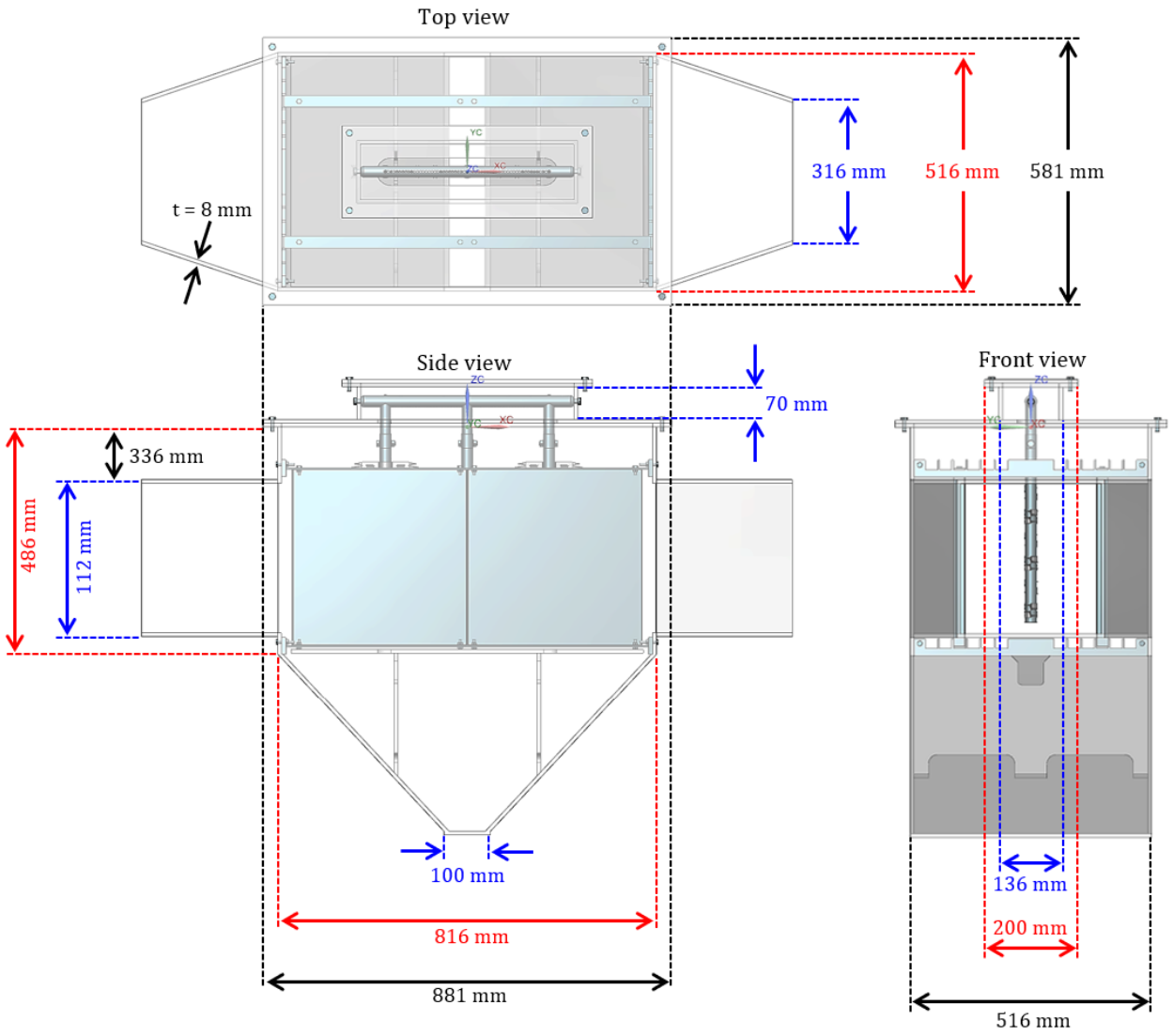

Figure B. 13. Dimensions for ESP chamber

The dimensions for the collection plates used in the ESP experiments are given in Table B. 10.

Table B. 10. Properties of collection plates

Property	Specification
Material of construction	Stainless steel
Total plate length	792 mm
Total plate height	383 mm
Plate width	25 mm
Plate thickness	1.3 mm
Top and bottom plate thickness	3.0 mm

The plate properties listed in Table B. 10 are demonstrated in Figure B. 14.

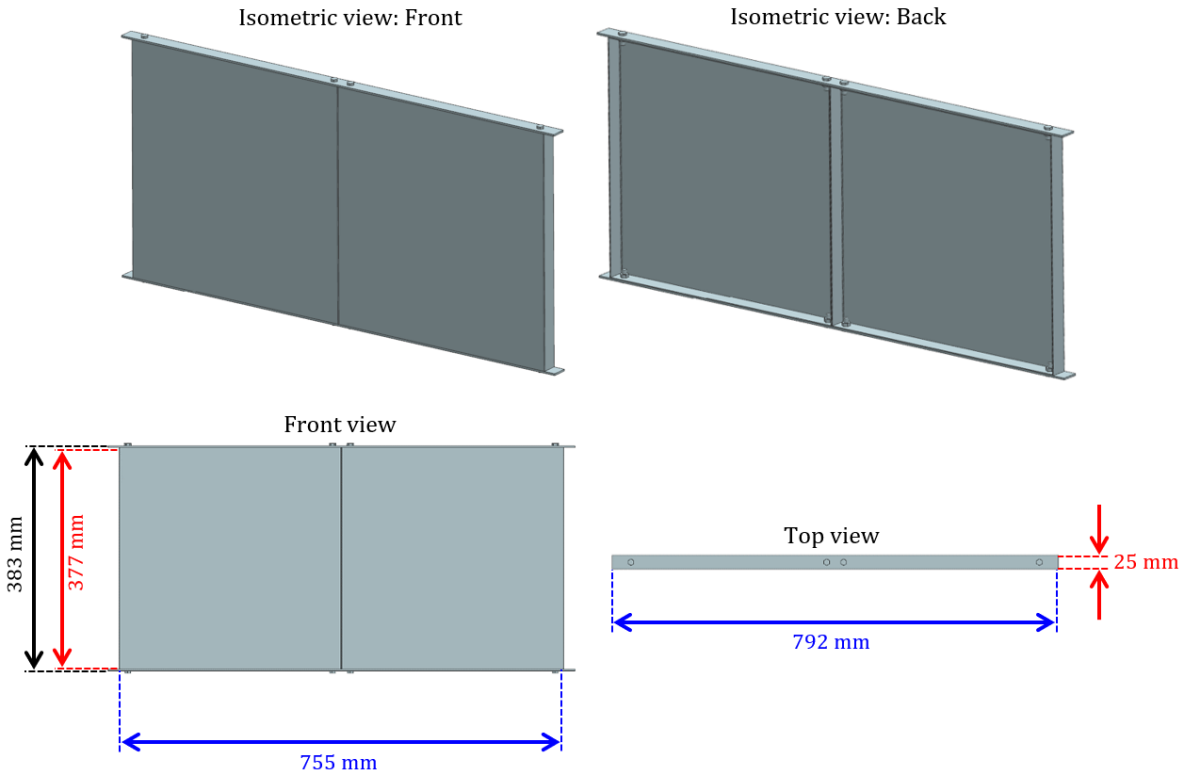

Figure B. 14. Dimensions for collection plates

The collection plates are rested upon four horizontal support bars positioned at the top and bottom on the opposite ends of the ESP chamber. The support bars are designed with equally spaced and sized slots into which the collection plates fit. The plate-plate distance is adjusted by shifting the collection plates between the slots across the support bars.

The properties and dimensions of the horizontal support bars are provided in Table B. 11.

Table B. 11. Properties of collection plate support bars

Property	Specification
Number of slots per side	6
Central bar width	100 mm
Slot width	26.5 mm
Slot spacing	3.5 mm
Possible plate spacings	100, 160, 220, 280, 340, and 400 mm
Total bar height	36 mm
Slot depth	20 mm
Total bar width	500 mm
Bar thickness	9.0 mm

The parameters in Table B. 11 are shown in Figure B. 15.

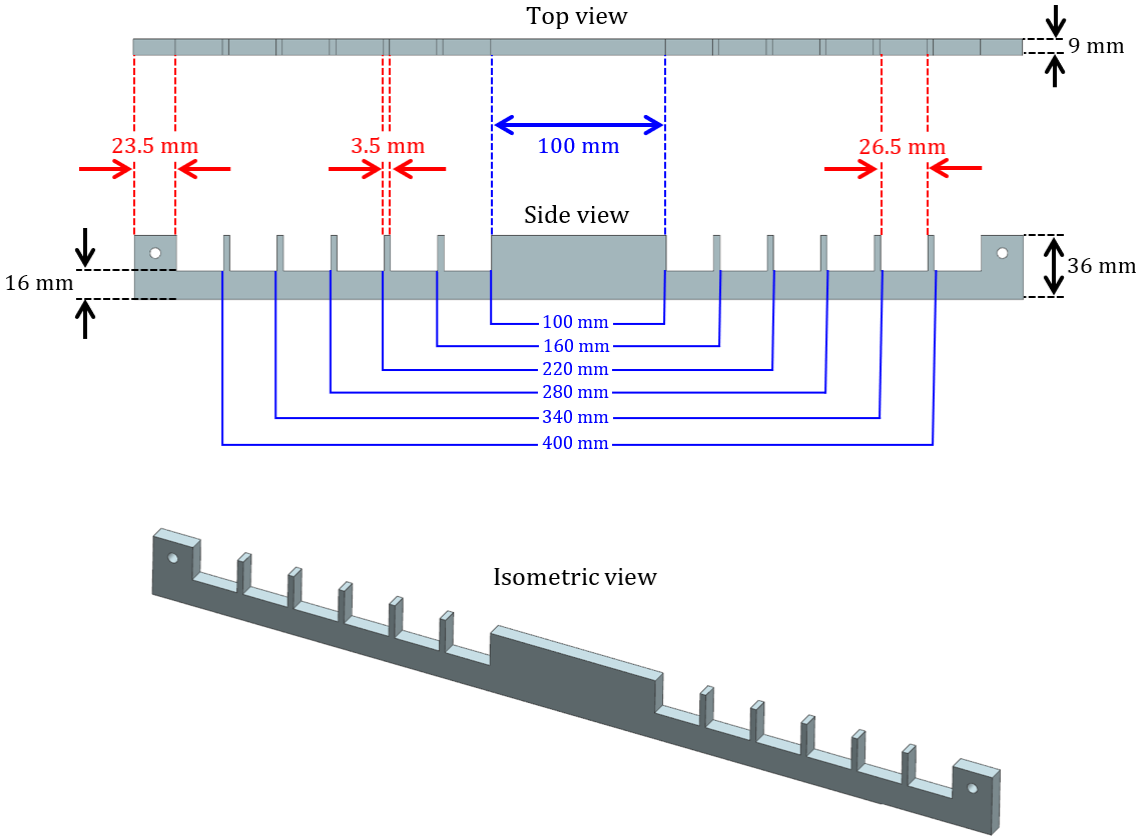

Figure B. 15. Dimensions for collection plate support bars

The discharge electrodes are also attached to an overhead support bar in the centre of the two collection plates. The support bar is connected to the power unit through a high-voltage cable to supply the discharge electrodes with direct current. The bar consists of a series of holes aligned at the top and bottom, which are used to adjust the positions of the electrodes on the bar to alter their spacings.

Table B. 12 includes a list of the properties of the discharge electrode support bar.

Table B. 12. Properties of discharge electrode support bar

Property	Specification
Number of holes (top and bottom)	57
Hole diameter	5.5 mm
Hole spacing	0.8 mm
Bar diameter	23 mm
Bar length	460 mm
Pipe thickness	1.0 mm

Some of the specifications in Table B. 12 are illustrated on the diagrams in Figure B. 16.

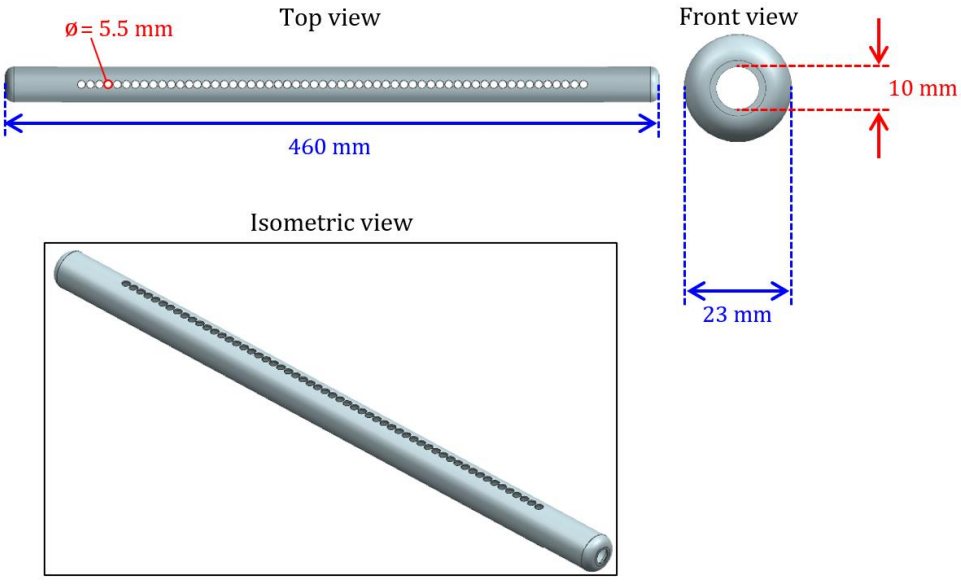

Figure B. 16. Dimensions for discharge electrode support bar

A plexiglass plate is positioned at the bottom of the ESP chamber to prevent the dust in the hopper from re-entering the air stream in subsequent experimental runs. The floor plate contains a central slot opening toward the hopper bin underneath the ESP section. Dust discards that fall onto the floor plate after being wiped off of the collection plate surfaces are scraped through the slot into the hopper. The properties of the ESP base plate are given in Table B. 13.

Table B. 13. Properties of floor plate in the ESP chamber

Property	Specification
Material of construction	Plexiglass
Plate width	498 mm
Plate length	760 mm
Plate thickness	8.0 mm
Slot width	60 mm
Slot length	389 mm

The floor plane dimensions are also indicated in Figure B. 17.

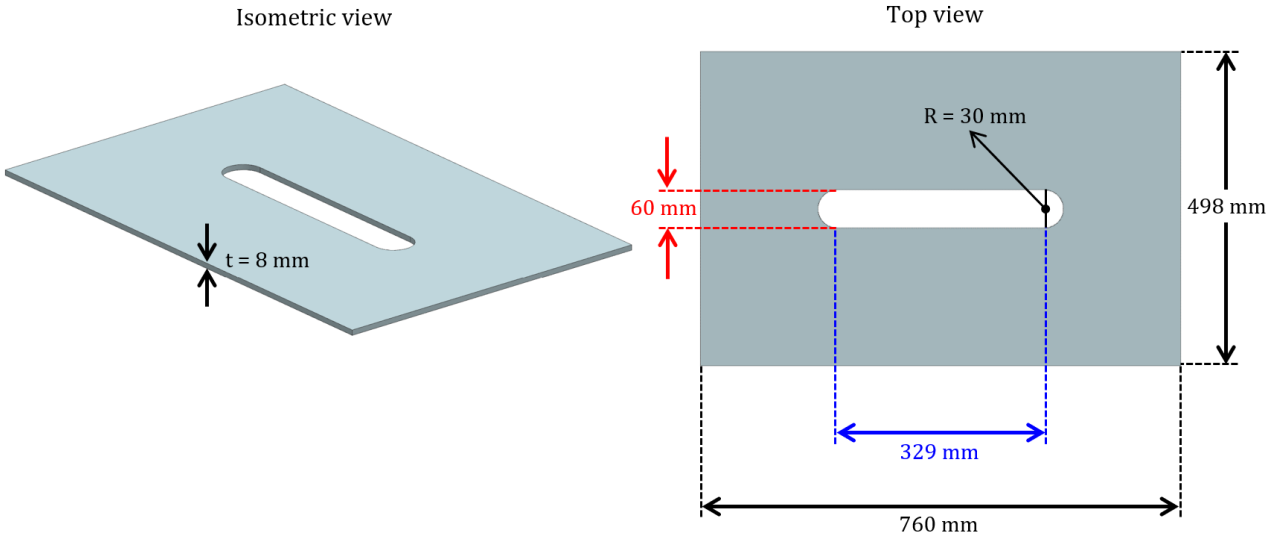

Figure B. 17. Dimensions of ESP floor plate

The floor plate in Figure B. 17 is supported by two vertical plates in the hopper bin. The dimensions of these support plates are demonstrated in Figure B. 18.

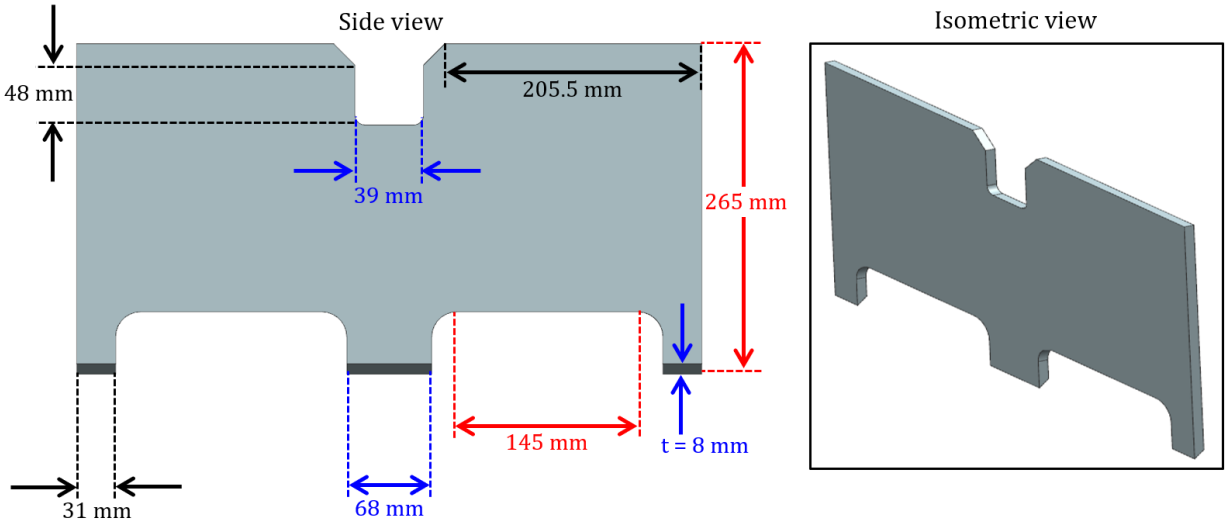

Figure B. 18. Dimensions of support plates for ESP floor plane

APPENDIX C : RESULTS

Appendix C gives information relevant to Chapter 5.

APPENDIX C-1. FLY ASH PROPERTIES

The PSD results obtained by Ribberink (2018) for the same ash samples used in this study are recorded in Table C. 1 [41].

Table C. 1. PSD results from Ribberink (2018) [41]

Ash sample	D_{10} (µm)	D_{50} (µm)	D_{90} (µm)
Fly ash A	4.7	13	155
Fly ash B	7.7	44	163

The XRF results obtained in this study compared to the results from Ribberink (2018) [41] are summarised in Table C. 2.

Table C. 2. Mineralogical composition of fly ash A and B obtained from XRF analysis

		This study		Ribberink	
Sample		**Fly ash A**	**Fly ash B**	**Fly ash A**	**Fly ash B**
Al_2O_3	**%**	30.2	26.6	30.4	27.2
CaO	**%**	4.40	3.45	4.3	3.4
Cr_2O_3	**%**	0.03	0.02	NP[*ii]	NP
Fe_2O_3	**%**	3.58	6.58	3.6	6.5
K_2O	**%**	0.70	0.83	0.7	0.8
MgO	**%**	0.97	1.08	1.0	1.0
MnO	**%**	0.02	0.08	<0.01	0.1
Na_2O	**%**	0.17	nd	0.4	<0.1
P_2O_5	**%**	0.36	0.39	0.3	0.4
SiO_2	**%**	57.3	59.1	57.2	58.5
TiO_2	**%**	1.53	1.29	1.5	1.3
V_2O_5	**%**	0.02	0.03	NP	NP
ZrO_2	**%**	0.06	0.06	NP	NP
BaO	**%**	0.09	0.13	NP	NP
SrO	**%**	0.10	0.05	NP	NP
ZnO	**%**	nd[*i]	0.02	NP	NP
SO_3	**%**	0.24	0.29	0.3	0.5

[*i] nd = not detected, [ii] NP = not provided.

The resistivities for the -75 µm and -150+75 µm size fractions of fly ash A and B are illustrated at different voltages in Figure C. 1.

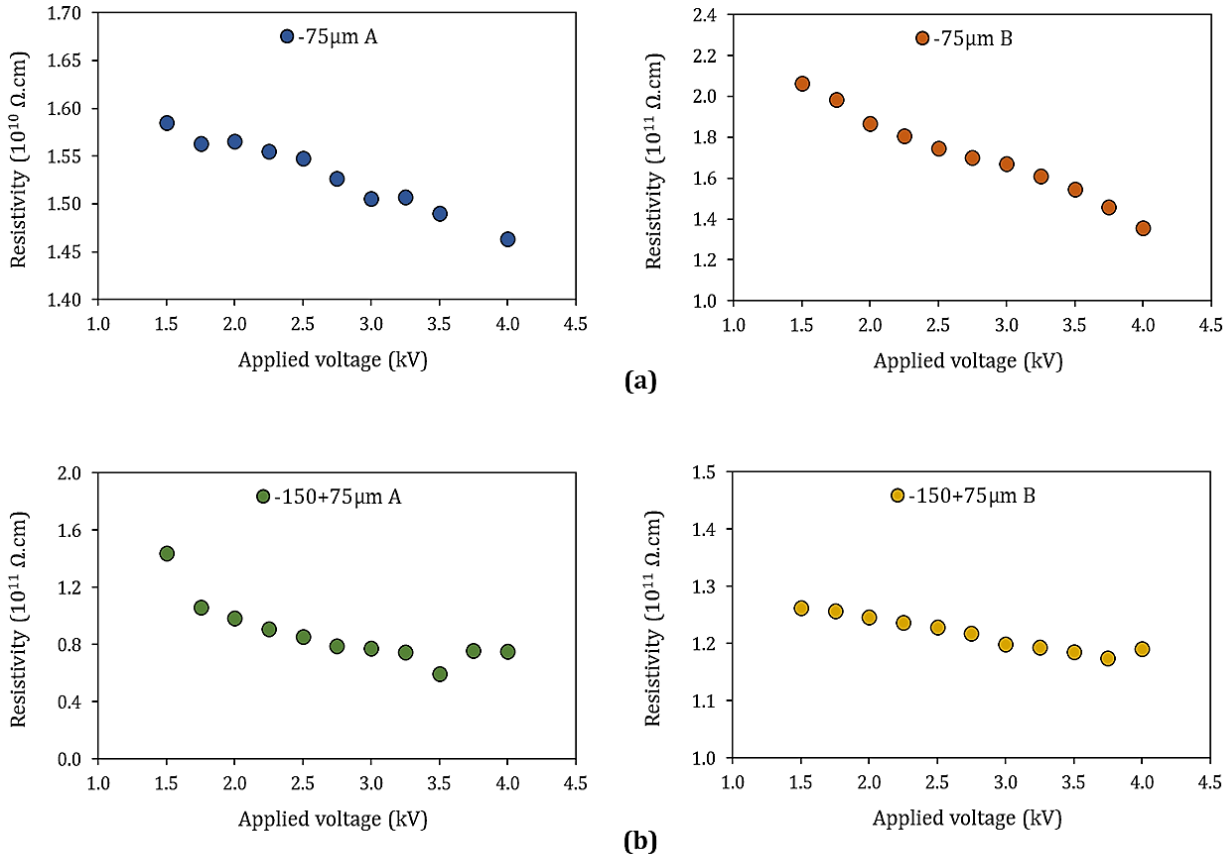

Figure C. 1. Resistivity of fly ash A and B at 1.5 – 4.0 kV for the (a) -75 µm and (b) -150+75 µm size fractions

The resistivity dependence on applied voltage is discussed in more detail in Section 5.1.4. As previously mentioned, ash B in the -75 µm size fraction shows a larger change in resistivity along the 1.5 – 4.0 kV voltage range than the -75 µm ash A. The opposite is true for the -150+75 µm size fraction, which shows a stronger relation between resistivity and applied voltage for ash A than for ash B. These observations are also evident from the relative sizes of the R^2-values on the current-voltage plots in Figure A. 2 (Appendix A-1.2). The smaller the R^2-value, the larger the deviation from linear current-voltage behaviour and, therefore, the larger the change in ash resistivity for a change in applied voltage.

The current-voltage plots for the -75 µm size range of ash A and B yielded R^2-values of 99.9% and 98.7%, respectively. Therefore, for the -75 µm size range, the resistivity of ash B is more susceptible to change with voltage than that of ash A. Conversely, the current-voltage plots show R^2-values of 99.5% for ash A and 99.9% for ash B in the -150+75 µm size fraction. Accordingly, ash A is more prone to resistivity change for a change in voltage than ash B in the -150+75 µm size range. This is consistent with the conclusions drawn from the resistivity-voltage plots in Section 5.1.4.

It is further stated in Section 5.1.4 that the resistivity decreases with an increase in voltage, due to the improved conduction resulting from the stronger electric field (Schottky effect). However, it was also noted in Appendix A-1.2 that this effect is small.

APPENDIX C-2. RSM MODELLING

Figure C. 2 illustrates the regression plot for the generalised RSM model from Section 5.2.1.

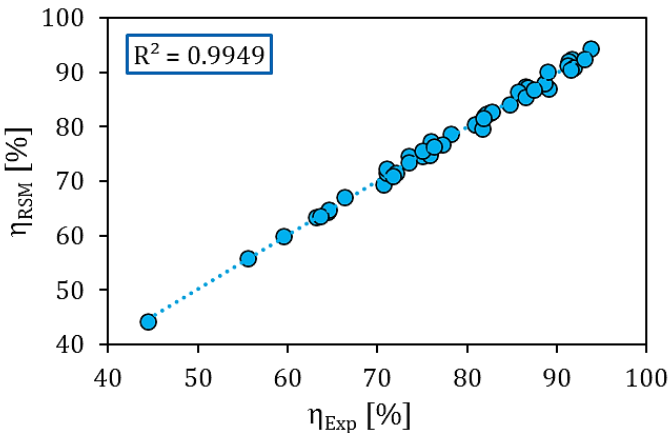

Figure C. 2. Regression plot for general RSM model

Table C. 3 provides the collection efficiency results obtained from the ESP experiments (η_{EXP}) and generalised RSM model (η_{RSM}) for different settings of the G-spike electrodes. The ESP settings are given in uncoded units, where PLTSP, ELCP, PMCONC, NOELEC, and TYPASH denote the plate spacing, electrode spacing, fly ash feed concentration, number of electrodes, and the type of ash, respectively. Furthermore, -75 A, -75 B, -150+75 A, and -150+75 B represent the -75 µm and -150+75 µm size fractions of the corresponding ash A and B.

Table C. 3. Generalised RSM model results for G-spike electrodes

Run	PLTSP (mm)	ELCSP (mm)	PMCONC ($mg.m^{-3}$)	NOELEC	TYPASH	η_{EXP} (%)	η_{RSM} (%)
G-1	160	112	3	3	-75 A	86.5	85.5
G-2	400	175	3	3	-150+75 B	63.6	63.7
G-3	280	144	13	2	-75 B	89.4	90.2
G-4	160	175	21	3	-75 B	91.5	90.5
G-5	280	144	13	2	-75 A	88.6	87.9
G-6	280	144	9	2	-150+75 B	87.4	86.9
G-7	160	175	31	3	-75 A	93.7	94.3
G-8	280	144	11	3	-75 A	88.9	90.0
G-9	400	112	22	3	-75 B	84.6	82.0
G-10	160	112	3.8	3	-75 B	93.1	92.5
G-11	400	112	25	3	-75 A	81.8	81.6
G-12	400	175	5	3	-75 A	76.3	76.4

Table C. 4 gives the experimental and RSM model efficiencies for various sawtooth electrode settings.

Table C. 4. Generalised RSM model results for sawtooth electrodes

Run	PLTSP (mm)	ELCSP (mm)	PMCONC ($mg.m^{-3}$)	NOELEC	TYPASH	η_{EXP} (%)	η_{RSM} (%)
S-1	220	164	5	3	-75 B	80.9	80.5
S-2	220	101	50	3	-75 B	75.0	74.6
S-3	220	101	6	3	-75 A	76.0	77.3
S-4	220	101	20	4	-75 A	86.5	87.5
S-5	220	57	20	3	-75 B	86.7	87.2
S-6	220	101	20	3	-75 B	91.6	92.5
S-7	220	164	7	3	-150+75 A	81.9	81.9
S-8	280	101	18	3	-75 B	91.3	92.0
S-9	220	101	29	3	-75 A	85.7	86.5
S-10	220	101	14	3	-75 B	91.2	91.2
S-11	220	101	13	3	-75 A	82.5	82.6
S-12	220	101	13	2	-75 B	89.1	87.0
S-13	280	101	26	3	-75 A	82.2	82.4
S-14	280	57	12	4	-75 A	75.8	74.8
S-15	220	101	3	3	-150+75 B	80.8	80.5
S-16	160	101	13	3	-75 A	84.8	84.2
S-17	220	101	13	2	-75 A	78.2	78.8
S-18	160	101	10	3	-150+75 A	82.8	82.8
S-19	220	101	13	4	-75 B	91.8	90.8

The ESP settings and collection efficiencies measured experimentally and calculated by the RSM model for the threaded rod electrodes are listed in Table C. 5.

Table C. 5. Generalised RSM model results for threaded rod electrodes

Run	PLTSP (mm)	ELCSP (mm)	PMCONC ($mg.m^{-3}$)	NOELEC	TYPASH	η_{EXP} (%)	η_{RSM} (%)
T-1	280	164	21	3	-75 A	70.7	69.4
T-2	280	164	3	2	-150+75 B	59.6	59.8
T-3	160	164	17	2	-75 B	73.5	74.7
T-4	280	57	20	2	-75 B	63.1	63.5
T-5	220	101	14	4	-75 B	81.7	79.8
T-6	160	57	20	6	-75 B	71.0	71.5
T-7	280	164	23	2	-75 B	71.1	72.2
T-8	280	57	5	4	-75 A	55.6	55.9
T-9	280	164	3	2	-150+75 A	64.4	64.4
T-10	160	57	23	4	-75 A	72.1	71.5
T-11	280	57	3	4	-75 B	54.2	47.4
T-12	160	112	4	2	-75 B	73.5	73.5
T-13	220	101	9	3	-150+75 B	75.0	75.6
T-14	160	164	23	2	-75 A	77.2	76.8
T-15	220	101	13	3	-75 A	71.7	70.9
T-16	220	101	9	4	-75 A	66.4	67.1
T-17	160	164	4	3	-75 A	64.6	64.7
T-18	280	57	13	2	-150+75 A	44.4	44.4
T-19	160	164	4	3	-75 B	79.4	68.77

The regression plot for the RSM model developed with respect to ash particle size (Section 5.2.2) is given in Figure C. 3.

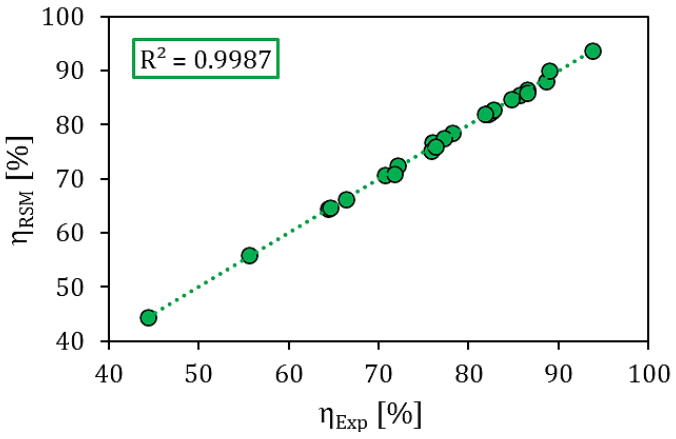

Figure C. 3. Regression plot for ash particle size RSM model

The model coefficients for the RSM model based on fly ash particle size is listed in Table C. 6.

Table C. 6. Model coefficients for RSM model in terms of fly ash particle size

First-order response							
β_1	β_2	β_3	β_4	a	b	β_5 c	d
-3.36	3.57	5.49	0.971	-0.61	0	0.61	0
Constant	**Block response**						
β_0	X_I	X_{II}	X_{III}				
83.9	10.4	-11.0	0.611				
Second-order response							
Interaction-1							
β_{11}	β_{12}	β_{13}	β_{14}	a	b	β_{15} c	d
-0.615	0.579	-0.515	2.30	0.31	0	-0.31	0
Interaction-2							
	β_{22}	β_{23}	β_{24}	a	b	β_{25} c	d
	-2.61	-0.473	-2.60	-1.29	0	1.29	0
Interaction-3							
		β_{33}	β_{34}	a	b	β_{35} c	d
		-2.41	1.67	-0.57	0	0.57	0
Interaction-4							
			β_{44}	a	b	β_{45} c	d
			-1.41	0	0	0	0

The regression plot for the RSM model developed with respect to fly ash resistivity (Section 5.2.3) is illustrated in Figure C. 4.

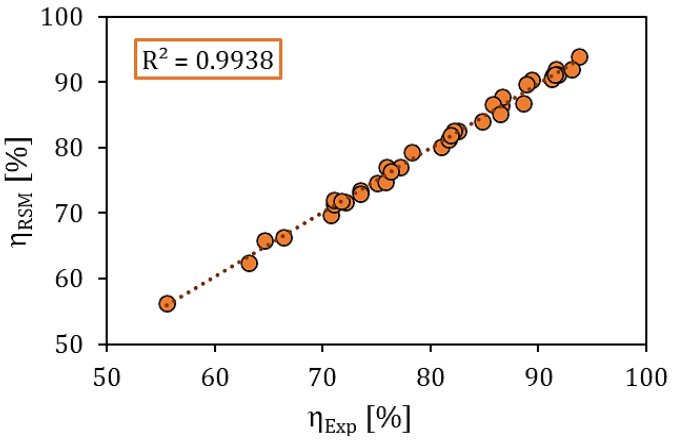

Figure C. 4. Regression plot for ash resistivity RSM model

Table C. 7 provides the model coefficients for the ash resistivity RSM model.

Table C. 7. Model coefficients for RSM model in terms of fly ash resistivity

First-order response							
β_1	β_2	β_3	β_4	a	b	β_5 c	d
-1.31	0.149	3.70	1.85	-3.19	3.19	0	0
Constant	**Block response**						
β_0	X_I	X_{II}	X_{III}				
86.7	9.88	-10.3	0.376				
Second-order response							
Interaction-1							
β_{11}	β_{12}	β_{13}	β_{14}	a	b	β_{15} c	d
-0.548	-0.156	-1.22	2.61	-1.27	1.27	0	0
Interaction-2							
	β_{22}	β_{23}	β_{24}	a	b	β_{25} c	d
	-2.92	-0.896	-1.82	1.73	-1.73	0	0
Interaction-3							
		β_{33}	β_{34}	a	b	β_{35} c	d
		-2.02	2.34	0.91	-0.91	0	0
Interaction-4							
			β_{44}	a	b	β_{45} c	d
			-1.41	-1.00	1.00	0	0

Figure C. 5 shows the current-voltage plots for runs S_{H-1}, S_{L-1}, S_{H-2}, S_{L-2}, G_H, and G_L that are evaluated in Section 5.2.3.

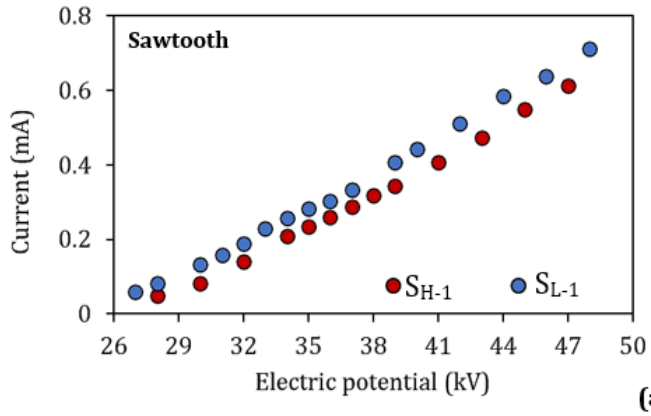

Run	S_{H-1}	S_{L-1}
Plate spacing (mm)	220	220
Electrode spacing (mm)	101	101
Ash loading (mg.Nm^{-3})	22	34
No. of electrodes	3	3
Ash resistivity (Ω.cm)	1.2E+11	1.7E+10
η_{EXP} (%)	91.6	85.7
η_{RSM} (%)	91.9	86.6

(a)

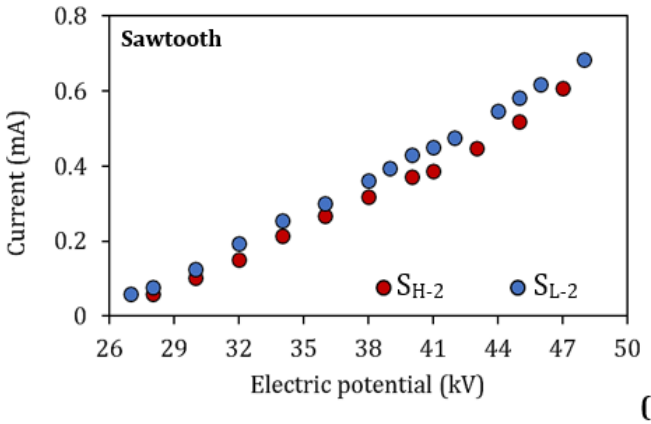

Run	S_{H-2}	S_{L-2}
Plate spacing (mm)	220	220
Electrode spacing (mm)	101	101
Ash loading (mg.Nm^{-3})	16	14
No. of electrodes	3	3
Ash resistivity (Ω.cm)	1.2E+11	1.7E+10
η_{EXP} (%)	91.2	82.5
η_{RSM} (%)	90.5	82.5

(b)

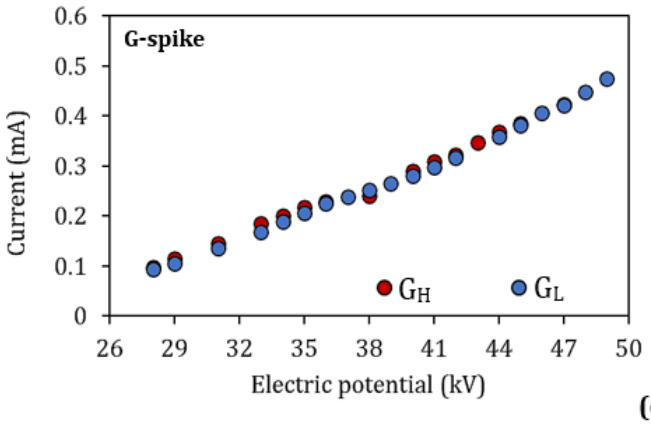

Run	G_H	G_L
Plate spacing (mm)	280	280
Electrode spacing (mm)	144	144
Ash loading (mg.Nm^{-3})	16	16
No. of electrodes	2	2
Ash resistivity (Ω.cm)	1.2E+11	1.7E+10
η_{EXP} (%)	89.4	88.6
η_{RSM} (%)	90.4	86.8

(c)

Figure C. 5. Current-voltage plots for different ash resistivities in S_{H-1}, S_{L-1}, S_{H-2}, S_{L-2}, G_H, and G_L

APPENDIX C-3. CFD MODELLING

Appendix C-3 contains information regarding additional results obtained from the CFD modelling.

C-3.1. Gravitational settling of -150+75 µm ash

In addition to the gravitational settling of the -75 µm ash discussed in Section 5.3.2, gravity-only runs were also performed for the ash in the -150+75 µm size fraction. However, since most of the particles in the -150+75 µm samples have sizes far beyond what the DustTrak monitors could detect, the corresponding concentration measurements obtained for this size range are not considered accurate. Therefore, the alternative gravimetric thimble measuring technique was used for the gravitational settling experiments with the -150+75 µm ash. The gravimetric measurement procedure is explained in Appendix A-2.4.

Table C. 8 shows the particle settling rates for the -150+75 µm ash, as well as the -75 µm ash from Section 5.3.2, as measured by the DustTrak monitors and gravimetric thimbles.

Table C. 8. Gravitational settling rates for -75 and -150+75 µm ash measured by DustTraks and thimbles

Run	Electrode shape	Plate spacing (mm)	Electrode spacing (mm)	No. of electrodes	Ash PSD (µm)	Average settling rate (%)	
						DustTrak	Thimble
GR-1	None	N/A	N/A	N/A	-75	34.3	36.7
GR-2	Sawtooth	400	164	2	-75	38.6	28.5
GR-3	G-spike	160	112	3	-75	34.9	21.6
GR-4	None	N/A	N/A	N/A	-150+75	26.6	56.3
GR-5	Sawtooth	400	164	2	-150+75	30.1	43.4
GR-6	G-spike	160	112	3	-150+75	31.4	49.8

It is clear from Table C. 8 that the gravimetric determination of particle settling rates yielded notably different results than the DustTrak readings for the -150+75 µm ash. When considering the thimble measurements, the settling rates for larger particles are 15 – 20% higher than that of the finer particles. On the contrary, the DustTrak results indicate lower settling rates for the -150+75 µm fraction than the -75 µm particles.

In this case, the thimble data seems more reasonable, given that gravitational forces are stronger for coarser particles of larger mass, resulting in higher settling velocities. This statement is supported by Richards (2000), who obtained settling velocities between 19 – 70 $cm.s^{-1}$ for particles in the range of 80 – 200 µm, and settling velocities lower than 8 $cm.s^{-1}$ for particles smaller than 50 µm [19]. These results also confirm that the reasoning from the RSM modelling section (Section 5.2.2) was correct.

Therefore, the thimble data was used as reference for the modelling of the gravitational settling rates of particles in the -150+75 µm size fraction. For consistency, the thimble values were also used for the -75 µm ash in the gravity runs, and correspond to the values in Table 5-12 from Section 5.3.2.

In contrast to the -75 µm particles that show decreased settling rates for more obstructed flow regions (see Section 5.3.2), no specific trend is observed with relation to the level of obstruction in the ESP for the -

150+75 µm particles. This shows that, unlike small particles, the settling rate of large particles is controlled by gravity, rather than the pressure drop and air turbulence across the ESP section.

The average particle settling rates for runs GR-2, GR-3, GR-5, and GR-6 computed by the CFD model were compared to the thimble data and the results are summarised in Table C. 9.

Table C. 9. Modelled settling rates versus thimble values in gravity runs

Run	Average settling rate (%)	
	Thimble measurement	**Computational model**
GR-2	28.5	28.8
GR-3	21.6	20.1
GR-5	43.4	89.5
GR-6	49.8	91.8

As seen in Table C. 9, the computational model obtained a satisfactory degree of accuracy for runs GR-2 and GR-3 that involve the -75 µm ash. The simulated settling efficiencies for GR-2 and GR-3 differ from experimental data by only 0.3 % and 1.5 %, respectively. On the other hand, for the runs with -150+75 µm ash (GR-5 and GR-6), the model overestimates the settling efficiencies by 40 – 50 %. This suggests that the model fails to account for problems associated with coarser ash, such as re-entrainment and particles rebounding from the collection plates and ESP floor plane.

The particle flow paths and settling trends for the sawtooth electrodes in GR-2 and GR-5 are illustrated by the particle tracks in Figure C. 6.

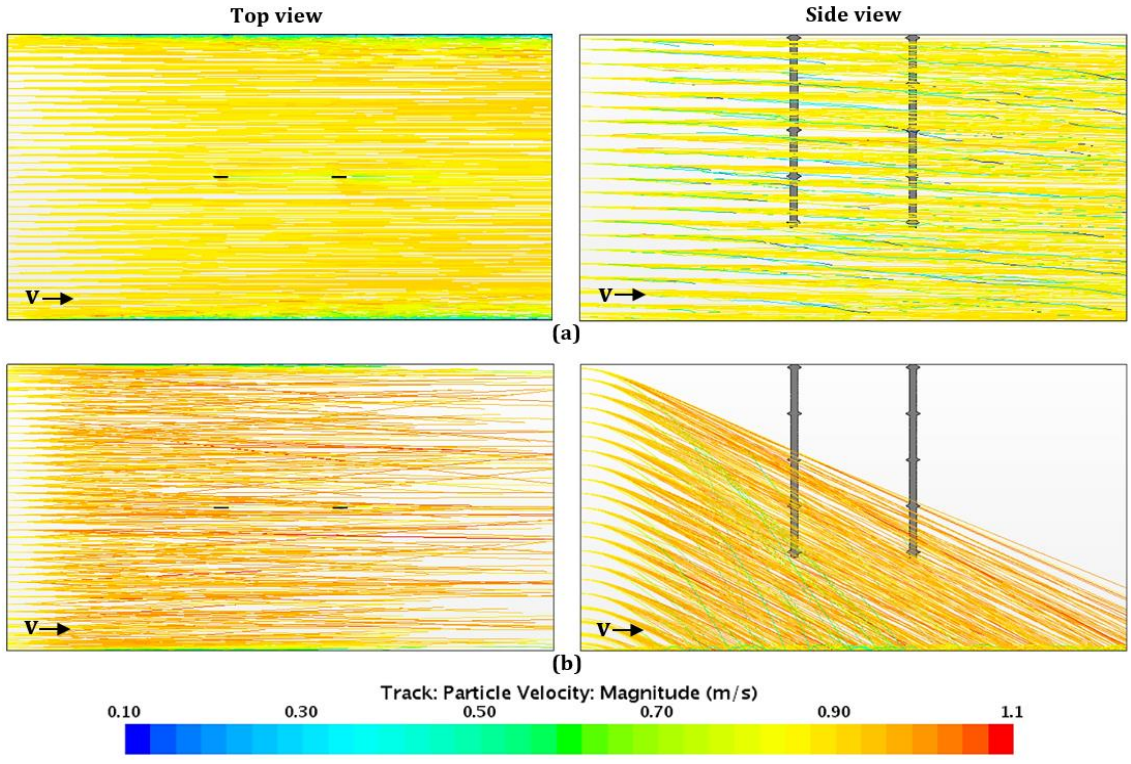

Figure C. 6. Particle track velocities for **(a)** GR-2 and **(b)** GR-5

The particle flows and settling velocities in the ESP setup with three G-spike electrodes (GR-3 and GR-6) are portrayed in the particle tracks from Figure C. 7.

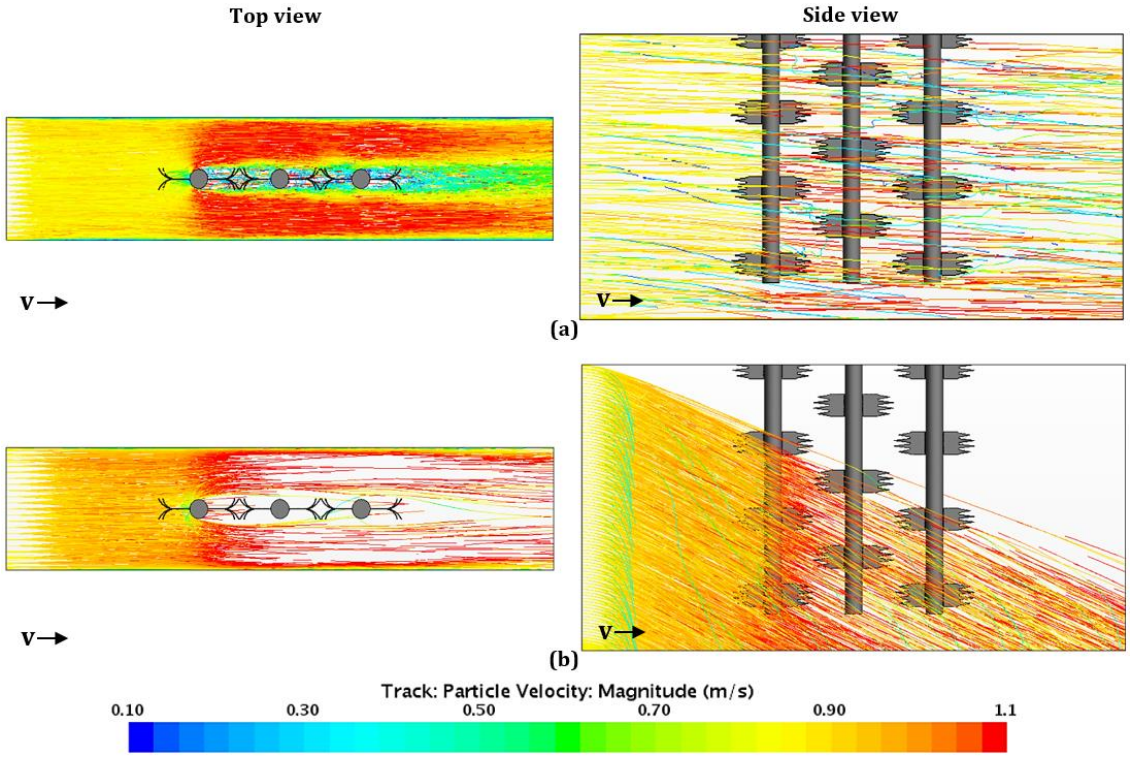

Figure C. 7. Particle track velocities for **(a)** GR-3 and **(b)** GR-6

Turbulence was not a major concern with the -150+75 µm particles, for which gravitational forces were large enough to far exceed the particles' dependence on air flow. Therefore, large particles settled out of the air stream, no matter the degree of turbulence in the air. In fact, it seems as if some particles instantly dropped to the ESP floor upon impact with the first G-spike electrode. This is visualised by the strong downward trends for the -150+75 µm particles in the side views of Figure C. 6 (b) and Figure C. **7** (b)

The smaller particles in the -75 µm size fraction, on the other hand, were more subjected to air flow patterns. As mentioned in Section 5.3.2, the flow paths of the -75 µm particles are equally dependent on the forces associated with the air conditions, turbulence, and pressure drop over the ESP as they are on gravity. This is demonstrated by the particle tracks, indicating smooth, linear trajectories paths for the laminar flow regime in Figure C. 6 (a), and sporadic movements for the turbulent flow in Figure C. **7** (a). These observations are supported by the literature of White (1977) [17]. This confirms that electrode settings and air conditions in the ESP typically show larger effects on the collection rates of fine ash particles relative to coarse ash particles.

APPENDIX C-4. EMPIRICAL MODELLING

Table C. 10 provides the empirical model results for ESP different configurations involving G-spike electrodes.

Table C. 10. Empirical model efficiency results and parameters for G-spike electrodes

Run	Pltsp (mm)	Elcsp (mm)	PMConc ($mg.m^{-3}$)	No. Elec	Ash	η_{Exp} (%)	η_D (%)	η_M (%)	k	w ($m.s^{-1}$)
g-1	160	N/A	29	1	-75 A	81.4	99.0	82.9	0.45	0.77
g-2	160	112	3	3	-75 A	86.5	98.3	89.1	0.63	0.74
g-3	280	144	13	2	-75 B	89.4	95.4	90.4	0.85	0.49
g-4	160	175	21	3	-75 B	91.5	97.4	92.8	0.79	0.77
g-5	280	144	13	2	-75 A	88.6	94.9	90.0	0.85	0.47
g-6	400	N/A	22	1	-75 B	83.4	90.4	83.6	0.87	0.33
g-7	160	175	31	3	-75 A	93.7	97.1	95.4	0.91	0.71
g-8	400	N/A	24	1	-75 A	86.0	87.5	86.3	0.98	0.29
g-9	280	144	11	3	-75 A	88.9	93.1	89.9	0.91	0.43
g-10	400	112	22	3	-75 B	84.6	86.4	84.7	0.97	0.28
g-11	400	N/A	6	1	-75 B	79.0	90.4	78.9	0.79	0.33
g-12	160	N/A	5	1	-75 A	71.8	98.9	72.2	0.28	0.77
g-13	160	112	3.8	3	-75 B	90.8	99.0	93.2	0.68	0.83
g-14	160	N/A	3	1	-75 B	78.2	99.2	78.7	0.38	0.76
g-15	400	112	25	3	-75 A	81.8	83.7	82.3	0.98	0.26
g-16	160	N/A	26	1	-75 B	76.3	82.7	76.6	0.90	0.25

Table C. 11 provides the empirical model results for various ESP settings with sawtooth electrodes.

Table C. 11. Empirical model efficiency results and parameters for sawtooth electrodes

Run	Pltsp (mm)	Elcsp (mm)	PMConc ($mg.m^{-3}$)	No. Elec	Ash	η_{Exp} (%)	η_D (%)	η_M (%)	k	w ($m.s^{-1}$)
s-1	220	57	21	3	-75 A	80.3	98.8	80.8	0.43	0.76
s-2	220	101	6	3	-75 A	76.0	98.1	76.1	0.43	0.66
s-3	220	101	20	4	-75 A	86.5	98.3	87.2	0.60	0.71
s-4	220	57	20	3	-75 B	87.1	99.3	88.2	0.49	0.90
s-5	220	101	20	3	-75 B	91.6	99.0	92.0	0.65	0.77
s-6	280	101	18	3	-75 B	91.3	98.2	91.5	0.74	0.60
s-7	220	101	29	3	-75 A	85.7	98.1	86.6	0.61	0.67
s-8	220	101	14	3	-75 B	91.2	99.0	92.0	0.65	0.78
s-9	220	101	13	3	-75 A	82.5	98.4	83.0	0.50	0.73
s-10	220	101	13	2	-75 B	89.1	99.4	90.2	0.54	0.88
s-11	280	101	26	3	-75 A	82.2	96.8	82.6	0.64	0.52
s-12	280	57	12	4	-75 A	75.8	97.3	76.0	0.51	0.54
s-13	160	101	13	3	-75 A	84.8	99.4	85.0	0.44	0.85
s-14	220	101	13	2	-75 A	78.2	98.2	78.7	0.47	0.64
s-15	220	101	13	4	-75 B	91.8	99.0	91.8	0.62	0.85

Table C. 12 provides the empirical model results for different ESP settings with threaded rod electrodes.

Table C. 12. Empirical model efficiency results and parameters for threaded rod electrodes

Run	Pltsp (mm)	Elcsp (mm)	PMConc ($mg.m^{-3}$)	No. Elec	Ash	η_{Exp} (%)	η_D (%)	η_M (%)	k	w ($m.s^{-1}$)
t-1	280	164	21	3	-75 A	70.7	99.1	70.7	0.32	0.66
t-2	280	57	20	2	-75 B	63.1	99.1	63.1	0.21	0.66
t-3	220	101	14	4	-75 B	81.0	99.9	80.5	0.24	1.03
t-4	280	164	23	2	-75 B	71.1	99.2	71.0	0.31	0.68
t-5	280	57	5	4	-75 A	55.6	98.9	55.6	0.13	0.63
t-6	280	164	3	2	-150+75 A	64.4	100	88.4	0.10	1.79
t-7	160	57	23	4	-75 A	72.1	100	86.5	0.13	1.57
t-8	160	112	4	2	-75 B	73.5	100	85.7	0.13	1.52
t-9	220	101	9	3	-150+75 B	75.0	100	95.8	0.10	2.65
t-10	160	164	23	2	-75 A	77.2	100	77.7	0.01	1.49
t-11	220	101	13	3	-75 A	71.7	99.9	71.7	0.15	0.96
t-12	220	101	9	4	-75 A	66.4	99.9	66.3	0.07	0.96
t-13	160	164	4	3	-75 A	64.6	99.8	65.2	0.10	0.88
t-14	160	57	5	2	-75 A	65.0	100	84.9	0.13	1.49
t-15	160	164	4	3	-75 B	79.4	100	79.1	0.06	1.40